REPLICATING THE INTRINSIC BIOMECHANICAL CHARACTERISTICS OF CONNECTIVE TISSUE: AN EXPLORATION INTO THE DESIGN AND MANUFACTURE OF PVA CRYOGEL

By

Joseph Patrick Crolla

A thesis submitted to the University of Birmingham for the degree of

DOCTOR OF PHILOSOPHY

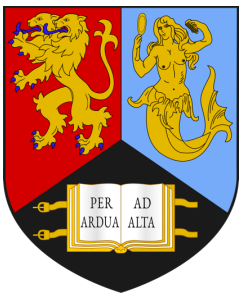

School of Engineering

College of Engineering and Physical Sciences

University of Birmingham

March 2022

ABSTRACT

Damage and disease of connective tissue (CT) pose a risk to an increasing percentage of the population, and the ability to develop biocompatible polymers that better replicate the intrinsic properties of CT would aid in improving the function of CT replacements. Poly(Vinyl Alcohol) (PVA) cryogel is a particularly versatile biomaterial because it has 'tuneable' mechanical properties which can mimic a wide range of soft tissues. PVA is compatible with magnetic resonance (MR) imaging; allowing tissue implants to be monitored non-invasively. PVA is compatible with novel sub-zero temperature additive manufacturing (AM) techniques, which provides considerably greater freedom in the design process, as well as social and economical benefits to implant manufacture. The overarching aim of this thesis is to explore the design for additive manufacture, and intrinsic material properties of PVA cryogels, with respect to their use as physical models of connective tissue.

Viscoelastic and MR T_2 characterisation was conducted to assess the relationship between PVA composition and its viscoelastic behaviour under dynamic loading,representing physiological conditions, and the relationship between composition and MR T_2 relaxation time. The AM of PVA has been progressed through a bio-inspired approach to control the 3D printing toolpath, allowing for the introduction of anisotropic and functionally graded material behaviour. This has been achieved through the analysis of key AM process parameters, and the development of a parametric method to vary the infill geometry, and in turn the mechanical properties of AM PVA.

This thesis establishes a composition-dependent correlation between the viscoelastic moduli and MR T_2 relaxation time. This thesis has also shown that AM PVA samples exhibit pronounced orthotropic properties; with the smallest nozzle size tested showing a ≈30% decrease in viscoelastic moduli when tested perpendicular to the print direc-

tion. Samples with custom infill geometries were successfully manufactured, and the empirically derived relationships have been shown between parameters used to define the toolpath shape, and hyperelastic mechanical properties.

Critically, this thesis has explored the design and manufacture of PVA cryogels; for the first to time assessing its viscoelastic properties under physiological loading, and defining bio-inspired AM methods to introduce and control orthotropic and functional graded properties intrinsic to CT.

ACKNOWLEDGMENTS

Dr Lauren Thomas-Seale, Dr Daniel Espino and Dr Melanie Britton for the many years of constant support, help, and advice (and free coffees).

Katie for somehow keeping me sane, Sanj for the free life coaching, and the rest of the biomed engineering group for making a dingy basement feel like home.

The Britton group, especially Claire and Gabrielle, for the patience to teach an engineer how MRI works.

My parents for always being there for me, and (not so much) for the "Are you done yet?" questions to keep me on track.

Dr & Dr Lewis for being the best role models a brother could ask for.

The Engineering and Physical Sciences Research Council (EPSRC) for funding my doctoral research (Grant no. EP/N509590/1).

PUBLICATIONS

The following novel papers have been presented in this thesis in chapters 3 and 4. Further information is included prior to their inclusion.

J. P. Crolla, M. M. Britton, D. M. Espino, L. E. J. Thomas-Seale, The dynamic viscoelastic characterisation and magnetic resonance imaging of poly(vinyl alcohol) cryogel: Identifying new attributes and opportunities, *Materials Science and Engineering: C*, 2021. DOI: https://doi.org/10.1016/j.msec.2021.112383.

J. P. Crolla, M. M. Britton, D. M. Espino, and L. E. J. Thomas- Seale. The orthotropic viscoelastic characterisation of sub-zero 3D-printed poly-(vinyl alcohol) cryogel. *MRS Advances*, 2021. DOI: https://doi.org/10.1557/s43580-021-00086-1.

OTHER PUBLICATIONS

J. P. Crolla, B. M. Lawless, A. A. Cederlund, R. M. Aspden, D. M. Espino. Analysis of hydration and subchondral bone density on the viscoelastic properties of bovine articular cartilage, *BMC Musculoskeletal Disorders*, 2022. DOI: https://doi.org/10.1186/s12891-022-05169-0.

CONFERENCES

J. P. Crolla, K. L Fegan, M. M. Britton, L. E. J. Thomas-Seale. The dynamic viscoelastic Characterisation and Imaging of Poly(Vinyl Alcohol) Cryogel. *25th Congress of the European Society of Biomechanics*. July 2019.

CONTENTS

LIST OF FIGURES

LIST OF TABLES

Dedicated to my family

"The quality of a person's life is in direct proportion to their commitment to excellence, regardless of their chosen field of endeavor."

— Vince Lombardi

Chapter 1

INTRODUCTION

This chapter aims to introduces the background literature pertinent to this thesis. This focuses on the role and structure of connective tissues (section 1.2); an overview of biomaterials, and a literature review of potential materials for CT replacement (section 1.3); the current uses of PVA cryogels, and its suitability to replace CT (section 1.3.4); a literature review on the status of additive manufacture of PVA (section 1.4); as well as an overview of imaging techniques used to analyse PVA. (section 1.5).

1.1 Clinical and economic importance of engineering novel biomaterials

The development of biomaterials for novel clinical applications offers significant social and economic impact. For example, damage to connective tissues of the human body impact on the quality of life, and life expectancy of a large percentage of the world population [12, 13]. Connective tissues include arterial tissues, articular cartilage, and bone among others. These tissues have a role in mechanical loading as they

typically bind, support and/or protect other tissues and organs in the human body. Cardiovascular Disease (CVD) was responsible for 164,000 deaths in the UK in 2019, and accounts for 27% of total deaths recorded [14]. Osteoarthritis (OA), a degenerative disease of synovial joints, is another prevalent example of connective tissue damage. In the USA, 1.5M hip and knee joint replacements were predicted for 2020, compared to 700,000 performed in 2012 [15].

It is apparent that the clinical impact of connective tissue damage and disease is heavy and ever increasing. The surgical intervention, often required to repair or replace diseased damaged tissue, poses an enormous and increasing cost to the worldwide economy. In 2017, CVD cost the UK economy £28 billion [12]. The total cost of CVD in the USA was $555 billion in 2016; in line with increasing population and obesity rates. This figure is projected to be $1.1 trillion per year by 2035 [13]. The design and engineering of biomaterials which better mimic the function of CT is one solution to providing precision healthcare to a growing section of the population.

Mechanical testing is a fundamental technique used to characterise the stiffness, hyperelasticity [16, 17, 18, 19, 20, 21] and viscoelasticity [22, 23, 24, 25, 26, 27, 28] of CT. It also allows for the assessment of the failure modes of CT [29, 30, 31, 25], and the impact of physiological changes caused by disease on the function of CT [32, 16, 20]. Most importantly to this thesis, mechanical testing is also crucial in assessing and characterising synthetic biomaterials for use as physical models of CT [33, 34, 35, 36].

Tissue mimicking phantoms are an efficient and cost effective method of experimentally simulating the design, development and testing of novel diagnosis or intervention techniques, whilst avoiding the use of animal tissue. One such synthetic biomaterial which demonstrates particular promise as a tissue mimicking material, is PVA. PVA exhibits tuneable mechanical properties [37], favourable biocompatibility [33, 38] as well as compatibility with imaging techniques such as MRI [39]. This has lead to PVA being particularly well known as a vessel mimicking material and forms an essential

tool in the research of cardiovascular biomechanics, diagnostic CVD techniques and medical device testing [40, 41, 42]. The mechanical characterisation of PVA has shown its applicability to be used as a tissue mimic for multiple CTs [43, 44, 45, 9], and has been shown to be hyperelastic and viscoelastic. However, the viscoelastic properties of PVA under dynamic loading conditions have not yet been studied. Dynamic mechanical analysis would allow for a better understanding of the viscoelastic properties of a material under dynamic loading, at frequencies representative of physiological conditions. For example, the frequency of loading most appropriate to test a biomaterial to replicate CT in the cardiovascular system would be comparable to physiological ranges of heart rate [23].

Additive manufacture has been swiftly adopted by the medical field, giving the opportunity to manufacture patient specific implants in short time scales [46, 47]. AM technology is most frequently used for the manufacture of patient-specific orthopaedic implants, medical models and instrumentation [47] although recent innovations have allowed for the AM of soft polymeric materials, more suitable for soft tissue scaffolds [48]. PVA has also been shown to be compatible with AM, if adaptations are made to use sub-zero temperature build plates [9]. However, the concept of sub-zero AM is still in its infancy, and the influence of AM techniques on the mechanical behaviour of PVA has not been quantified. This is especially important for PVA, where the use of controlled freezing and thawing is used to alter mechanical properties, therefore meaning the freezing process during sub-zero AM is likely to alter the formation of PVA crystallites.

Although a significant amount of research has been undertaken on the intrinsic material properties of PVA, this area of literature remains fragmented. For example consistent manufacturing parameters have generally not been used between studies, resulting in difficulty drawing conclusions and trends between the many process parameters, material properties and manufacturing techniques present. Hence, there is

scope to systematically evaluate the relationship between compositional changes in PVA, manufacturing methods, and the resulting intrinsic material properties; allowing for a more cohesive understanding of the material properties of PVA as a replacement biomaterial.

1.2 Mechanical function of connective tissue

1.2.1 Connective tissues and the ECM

Connective tissue (CT) encompasses a range of biological tissues, all of which perform mechanical functions in the body. Common examples are: articular cartilage, intervertebral discs, tendons and ligaments, and vascular tissues. Although the mechanical function of a CT depends on its application, the general structure will remain the same, with the key component of all CT being the *extracellular matrix* (ECM). This primarily consists of collagen fibres and a hydrated gel often referred to as the *ground substance* predominately consisting of hydrophilic *glycosaminoglycans* (GAGs).

Most CTs can be described as fibre reinforced composites, with collagen fibres present in the tissue, reinforcing the surrounding ECM. It should be noted, that due to the structure of collagen fibres, they will only reinforce the surrounding matrix when loaded under tensile forces. Therefore, the mechanical strength of CT is impacted significantly by the orientation of collagen fibrils within the tissue, as well as the percentage of the tissue made up by collagen. Due to the orientation of collagen having a significant impact on the mechanical properties of CT, they often exhibit anisotropic or orthotropic behaviour [49].

The primary mechanism which allows for fibre reinforcement, results from the shear forces present between collagen fibres and the ground substance [50]. If the collagen

fibres present in CT were the same length as the tissue itself, one would expect the collagen fibres to undergo a extension, with the restoring force in the fibres balancing the force applied. However, in most cases the collagen fibres will be significantly shorter than the length of the tissue; despite this they are still able to reinforce the CT. In this case, an applied tensile force will initially cause the ECM to flow, which will induce a shear force between the ground substance and collagen fibres. As the fibres undergo a shear force, they will extend, allowing a restoring force to still be able to reinforce the ECM, as long the shear force is high enough to cause significant elongation. The shear force induced in collagen fibres will not be constant throughout its length, with the maximum force being in the centre of the fibre, reducing to zero at either end. The total shear force present, and therefore the fibres ability to exhibit adequate reinforcement is dependant on the length of the fibre [50].

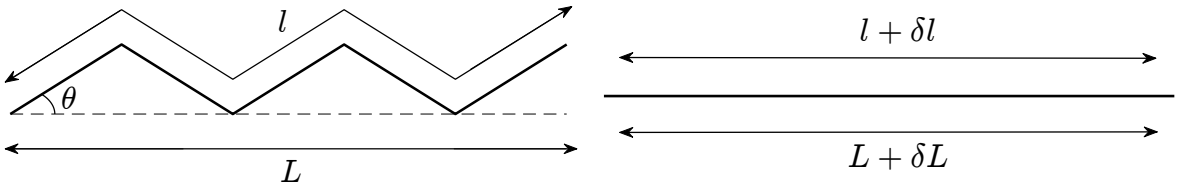

Figure 1.1: *The straightening seen in a crimped fibril of length, l, in a fascile of length L.*

A second mechanism which impacts collagen's function as a fibre reinforcement, called *crimping*, is also present [51]. This is related to the shape of the fibril itself, and describes the dimensional properties of collagen, where it will gradually straighten under a tensile load (figure 1.1. A useful example to understand the implication of crimping is to examine the stress/strain relationship of a tendon under uniaxial tension, which exhibits a 'toe region', where the tendon is more compliant, and a linear elastic region, resulting in a hyperelastic 'J' shaped curve (figure 1.2) [17, 18]. This 'J' shaped stress/strain relationship is common for connective tissues; a few examples include arterial tissue [52], articular cartilage [16], and nerve tissue [25]. Crimping aids in explaining the toe region of the this relationship, in which the fibre crimps are straightened, whilst applying minimal stress to the underlying structure of the

material.

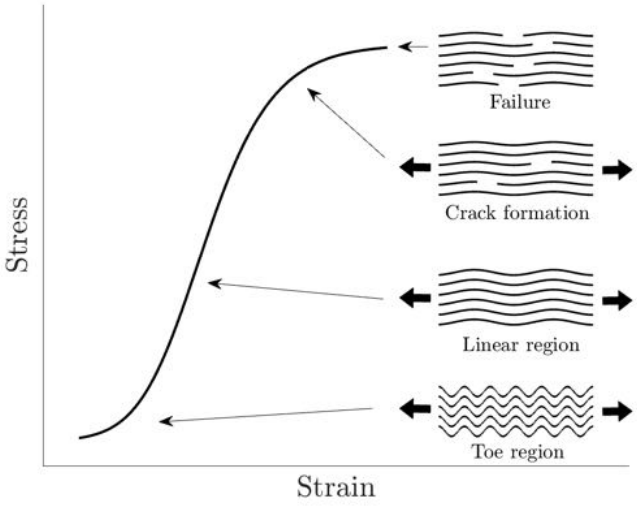

Figure 1.2: *Impact of crimping on the behaviour of a connective tissue under load.*

Although the collagen network provides the majority of a CTs resistance to mechanical force under tension and shear forces, proteoglycans also play an important role in contributing to the mechanical behaviour of CT under compression [53]. Within the ECM, proteoglycans are trapped within the collagen matrix, and the most common is aggrecan. This contain negatively charged chains of sulfated glycosaminoglycans (GAGs), which create a fixed charge density [54]. This fixed charge density in turn provides an osmotic swelling pressure, and also attracts positive cations which increases the osmotic swelling pressure further [50]. This process aids in resisting compressive forces [53], as well as influencing the water content of the CT. This mechanism is most often discussed with respect to the mechanical behaviour of articular cartilage under compression.

The important conclusion of this brief overview is that the structure of CT is non-trivial and the fundamental mechanisms that constitute fibre reinforcement, result in CTs frequently exhibiting anisotropic and hyperelastic properties. This knowledge proves fundamental when searching for a suitable material to mimic the mechanical response of CT. To further consider the mechanical behaviour of different CTs, sections

1.2.2 and 1.2.3 will give an overview of the structure and mechanical behaviour of two examples: the arterial wall and articular cartilage. The aim of this brief overview will be to view the histology of arterial tissue and articular cartilage from a biomechanical perspective, explaining how structural differences in CT on a microscopic scale, result in significant and complex differences in mechanical behaviour on a meso-scale.

1.2.2 The arterial wall

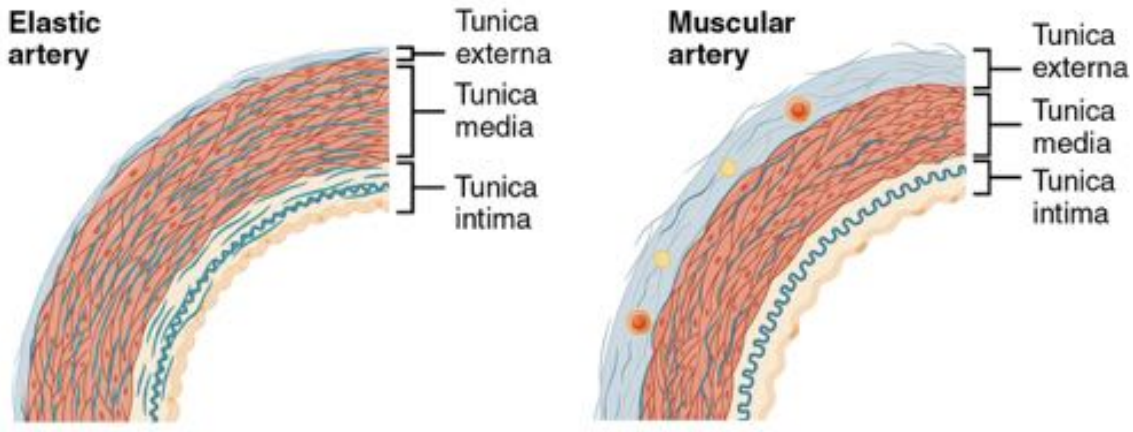

Figure 1.3: *A comparison of the walls of an elastic artery and a muscular artery. Reproduced from - [1] under creative Commons 4.0.*

All arteries consist of three layers: the intima, media, and adventitia where each layer of the arterial wall is responsible for a different function (figure 1.3) [55]. Arteries are classified as either elastic or muscular, where elastic arteries contain more collagen and elastin in the media compared to muscular arteries which contain a higher proportion of smooth muscle cells in the media. The majority of large arteries close to the heart (with the exception of the coronary artery) are considered elastic, whilst the majority of peripheral arteries are classified as muscular. The intima includes the endothelium, a thin layer of endothelial cells in direct contact with the bloodstream. Primary functions of the endothelium include aiding in vascular homeostasis and the formation and break-up of thrombi [56]. Endothelial cells proliferate due to mechanotransduction, where wall shear stresses caused by blood flow activates the cells.

Therefore the material properties of the arterial wall are fundamental to the function of the endothelium [57].

The media consists of collagen fibres, elastin and smooth muscle cells [58]. Thin elastic laminae separate the media into concentric, fibre-reinforced layers called musculoelastic fascicles [2]. The adventitia is a sheath of CT, predominately made up of collagen fibres. The adventitia aids in reinforcing the arterial wall, and anchors the vessel to surrounding tissue [58].

Through polarized light microscopy it has been shown that the orientation of collagen fibres varies between the layers of the artery, where alignment in the adventitia and intima are seen to be more dispersed than in media, where collagen fibres are aligned circumferentially [59] (figure 1.4).

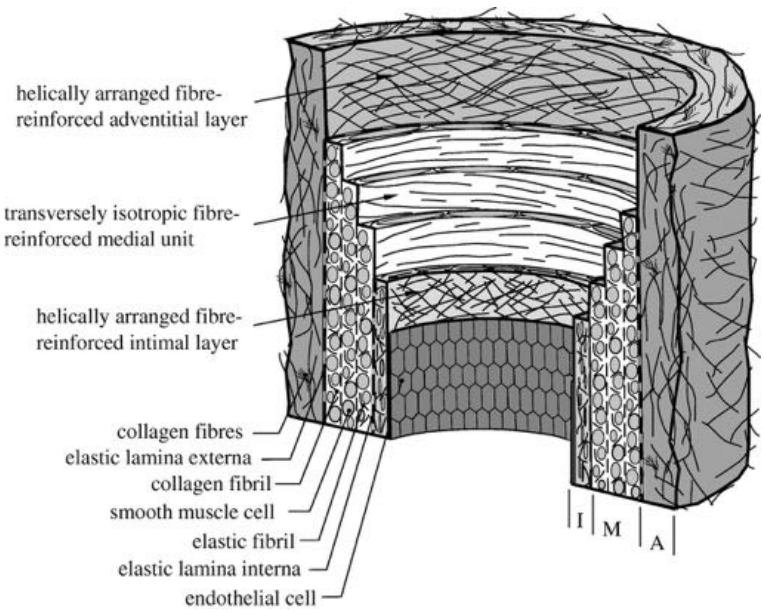

Figure 1.4: *Idealisation of the orientation of collagen fibres in each layer of the arterial wall. Reproduced with permission [2]*

Due to the principles of fibre reinforcement present in connective tissues (as explained in section 1.2.1), a difference in the mechanical behaviour between all three layers of the arterial wall is reported [2]. In a healthy artery at low stresses, the circumferential alignment of musculoelastic fascicles in the media mean it is generally

responsible for the majority of arterial strength. The dispersed, crimped nature of collagen in the adventitia does not immediately reinforce the ECM. However as the fibres straighten under significant high strains, the adventitia reinforces the arterial wall, reducing the likelihood of overstretching and rupturing [2].

As the structure of each layer of the arterial wall is tailored to its mechanical function, an ideal material replacement would allow the ability to control the both the material stiffness and hyperelastic response in order to accurately replicate each layer within the arterial wall. For example, the material used to replicate the adventitia should have a more 'J' -shaped response between stress and strain, only providing additional stiffness at high strains to prevent rupture.

1.2.3 Articular cartilage

The primary function of articular cartilage is to provide a low friction surface to allow smooth motion of synovial joints, as well protect the joint through the dissipation and storage of energy when subject to loading. Articular cartilage is comprised of approximately 70% water, 20% type II collagen, and 8% proteoglycans [3]. Articular cartilage has four layers: calcified cartilage, and the deep, transitional, and superficial zones (figure 1.5).

The deep zone is responsible for majority of cartilage's ability to withstand compressive forces; where collagen fibres orientated perpendicular to the articular surface, greater collagen fibre thickness, higher proteoglycan content, and lower water content result in a material tailored to resist compression [60]. Conversely, collagen fibres in the superficial zone are orientated parallel to the articular surface. In this case, the mechanical function of the superficial zone is to resist shear, tensile and compressive forces across the articular surface during articulation. Between these two layers is the transitional zone where collagen alignment is considerably less defined. Although the

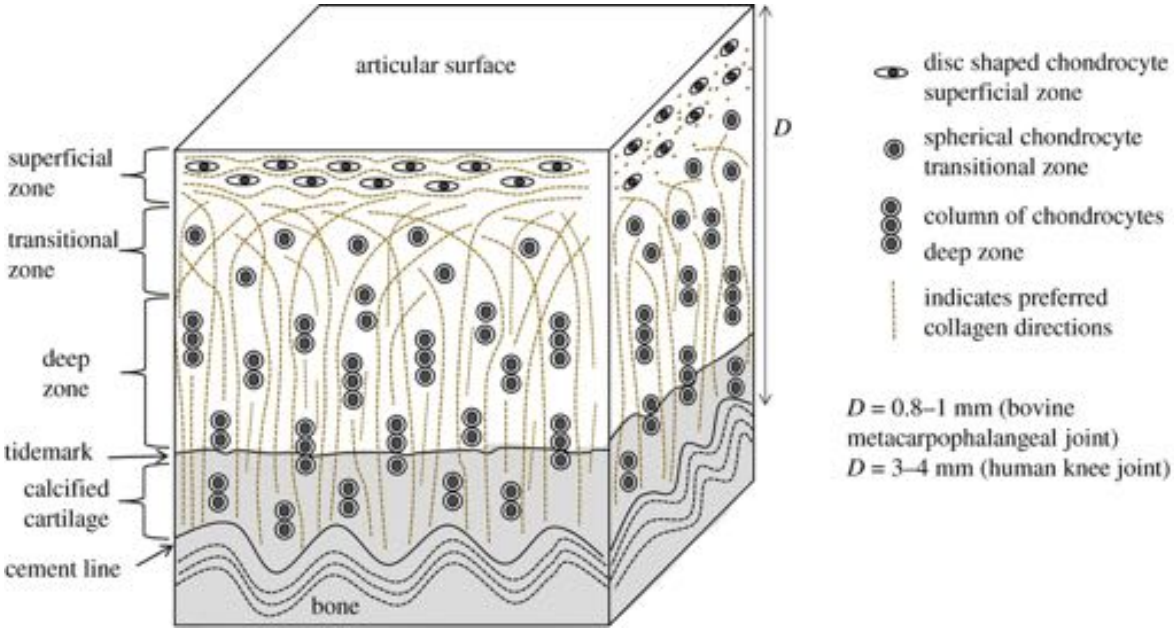

Figure 1.5: *A diagram illustrating the idealised orientation of collagen fibres across all layers of articular cartilage. Reproduced from - [3] under creative Commons 4.0.*

transitional zone does aid in resisting compressive forces, it crucially provides a smooth gradient between the structures and properties of the superficial and deep zones[3] [60]. As explained in section 1.2.1, the swelling pressure introduced by proteoglycans also aids in withstanding compressive forces, and as such water content has also been shown to significantly alter the mechanical response of articular cartilage [61].

In the case of articular cartilage the ideal material to replicate it's biomechanical behaviour would have an articular surface designed to resist forces associated with articulation, whilst having a sufficiently low coefficient of friction; a deep zone designed to resist compressive forces during loading (i.e. whilst walking or running); and a zone which provides a functionally graded transition between the two. As with the case-study in section 1.2.2 discussing the histology of arteries, this hypothetical material is non-trivial to manufacture and a complete understanding of the structure and mechanical behaviour of a candidate material is fundamental to its success.

1.3 Synthetic biomaterials

1.3.1 Overview of synthetic biomaterials

A biomaterial is classed as any material, either synthetic or biological, that has been manufactured and used for medical applications [62], including for example, materials for hip replacements [63], fracture fixation [64], heart valve replacement [42], stents [65], other connective tissue replacements [66], and dental implants [67]. The definition of a biomaterial does not include a requirement for invasive surgery, with materials used for less invasive applications such as contact lenses [68] and methods for drug delivery [69] also being included.

Broadly, biomaterials can be separated into three categories: biotolerant, biologically inert, and bioactive (figure 1.6) [70]. A biotolerant material should not cause any adverse reaction or rejection, however over time there will be a formation of fibrous tissue surrounding the implant. Polymers such as PMMA and polyethelene, as well as ceramics, are examples of biotolerant materials commonly used as bearing surfaces in total joint replacement [71]. The interaction between either the implant or wear particles and the surrounding tissue can cause inflammation, meaning the biological interaction must be comprehensively understood in order to make informed material choices [71]. This is not the case for bioinert materials, meaning they are better suited for implants that require direct interaction with biological tissues, as no fibrous capsule will develop around them. For example titanium is a bioinert material frequently used for hip replacements, where osseointegration can be utilised to increase implant fixation [72].

Bioactive materials are able to induce a biological response in the surrounding tissue, often stimulating tissue regeneration or releasing bioactive molecules [73]. Some

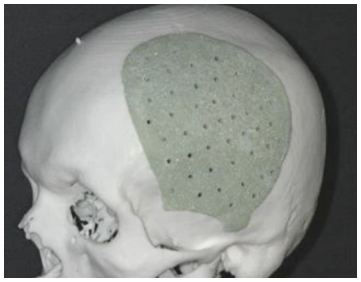

(a) Biotolerant: PMMA

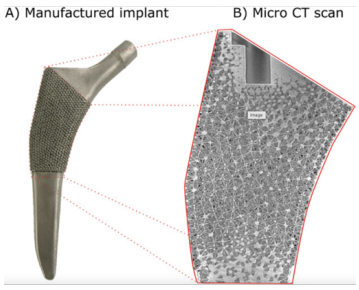

(b) Bioinert: Titanium

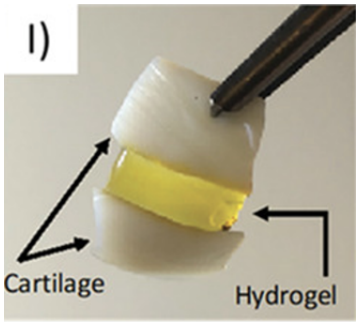

(c) Bioactive: GelMA

Figure 1.6: *(a) Cranial implant manufactured from PMMA (Reproduced from -[4] under creative Commons 2.0. (b) A titanium coated implant, showing close integration with bone (Reproduced from - [5] under creative Commons 2.0). (c) GelMA implant used for in situ cartilage repair (Reproduced from - [6] under creative Commons 4.0.).*

biomaterials can also be described as bioresorbable, meaning they break down in the body over time. Most commonly, polylactic acid (PLA) and polyglycolic acid (PGA) are used for fracture fixation implants where support is only required for a relatively short period of time. This means the implant can resorb, negating the need for additional surgery for the removal of implants, or the build-up and corrosion of metallic implants [74]. Clearly the field of biomaterials encompasses an incredibly broad range of materials, applications, and design or manufacturing considerations. Therefore, this section will focus closely on the use of biomaterials to replace soft connective tissues.

1.3.2 Materials for connective tissue replacement

As this thesis is focused on the replication of the intrinsic material properties of CT, an overview of the materials and methods currently used for soft tissue replication, replacement, and repair is crucial to identify specific gaps in research knowledge that could be improved upon. This section will broadly discuss the state of the art materials currently used in tissue engineering and for the replication of CT, focusing specifically on material requirements for this thesis. This section will then provide an overview of the structure and material properties for the material used throughout this thesis, as

well as justification for why it was chosen.

Due to the nuanced mechanical behaviour of CT (as discussed in section 1.2), not all biomaterials are suited to replicate or replace them. To be a viable candidate for CT replacement, the requirements listed here should be considered. It should be of course be noted that the exact requirements and order of importance will depend on the specific CT in question.

Key requirements for selecting CT replacement materials from a biomechanical perspective:

- Biocompatibility should be carefully considered, especially where cell proliferation or stimulus is required. Therefore the material (or derivatives of the material) must have proven cell compatibility.
- The ability of the material to withstand compressive, tensile, or shear forces should be as close as possible to the CT in question. An ideal material would have infinitely tuneable material properties, allowing the replication of many CTs without significant further investment in time or research.
- The specific mechanical behaviour relevant to the CT in question. It is important to note the difference between this, and the strength of a material. Two materials may have the same Young's modulus at low strains, but may respond very differently under high strains or at different loading frequencies. As above, an ideal material would have infinitely tuneable hyperelastic and viscoelastic properties.
- The manufacturability of the material should be considered with respect to the ability to design and manufacture heterogeneous materials. Compatibility with AM will be crucial to meeting this requirement (section 1.4)

1.3.2.1 Biocompatible AM materials

Common methods of AM will be discussed in full in section 1.4. However, as compatibility with AM is an important material requirement, well established AM materials that are also biocompatible will be briefly discussed here. This list is actually quite extensive, encompassing metals, polymers, and resins used for applications such as joint replacement, fracture fixation, and dental implants [75]. With respect to the mechanical function of CTs, these materials are orders of magnitudes too stiff. That said, some flexible polymers developed for AM are biocompatible and should be drawn to the readers attention, although are ultimately not suitable for CT replacement.

Most of the flexible materials compatible with traditional AM techniques (such as fused deposition modelling) are thermoplastics, with thermoplastic elastomer (TPE), thermoplastic polyamide (TPA), and thermoplastic polyurethane (TPU) being examples of biocompatible 3D printable materials which are less stiff compared to traditional polymers. For example NinjaFlex (NinjaTek, Mannheim, USA) is TPE variant that has been shown to be biocompatible, and can be elongated by 800% strain before material failure[76] [77]. With an elastic modulus of 26 MPa, significantly less stiff than most polymers (with elastic moduli in the order of GPa), Ninjaflex is in the order of magnitude of some stiffer CTs such as tendon [78]. However, little research has explored the use of TPEs as CT replacements, and all flexible 3D printable thermoplastics (such as NinjaFlex) have the same problem with respect to the material requirements previously described: It is not possible to tune their intrinsic material properties. This means they are unable to replicate softer connective tissues, and they do not offer the potential to tune viscoelastic or hyperelastic properties through material composition parameters. The cell compatibility of materials such as TPE has also not been extensively researched.

1.3.2.2 PDMS

Polydimethylsiloxane (PDMS) is the most widely used silicone based biomaterial and is generally considered to be bioinert [79]. PDMS has been used for a wide range of biomedical applications due the ability to tune mechanical, acoustic and optical properties [80]. It has also been shown to exhibit viscoelastic behaviour [81]. Although the use of PDMS as a material to replicate CT is quite limited, it has been extensively used for the fabrication of arterial phantoms [82] [81]. This is accompanied by good stability and durability, meaning PDMS is a good candidate for *in vitro* testing where an approximation of the mechanical behaviour of CT is required [80].

However, crucial limitations mean PDMS is not a suitable material choice to directly replace CT. Firstly, although it is well suited for use as a phantom, PDMS lacks the breadth of knowledge and research in replacing a wide range of connective tissues compared to other materials. Secondly, although it is possible to change the mechanical properties of PDMS by varying the ratio of the elastomer and curing agent, it does not offer a fine level of design control over material properties and structure. Additionally, to the authors knowledge little research has been conducted on the viability of AM, although Hinton *et al.* successfully 3D printed PDMS structures [83]. However, this study was unsuccessful in fusing filament strands together in the XY plane, resulting in effectively zero strength [83]. Therefore, this thesis has focused on more versatile materials with greater compatibility with AM techniques.

1.3.3 Hydrogels

Hydrogels are a category of polymeric materials which are swollen with water, and can maintain a given geometry [84]. The structure of a hydrogel is maintained by the introduction of crosslinking, which is the formation of bonds from one polymer

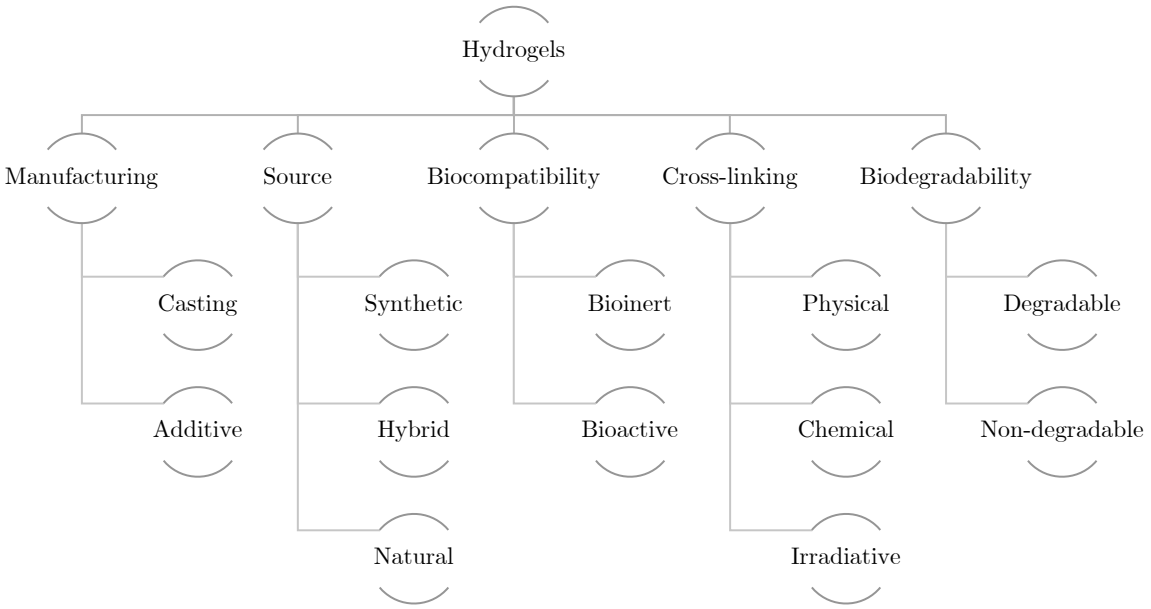

Figure 1.7: *A non-exhaustive list of key properties to considered when comparing hydrogels.*

chain to another. This cross-linking can either be done through chemical, physical, or irradiative processes, where either covalent or physical bonds will be formed respectively [64] (figure 1.7). Due to the high water content of hydrogels, they normally exhibit good biocompatibility, and were among the first biomaterials used in the 1950's and 60's [64].

The addition of cross-linking within a hydrogel can influence: its mechanical properties, where an increase in the number of crosslinks will increase the rigidity of the crystalline structure; decrease its viscosity, as polymer chains will be less able to flow; and reduce the solubility of the material, although they are able to absorb the solvent they are situated in until reaching an equilibrium swollen state [85]. The equilibrium state will be a balance between the osmotic pressure in the hydrogel, and the retractive force of the 3D structure of the polymer network. Physical cross-linking involves the formation of hydrogen bonding, entangled chains, hydrophobic interactions, or crystallite formation [85]. Chemical cross-linking on the other hand, is the formation of

more permanent covalent bonds between polymer chains, often using chemicals like glutaraldehyde [86, 87].

Hydrogels can be synthesised either from natural or synthetic compounds [88]. Synthetic hydrogels (such as poly(ethylene glycol) [PEG] and poly(vinyl alcohol) [PVA]) have been extensively used in tissue engineering as replacements for CTs due to good biocompatibility and mechanical strength [88]. Natural hydrogels (such as alginate, gelatin and their derivatives) typically have significantly lower mechanical strength, but are still widely used in biomedical applications as they are derived from organic compounds [89]. This means they are non-toxic and elicit little to no inflammatory response when implanted.

To give more detail on the benefits and limitations of natural hydrogels with respect to this thesis, two examples will be discussed: Alginate and gelatin based hydrogels. However, due to the constraints created by the material requirements of CT, the most promising materials discussed in this chapter are synthetic hydrogels. PVA will be the primary synthetic hydrogel discussed, as it meets all the material requirements specified, whilst also being efficient to manufacture, adjust, and refine material properties.

1.3.3.1 Natural hydrogels

Alginate is one of the most commonly used hydrogels used for biomedical applications, and is well suited to aiding wound healing, drug delivery, and tissue engineering [90]. Alginate is a natural hydrogel normally synthesised from brown algae through treatment with aqueous alkaline solutions [91]. Depending on the application, different additives can be introduced to alginate. For example cell-adhesive peptides can be introduced to increase cell adhesion [90]. Despite well documented biocompatibility, one of the key issues of alginate derived hydrogels is a lack of mechanical strength. The most common form of gelling alginate uses a cross-linking agent to introduce ionic

bonds. When a force is applied these ionic bonds have a tendency to dissociate, and reform elsewhere. This results in a loss of water content and plastic deformation, and ultimately poor mechanical properties [90]. For example gelatin sodium alginate was shown to have a Young's modulus of 3.21 kPa, several orders of magnitude below the the vast majority of CT [92]. Physical crosslinking can increase the mechanical strength, however toxicity caused by the cross-linking process causes added complexity in ensuring biocompatibility [90].

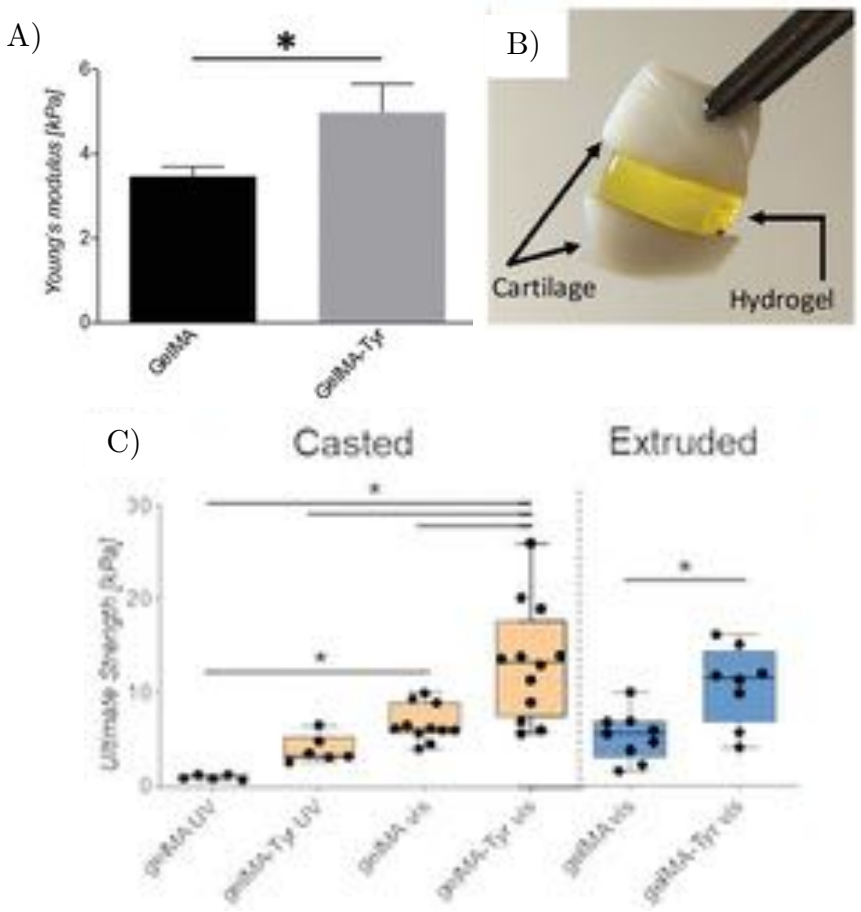

Figure 1.8: *(A) Young's modulus of gelMA and gelMA-tyr. (B) Cartilage biopsies adhered together using GelMA-Tyr. (C) Ultimate strength og gelMA and gelMA-tyr. Reproduced under Creative Commons licence 4.0 [6].*

Similarly to alginate, gelatin based hydrogels are a group of natural hydrogels that are frequently used for biomedical applications, again most commonly in drug delivery and tissue engineering [93]. Gelatin is a particularly attractive hydrogel for tissue engineering as it is water soluble at 30 $°C$, and non-immunogenic [93]. Additives

are frequently added to gelatin to effect material characteristics such as mechanical behaviour, and gelatin methacrylamide (gelMA) has been shown to have tuneable viscoelastic properties [94]. GelMA has also shown promise in connective tissue regeneration. For example, a tyramine gelAM (gelAM-tyr) hydrogel was shown to act as both a cell carrier and cartilage-binding glue to aid cartilage repair [6] (figure 1.8). It should be noted that it was not possible for gelMA-tyr to act as a cartilage replacement, rather it was used to bind damaged cartilage together. This is due to the low mechanical strength of gelMA and gelMA-tyr, with elastic moduli and ultimate strength in the range of 2 - 6 and 5 - 20 kPa respectively (figure 1.8) [6] .

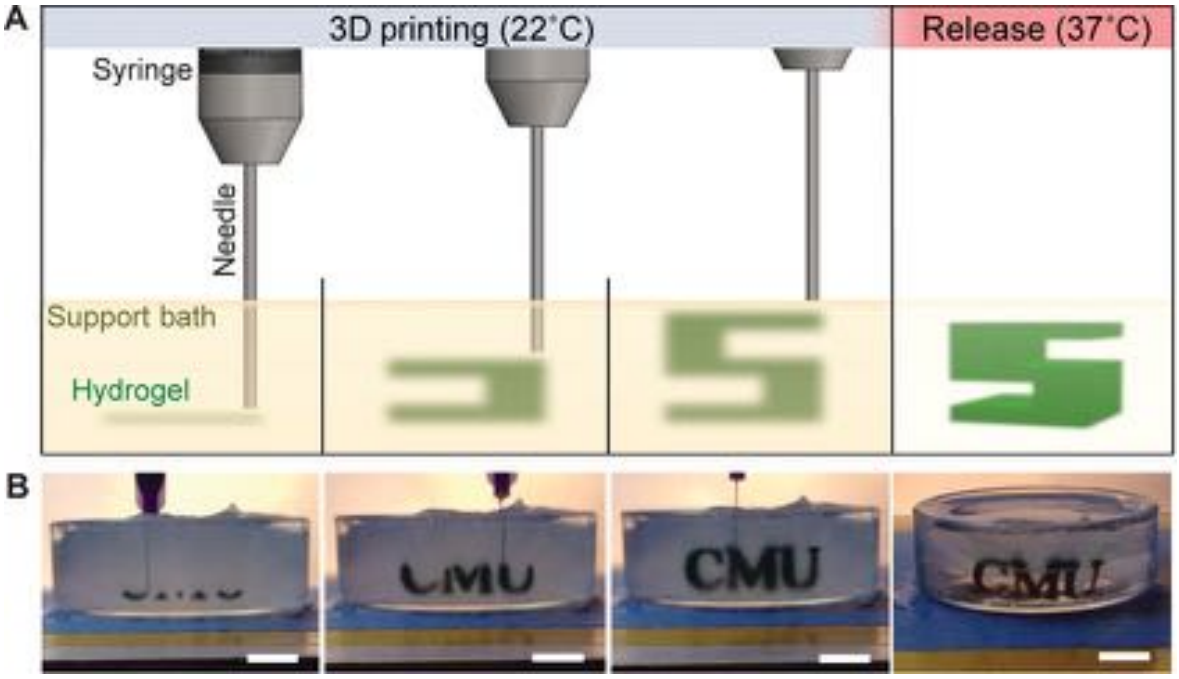

Figure 1.9: *(A) Schematic of the FRESH process showing the hydrogel (green) being extruded and cross-linked within a gelatin support bath (yellow). (B) Images of the letters "CMU" FRESH printed in alginate illustrating the ability to 3D print complex free-standing structures. Reproduced under Creative Commons licence 4.0 [7]*

Alginate and gelatin based hydrogels are well studied with respect to additive manufacturing. The most common technique used is Freeform Reversible Embedding of Suspended Hydrogels (FRESH) (figure 1.9). This process involves extruding a hydrogel into a shear thinning fluid. As the needle moves through the fluid, the shear forces

reduce fluids viscosity and allow the hydrogel to be easily extruded. Once the hydrogel has been extruded and is static, the viscosity of the surrounding fluid increases and supports the hydrogel. [7] [95] [96]. This technique has been well studied has been used to successfully manufacture complex geometries from hydrogels such as alginate.

Despite clear compatibility with AM, alginate is ultimately more suited to applications in tissue engineering where mechanical strength is less crucial. As well as for uses in drug delivery and wound healing, alginate has been shown to be useful for aiding bone healing and cartilage repair [90]. However, it is seldom used to replace the mechanical function of CT; for example in the case of cartilage repair, alginate has shown potential in transplanting chondrogenic cells to restore damaged cartilage, not as a cartilage replacement [90]. Ultimately, due to the lack of mechanical strength, natural hydrogels are unable to meet the material requirements to suitably replace CT.

1.3.3.2 Synthetic hydrogels

The material requirements described in section 1.3 are fundamental to the success in the aims set out in this thesis, where the material must have adequate, tuneable mechanical properties, good biocompatibility, and compatibility with AM. This section has shown that very few materials meet all of these requirements, where materials such as PDMS have mechanical strength, but do not have the control over mechanical behaviour that is required, or suitable compatibility with AM; or hydrogels such as alginate or GelMA, which have very good compatibility with AM and are used extensively in tissue engineering, but are not suitable to replicate the mechanical function of CTs (figure 1.10).

Synthetic hydrogels are a group of biomaterials that most closely fit the material requirements outlined. Most focus will be placed on poly(vinyl alcohol) cryogels (which this thesis will refer to as PVA), as with its good biocompatibility, tuneable material

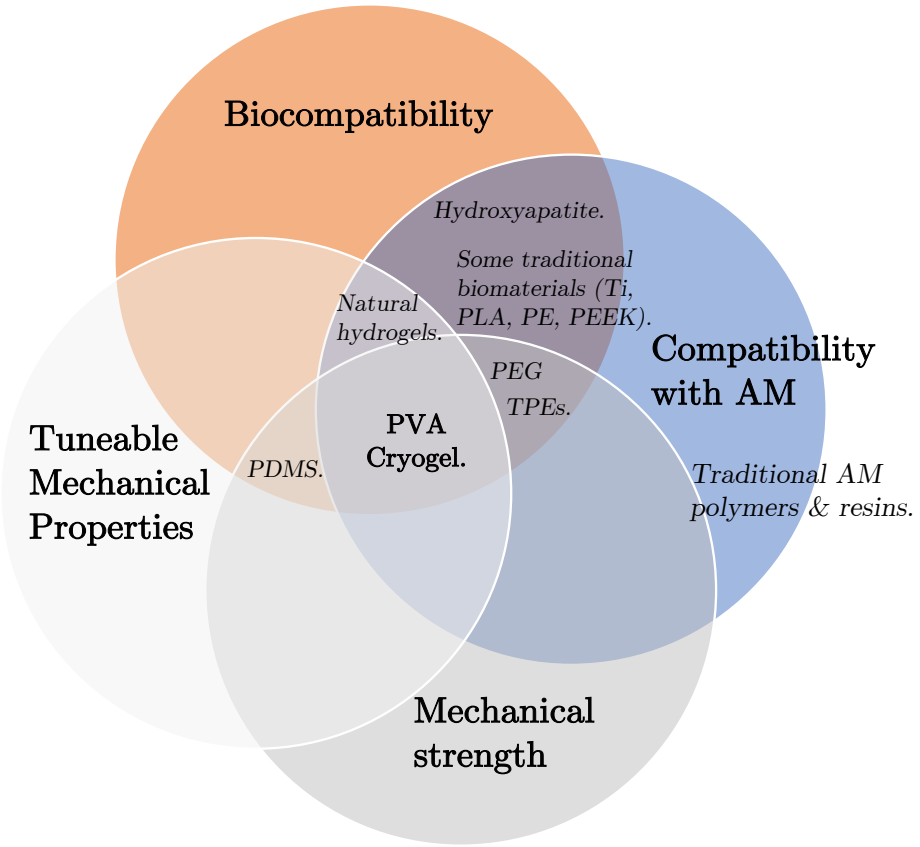

Figure 1.10: *Venn diagram comparing materials and their suitability for the material requirements as a replacement for CT.*

properties, evidence of using manufacturing parameters to tune specific behaviour, compatibility with AM, and a wealth of literature proving its ability to replicate many connective tissues, it will be the material used throughout the research presented in this thesis. Firstly however, synthetic hydrogels will be broadly discussed.

Despite their ubiquity in tissue engineering, natural hydrogels have been slowly replaced by, or hybridised with synthetic hydrogels for some applications due to better mechanical strength and longer lifespans [88]. Alongside PVA, commonly used synthetic polymers for biomedical applications include poly(ethylene glycol) (PEG), polyaxomers (also known as pluronics) and Poly(hydroxyethyl methacrylate) (pHEMA) [88]. As with their natural counterparts, synthetic hydrogels have been broadly used for tissue engineering, drug delivery and wound dressings [88] [97] [98]. Due to their superior mechanical strength, synthetic hydrogels have also been used to replicate or

replace the mechanical function of CT. PVA is most frequently discussed with respect to CT, and in a 2017 review which extensively assessed natural and synthetic hydrogels, PVA was the only material explicitly described as "highly viable for replicating tissue structure", as well as being a "feasible replacement for current artificial grafts" [88]. For example, PVA been used to replicate the structure of various CTs including cartilage, inter-vertebral discs, meniscal tissue, and for heart valve replacement (section 1.3.4).

Broadly, PVA is the most widely used synthetic hydrogel used specifically to replicate the structure of CT, and will be the focus of the rest of this literature review. The structure, chemical composition of PVA, and biomedical uses of PVA will be discussed in section 1.3.4, whilst the the state of the art of PVA AM will be reviewed in section 1.4. Common imaging techniques used to analyse PVA will then be evaluated in section 1.5.

1.3.4 Poly(vinyl alcohol)

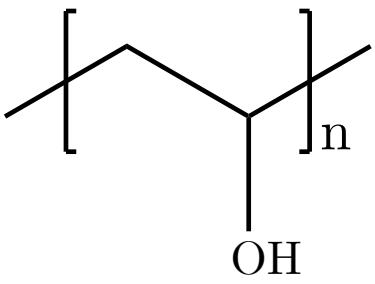

Figure 1.11: *Chemical structure of PVA*

PVA is a widely used biocompatible, synthetic polymer[99, 33], that consists of a mixture of PVA polymer chains and water, that is physically cross-linked through one or more freeze-thaw cycles (FTCs). It is particularly prevalent as a component of tissue scaffolds and as a tissue mimicking material. It is possible to refine mechanical properties of PVA by altering the concentration, molecular weight of the hydrogel,

and the temperature, duration, and number of FTCs during manufacture. This allows the material to replicate a broad-spectrum of soft tissues [43, 100], and has led to its frequent application as:

- A component of heart valve stents [43], prostheses [42];
- Intervertebral disc prostheses [45];
- As a material for articular cartilage [101, 44, 102, 103, 104, 105] and meniscus replacement [106];
- A carrier for drug delivery [69];
- and to model the mechanical properties of super-soft biological materials such as brain and lung tissue [9];
- A phantom material for arterial flow studies [39], and a vessel mimicking material for cardiovascular phantoms [40, 107, 108, 109].

PVA is a synthetic polymer with the chemical structure $[CH_2CH(OH)]_n$ (figure 1.11), and can be cross-linked using either chemical, physical, or irradiative processes. PVA is manufactured through the polymerisation of vinyl acetate into poly(vinyl acetate), followed by the hydrolysis of poly(vinyl acetate) into PVA [38]. This reaction does not undergo completion, meaning a percentage of the functional groups will remain poly(vinyl acetate). This percentage is referred to as the degree of hydrolysis, and impacts material properties such as solubility and its ability to crosslink [110].

This thesis is concerned with physical cross-linking formed during the process of undergoing FTCs. The process of undergoing FTCs introduces hydrogen bonds between the hydroxyl groups of polymer chains, and between polymer chains and water molecules (figure 1.12) [111]. During the freezing process, PVA-rich and PVA-poor

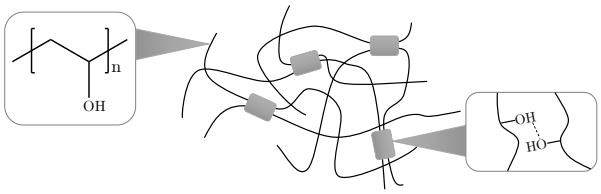

Figure 1.12: *Diagram illustrating the formation of hydrogen bonds between PVA polymer chains.*

regions begin to form due to phase separation. Ice crystal formation further concentrates PVA-rich areas, which allows an increase in formation of hydrogen bonding and therefore PVA crystallites [112]. A network of PVA is formed as the hydrogel thaws, where bulk water will occupy pores within the PVA matrix. As the number of freeze thaw cycles is increased, this process is repeated, with the crystalline structure of PVA incorporating more PVA chains, therefore further reinforcing the hydrogel [113].

Due to a broad range of variable parameters during manufacture, as well as the capability of producing hydrogels free from non-biocompatible crosslinking agents, PVA lends itself to a wide range of applications as a physical model for connective tissue. The stiffness of various compositions of PVA has been documented, and table 1.1 gives a brief overview of the range of elastic moduli that have been recorded. The material properties of PVA span the range of values expected of natural tissues; which provides the ability to 'tune' the mechanical properties for a specific application.

Table 1.1: *Table indication key measurements of the mechanical properties of PVA in literature.*

MW /kDa	Concentration	No. FTC	Elastic Modulus / MPa or equivalent	Notes	Ref.
95	10-16%	15-45	40-90	Sheets with thicknesses 0.19-0.22 mm tested under tension	[114]
89-98	10-35%	2-10	0.0012 - 0.8	Compression modulus, 1-5% strain	[112]
78.4	9% PVA, 1% gelatin	1-3	0.1 - 0.9	Uniaxial tension to 60% strain	[115]
N/A	15%	1-6	0.2 - 0.8	This value is for 6 FTC given across range of strains of 10-70%.	[43]

Although the elastic modulus of PVA has been extensively researched, considerably less has literature has explored its viscoelastic behaviour. PVA has been shown to be viscoelastic [116] [117] [118], however it has not previously been tested under dynamic loading. Dynamic mechanical analysis aims to model physiological loading by applying a sinusoidal load across a range of frequencies, quantifying how much energy has been stored (the elastic response) or dissipated (viscous response). For a materials suitability to replace a connective tissue to be fully validated, it must not only have a suitable elastic modulus, but also respond consistently across the range of loading conditions expected *in vivo*. DMA provides an invaluable tool to quantify this, and section 2.1.5.1 briefly explains how it is used to calculate the viscous and elastic response of a material.

One of the most frequent applications of PVA is as a replacement for the mechanical function of articular, where it has been shown to have sufficient mechanical strength, able to replicate the tensile and compressive moduli of cartilage (approximately 17 and 0.53 - 1.82 MPa respectively) [105]. Another key characteristic that allows PVA to be a suitable material for cartilage replacement is the favourable wear properties, where PVA has a similar coefficient of friction to cartilage due to fluid-film formation when subject to compression [104]. Advances in AM methods for PVA will also be discussed in section 1.4, showing potential to replicate the transition of mechanical strength from the deep to superficial zones.

Most promisingly to this thesis, it has been shown that intrinsic mechanical behaviour of PVA hydrogels can be precisely controlled through adjusting manufacturing parameters. For example, Millon *et al.* showed the ability to introduce anisotropic behaviour in PVA by applying tensile forces to the hydrogel during the FTC process (figure 1.13) [34]. This anisotropy can be explained by due to the microstructure of PVA; where, in brief, the application of strain during the FTC process causes alignment of PVA crystallites in the direction of tension. These crystallites will continue to grow in the direction of stress during further FTCs, resulting in anisotropic behaviour

relative the induced stress and number of FTCs [34] [8]. This technique has allowed the close replication of the anisotropic properties of the porcine aorta [34] [8]. Due to freezing and thawing of PVA being fundamental to this process, combined with the shear thinning nature of PVA, the advent of AM techniques reliant on a freezing process (section 1.4) provide the exciting potential to create similar anisotropic effects through manufacturing parameters alone.

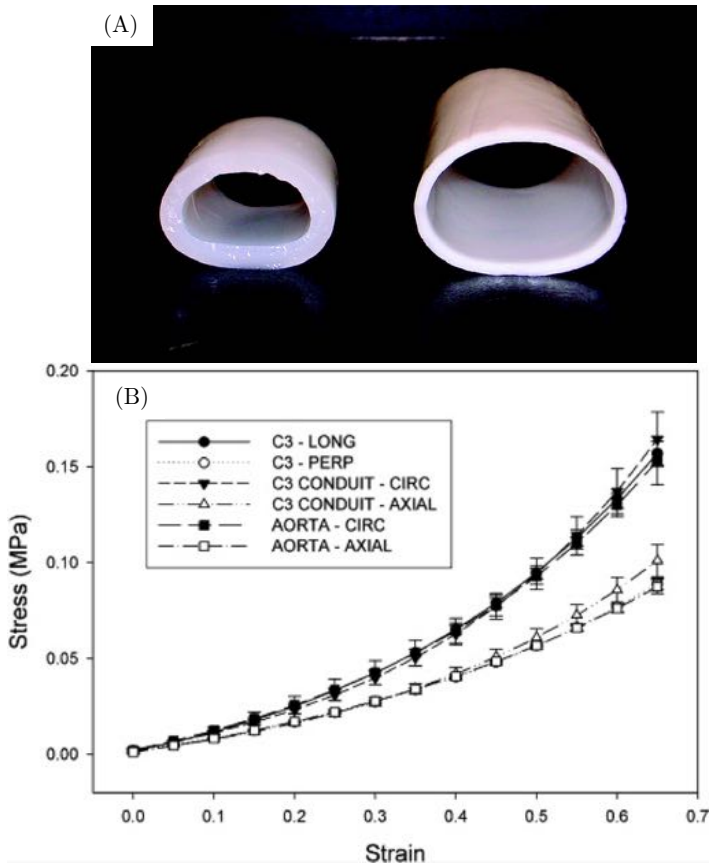

Figure 1.13: *PVA conduit ((A) cycle 1, left) and the 75% initially strained PVA conduit (cycle 3, right). (B)Stressstrain curves for the anisotropic PVA conduit (75% initial strain, cycle 3), the anisotropic PVA sheet sample (75% initial strain, cycle 3), and porcine aorta (both directions). Reprinted with permission from [8]. Copyright 2007 American Chemical Society .*

Ultimately, PVA meets all the material requirements to replace CT described in section 1.3, and to summarise:

- PVA has suitable mechanical properties, whilst also having greater control over these properties compared to flexible polymers or PDMS.
- Like most hydrogels PVA has good biocompatibility, but has significantly better mechanical strength compared to natural hydrogels.
- PVA is one of the most studied synthetic hydrogels for replicating CTs, for example being used to replicate cartilage, heart valves, inter-vertebral discs, and menisci.
- The simple structure of PVA allows it to be carefully controlled to tune its mechanical behaviour.
- Like other hydrogels, PVA is compatible with some types of AM.

1.4 Additive manufacture

1.4.1 AM technologies

Traditional manufacturing techniques can be broadly split into machining, casting and forming. Using these techniques, it is possible to manufacture an extensive range of solid and hollow body objects, from a broad range of materials. However, additive manufacture (AM) has allowed a new wave of innovation in design and engineering in the past two decades, allowing for rapid prototyping of complicated geometries, functionally graded material properties [119, 120], and an improvement in resource efficiency and sustainability [121, 122]. AM also has the potential to reduce costs and save time compared to more traditional manufacturing techniques, when manufacturing highly intricate parts in low volumes, as well as simplifying supply chains [123].

A key advantage of AM compared to other techniques is the ability to control in-

trinsic material properties through the manufacturing process, for example enabling the design of heterogeneous material properties [124]. As hydrogels are viscous, water-based materials, the vast majority of traditional manufacturing techniques are incompatible, with only casting being a viable choice. However, the casting process cannot be used to influence material heterogeneity, and in the case of PVA, the resulting sample homogeneity will only be affected by the FTC process described in section 1.3.4.

Additive manufacture provides the only compatible manufacturing method that offers the potential to influence the intrinsic properties of PVA through highly controlled adjustment of process parameters. This section will broadly outline various AM techniques, highlighting those which hydrogels are compatible with; as well as outlining key literature into the research of AM PVA, and discussing the gaps in this literature.

AM or 3D printing, are terms used to describe any manufacturing process which involves the gradual fabrication of a part by building thin layers (typically 25 - 300 μm) of material upon another. A diverse selection of materials, such as metals, polymers, ceramics, resins, and hydrogels can be manufactured using AM [125, 46]. Depending on the material being used, different types of AM may be preferable, and whilst this thesis will focus on bio- and hydrogel printing, as well as the clinical applications of AM, the five core processes at the heart of AM will be outlined briefly:

- *Material extrusion*, such as Fused Deposition Modelling (FDM), where a material is extruded above its melting temperature as a strand to 'draw' a 3D object [126]. This is the most prevalent form of AM;
- *Vat polymerisation*, such as stereolithography (SLA) which generally consists of a vat of polymer resin that is sensitive to ultra violet or visible light, and an energy source which selectively cures the material [127];
- *Material jetting*, where droplets of material are deposited to build up the object [128]. This has been frequently used for bioprinting (section 4.2.1);

- *Powder bed fusion*, in which a powder bed is selectively melted and fused to form a solid object [129];
- *Directed energy deposition*, where a powder is deposited and essentially welded onto the surrounding material, slowly building it up [130].

Additive manufacture has proved to be a disruptive technology in the medical field, allowing for the manufacture of low volume, patient specific implants and medical instrumentation to be fabricated. For example, FDM has been frequently used with biocompatible, and often biodegradable polymers such as polylactic acid [131, 132] and polycaprolactone [133, 134], to manufacture implants and drug delivery devices; whilst techniques such as powder bed fusion have been used to manufacture patient specific implants for craniofacial [135], loading bearing [136], and spinal fusion applications [137] using titanium.

1.4.2 AM of Hydrogels

The additive manufacture of hydrogels is often referred to as *bioprinting*, which has become a prominent area of research within biomedical engineering over the last two decades [138]. Methods of bioprinting which use one of the core techniques described in section 1.4.1 have been developed, and are tailored specifically to the AM of hydrogels whilst often supporting cell growth [138]. Methods for AM of hydrogels will be briefly discussed here, and a review of state of the art methods compatible specifically with PVA will be discussed in section 1.4.3

Bioprinting encompasses a broad range of technologies and disciplines, aiming to combine tissue engineering and core engineering principles, to produce intricate 3 dimensional (3D) geometries, whilst allowing for the proliferation of living cells [46]. Bioprinting shares many of the same advantages as AM over traditional manufactur-

ing methods including rapid prototyping and potentially lower costs on small scale manufacturing. This allows for the economic feasibility for patient specific manufacture [139] - a significant advantage over other methods of manufacturing. However, key disadvantages have slowed the wider adoption of bioprinting for connective tissue applications, including cell viability [140], and mechanical stiffness of commonly used hydrogels [48], with a lack of literature describing and characterising the mechanical behaviour of potential materials [141]. This thesis hones in and focuses on the latter, aiming to use and develop bioprinting techniques to work with stiffer biocompatible materials.

The majority of bioprinting aims to produce either tissue scaffolds or tissue replacements. Tissue scaffolds aim to provide support to surrounding tissue, whilst allowing regrowth, either becoming incorporated into the tissue, or biodegrading. An implant on the other hand, is a permanent replacement for tissue that aims to replicate the tissues function. In the case of tissue scaffolds, there is a requirement for cellular growth, both to allow tissue growth around a scaffold, and decrease the likelihood of rejection, it is therefore important for the materials used to be conductive to cells and mimic the extracellular environment as closely as possible. Cell laden hydrogels meet the requirement of cell conductivity, and are normally referred to as bioinks [46]. Bioinks are commonly 3D printed using ink jetting, however due to the lower viscosity of bioinks, they tend to lack mechanical stiffness, and are not necessarily capable of acting as mechanical replacements to tissue [48]. In this case, when the material needs to directly replace connective tissue, the material properties produced from droplet based techniques will likely be too low [141]. Direct ink writing (DIW), follows a similar process to FDM, where a constant stream of material is extruded from a nozzle. Typically, shear thinning, viscous materials are the best suited to DIW, as they decrease in viscosity whilst being extruded, and then increase in viscosity and therefore stiffness afterwards, allowing the geometry of the part to be maintained. As with PVA (where undergoing FTCs are used to crosslink polymer chains), processing either dur-

ing, or post manufacture (normally either chemical or photoactive) is often required to increase mechanical stiffness [142].

1.4.3 AM of PVA

Some forms of PVA are commonly used in AM across many disciplines as a material support, with PVA filaments widely available for FDM. The forms of PVA used are water soluble, and offer no long term structural support meaning that PVA manufactured with traditional FDM, would not be suitable for replication of the structure of connective tissues. This has however found use in the bioprinting discipline as a dissolvable drug delivery material [69, 143, 144]

Given the low viscosity of PVA solutions, it does not immediately lend itself to being a prime candidate for AM. This means that it is not able to maintain its geometry post-extrusion due to its initial low viscous state, requiring physical or chemical cross-linking to increase in stiffness. However, as PVA proves to be a compelling, widely used biomaterial, several studies have been undertaken, showing the potential to 3D print PVA solutions. The majority of these use a technique that will be referred in this thesis as *sub-zero AM*. Freezing has also previously been put forward as method of scaffold manufacture for other materials [145]. PVA is extruded onto a print bed cooled to sub-zero temperature, allowing it to freeze immediately after extrusion and therefore allowing it to retain spatial geometry. An brief overview of key literature on sub-zero AM is given in Table 1.2, showing key findings for each.

Sub-zero AM was first proposed by Adamkiewicz & Rubinsky who demonstrated the potential of freezing extruded hydrogels during the AM process in order to manufacture tissue scaffolds [146]. This methodology retained the geometry of extruded agar by 3D printing directly into a container of liquid nitrogen. Although this study showed the huge potential of this technique, it did not test either the accuracy of the

printing technique, or ascertain the mechanical properties of the AM structures [146]. A similar technique was used by Wang *et al.* for the bioplotting of scaffolds manufactured from PLA based materials [147]. This system used a flow of coolant beneath the print bed to allow the the extruded material to freeze on contact. As before, neither print resolution or mechanical properties were reported. Tan *et al.* were the first to comprehensively study sub-zero AM, developing a system that used dry ice (which has a sublimation temperature of -78.5^{o}C) to cool a stainless steel print bed [9]. This was also the first study to use PVA as the hydrogel used for manufacture, and also to report the mechanical properties of the 3D printed structures, showing comparisons between mechanical properties of cast samples, and super soft biological tissues (such as brain and lung tissue)[9]. Although Tan *et al.* reported print resolutions of 0.26 mm, the images presented show promising but inaccurate print accuracy, where the final geometry is distorted compared to the CAD model used (Figure 1.14).

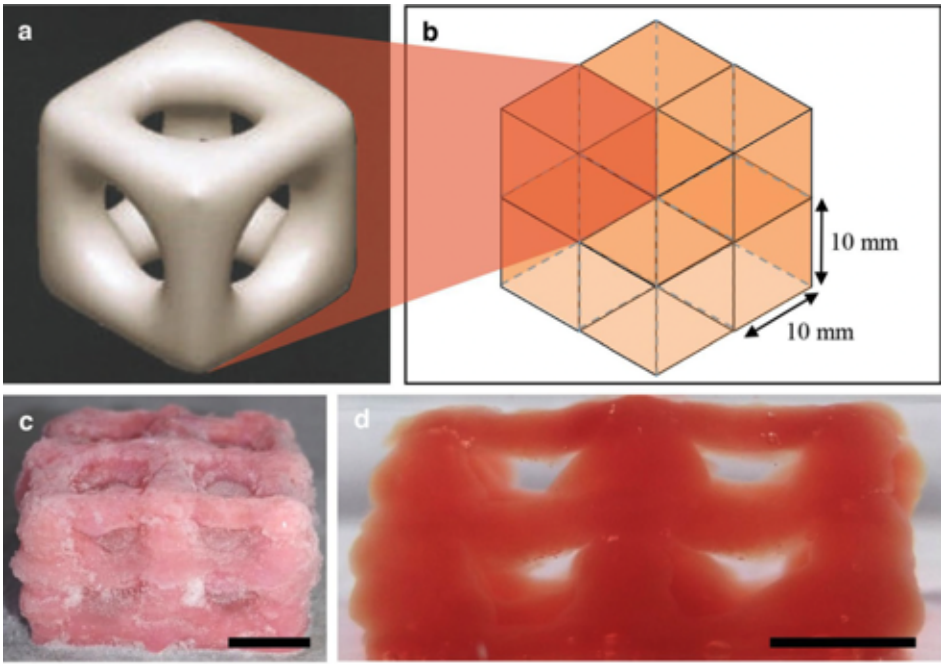

Figure 1.14: *Taken from [9] under creative commons attribute 4.0. (a) Cylindrical pore microstructure, adapted from [10] and (b) 8 unit cells printed; thawed printed 8 cell structure in (c) isometric view and (d) side view. Scale bars, (c) 10 mm and (d) 5 mm.*

Table 1.2: *Recent literature on sub-zero AM of PVA.*

PVA type	Print bed	Print temperature /ºC	Resolution /mm	Key results	Reference
PVA & PVA/GO-HA	Not described	-10	0.45	Use of additives (graphene oxide) to improve printability of PVA.	[148]
PVA/gelatin	Not described	-10	0.29	Comparison of printability of PVA and PVA/gelatin.	[149]
PVA	Dry ice.	Dry ice = -78.5. Temp of bed not given	0.26	Lattice structures 3D printed. Comparable mechanical properties to brain/lung tissue. Successful cell seeding.	[9]
P(DLLA-co-TMC)	Not described	-40	Not given	Additive manufacture of porous shop memory scaffolds.	[147]
Agar	Printed directly into LN2	None given (assumed -195)	Not given	3D printing directly into liquid N_2, allowing better Z-axis resolution.	[146]

Understanding and improving the print quality, and effect of additives, were the focus of the next two important studies undertaken on sub-zero AM. Firstly, Kim *et al.* studied inclusion of gelatin to increase cell viability, fabricating scaffolds for hard tissue regeneration [149]. This study freeze-dried scaffolds post manufacture before chemically cross-linking, giving higher mechanical stiffness to Tan *et al.* Kim *et al.* noted a significant decrease in scaffold pore size as the concentration of PVA was reduced (and concentration of gelatin was increased), as well as a significant decrease in compressive modulus [149].

Finally Meng *et al.* fabricated structures for articular cartilage replacement using a composite of PVA, graphene oxide, and hydroxyapatite (PVA/GO-HA) [148]. Primarily this study showed a significant increase in print quality as the concentration of PVA/GO was increased, as the extruded polymer showed better shear-thinning properties, as well as increased print quality with the addition of hydroxyapatite. This was the first study to also attempt to 3D print a gradient structure using sub-zero AM, achieving to fabricate a structure with a higher density at the surface, allowing increased stiffness, whilst having greater porosity at its base, allowing for stronger bioactive connections with biological tissues. Meng *et al.* also noted the temperature gradient present, with higher temperatures further away (Z axis) from the print bed. This introduced a gradient of pore size in the PVA, as the growth of ice crystals slowed down higher above the print bed. Although three of these have performed simple mechanical tests (uniaxial compression) on AM PVA, it should be noted that the impact of AM on the mechanical properties of PVA has yet to be fully explored.

These studies have proven the feasibility of using AM to manufacture PVA constructs, and most interestingly to harness the AM process to introduce graded properties, as shown by Meng *et al* [148]. However, all these studies lack thorough analysis of the mechanistic consequence of the AM process, with most only performing uniaxial compression testing. Although this successfully quantifies the elastic modulus of the

3D printed construct, it does not give much insight into how the AM process alters the structure of PVA compared to casting. For example, tensile testing will also give insight into potential weaknesses between filament strands. For the knowledge of sub-zero AM of PVA to progress, it is therefore crucial to understand the mechanistic consequence of AM parameters on the mechanical behaviour of the resulting construct. This will allow insight into how the design for manufacturing process should be alternated to both avoid unwanted stress concentrations, and to quantify how process parameters can be adjusted to alter and control the mechanical behaviour of PVA.

1.5 Imaging techniques for material characterisation

Imaging techniques are broadly used in materials science to analyse material characteristics such as heterogeneity, crack propagation, and surface properties. These techniques range from methods of optical microscopy, non-optic microscopy (for example scanning electron (SEM), or atomic force microscopy), X-ray techniques, ultrasound, and NMR or MRI. The most suitable imaging technique for a given application will depend on the material in question, and the aim of the analysis.

Multiple techniques have been used to analyse PVA, with most of these techniques being used to image surface properties of the hydrogel. Sardinha *et al.* for example used atomic force microscopy to compare the surface roughness of PVA to articular cartilage [11] (figure 1.15). AFM is a useful imaging technique for this application, as it allows the surface properties of the hydrogel (or cartilage) to be measured without dehydration. However, it is not possible to use this technique to image the internal structure of PVA.

SEM has been extensively used to analyse the structure of PVA [150] [151] [101]. For

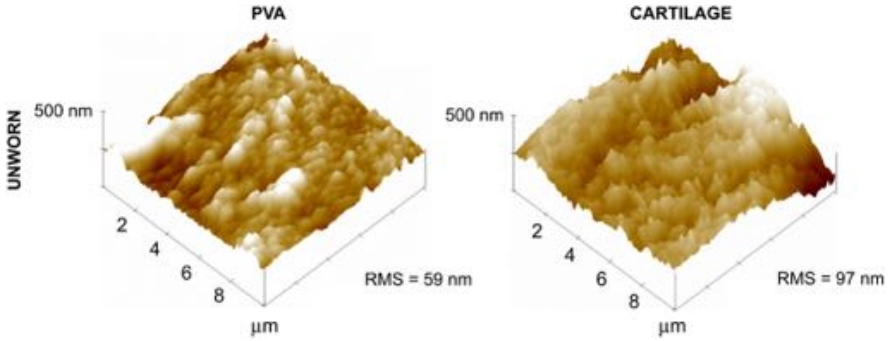

Figure 1.15: *Atomic force microscopy (AFM) scans (10 m×10 m) of unworn PVA and bovine articular cartilage and respective surface roughness values (RMS). Reproduced with permission [11].*

example the difference in effect of freeze thaw cycle on the micro-structure of PVA was shown by Jiang *et al.* [151]. However, a key limitation of SEM is the requirement for the hydrogel to be fully dehydrated prior to imaging. As with AFM, SEM also only allows the imaging of surface properties; in order to image the internal structure of a sample it must be cut open. Therefore, these imaging techniques can be classified as 'destructive', where either dehydration or physical damage mean the hydrogel cannot be used for its primary purpose once it has been imaged.

Non-destructive techniques used to analyse PVA include X-ray diffraction (XRD). XRD is frequently used to study the crystalline structure of materials, and has been used to study the structure of PVA [152]. Unlike SEM, XRD does not require dehydration or damage to the sample and is not limited to the surface properties of the sample. Although diffraction techniques allow for analysis of the micro-structure of PVA, XRD does not produce an image of the sample. This means XRD does not allow easy visualisation of the heterogeneity of the sample.

Both ultrasound and MRI allow imaging of the interior of the hydrogel whilst not dehydrating or otherwise permanently damaging the sample. The use of PVA with these techniques has predominately been aimed towards developing MRI and ultrasound techniques such as elastography [41] [153] [109]. It is important to note that the use of PVA in these studies was to aid in developing diagnostic techniques; the

imaging techniques were not used to as a method to analyse the material itself.

The distinction between the aim of disease diagnostics or material characterisation is most clear with Ultrasound. Ultrasound is a prevalent clinical imaging technique that has been widely adopted due to its low cost and complexity, whilst being non-invasive. Compatibility with ultrasound results in PVA being used as a phantom material to further improve clinical ultrasonic diagnostic techniques. However, ultrasound does not present itself as the best method to analyse the material itself, where resolution and image noise are unlikely to be sufficient to analyse the heterogeneity of PVA.

MRI proves to be the most promising non-invasive technique. Non clinical MRI instruments offer very high resolution (0.1 - 0.2 mm). MRI is well suited to characterising PVA due to its inherent dependence on water content and how water molecules interacts with its surroundings. It is therefore possible to non-invasively and non-destructively analyse differences in PVA composition, and the heterogeneity within a sample. Orr *et al.* characterised PVA using MRI, exploring the effect of PVA concentration on T_1 and T_2 relaxation times [154]. However, this study was focused on replicating the T_1 and T_2 relaxation times of the neonatal brain and did not ascertain differences in hydrogel heterogeneity. As MRI technology improves, the advent of small, high resolution MRI instruments designed specifically for non-clinical applications allows the suitability of MRI as a method to assess the heterogeneity of PVA hydrogels. Ultimately due to the better resolution of MRI, and its intrinsic relationship with water content to produce image contrast (which are inherent to the characteristics of hydrogels), it is the most compelling imaging technique to non-invasively study PVA.

1.5.1 Diagnostic imaging techniques

Imaging techniques are fundamentally important to the investigation of many diseases and injuries, as a tool to both aid diagnosis and long term treatment. These techniques

are also useful for analysing biomaterials, and the interactions between implants and biological tissues [155]. Medical imaging encompasses a wide variety of techniques, and the 5 most commonly used by the NHS as of 2020 [156] are Magnetic Resonance Imaging (MRI), ultrasound, and 3 subsets of radiography.

Most pertinent to this thesis, MRI relies on fundamental properties of atomic particles (most commonly protons) to non-invasively image internal biological structures within the body. Section 2.2 gives an overview of the core concepts of MRI required for this thesis. MRI is widely used in routine diagnosis for many purposes, for example:

- Imaging of the cardiovascular system [157]. Examples include diagnosing and treating atherosclerosis [158, 159, 160], imaging of ventricular function [161], and the diagnosis of different cardiomyopathies [162];
- Imaging of other connective tissues. For example: the pathology of achilles tendon injuries [163], to study the changes in the synovial joint from osteoarthritis [164] and obesity [165], as well as for the assessment of intervertebral disc degeneration [166];
- Non-invasive imaging of implants and biomaterials, for example:
  - Imaging the fatigue of bioprosthetic heart valves [167];
  - Characterisation of cartilage replacements [168];
  - To assess bone healing after the implantation of scaffolds [169].
- The assessment of tumours or cancers, for example: for brain tumour detection; [170], and for prostate [171] and breast cancer screening [172, 173].

Ultrasound is a non-invasive imaging technique which applies acoustic energy at high frequencies (typically $> 20kHz$), constructing an image based on the reflection of the emitted waves at tissue boundaries [174], and is most commonly used to image soft

tissues. Owing to the Doppler effect, ultrasound can also be used to study blood flow [175].

Radiography utilises a form of ionizing radiation, most commonly X-rays or gamma rays. The most commonly techniques are:

- Simple X-ray scans, routinely used for the diagnostic assessment of bone fractures and dislocations.
- Computed tomography, which offers higher resolution than X-ray, allowing it to be used for the diagnosis of more subtle fractures, organ injuries, as well as blood clots, and 3D reconstruction of biological structures and organs [176].
- and Fluoroscopy, which is a type of X-ray imaging used to image biological processes over time, showing a continuous X-ray image on a monitor. One of the most common uses Fluoroscopy is the assessment of joint and spinal stability in orthopaedics [177],

The purpose of this overview is to show that MRI is also the only well established diagnostic technique that allow for the non-destructive imaging of PVA constructs. This therefore gives future diagnostic benefits to analysing PVA using MRI, where well established clinical technique allows for the future potential of using MRI to analyse *in situ* PVA implants, where it could enable future non-invasive identification or monitoring of implants manufactured from PVA.

1.6 Aims & objectives

The aim of this thesis is to explore the design for additive manufacture, and intrinsic material properties of PVA cryogels, with respect to their use as replacement for connective tissue. Intrinsic viscoelastic and MR properties of PVA will be analysed, and

the potential of AM to control the mechanical behaviour of 3D printed samples will be explored. The objectives of this thesis are as follows:

- To explore the relationship between the compositional changes in PVA on both its dynamic viscoelastic properties and MR T_2 relaxation time, as well as explore the correlation between these two intrinsic material properties;
- To develop a sub-zero AM platform, and to validate the effect of AM on the viscoelastic properties of PVA;
- To further explore the use of AM to control the material properties of PVA, by developing a method to parametrically control the AM toolpath.

1.7 Thesis structure

As this is a multidisciplinary thesis, chapter 2 includes key relevant theory required to understand the methodologies, results and conclusion presented. Section 2.1 presents the fundamental mechanics of materials that underpins the viscoelastic and hyperelastic work presented in chapters 3, 4, and 5. Section 2.2 then gives a brief overview of the theory of MRI, which is fundamental theory required to interpret the results and discussion presented in 3 regarding the MRI of PVA. This information has been included to enhance communication between different disciplines. If the reader is already familiar with these subjects, they may wish to proceed to chapter 3.

Chapter 3 presents the dynamic viscoelastic characterisation of PVA, exploring the impact of concentration, molecular weight, and the number of freeze thaw cycles. The MR T_2 relaxation time has also been characterised for the same compositions, and the correlation between the two properties has been explored.

Chapter 4 explores a method to additively manufacture PVA at sub-zero temper-

atures, and explores the anisotropy caused by the additive manufacturing process of 3D printed samples with different nozzle sizes. This chapter also analyses the effect of true stress and strain on the viscoelastic properties of AM and cast PVA.

Chapter 5 further explores the additive manufacture of PVA, presenting a method to introduce functionally graded mechanical properties into 3D printed PVA. Exploring and defining the effect of different parameters of the tool path on both the stiffness (Young's modulus) and hyperelastic material properties under uniaxial tension.

Finally, chapter 6 presents the overall findings of this thesis, and discusses where this research could lead in the future.

This thesis contains appendices presenting material not included within the main body, to avoid repetition and disrupting the main reporting, but are included for completeness. Appendix A contains viscoelastic and MRI T_2 data relevant to chapter 3. Appendix B contains viscoelastic data relevant to chapter 4, as well as the Matlab code used to calculate the viscoelastic properties based on both engineering and true stress and strain. Appendix C includes further figures of AM PVA samples relevant to chapter 5, and appendix D gives the Matlab code written to generate G-code for the toolpaths presented in chapter 5.

Chapter 2

THEORY

The purpose of this chapter is to outline the relevant theory required to understand the methodologies, results and conclusion presented in this thesis. Section 2.1 presents the fundamental mechanics of materials that underpins the viscoelastic and hyperelastic work presented in chapters 3, 4, and 5. Section 2.2 then gives a brief overview of the theory of MRI; most importantly how T_2 relaxation time is calculated. This is fundamental theory required to interpret the results and discussion presented in 3 regarding the MRI of PVA.

2.1 Mechanics of materials

The following section outlines the fundamental mechanics that define elastic, hyperelastic, and viscoelastic mechanical properties. The following references provide further information regarding: the mechanics of materials [178]; constitutive modelling of CT [21, 179]; viscoelasticity [180]; and DMA [181].

2.1.1 Stress & strain: An introduction

The deformation of materials under load is a key principle of material mechanics, where the basics of how materials deform, and how deformation is measured underpins the majority of materials engineering. Understanding the core concepts of deformation is vital knowledge before discussing more intrinsic material properties such as hyperelasticity and viscoelasticity. Forces (normally given in Newtons, N) are fundamentally important when studying engineering within a biomedical context - from the biomechanics at play whilst running, or lifting heavy objects; the cyclic forces exerted on the arterial wall or heart valves from blood circulation; to the forces vital to bone formation and healing through mechanotransduction. However, the shape and size of a given structure must be considered to gather a complete picture of how it will deform (figure 2.1). Taking into account a structures geometry allows a force to be normalised with respect to the surface area it is applied to, and deformation to to be normalised in terms of a unit length.

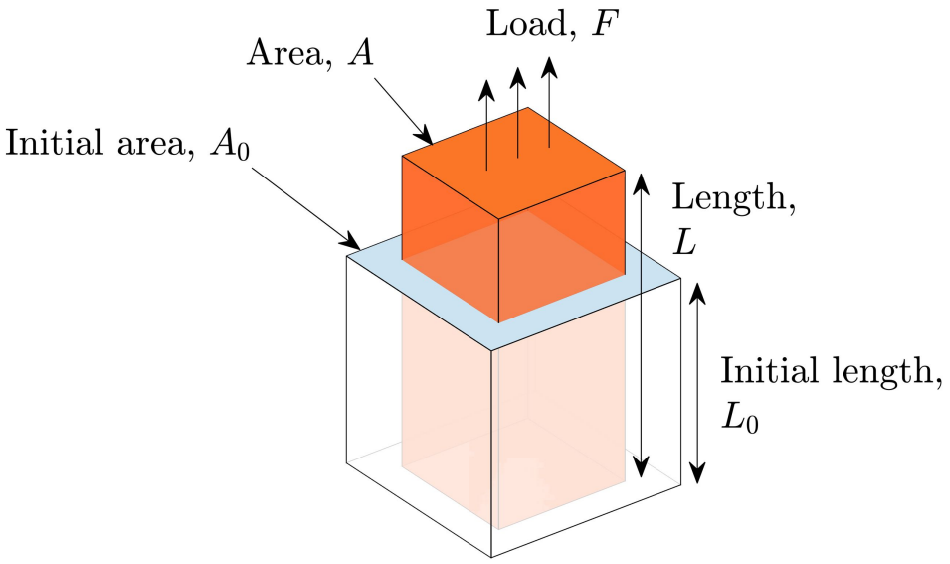

Figure 2.1: *Uniaxial tension of rectangular sample, showing force (F), length L, and initial length L_0*

In most cases, *stress*, (σ) Nm^{-2} (or Pa) is a much more useful unit of measure,

giving insight into how much force is being applied per unit area of a material, and is calculated by dividing the force applied (N) by the cross-sectional area, A of the sample (Equation 2.1). It is important to note that the area used to measure stress is normally measured as the *initial* cross-sectional area, A_0 - the importance of this will be become more relevant in section 2.1.2.

$$\sigma = \frac{F}{A_0} \tag{2.1}$$

When deformation is measured, the change in dimension that occurs in the direction of the applied force is of most interest. As with the value for force, this measurement, ΔL can be normalised to the sample geometry, where the ratio of the change in sample length to the initial length can be calculated to give the relative change in length. This measurement is called *strain*, ε, and is unitless (Equation 2.2).

$$\varepsilon = \frac{L - L_0}{L_0} = \frac{\Delta L}{L_0} \tag{2.2}$$

2.1.2 True stress & strain

The measurements that have just been described are known as engineering stress and engineering strain, and in most cases are good approximations of the stresses and strains present in a material. This is because instantaneous changes in area and length have not been taken into account when calculating these values. Taking into account these changes is not as simple as it may first seem, and will either require taking very accurate measurements of the cross-sectional area during testing, or making assumptions about how the material deforms. For most materials, an assumption of incompressibility is made, meaning that the volume of the sample is assumed to remain constant throughout deformation. Therefore the product of A and L will remain constant, and

the instantaneous A can be calculated (Equation 2.3). This allows the formation of an definition for true stress, σ_t (Equation 2.4)

$$AL = A_0 L_0 \quad \therefore A_0 = \frac{AL}{L_0} \tag{2.3}$$

$$\sigma_t = \frac{F}{A} \quad = \quad \frac{FL}{A_0 L_0} \quad = \quad \frac{F}{A_0}(1+\varepsilon_e) \quad = \quad \sigma_e(1+\varepsilon_e) \tag{2.4}$$

In order to calculate true strain (ε_t), it is required to sum the instantaneous strain values throughout the total deformation range. The instantaneous strain can therefore be integrated with limits of L and L_0 in order to calculate ε_t (Equation 2.5).

$$\varepsilon_t = \int_{L_0}^{L} \frac{dL}{L}\, dL \quad = \quad ln\frac{L}{L_0} \quad = \quad ln(1+\varepsilon_e) \tag{2.5}$$

2.1.3 Elasticity

A material can be described as elastic if it returns to its original shape after being unloaded. The majority of solid materials, for example metals, are linearly elastic. This means they follow Hooke's law (Equation 2.6), stating that the force applied, F to the material is in direct proportion to the induced displacement, x, where k is a material specific constant.

$$F = kx \tag{2.6}$$

Alternatively linearly elastic materials can be described by the relationship between stress and strain (Equation 2.7), where the constant, E is the modulus of elasticity (or

Young's modulus). The Young's modulus is an often cited material property that describes the material's stiffness, and is calculated as the ratio of stress, σ to strain, ε (Equation 2.7).

$$\sigma = E\varepsilon \quad \therefore E = \frac{\sigma}{\varepsilon} \tag{2.7}$$

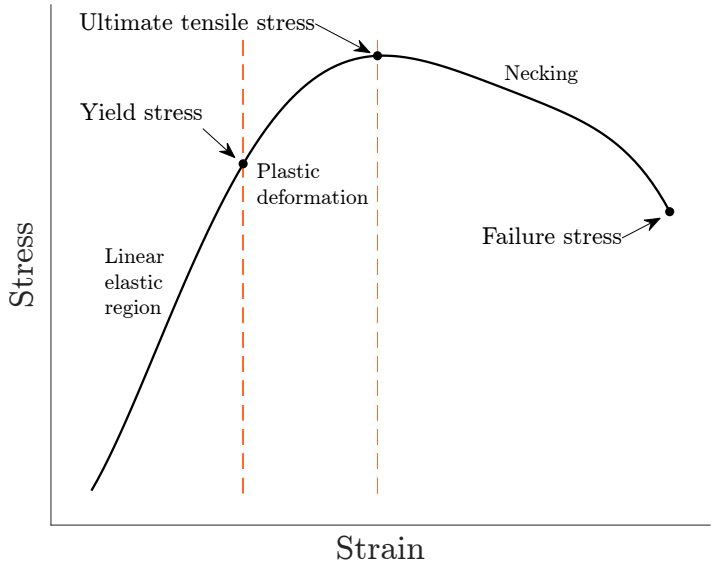

Figure 2.2: *Typical stress & strain response of a linearly elastic material indicating: the elastic region, yield stress, ultimate tensile stress, and failure stress.*

It is important to note that E can only be accurately calculated for a material in the linear elastic region, prior to occurrence of any plastic deformation. For this reason, other commonly given mechanical properties include the yield strength - which indicates the maximum stress a material can undergo before plastically deforming, and ultimate tensile strength - which is the maximum stress before the material breaks. Figure 2.2 shows the typical stress and strain response of a linearly elastic material until failure.

2.1.4 Hyperelasticity

Even though most materials can be modelled as linearly elastic at low strains, the majority of soft connective tissues and hydrogels are non-linear (figure 2.3). A common constitutive model of non-linear mechanics is hyperelasticity, which derives the relationship between stress and strain from a strain energy density function, where the strain energy density is simply the energy per unit volume required to deform the material.

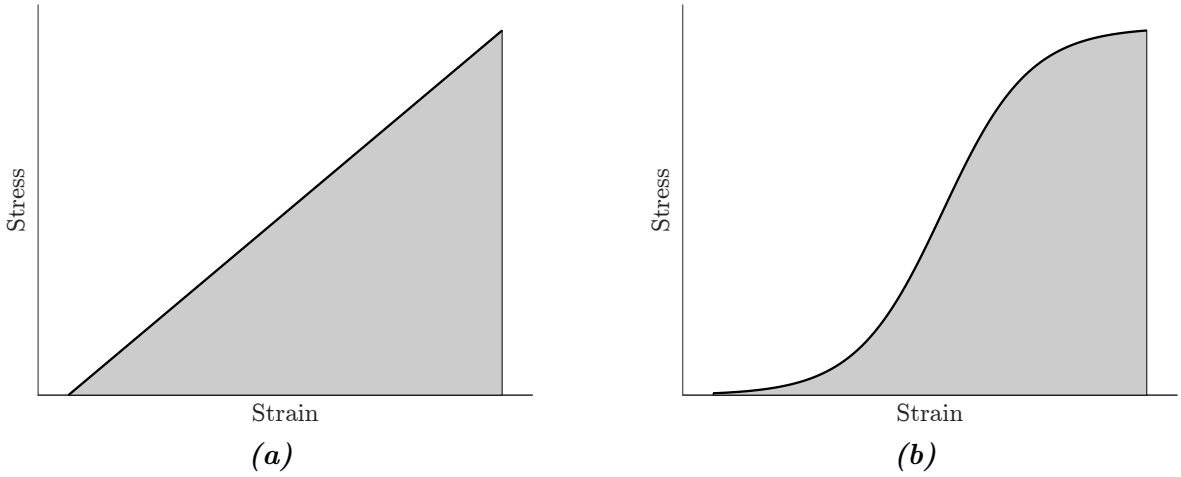

Figure 2.3: *Example plots showing the stress & strain relationship for linear elastic (a) and a typical hyperelastic (b) material. The area under the graph gives the strain energy per unit volume.*

There are two classifications of hyperelastic model: phenomenological, which are used to model the observed behaviour of a material under deformation; and mechanistic models, which derive the model based on the underlying material structure. For the purpose of this thesis only phenomenological models of hyperelasticity will be covered, as hyperelastic models will be fitted to data collected through mechanical testing.

For a hyperelastic material, the mode of deformation is crucial when ascertaining its mechanical behaviour, given a material will respond differently when loaded under uniaxial tension, compression or shear. As the hyperelastic data presented in this thesis is under uniaxial tension, this is will be the focus of this section when understanding

the material behaviour of hyperelastic materials.

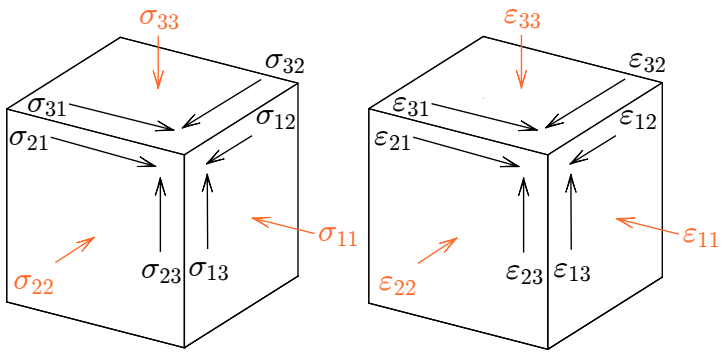

(a) *Stress tensor* ***(b)*** *Strain tensor*

Figure 2.4: *Figures indicating the components of stress (a) and strain (b) for a three dimensional material. Principal stresses and strains are shown in orange*

.

The strain energy function, W is most commonly defined as a function of the strain tensor, ε (Equation 2.8), with the stress at any given deformation being calculated from this function. This function is often calculated as the sum of the deviatoric and volumetric strain energies. For materials deformed under uniaxial tension, only the principal strains (shown in orange in figure 2.4 b) are relevant as no shearing should occur.

$$W = f(\varepsilon) \tag{2.8}$$

2.1.4.1 Principal stretches

There are two methods for deriving a strain energy density - either by using principal stretches, or strain invariants. The principal stretches are given by the ratio of the final length L to the original length L_0 in all three dimensions (x, y, z) (Equation 2.9)(figure 2.5). For a material under no stress, the principal stretches will equal zero, with uniaxial tensions and compression giving positive and negative results respectively.

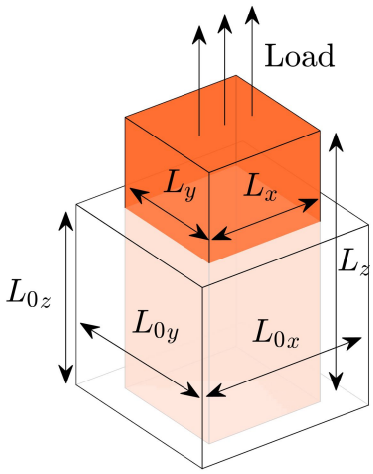

Figure 2.5: *Diagram showing the change in dimensions used to calculate principal stretches in the x, y and z axes.*

$$\lambda_x = \frac{L_x}{L_{0x}} \quad \lambda_y = \frac{L_y}{L_{0y}} \quad \lambda_z = \frac{L_z}{L_{0z}} \tag{2.9}$$

Note that the principal stretches, λ are equal to $1 + \varepsilon_e$ (Equation 2.10), and can therefore be used to describe the amount of strain that a material undergoes under any mode of deformation.

$$\lambda_i = \frac{L_i}{L_{0i}} = \frac{L_{0i} + \delta_i}{L_{0i}} = 1 + \frac{\delta_i}{L_{0i}} = 1 + \varepsilon_{ei} \tag{2.10}$$

2.1.4.2 Strain invariants

The strain invariants can be used to describe the overall strain applied to a material (Equations 2.11, 2.12, and 2.13, note $tr(\varepsilon)$ refers to the trace of the tensor, and $det(\varepsilon)$ refers to its determinant). Unlike the principal stretches, the strain invariants do not vary depending on the coordinate system, and therefore remain constant regardless of the mode or axis of deformation. These invariants are calculated from the strain tensor

(figure 2.4b, where $\varepsilon_{a,b}$ is the strain in a given mode and axis.

$$I_1 = tr(\varepsilon) = \varepsilon_{11} + \varepsilon_{22} + \varepsilon_{33} \tag{2.11}$$

$$I_2 = \frac{1}{2}\{[tr(\varepsilon)]^2 - tr(\varepsilon)\} = \varepsilon_{12}^2 + \varepsilon_{23}^2 + \varepsilon_{31}^2 - \varepsilon_{11}\varepsilon_{22} - \varepsilon_{22}\varepsilon_{33} - \varepsilon_{33}\varepsilon_{11} \tag{2.12}$$

$$I_3 = det(\varepsilon) = \varepsilon_{11}\left(\varepsilon_{22}\varepsilon_{33} - \varepsilon_{23}^2\right) - \varepsilon_{12}\left(\varepsilon_{11}\varepsilon_{33} - \varepsilon_{23}\varepsilon_{31}\right) + \varepsilon_{13}\left(\varepsilon_{21}\varepsilon_{32} - \varepsilon_{22}\varepsilon_{31}\right) \tag{2.13}$$

The majority of the hyperelastic models shown below only use I_1 and I_2 to define the strain energy function. I_1 and I_2 can be most often interpreted as the dilatational and distortional components of the strain tensor respectively, where the dilatational component relates to changes in volume, and the distortional component relates to changes in shape [182].

2.1.4.3 Common hyperelastic models

The strain energy function of a general polynomial model for a compressible material is given in equation 2.14. This has two components, the first is a function of I_1 and I_2, and the second term is a function of the strain energy potential, J. For an incompressible material, the volumetric term is not required, so the function can be simplified to equation 2.15.

$$W = \sum_{i,j=0}^{n} C_{ij} \left(\bar{I}_1 - 3\right)^i \left(\bar{I}_2 - 3\right)^j + \sum_{k=1}^{m} D_k (J-1)^{2k} \tag{2.14}$$

$$W = \sum_{i,j=0}^{n} C_{ij} \left(I_1 - 3\right)^i \left(I_2 - 3\right)^j \tag{2.15}$$

where C_{ij} are material constants, and $C_{0,0} = 0$.

For all polynomial models (i.e. for any value of n), the initial shear, μ_0 and bulk moduli k_0 are calculated based only on the first order polynomial (where $n = 1$), from equations 2.16 and 2.17.

$$\mu_0 = 2(C_{1,0}C_{0,1}) \tag{2.16}$$

$$k_0 = \frac{2}{D_1} \tag{2.17}$$

The reduced polynomial model is a special case of the polynomial model, where the impact of the second invariant is ignored. Yeoh (1993) justified this as the impact of I_2 on W, is generally much lower than I_1, and is also more difficult to isolate and assess [183]. This results in it often being sensible to ignore, resulting less error that cannot be easily assessed or quantified. The general equation of a reduced polynomial model for an incompressible material is given in equation 2.18. For any reduced polynomial model, the intial shear is given by $C_{1,0}$.

$$W = \sum_{i=0}^{n} C_{i0} \left(I_1 - 3\right)^i \tag{2.18}$$

Common special cases of the reduced polynomial model are the Neo-Hookean model

where $n = 1$, and the Yeoh model where $n = 3$.

The Ogden model (equation 2.19) bases the strain density function on the principal stretches $(\lambda_1, \lambda_2, \lambda_3)$. It is assumed for that for an incompressible material that $\lambda_1\lambda_2\lambda_3 = 0$.

$$W(\lambda_1, \lambda_2, \lambda_3) = \sum_{p=1}^{N} \frac{\mu_p}{\alpha_p} \left(\lambda_1^{\alpha_p} + \lambda_2^{\alpha_p} + \lambda_3^{\alpha_p} - 3\right) \tag{2.19}$$

where N, μ_p and α_p are material constants.

An Ogden model is defined in terms of an initial shear modulus given by μ, and the material property α. Although this does not directly correlate to a material property, it describes the shear behaviour of the the material. A value of $\alpha = 2$ describes a Newtonian material, whilst $\alpha < 2$ and $\alpha > 2$ describe shear thinning and thickening behaviour respectively. As it describes a materials properties under shear, it α should be constant for a given material, and shear thickening behaviour should require an explanation (for example the presence of fibre reinforcement) [184].

2.1.5 Viscoelasticity

As previously mentioned (in section 2.1.3) a purely elastic material will return to its original shape once a load has been removed, provided, of course, that it does not undergo plastic deformation. This is because the material is able to store the energy applied to it; that energy is then released when the material is unloaded, and it is able to 'spring' back to original shape. A purely *viscous* material on the other hand, will dissipate all of the energy applied to it during loading, and will retain its new shape once unloaded. The vast majority of biological soft tissues are somewhere in between, and exhibit *viscoelastic* mechanical behaviour, meaning they will both store

and dissipate a proportion of the energy applied to the material during loading. A good visual representation of this difference between elastic and viscoelastic materials can be seen when examining the impact of unloading a material. As a purely elastic material does not dissipate energy, the unloading cycle should mirror the loading cycling (figure 2.6 a). However, due to the dissipation of energy a hysteresis loop is present when plotting the loading and unloading of a viscoelastic material (figure 2.6 b), where the area between the lines gives the amount of energy dissipated.

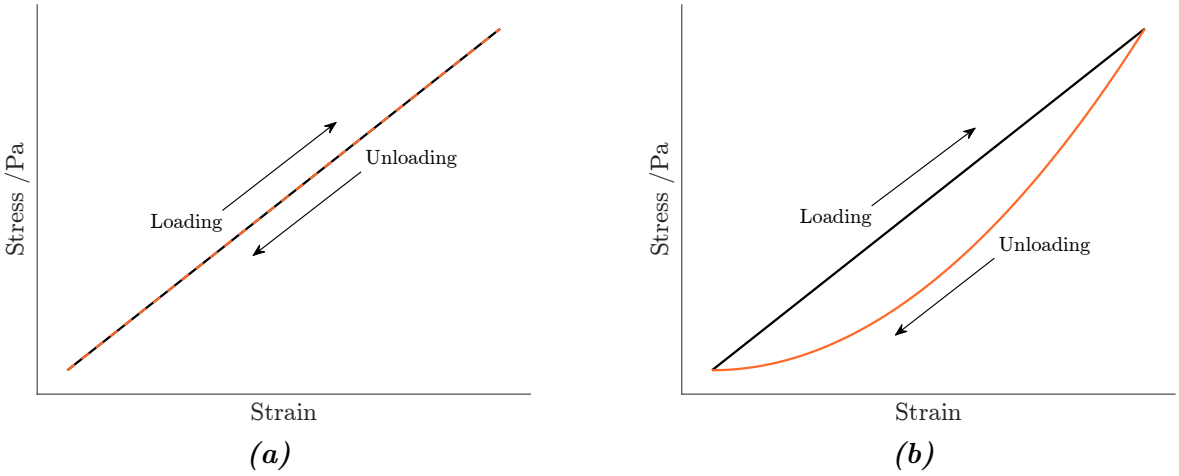

Figure 2.6: *Example plots showing the loading and unloading cycle for a linear elastic (a) and linear viscoelastic (b) material.*

Viscoelastic materials also exhibit stress relaxation and creep. When a purely elastic material is held under a constant load, the material deformation will remain constant, as no energy is dissipated over time. Conversely, due to a viscoelastic material's ability to dissipate energy, the strain applied to the material will begin to *creep*, meaning the deformation will increase over time at a constant load (figure 2.7 a). Similarly, a viscoelastic material held a constant strain, will exhibit *stress relaxation*, mean the induced stress will decrease over time under a constant displacement (figure 2.7 b). Depending on the precise nature of the material, the induced stress will either asymptote to a final value, or potentially to zero.

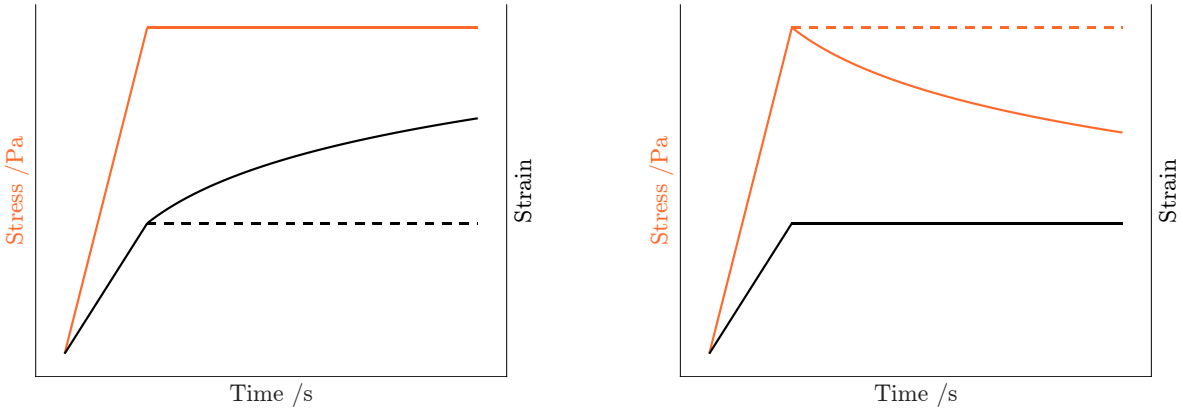

(a) *Stress relaxation* ***(b)*** *Creep*

Figure 2.7: *Example plots showing the effects of stress relaxation (a) and creep (b) for a viscoelastic material. The response for an elastic material is shown for reference (dashed).*

2.1.5.1 Dynamic mechanical analysis

Up until this point, only quasi-static material properties have been discussed. That is to say, the tests performed to calculate either the Young's modulus of a material, fit a hyperelastic model, or assess the impact of stress relaxation, require only the application of a load to a material. This can be useful to understand fundamental mechanical properties of a material, however, especially with viscoelastic materials, testing under dynamic conditions is fundamental in simulating the stress and deformation that occur under physiological conditions. For example, applying a static load to a heart valve will not simulate the stress induced at 180 *bpm*. This is due to the fact a lot of viscoelastic elastic materials exhibit frequency dependant material properties, and may respond very different at low strain rates compared to high [28].

Dynamic mechanical analysis (DMA) is a method used to characterise the viscoelastic mechanical properties of a material, ultimately outputting: a storage modulus, E', which characterises the amount of energy stored; and a loss modulus, E'', which characterises the energy dissipation of the material. DMA involves applying a sinusoidal displacement, x to a material at a given frequency, and measuring the corresponding

sinusoidal load, F (figure 2.8). Given that for a viscoelastic material the strain will 'lag' and return back to its original state after the load does so (as seen in the hysteresis loop of figure 2.6 b), there will be a phase lag, δ, between the two waveforms.

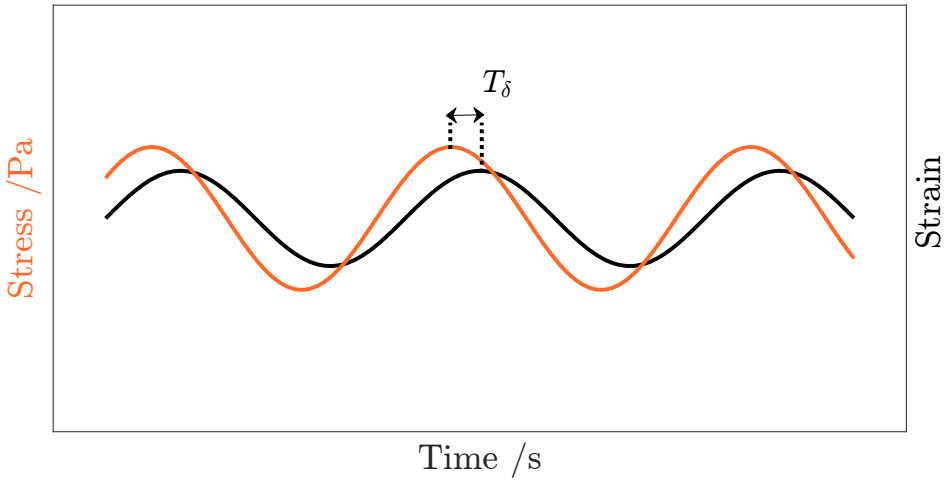

Figure 2.8: *Sinusoidal load, and corresponding displacement plotted against time. T_δ shows the time lag between the two waveforms.*

In order to calculate the relevant mechanical properties, the data acquired from testing needs to be transformed from the time domain to the frequency domain. This means that Fourier analysis needs to be performed. A fast Fourier transform (FFT) of both the waveforms for displacement and load should be calculated, and the magnitudes of dataset length for the fundamental frequency can then be found; harmonics are ignored for both. (figure 2.9). The phase lag, δ can be calculated as the difference between the phase angles of the displacement δ_x, and force, δ_F (Equation 2.20).

$$\delta = \delta_x - \delta_F \tag{2.20}$$

Once Fourier analysis has been performed, the complex stiffness, K^* can be calculated by dividing the peak load magnitude, F^* by the peak displacement magnitude, x^* (Equation 2.21). The complex modulus (which can be seen as the dynamic counterpart to the elastic modulus) can then be calculated by taking into account the specimen shape, dividing K^* by the shape factor, S of the material (Equation 2.22). The shape

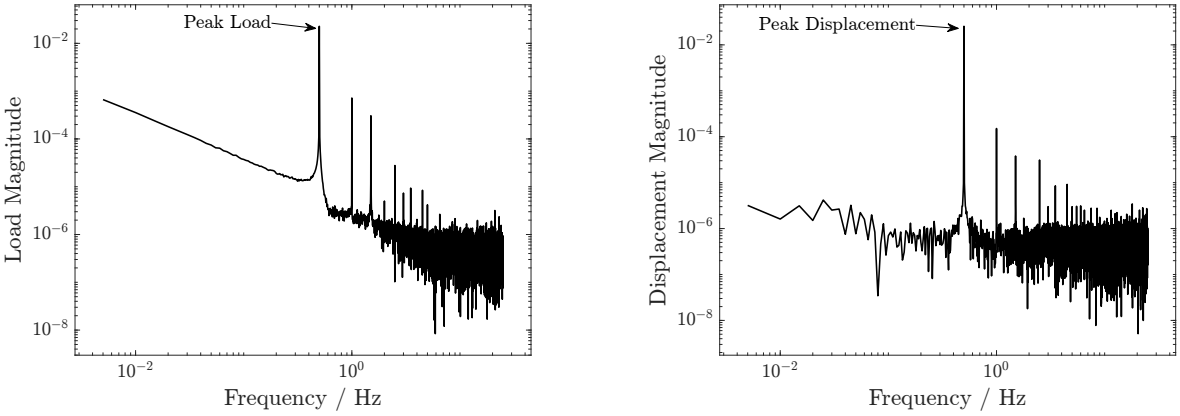

(a) *Load* ***(b)*** *Displacement*

Figure 2.9: *FFT plots indicating peak magnitudes for load and displacement in the frequency domain.*

factor is calculated as the volume of the specimen.

$$K^* = \frac{F^*}{x^*} \tag{2.21}$$

$$E^* = \frac{K^*}{S} \tag{2.22}$$

At this point it should be noted that, because acquired data has been Fourier transformed, both K^* and E^* are complex numbers, meaning they have both real and imaginary components. We can understand how to calculate the storage and loss moduli by plotting E^* on an argand diagram (figure 2.10).

From figure 2.10, it can be see that the real and imaginary components can be calculated using trigonometry given a known value for δ. In the case of E^*, the real component gives the value for the storage modulus (Equation 2.23), and the imaginary component gives the value for the loss modulus (Equation 2.24).

$$E' = E^* cos(\delta) \tag{2.23}$$

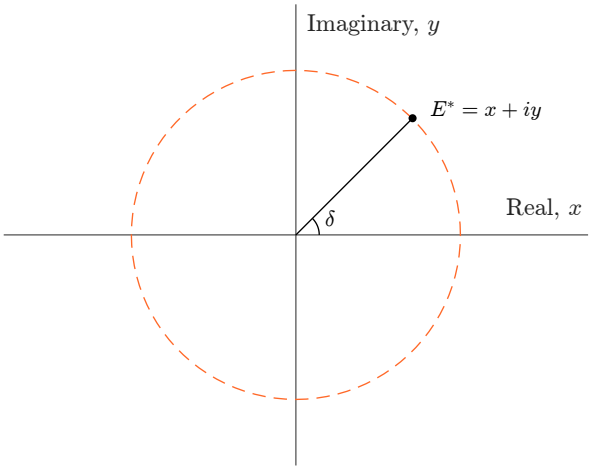

Figure 2.10: *Argand diagram visualising the real and imaginary components of E^*.*

$$E'' = E^* sin(\delta) \tag{2.24}$$

2.2 A brief overview of NMR & MRI

This section will give a brief overview of the theory required to understand the concepts of MRI and T_1 & T_2 relaxation times. A complete explanation of the MRI phenomenon is beyond the scope of this thesis. For further reading, the following references may be of interest [185, 186].

MRI is an application of Nuclear Magnetic Resonance (NMR), and is reliant on a property of atomic particles called *spin*, I. Spin describes two intrinsic quantum mechanical properties: angular momentum, and the magnetic moment of the particle. An atom exhibiting spin is often depicted as a small spinning top (2.11). Although this is a helpful way to picture spin, it is not entirely accurate as the particle does not actually rotate about an axis. Rather, spin is a fundamental property of nature and interacts with the electromagnetic force, in the same way that mass is a fundamental property interacting with the gravitational force.

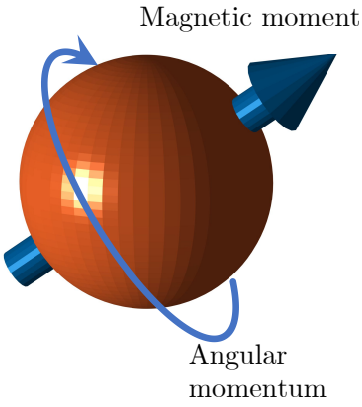

Figure 2.11: *A representation of atomic spin. This visualisation helps understand the core principles of NMR.*

In the case of a proton, $I = 1/2$ and under the influence of an external magnetic field, $\mathbf{B}_0$, the spin will have two states: spin up $I = +1/2$, where it is parallel to the magnetic field and spin down $I = -1/2$, where it is anti-parallel. As the magnetic field will apply a torque to the particle, the angular momentum caused by spin will cause it to precess about the axis of the magnetic field, much like a gyroscope (figure 2.12). The frequency, ω of precession is directly proportional to the strength of the magnetic field, $\mathbf{B}_0$ (equation 2.25)

$$\omega = \gamma \mathbf{B}_0 \tag{2.25}$$

where γ is an atom specific constant.

For a collection of protons, the probability of the state of a particle being spin up and spin down can be calculated, and the net magnetisation, M_0 of the system, can be calculated. The net magnetisation can be treated in terms of classical mechanics, and would be expected to act like a vector. Under equilibrium, M_0 will align in the direction of $\mathbf{B}_0$, which we will assign to the z axis. During the acquisition of an MR image, a radio frequency pulse (with a frequency equal to that of the precession), will

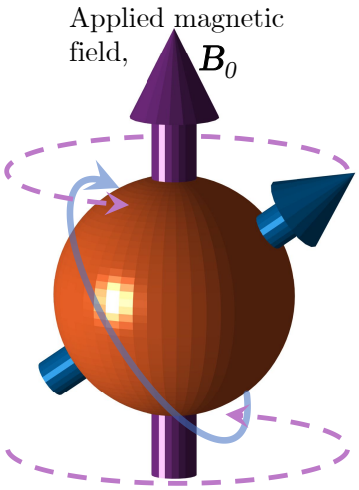

Figure 2.12: *A representation of atomic precession caused by the introduction of an external magnetic field. (The axis of precession is shown by the dashed purple arrows.)*

be applied to the system, causing the vector, M to precess around $\mathbf{B}_0$, aligning with the xy plane (figure 2.13). This excitation is what is measured as an NMR signal.

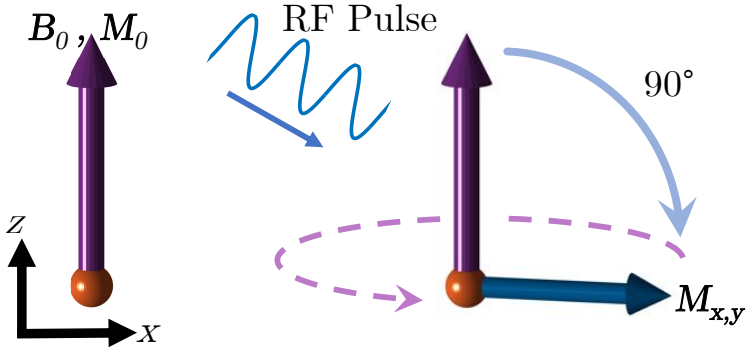

Figure 2.13: *A representation of the excitation of the net magnetisation by an RF pulse, causing M to flip from the z axis to the x, y plane.*

There are two key relaxation processes which are most commonly measured in MRI, T_1, which is related to the signal measured in the longitudinal axis (parallel to $\mathbf{B}_0$) and T_2, related to the signal measured in the transverse (the x, y plane). The maximum signal you could expect to measure in the x, y plane, is when the precession of all spins in a system are in phase, and in an ideal scenario this should be the case immediately after an excitation pulse has been applied. However, as the spin of an individual proton will be dependant on the its localised magnetic field and interactions between nearby spins, the spins will dephase and the resulting signal will exponentially decay. The

time constant of this decay is the T_2 relaxation time (figure 2.14).

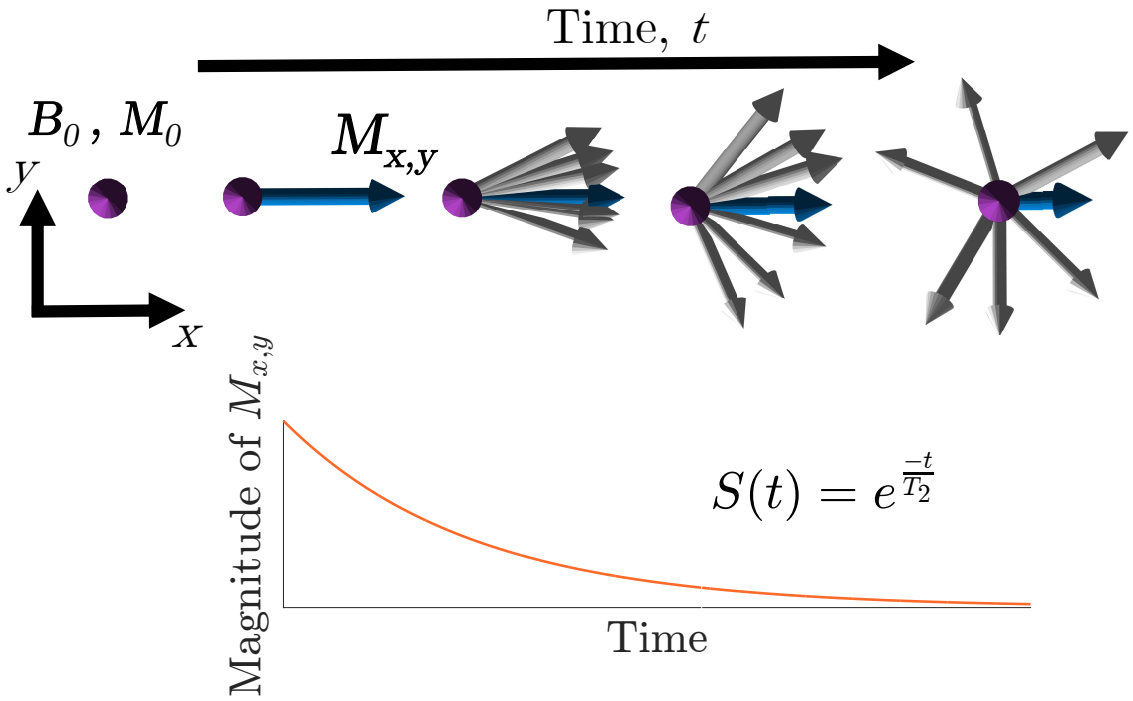

Figure 2.14: *A diagram illustrating the dephasing of spins in the x, y plane that results in a decrease in signal intensity. Grey arrows indicate the spin of individual particles, whilst the blue arrow represents the net magnetisation $M_{x,y}$. Note that the proportion of spins that will be in phase, and contribute to the NMR signal, is grossly overestimated in diagrams such as this.*

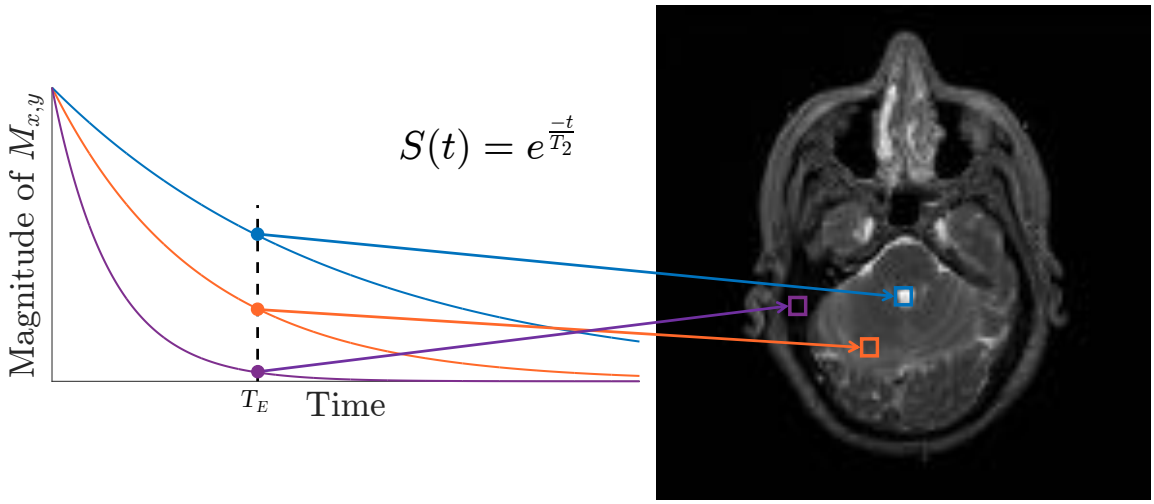

Figure 2.15: *An example of how contrast is created in a T_2 weighted image. Materials with longer T_2 times will have more signal after T_E, and will appear brighter. Image taken from the visible human project (public domain).*

T_2 relaxation is an intrinsic property of a tissue or material, and the signal will

most likely decay at a different rate for different materials. Therefore contrast can be created in an image by acquiring data at a specific time, T_E after excitation. Figure 2.15 shows an example of this, where one material with a longer T_2 (shown in blue) and therefore a comparatively higher signal after T_E, is depicted as brighter. Whereas another material (purple) with almost no signal after T_E, is shown as black.

The other key relaxation process that is commonly observed in MRI, is the return of the net magnetisation to equilibrium, returning to its initial state prior to RF excitation, where it is aligned with $\mathbf{B}_0$. If the magnitude of M_z is measured during this relaxation process, it will increase according to an exponential function, tending to M_0, and the time constant of this function is called T_1 (figure 2.16).

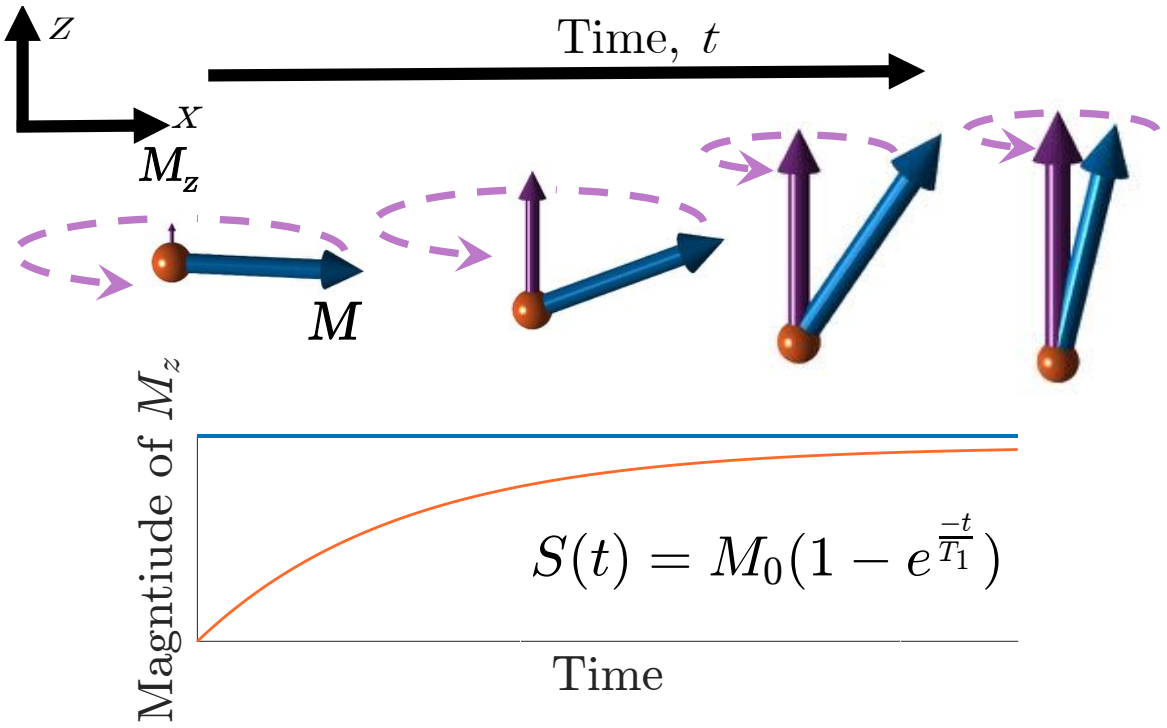

Figure 2.16: *A diagram illustrating the measurement of T_1, where the net magnetisation slowing returns to equilibrium, where it is aligned with $\boldsymbol{B}_0$.*

As with T_2, T_1 is an intrinsic property for a biological tissue or material. Therefore contrast can be created in images with materials that exhibit different values of T_1. In this case the repetition time, T_R, which is the time between excitations, is varied. For a chosen value of T_R, a material with a longer T_1 relaxation time will not have fully

returned to equilibrium. Therefore the magnitude of M_z will not reached its maximum (equal to M_0), and will appear darker in MR images.

Finally, it is important to note that, although T_1 and T_2 have been described independently, it is not possible to fully isolate the two processes. Instead, T_1 and T_2 weighted images are produced by carefully controlling the input parameters when acquiring an image, so that one of the two relaxation processes is the determining factor for image contrast.

STATEMENT OF CONTRIBUTIONS I

The research presented in chapter 4 has been previously published in *Materials Science and Engineering: C*, a peer reviewed scientific journal. As the primary author of this publication, I retain the right to include it in a thesis or dissertation, provided it is not published commercially. (https://www.elsevier.com/about/our-business/policies/copyright#Author-rights). Further information regarding the publication, including author contributions is given below.

J. P. Crolla, M. M. Britton, D. M. Espino, L. E. J. Thomas-Seale, The dynamic viscoelastic characterisation and magnetic resonance imaging of poly(vinyl alcohol) cryogel: Identifying new attributes and opportunities, *Materials Science and Engineering: C*, 2021. DOI: https://doi.org/10.1016/j.msec.2021.112383.

AUTHOR CONTRIBUTION

- **J.P. Crolla**: Conceptualization, investigation, data analysis, draft manuscript.
- M.M. Britton: Supervision, coordination, review & editing.
- D.M. Espino: Supervision, coordination, review & editing.
- L.E.J. Thomas-Seale: supervision, conceptualization, coordination, review & editing.

Chapter 3

THE VISCOELASTIC CHARACTERISATION AND MRI OF PVA.

3.1 Introduction

As made evident in chapter 1 (section 1.2.1), the mechanical behaviour of a given CT is specific to its biological function. CTs exhibit, viscoelastic, hyperelastic, anisotropic, and functionally graded behaviour. Replicating all these functions for a given CT is non-trivial, and prior to exploring the potential of AM to control some of these intrinsic material properties (chapters 4 and 5), it is important to fundamentally understand the mechanical behaviour and structure of cast PVA. This allows for a more informed understanding of how the additive manufacturing process changes the intrinsic properties of PVA.

The material properties of PVA have been broadly studied, showing its potential

to replicate the stiffness of many CTs (As discussed in section 1.3.4). However, few studies have comprehensively studied the effect of concentration, freeze thaw cycle, and MW. Further to this, to the authors knowledge no previous studies have systemically studied the viscoelastic response of PVA under a range of frequencies relevant to the physiological loading of CT. This is important because the viscoelastic behaviour of CTs is often frequency dependant. For example, articular cartilage responds differently when loading expected whilst walking (1 Hz), vs. when running (8-12 Hz). Viscoelastic behaviour is intrinsic to the structure of a material, and so is difficult to directly control. However, for the viability of a material to replace a CT, it must behaviour in a predictable manner across a wide range of frequencies. The first key contribution to knowledge from this chapter will therefore be to comprehensively assess the effect of PVA composition on its viscoelastic behaviour across a range of physiologically relevant frequencies.

As noted in section 1.5, MRI offers the best potential to non-invasively image PVA due to intrinsic dependence on water content to produce image contrast; for example, a change in PVA concentration will directly correspond to a change in MRI signal [154]. However, the use of high-resolution MRI to assess PVA material heterogeneity has not been assessed. PVA has been described as a biphasic material, consisting of a solid and liquid phase, and the interaction between the two phases is a driving factor of viscoelastic behaviour [187] [188]. As the interaction between PVA crystallites and water is dependant on concentration, FTC, and MW, it is hypothesised these parameters will affect the viscoelastic response of the hydrogel. Therefore, both MRI signal and viscoelastic behaviour are primarily driven by PVA composition, allowing the potential to correlate the two measurements. The second key contribution to literature of this study will therefore be to assess if a significant trend can be measured between MRI T_2 relaxation time and viscoelastic properties, as well as assessing the heterogeneity of PVA with MRI.

PVA cryogels are extensively used for numerous applications and possess the distinctive advantages that the mechanical properties can be designed through manufacturing. Yet, the extensive use of PVA, and ultimately the clinical translation, must be supported by relevant and thorough mechanical and chemical characterisation. To date, there are some key omissions in research literature which aim to characterise this biomaterial.

The majority of soft tissues in the body are viscoelastic [26, 27, 23], including connective tissue [141], therefore mechanical viscoelastic characterisation is crucial to under pin any research involving PVA tissue scaffolds or mimics. It has been reported in the literature that PVA exhibits viscoelastic properties [116, 117, 118], yet it has not yet been characterised using dynamic mechanical analysis (DMA). DMA measures dynamic viscoelasticity; characterising a material in terms of its ability to store energy (storage modulus) and its ability to dissipate energy (loss modulus). An induced stress results in instantaneous strain (the elastic response) and a time-dependent strain (the viscous response). This characterisation technique is analogous to *in vivo* dynamic loading, and as such, is a crucial methodology to describe the mechanical response of the material.

PVA can be imaged by magnetic resonance (MR) imaging (MRI) using the nuclear magnetic resonance (NMR) signal of the water within the material. This is regarded as an important characteristic, particularly in its application as a vessel mimicking material [109, 39]. Chu *et al.* demonstrated, for a fixed concentration, the change in MR T1 and T_2 relaxation times with FTCs. Orr *et al.*[39]. Orr *et al.* showed the effect of PVA concentration and temperature on the MR T1 and T_2 relaxation times, using a 3T MRI instrument [154]. In these studies, the relationship between manufacturing parameters and MR relaxation is incomplete. This study will investigate MW, concentration and FTCs simultaneously, and thus, it will comprehensively support the dynamic mechanical analysis. Neither of these previous studies [39, 154] were able to confirm sample

homogeneity, due to the lower spatial resolution, typical of clinical MRI instruments. This research will apply a high-resolution micro-imaging instrument ($7T$) and thus determine the impact of the manufacturing protocol on the sample homogeneity.

3.1.1 Aims and objectives

The research presented in this chapter will mechanically and chemically characterise PVA cryogel against compositional and manufacturing parameters, which to date have not been addressed in research literature. The chapter aims to characterise the effect of composition against MW and number of FTCs on the viscoelastic mechanical properties and the MR T_2 relaxation time of PVA. This will be achieved through the following objectives:

- The relationship between concentration, MW and the number of FTCs, and the viscoelastic mechanical properties of PVA will be assessed;
- The relationship between compositional variation and MR T_2 will be assessed, as well as the use of MRI to identify material heterogeneity;
- The potential relationship between viscoelastic and MR properties will be explored.

3.2 Methodology

3.2.1 Sample preparation

Cylindrical specimens with dimensions of 20 mm diameter and 10 mm height were used for all DMA and MRI analyses. The specimen size was chosen to give the maximum

surface area to assess the heterogeneity of PVA compositions through MR Imaging (relative to the core of the instrument). PVA was acquired from Sigma Aldrich (St Louis, Missouri, USA) and had a hydrolysis of 99+%. To incorporate the range of molecular weights (MW) of PVA this study utilised two different MWs; 89-98 kDa and 146-186 kDa. Each MW was manufactured at concentrations of 10, 15, 17.5, and 20%. A total of 72 samples (six samples for each composition of PVA) were used for mechanical testing; with another 36 (three samples per composition of PVA) samples used for imaging (table 3.1).

Table 3.1: *Reference table for molecular weight, freeze thaw cycles, and concentrations of PVA compositions used in this study.*

Composition reference	Molecular Weight (kDa)	No. Freeze thaw cycles	Concentrations (% x)
PVA-A	89-98	3	10 15 17.5 20
PVA-B	146-186	1	10 15 17.5 20
PVA-C	146-186	3	10 15 17.5 20

PVA powder was stirred into distilled water, covered (to reduce evaporation) and stirred using an automatic overhead stirrer, at 90°C for one hour, where upon it was fully dissolved. The mixture was stirred for another 1 hour, to retain homogeneity, whilst the solution was allowed to cool down to room temperature. The solution was poured into cylindrical moulds and then underwent 3 FTCs. The FTC process consisted of three phases across 24 hours; 12 hours in the freezer at -20°C , 4 hours in the freezer without active cooling (to increase temperature gradually), and finally 8 hours at a room temperature of 22 $\pm$ 1°C (figure 3.1. After the required FTCs, the samples were stored in distilled water for three days to reach hydrostatic equilibrium. Each MW and all concentrations were assessed after 3 FTCs. Molecular weight 146-186 kDa was

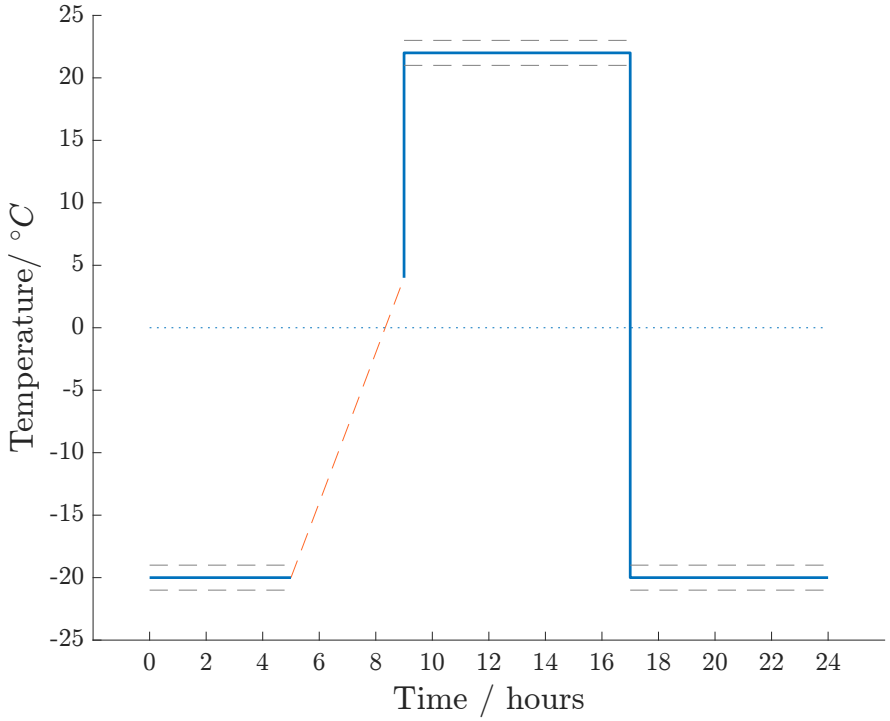

Figure 3.1: *Approximate freeze thaw cycle process over a 24 hour period. 4 hour period without active cooling is approximated (dashed orange). Grey dashed lines show* $\pm 1°C$ *uncertainty in freezer and room temperature.*

assessed at 1 FTC. Molecular weight 89-98kDa was not assessed at 1 FTC due to low stiffness.

3.2.2 Experimental Protocol

3.2.2.1 Magnetic resonance imaging

MR images of 3 PVA samples at four different concentrations of PVA-A, PVA-B, and PVA-C, were collected using a Bruker Biospin DMX-300 spectrometer (Bruker UK Limited, Coventry, UK) operating at a proton resonance frequency of 300.13 MHz with a field strength of 7T. A Micro 2.5 imaging probe, with a 25 mm ^1H quadrature Radio Frequency (RF) coil, was used for all experiments. MR T_2 relaxation maps were determined from a series of 8 echo images using the spin-echo imaging sequence RARE (Rapid Acquisition with Relaxation Enhancement) [189]. Images were collected using

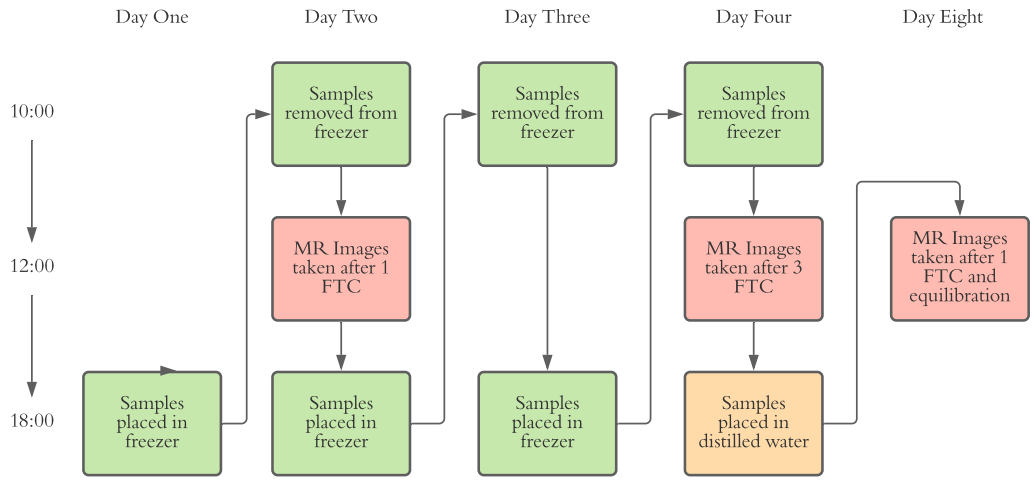

Figure 3.2: *Flow-chart showing protocol used to assess the effect of 3 repeat freeze thaw cycle and equilibration on T_2 relaxation time*

a 128 × 128 pixel array, 25 × 25 mm^2 of view and a slice thickness of 1 mm. MR T_2 relaxation maps were calculated using a repetition time (TR) of 15,000 ms, with a RARE factor of 8. To quantify the difference between the number of FTCs, and storage in water on the MR T_2 relaxation time of PVA, nine samples of 10% 146-186 kDa PVA were imaged immediately post-thawing, after 1 and 3 FTCs without storage in water (figure 3.2). They were then allowed to reach equilibrium in distilled water for three days, and subsequently imaged again. These samples were not mechanically tested in order to remove any additional variables which may alter their MR T_2 relaxation time.

3.2.2.2 Dynamic mechanical analysis

A Bose Electroforce 3200 (Bose Corporation, Electroforce systems Group, Minnesota, USA; now TA Instruments, Delaware, USA) mechanical testing machine, running Wintest software (TA Instruments, Delaware, USA) was used to perform all DMA. A sinusoidal displacement (d) was applied to the samples, and corresponding load (F) and phase lag (δ) were measured. A Fast Fourier Transform (FFT) of both the load (F^*) and displacement (d^*) was then performed, with the ratio between their respective

data-set lengths giving a dynamic stiffness (K^*); equation 3.1. The storage (k') and loss (k'') stiffness were then calculated using equations 3.2 and 3.3. The sample diameter (D), and height (h) were measured for all samples in order to calculate their shape factor (S); which for a cylinder is given by equation 3.4. The storage (E') and loss (E'') moduli were then calculated using equations 3.5 and 3.6, respectively. This method is consistent with characterising the dynamic viscoelasticity of natural and synthetic biomaterials [26, 23].

$$F^* = \frac{F^*}{d^*} \tag{3.1}$$

$$k' = k^* cos(\delta) \tag{3.2}$$

$$k'' = k^* sin(\delta) \tag{3.3}$$

$$S = \frac{\pi D^2}{4h} \tag{3.4}$$

$$E' = \frac{k'}{S} \tag{3.5}$$

$$E'' = \frac{k''}{S} \tag{3.6}$$

Samples were compressed by 20% of their measured height using a frequency sweep of 0.5 – 10 Hz. This frequency range was chosen to replicate the strain rates expected in different connective tissues; such as coronary arteries (0.5 – 10 Hz) [23], heart valve

leaflets (0.5 – 10 Hz) [22], chordae tendineae (0.5 – 10 Hz)[24], and articular cartilage under physiological loading (1 – 10 Hz). A preconditioning cycling of 5 Hz for 60 seconds was run prior to each test to negate the effects of stress relaxation. Complex moduli can be calculated from storage and loss moduli using equation 3.7 (note it is not included in the results or supplementary sections to avoid repetition of data).

$$E^* = \sqrt{E'^2 E''^2} \tag{3.7}$$

3.2.2.3 Data analysis

All statistical analyses were performed using SigmaPlot (SYSTAT, San Jose, CA, USA). Data has been represented as mean ± standard deviation (SD) unless otherwise stated. Regression analysis has been used to empirically fit trendlines for comparisons between viscoelastic properties (storage, E' and loss, E'' moduli) and concentration (equations 3.8 and 3.9); MR T_2 relaxation rate, MR R_2 and concentration (equation 3.10); and viscoelastic properties and MR T_2 relaxation rate (equations 3.11-3.14). All the constants of the equations for regression and coefficients of determination (R^2) for trend lines are given in supplementary data.

$$E', E'' = a + be^{dC} \tag{3.8}$$

$$E' = f + gC \tag{3.9}$$

$$R_2 = x + yC \tag{3.10}$$

$$E'_A = a_s + b_s e^{d_s R_2} \tag{3.11}$$

$$E'_B = a_s + b_s R_2 \tag{3.12}$$

$$E''_A = a_l + b_l e^{d_l R_2} \tag{3.13}$$

$$E''_B = a_l + b_l R_2 \tag{3.14}$$

Where a_s, b_s, and d_s are constants for E' ; and a_l, b_l, and d_l are constants for E''; and C is the concentration of PVA.

A one way ANOVA was used to ascertain whether a statistically significant difference between the loss moduli of 15, 17.5 and 20% PVA-C was present. Results with $p < 0.05$ were considered significant.

3.3 Results

3.3.1 Dynamic viscoelasticity and composition of PVA

3.3.1.1 PVA concentration and viscoelastic properties

Storage Modulus: An increase in PVA concentration from 10-20% resulted in an increase in Storage modulus at all frequencies (figure 3.3); this was the case for the three compositions of PVA (A, B, C). For example, for PVA-A tested at 0.5 Hz, the storage modulus increased from 158 ± 9.5 kPa at 10% concentration to 484 ± 24 kPa at 20% concentration. Frequency affected all compositions in a similar manner, with an increase in storage modulus as the frequency was increased (figure A.1). For PVA-A, between 0.5 and 10 Hz, average increases of 8.2, 8.1, 15, and 13% were calculated for 10, 15, 17.5, and 20% concentrations.

An exponential relationship was evident between storage modulus and concentration for PVA-A ($R^2 = 0.99$) and PVA-B ($R^2 = 0.96$) (figures 3.4a and 3.4b). This differed to the linear relationships shown by PVA-C ($R^2 = 0.94$) (3.4c). These relationships were apparent for all frequencies.

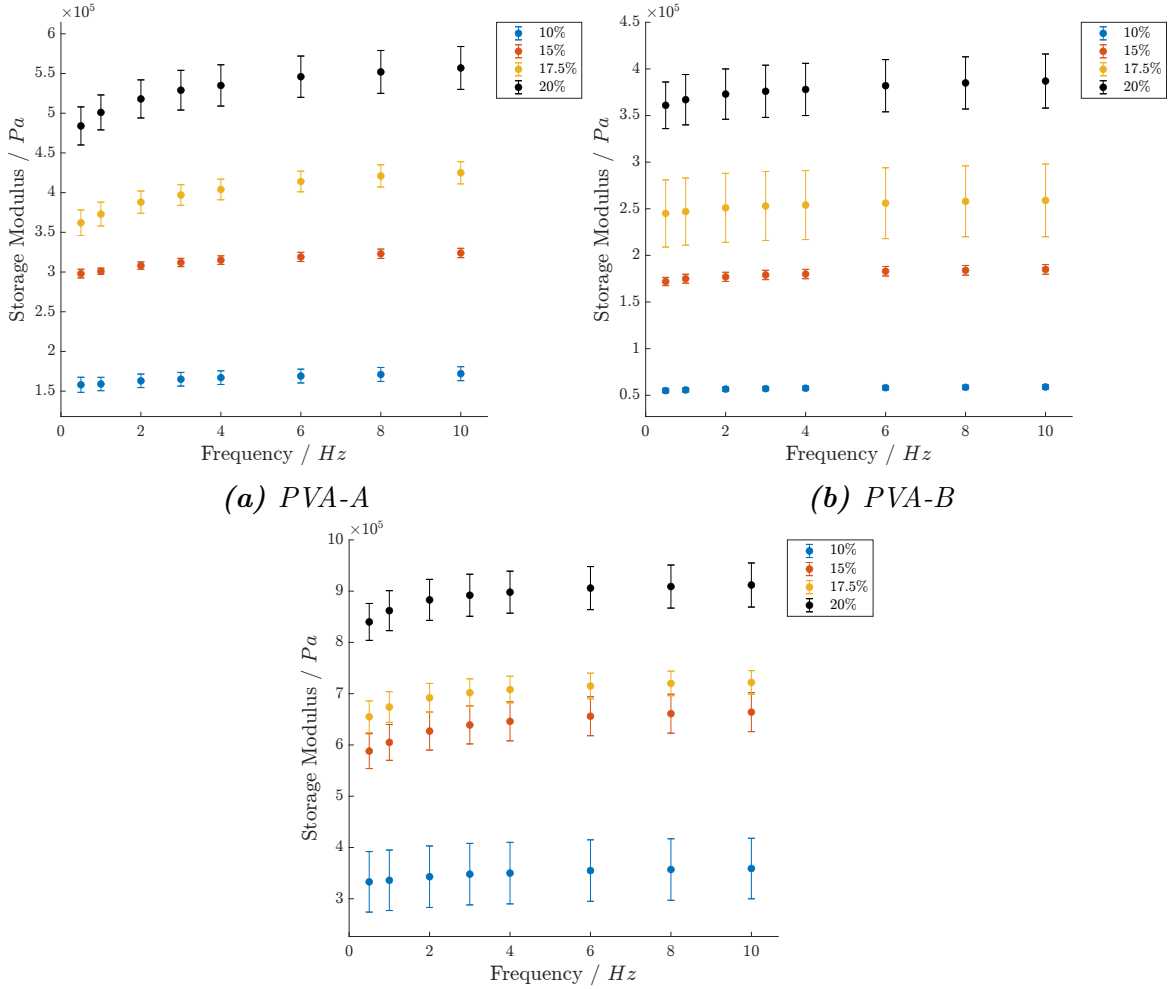

(a) PVA-A

(b) PVA-B

(c) PVA-C

Figure 3.3: *Storage modulus for PVA-A (a), PVA-B (b), and PVA-C (c), at concentrations of 10, 15, 17.5 and 20% w/w. Error bars show 95% confidence intervals (n = 6).*

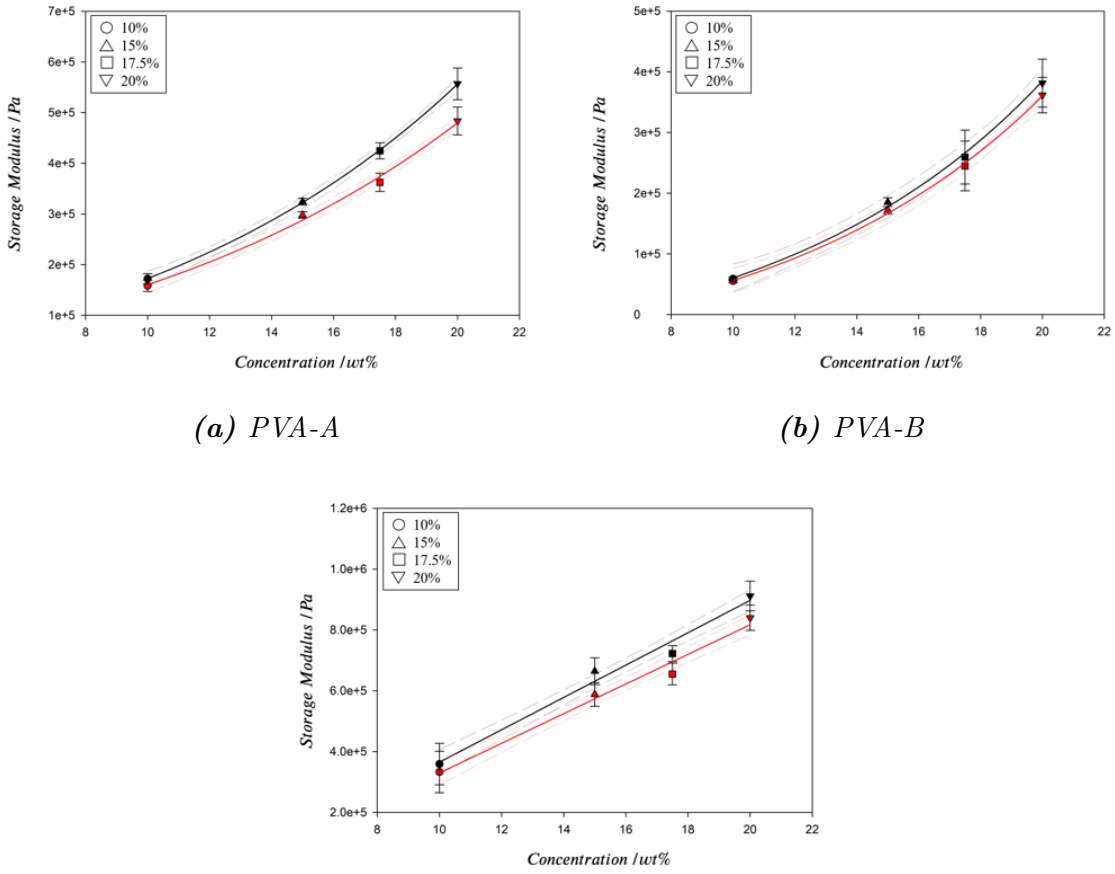

(a) *PVA-A*

(b) *PVA-B*

(c) *PVA-C*

Figure 3.4: *Storage Modulus plotted against concentration for 0.5 Hz (red), and 10 Hz (black) for PVA-A (a), PVA-B (b), and PVA-C (c). Error bars show 95% confidence (n= 6). Regression lines for 0.5 Hz (red), and 10 Hz (black) are also given; dashed lines show 95% confidence intervals for regression.*

Loss Modulus: For all samples, loss modulus was found to be lower than storage modulus. For PVA-A and B, a similar relationship was seen between loss modulus and PVA concentration, with an increase in concentration resulting in an increase in loss modulus at all frequencies tested (figure 3.5). For example, for PVA-A tested at 0.5 Hz, an increase from 25.4 ± 2.3 kPa at 10% concentration to 86.5 ± 2.3 kPa at 20% concentration was measured. A large increase in loss modulus was seen at all frequencies between 10 and 15% concentration for PVA-C (increasing from 38.1 ± 5.4 kPa to 87.8 ± 11 kPa at 0.5 Hz, and 39.9 ± 3.0 kPa to 73.1 ± 13 kPa at 10 Hz). However, no statistically significant difference was seen between 15, 17.5 and 20% at any frequency ($p = 0.53 \pm 0.25$) (figure 3.5).

Frequency was shown to impact loss modulus; for PVA-A between 0.5 and 10 Hz, average changes of 22%, 4.8%, 10%, and 7.8% were seen at 10 ,15, 17.5, and 20% w/w, respectively (figure A.2). A more consistent increase of 49, 49, 50, and 41% at each concentration was seen for PVA-B (figure A.2). For PVA-C, a change of 0.1% was seen at 10%, and a decrease of 20, 21, and 27% was seen for 15, 17.5, and 20% w/w (figure A.2), respectively. An exponential relationship was derived empirically between the loss modulus and concentration for PVA-A ($R^2 = 0.95$) and PVA-B ($R^2 = 0.91$) (figures 3.6a and 3.6b). However, a similar relationship was not observed for PVA-C (figure 3.6c), thus no trend line has been empirically fitted.

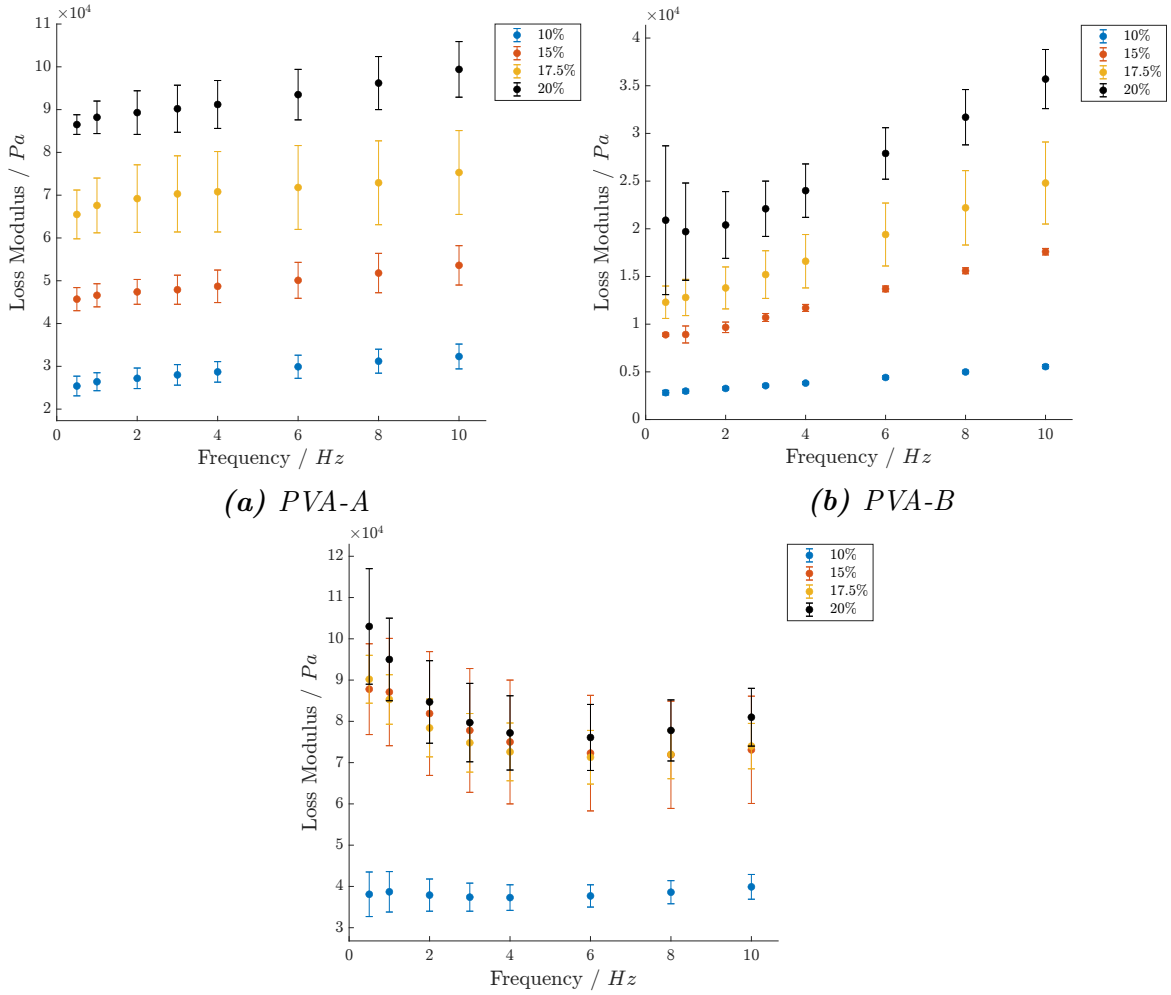

(a) *PVA-A*

(b) *PVA-B*

(c) *PVA-C*

Figure 3.5: *Loss modulus for PVA-A (a), PVA-B (b), and PVA-C (c), at concentrations of 10, 15, 17.5 and 20% w/w. Error bars show 95% confidence intervals (n = 6).*

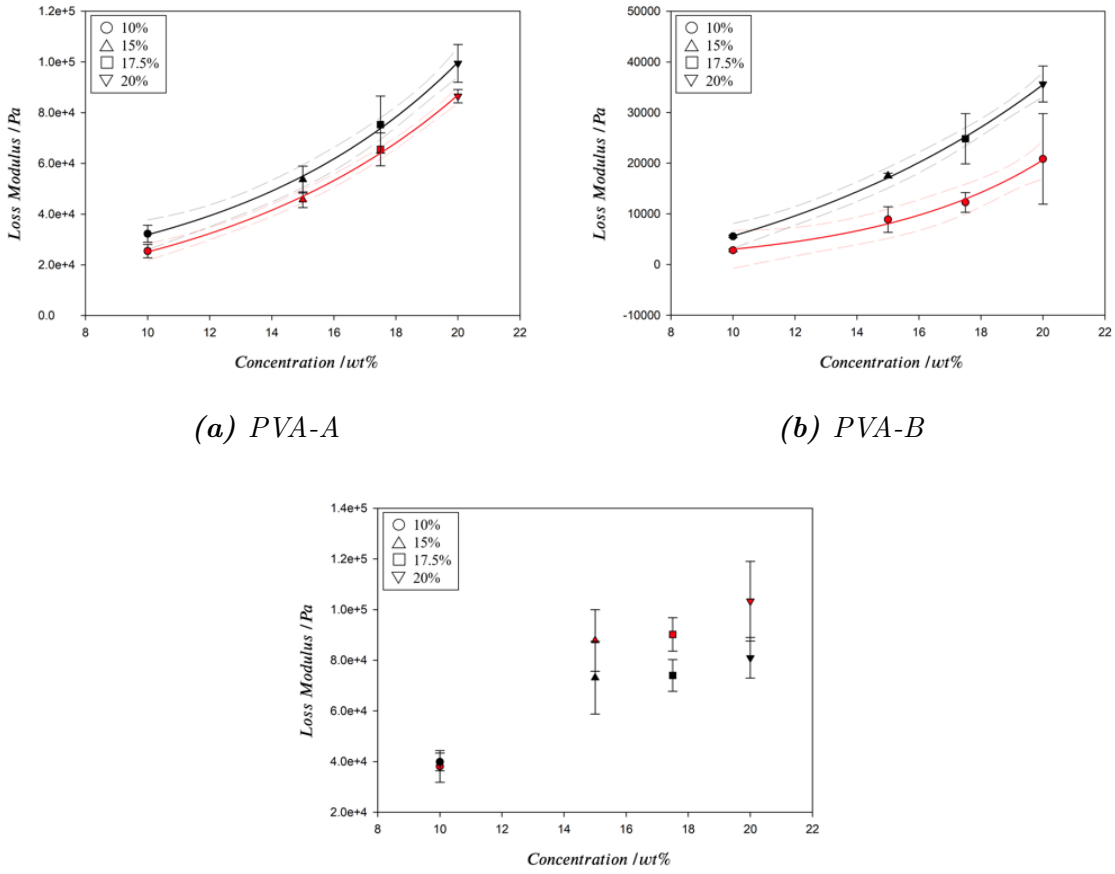

(a) *PVA-A*

(b) *PVA-B*

(c) *PVA-C*

Figure 3.6: *Loss Modulus plotted against concentration for 0.5 Hz (red), and 10 Hz (black) for PVA-A (a), PVA-B (b), and PVA-C (c). Error bars show 95% confidence (n= 6). Regression lines for 0.5 Hz (red), and 10 Hz (black) are also given; dashed lines show 95% confidence intervals for regression.*

3.3.1.2 Molecular weight of PVA and viscoelastic properties

The Storage modulus increased for all concentrations of PVA with increasing molecular weight, from 89-98 kDa to 146-186 kDa (figures 3.3a and 3.3c). This increase was observed for all frequencies, with an average of a 2.1 × increase at 10% w/w concentration; 2.0 × at 15% w/w concentration; 1.8 × at 17.5% concentration; and 1.7 × at 20% concentration. As stated in section 3.1.1, the frequency dependency of storage modulus showed little change, and both compositions could be empirically characterised using an exponential trend line to compare storage modulus and PVA concentration (figures 3.5a and 3.5c). An increase in loss modulus was also observed for 10, 15, and 17.5% at all frequencies. An average increase of 1.3 × at 10% w/w concentration; 1.6 × at 15% w/w concentration; 1.1 × at 17.5% concentration. A decrease of 0.91 × was noted for 20% w/w concentration. As per section 3.1.1, the frequency dependency of the loss modulus was shown to be different for the two MWs of PVA, with the loss modulus increasing with respect to frequency for PVA-A, and decreasing for PVA-C. It was also previously noted that no significant trend could be used to describe the effect of concentration on loss modulus for the higher MW PVA, as compared to lower MW PVA concentrations where the trend could be empirically characterised using an exponential trend line.

3.3.1.3 Freeze thaw cycles on viscoelastic properties

The storage modulus increased for all concentrations of PVA with an increase from 1 to 3 FTCs (figures 3.3b and 3.3c). This increase was observed for all frequencies, with an average 6.1 × increase at 10% w/w concentration; 3.5 × at 15% w/w concentration; 2.8 × at 17.5% concentration; and 2.4 × at 20% concentration. An increase in loss modulus was also observed for all samples at all frequencies when the number of FTCs was increased. However, smaller increases were seen at higher frequencies for each

concentration. This decrease varied from 14 × at 0.5 Hz to 7.2 × at 10 Hz at 10% w/w concentration; 9.9 × to 4.2 × at 15% w/w concentration; 7.3 × to 3 × at 17.5% w/w concentration; and 4.9 × to 2.3 × at 20% w/w concentration. The inter sample variation increased for 10% PVA when the number of FTCs was increased to 3. With SD being 2.8 ± 0.08% of the mean after 1 FTC, and 17 ± 0.4% of the mean after three cycles.

3.3.2 Magnetic resonance imaging and composition of PVA

3.3.2.1 Molecular Weight, Concentration and MR T_2 Relaxation Time.

MR T_2 Relaxation time was shown to decrease as concentration of PVA was increased from 10 to 20% (Table 3.2). The plot of MR T_2 relaxation rate against concentration for all compositions shows a linear relationship (Figure 3.7). The difference in MW (comparing PVA-A and PVA-C), created a minimal difference in MR T_2 relaxation times $\leq$ 5%. Comparing PVA-B and PVA-C showed that as the concentration was increased, the difference between the MR T_2 relaxation time increased with FTC.

Table 3.2: *MR T_2 Relaxation times (mean ± SD) for PVA-A, B, and C, at concentrations of 10, 15, 17.5 and 20 % w/w.*

%w/w	PVA-A		PVA-B		PVA-C		Increase in MW (A-C)	Increase in FTC (B-C)
	Mean (ms)	SD	Mean (ms)	SD	Mean (ms)	SD	% Mean difference	
10	117	0.8	119	5.2	123	3.6	5.1	3.4
15	90.2	1.1	86	2.6	90.3	1	0.1	5
17.5	82.8	0.4	70	1.5	82.2	1.3	-0.7	17.4
20	77.9	1	59.1	0.7	78	0.1	0.1	32

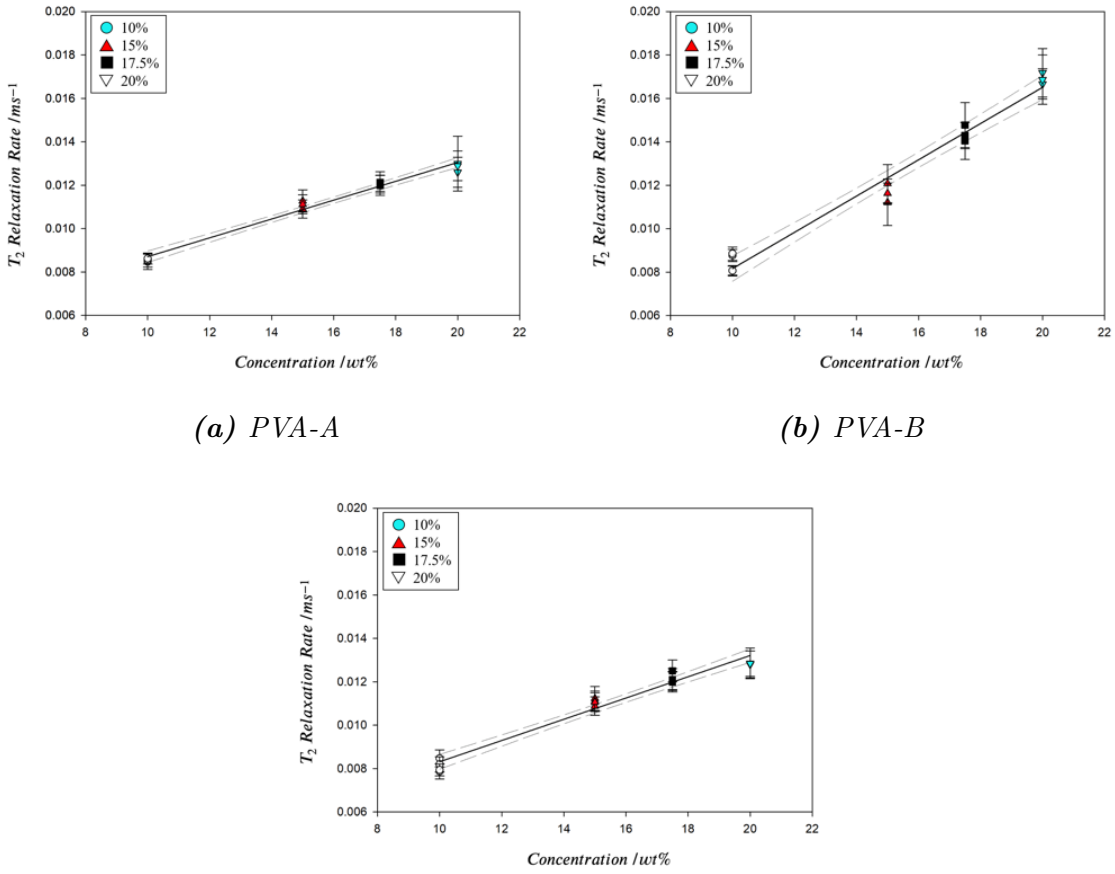

(a) *PVA-A*

(b) *PVA-B*

(c) *PVA-C*

Figure 3.7: *MR T_2 Relaxation Rate vs. concentration for PVA-A (a), PVA-B (b), and PVA-C (c). Points show average T_2 Relaxation Rate for each sample. Error bars show intra-sample standard deviation. Dashed lines show 95% confidence intervals for regression.*

3.3.2.2 Freeze thaw cycles and MR T_2 relaxation time

An increase in the number of FTCs led to an increase in the mean MR T_2 relaxation time of a sample, increasing from 101 ± 5.5 ms after one FTC, to 109 ± 8.6 ms after three FTCs (table 3.3). A further increase to 122 ± 5.7 ms was seen after three days of equilibration in distilled water. No clear trend can be see when analysing the change in inter-sample SD of the mean with FTCs. Figure 3.8 qualitatively demonstrates that the number of FTCs and further equilibrium altered the heterogeneity of samples. This observation is quantified by the increase in the mean intra sample standard deviation from 4.1% of the mean after 1 FTC, to 8.1% after 3 FTCs, and to 10.6% after equilibration (table 3.3). This increase in the intra-sample variation can also be seen when analysing the distribution of MR T_2 relaxation times for all pixels within each relaxation map (figure 3.9). The pixel distributions from three of the nine samples after 1 and 3 FTCs and after equilibration, are displayed, and a broader peak in MR T_2 distribution after 3 FTCs (figure 3.9b) can be observed, compared to the distribution after 1 FTC (figure 3.9a).

Table 3.3 shows the measurement of the sample cross-section from the MR T_2 relaxation map as an indicator of the change in sample shape after each step. This showed a decrease in area between 1 and 3 FTCs from 298 ± 6 mm2 to 275 ± 4 mm2, and a further decrease to 246 ± 4 mm2 after three days of equilibration.

Table 3.3: *MR T_2 Relaxation times for 10% w/w PVA at 1 and 3 freeze cycles, and after a further 3 days of equilibration. (n = 9 samples)*

No. Freeze thaw cycles	Mean (ms)	Inter-sample SD of Means (ms)	Inter-sample SD of means (% of mean)	Mean of Intra-sample SDs (ms)	Mean Intra-sample SD (% of mean)	Mean Δ Cross-sectional area (mm^2)
1 (equivalent to PVA-B)	101	5.5	5.4	4.1	4.1	298 ± 6
3 (equivalent to PVA-C)	109	8.6	7.9	8.8	8.1	275 ± 4
3 + Equilibration	122	5.7	4.8	12.9	10.6	246 ± 4

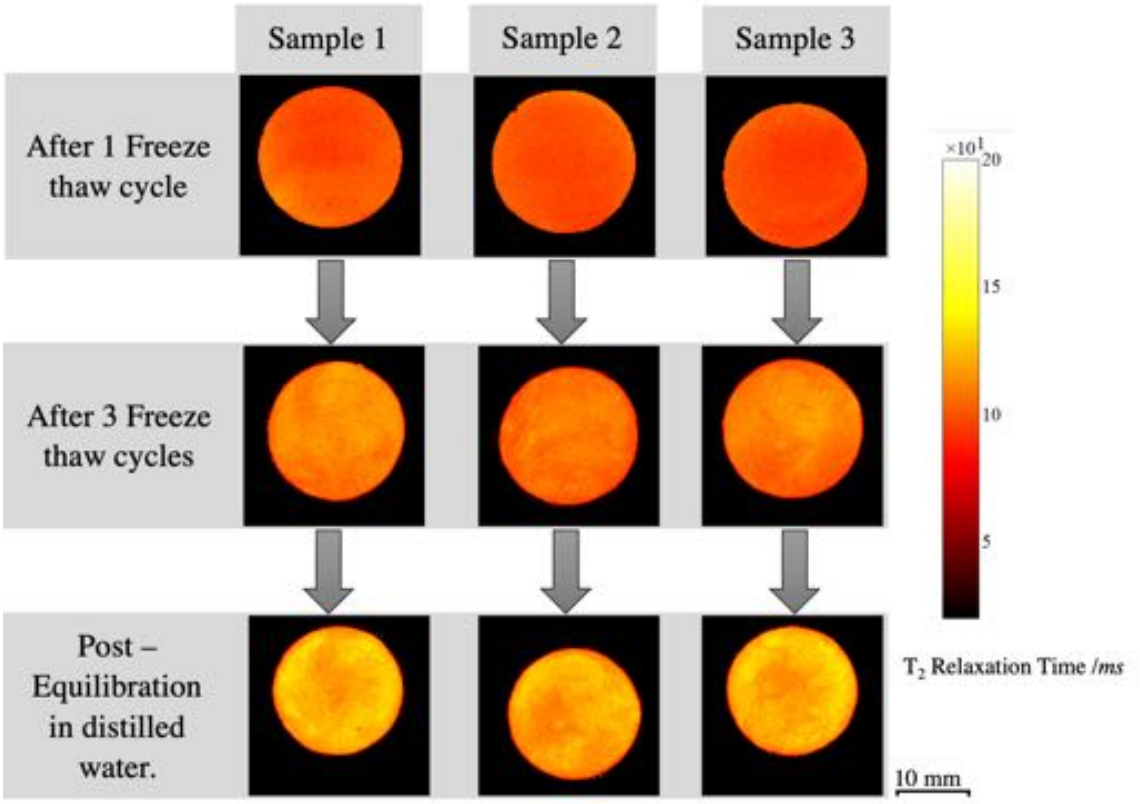

Figure 3.8: *MR T_2 Relaxation maps of three samples of 146-186 kDa PVA with a concentration of 10% w/w, after 1 and 3 cycles, and after 3 days of storage in distilled water to allow for equilibration.*

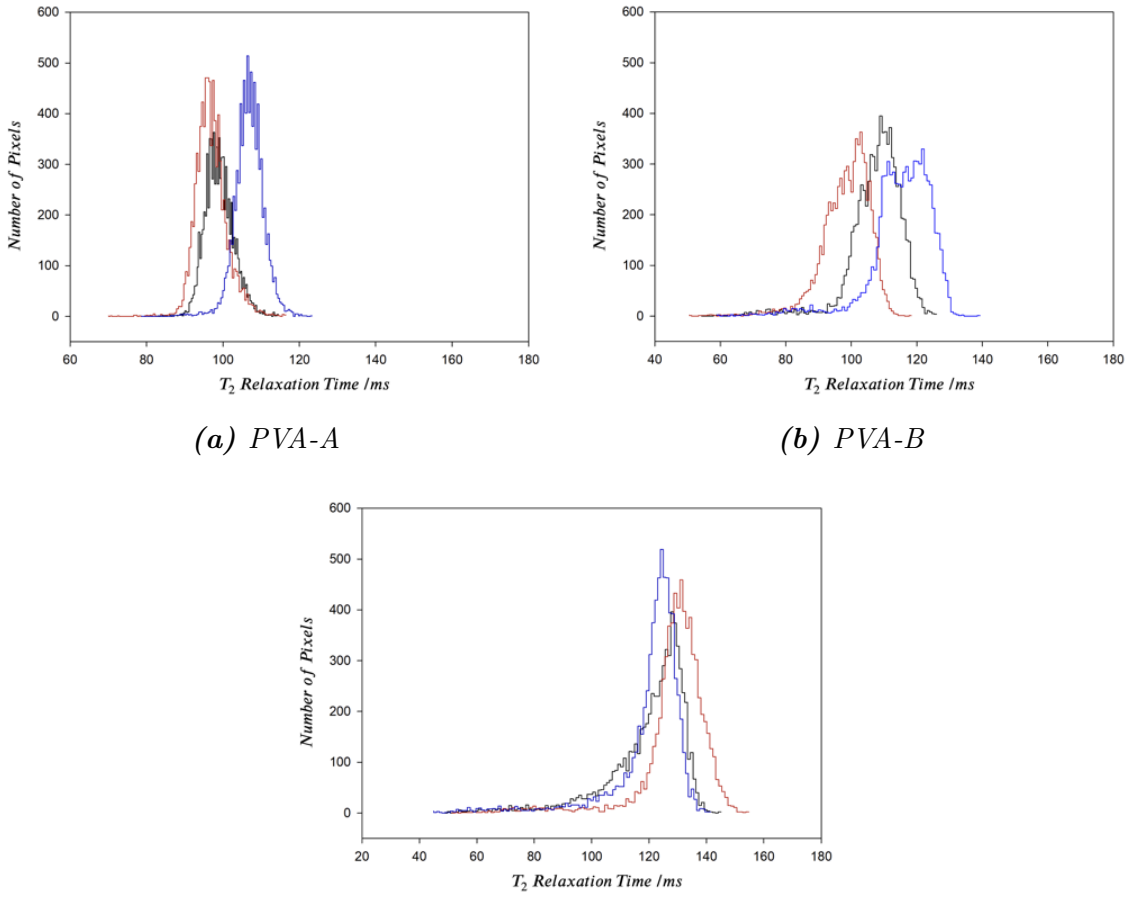

(a) *PVA-A*

(b) *PVA-B*

(c) *PVA-C*

Figure 3.9: *Histograms showing the distribution of MR T_2 relaxation time across all pixels for three samples after 1 (a) and 3 (b) FTCs, and after a further 3 days of equilibration (c). Each colour refers to a single sample. (i.e. blue refers to the same sample after 1 and 3 FTCs, and after equilibration.)*

3.3.3 Viscoelastic properties and MR T_2 relaxation time

Based on the empirical evidence, the PVA-A data could be fitted to an exponential function ($R^2 = 0.99$) between storage modulus and MR T_2 relaxation rate (figure 3.10a). For PVA-B a linear relationship ($R^2 = 0.95$) was empirically fitted (figure 3.10b). For PVA-C it was not possible to identify a correlation between storage modulus and MR T_2 relaxation rate; therefore, no trend line has been fitted (figure 3.10c). These trends (or lack of) were consistent for all frequencies.

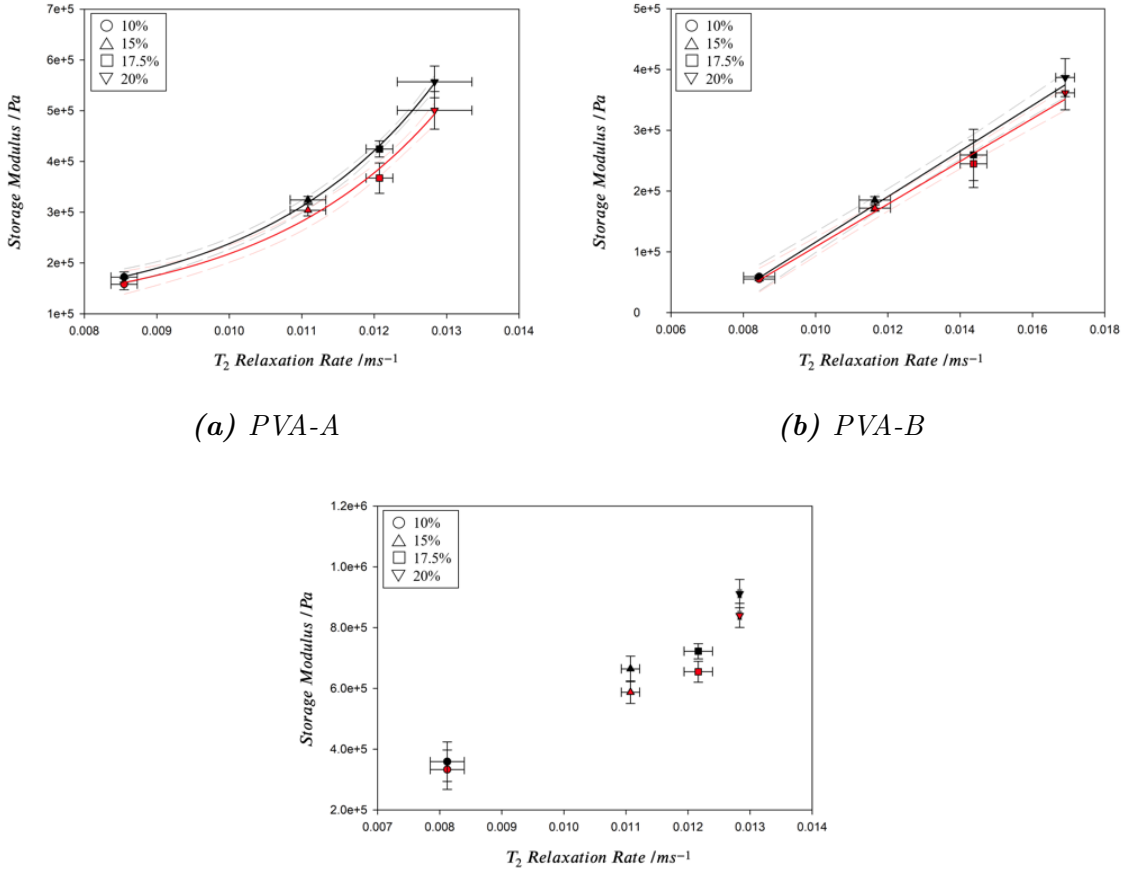

(a) PVA-A *(b) PVA-B*

(c) PVA-C

Figure 3.10: *Storage Modulus plotted against MR T_2 Relaxation Rate for 0.5 Hz (red), and 10 Hz (black) for PVA-A (a), PVA-B (b), and PVA-C (c). Error bars show 95% confidence (n= 6). Regression lines for 0.5 Hz (red), and 10 Hz (black) are also given; dashed lines show 95% confidence intervals for regression.*

For PVA-A, an exponential empirically-derived relationship was derived between

loss modulus and MR T_2 relaxation rate ($R^2 = 0.95$) (figure 3.11a). It was also noted that the fit appeared to improve as frequency decreased, with R^2 ranging from 0.98 at 0.5 Hz to 0.94 at 10 Hz. A linear relationship was observed between loss modulus and MR T_2 relaxation rate for PVA-B ($R^2 = 0.88$) (figure 3.11b). R^2 increased from 0.70 at 0.5 Hz to 0.94 at 10 Hz. As with the comparison between storage modulus and MR T_2 relaxation rate for PVA-C, it was not possible identify a correlation between loss modulus and MR T_2 Relaxation rate; therefore, no trend line has been presented (figure 3.11c).

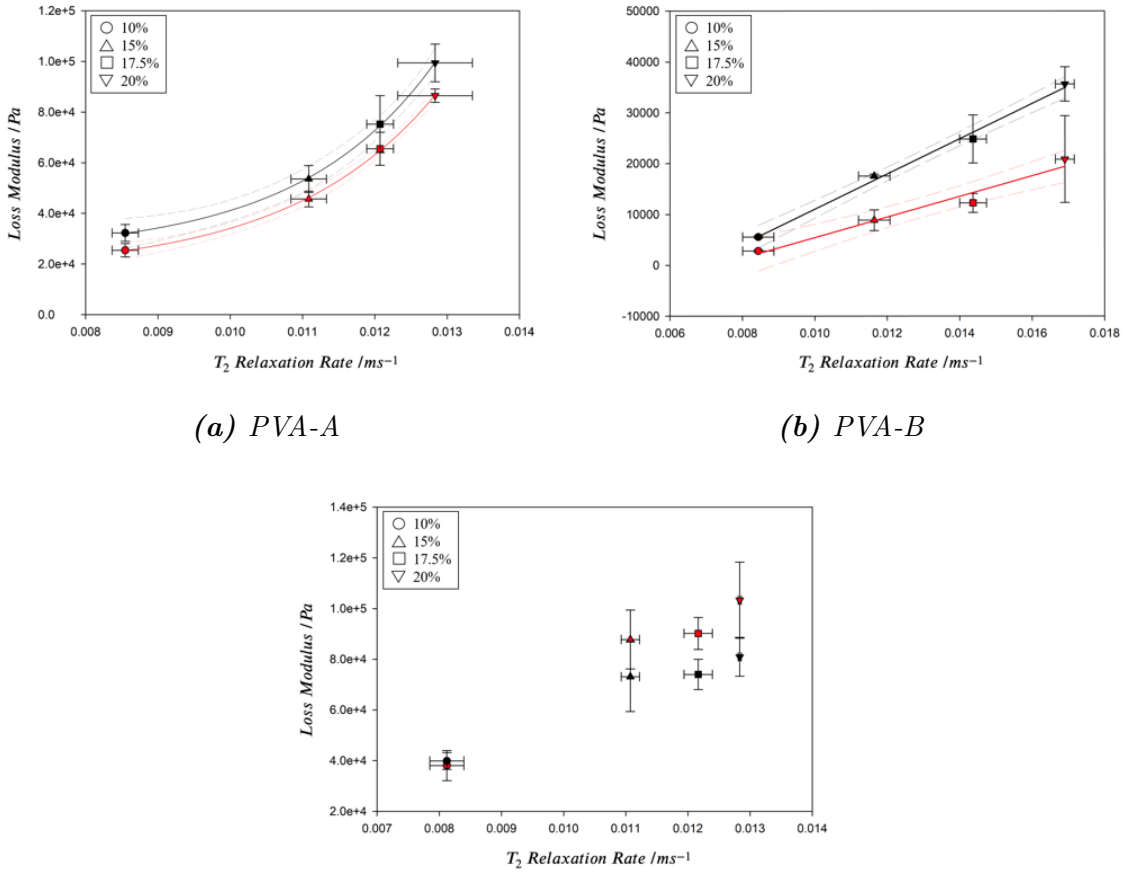

(a) *PVA-A*

(b) *PVA-B*

(c) *PVA-C*

Figure 3.11: *Loss Modulus plotted against MR T_2 Relaxation Rate for 0.5 Hz (red), and 10 Hz (black) for PVA-A (a), PVA-B (b), and PVA-C (c). Error bars show 95% confidence (n= 6). Regression lines for 0.5 Hz (red), and 10 Hz (black) are also given; dashed lines show 95% confidence intervals for regression.*

3.4 Discussion

This study evaluated the effect of PVA concentration for two MWs, 1 and 3 FTCs on the dynamic viscoelastic properties, characterised using DMA, as well as demonstrating the potential to link routine clinical imaging to the material properties of an implant. For PVA-A and B, there was a statistically significant correlation, between increasing concentration of the polymer and an increase in the storage and loss moduli. The storage modulus was shown to increase with concentration for PVA-C, however no statistically significant increase was seen in loss modulus between 15 and 20% ($p < 0.05$). Furthermore, the dynamic (complex) modulus increased with concentration for all compositions. This increase in the parameters of viscoelasticity as concentration is increased, is in agreement with previous literature, where a higher concentration of PVA resulted in a higher Young's Modulus [114]. It was noted that for PVA-C, that whilst a linear relationship was identified between complex modulus and concentration, a non-linear relationship was identified between loss modulus and concentration. As the concentration of PVA-C increases, the behaviour of the loss moduli implies that the sample is storing a greater proportion of energy, to enable elastic recoil, and therefore dissipating a lower proportion of energy. This behaviour is only occurring for PVA-C samples, which are a higher MW composition, and have undergone 3 FTC.

Previous research, modelling the poro-viscoleastic properties of PVA, showed that it can be described as a biphasic material [187]. However, in this study, the difference in viscoelastic response with the proportion of water in the hydrogel, does not correlate with loss modulus for all compositions i.e. PVA-C. Other studies have shown that as the concentration and MW of PVA is increased, an increase in polymer cross-linking occurs during FTCs, resulting in a denser polymer structure and a reduction in pore size [45], further resulting in an increase in the mechanical stiffness of the hydrogel [114]. This

hypothesis is further supported by the behaviour of the viscoelastic properties presented in this study. An increase in crosslinking present in PVA-C compared to PVA-B (due to an increase in FTCs) and PVA-A (due to MW), increases the restriction on water movement in the samples due to an increase in in polymerisation and decrease in pore size. It is hypothesised that this restriction on the water, reduces the hydrogel's ability to dissipate energy, as its freedom to flow out of the sample when a force is applied, will be reduced [37]. This theory is in agreement with several studies of the creep and stress relaxation properties of PVA; which have shown that as polymer concentration is increased, the response of creep and stress relaxation decreases [45, 187, 35]. This hypothesis would need to be tested on a wider range of MWs and FTCs, to confirm this theory. However, this study has shown that whilst compositional changes greatly affect the viscoelastic properties of PVA, the various parameters (for example concentration) do not affect different compositions in a consistent manner.

Miramini *et al.* [141] conducted a literature review to characterise the mechanical properties of connective tissue; this study yielded an elastic modulus (or equivalent) range of 0.09 – 10 MPa, 0.2 – 8 MPa and, 0.1 – 7 MPa for coronary, aortic, and femoral arteries respectively, and <1 – 170 MPa for articular cartilage. This range of values for connective tissue is extremely wide. Burton *et al.* [23] showed that the storage modulus of coronary arterial tissue is even higher (14.47 to 25.82 MPa). Yet, Holzapfel *et al.* [20] calculated the ultimate tensile stress of coronary arteries to be between 0.4 – 1.4 MPa. The values for the stiffest composition of PVA cryogel shown in this study, has a storage and loss moduli (0.8 MPa and 0.1 MPa respectively), which fall on the lower side of these reported literature values.

Proton (^1H) MRI is able to map the distribution of hydrogen within a sample [190]. The lifetime of the MR signal, is dependent on two primary relaxation times, MR T1 and MR T_2, which are sensitive to the chemical and physical environment of protons in a sample. In particular, both relaxation times are sensitive to molecular mobility and

in the case of MR T_2 relaxation, the relaxation time decreases with decreasing mobility [190, 185]. Therefore, solids have typically lower MR T_2 relaxation times compared to liquids. Additionally, MR T_2 relaxation time is also sensitive to chemical exchange and internal magnetic field gradients [191], in the presence of interfaces between materials of different magnetic susceptibilities, which is measured by MR T_2* [190]. In the case of MRI, measured T_2 relaxation times can be sensitive to diffusion, to an extent dependent on the experimental imaging parameters. In this study, the imaging parameters were fixed throughout, and thus relative differences and trends can be identified.

This study evaluated the effect of PVA concentration for two MWs, 1 and 3 FTCs on MR T_2 relaxation time. It was found that MR T_2 relaxation time decreased as concentration was increased for PVA-A, B and C (Table 3.2). The reduction in MR T_2 relaxation time, and thus signal, correlates with the reduction in the $\%wt.$ of water in the samples. This result is in agreement with Orr *et al.* [154]. The additional parameters assessed in this study, identified further trends. There was an increase in MR T_2 relaxation time with FTC, which contradicts the trend reported by Chu and Rutt [39]. Table 3.2 also identifies that the difference in MR T_2 relaxation time, between 1 and 3 FTCs, increases with the concentration (previously unreported). Table 3.3 shows that there was a reduction in cross-sectional area with the FTCs and subsequent equilibrium process, which further aligns with results from [39], and is attributed to water being expelled by crystallite growth. The robustness of the observations between FTCs and MR T_2 relaxation time are inherently limited due to two discrete data points. Whilst it potentially identifies two novel trends, these require further investigation to establish correlation and statistical significant. Nevertheless, some observations can be made about research methodology, and hypotheses can be drawn based on scientific insight.

MRI was able to qualitatively and quantitatively assess the change in sample heterogeneity with manufacturing protocol, showing that an increase in FTCs results in

an increased pixel distribution of MR T_2 relaxation time throughout a sample (table 3.3, figures 3.8 and 3.9). Figure 3.9 also shows a deviation from normal distribution after equilibration, with a skew to lower values of MR T_2 relaxation times. In part, this can be attributed to the 'halo' of lower signal intensity around the edge of the samples (figure 3.8), which further agrees with the expulsion of water described by Chu *et al.* [39], occurring at the boundary of the sample. The literature reports that increasing the number of FTCs during manufacture, results in compositional heterogeneity within the hydrogel [38]. This is due to the formation of ice crystals during the freezing process, resulting in an increase in the concentration of the polymer solution in surrounding regions and promoting more interactions between the polymer chains, and between the polymer and ice crystals [111]. Thawing of the ice crystals, results in pockets of water, which can lead to a microporous structure throughout the hydrogel. Subsequent FTCs reinforce this process, which results in the formation of polymer rich and polymer poor regions [38, 192].

The generation of water pockets, and increased mobility of the water molecules, in the microstructure of the material is hypothesised to cause the increase in MR T_2 relaxation time with FTC. It is important to emphasise, that the increase in MR T_2 relaxation time with FTC, is attributed to an increase in water mobility, as opposed to water concentration, which through the cross-sectional area results in table 3.3 and [39] was assumed to reduce. This observation is further strengthened by table 3.3, which shows (by comparing PVA-B and PVA-C) that by reducing $\%wt.$ water concentration, has less impact than the increase in water mobility from additional FTCs. To confirm the microstructural changes of the PVA with FTC requires further investigation. The phase heterogeneity of PVA has been previously measured using different experimental methods, including X-ray diffraction [152], small angle neutron scattering [193, 8], and confocal laser scanning microscopy [194]. MRI is not able to resolve the microscopic pore structure of PVA however, this study has demonstrated that the formation of polymer-rich and polymer-poor regions can be indirectly measured through the result-

ing variation in polymer and water content of these regions and thus the signal. It is unlikely that this microscopic variation in composition has an impact on the viscoelastic properties of the hydrogels, as these are bulk measurements.

Comparing tables table 3.2 and table 3.3, the mean MR T_2 relaxation time for 10% PVA-C in Table 3.2 (123ms) is equivalent to 10% PVA-C after 3 days of equilibrating in water in Table 3.3 (122ms). Reflecting on the difference in methodology between these experiments, the difference in MR T_2 relaxation time pre and post equilibration (10%), demonstrates the critical importance of the storage conditions of PVA cryogels. This parameter was not reported in [39], and was approximately 4 weeks in [154]. Chu and Rutt [39] also described different manufacturing and imaging protocol, most notably, they state long echo times, which would increase susceptibility to internal magnetic field gradients. To robustly determine the source of the opposing trends between MR T_2 relaxation time and FTC reported in [39] and this study an increased and more detailed assessment of manufacturing parameters, under matched imaging parameters, would be required.

Finally and importantly, this study has demonstrated, for the first time, a correlation between viscoelastic mechanical properties and the MR T_2 relaxation time for a defined composition. Note that "correlation does not imply causation", and in this case both the viscoelastic and MRI properties of PVA are dependent on the hydrogel's water content. The mechanical properties and MR T_2 relaxation time of PVA are correlated because both are affected by changes in PVA composition. This unique result suggests the possibility of MRI based quantification of the composition-dependent mechanical properties of PVA. Such a development would have huge ramifications in the development and application of tissue scaffolds, implants and phantoms. Future development and validation could allow *in situ* and non-invasive imaging of the mechanical function of PVA cryogels, with the wider principles shown in this study also applicable to be used with other biocompatible hydrogels [195]. Magnetic resonance

elastography (MRE) is currently the most researched method used to measure mechanical properties *in vivo*, with PVA being a commonly used phantoms material to develop MRE [196]. The techniques presented here could be used to enhance and validate such developments by using *in vivo* imaging to validate mechanical properties and monitor the changes in homogeneity in a sample or implant.

With the advent of alternative manufacturing techniques for hydrogels, such as additive manufacture, the ability to create both more intricate geometries [9], multi-material models [197, 198] and to alter the mechanical properties of PVA by varying AM parameters has been shown [199]. These advances show the opportunity to have considerably more accurate material models for soft connective tissues, allowing for changing mechanical properties throughout an implant or phantom [200]. It will therefore become increasingly more important that the optimal PVA composition is chosen for manufacture. This study has shown the impact of changes in PVA composition on viscoelastic mechanical properties, and therefore will allow researchers to make not only more informed material choices, but gives further insight into the impact of each manufacturing parameter on its mechanical properties, allowing future research to focus on which parameters to vary in order to achieve a given stiffness, or to obtain certain viscoelastic properties. As this study presents data in the frequency domain, it is also beneficial for stress analysis of the dynamics involved in an implant or connective tissue model under physiological loading conditions [201].

This study has successfully shown the impact of the compositional and manufacturing parameters of PVA cryogel on its viscoelastic properties and MR T_2 relaxation time. Future research will require an increased number of parameters to explore the impact on the loss modulus and MR T_2 relaxation time. Further to this, an increased number of FTCs would be required to increase the dynamic moduli of the cryogel to the equivalent range for some arterial tissue reported in the literature.

3.5 Conclusion

This study has explored the effect of MW, concentration and the manufacturing protocol of PVA cryogel on its viscoelastic mechanical properties and the MR T_2 Relaxation time. It was shown that:

- An increase in concentration results in an increase in storage and loss moduli.
- The trend between concentration and viscoelastic moduli is dependent on the MW and the manufacturing protocol.
- A linear relationship exists between MR T_2 relaxation rate and concentration, inclusive of both MWs and variations in manufacturing protocol.
- MRI can qualitatively and quantitatively identify sample heterogeneity, which was shown to increase with number of FTCs and further equilibrating in water.

This chapter has contributed a comprehensive assessment of the viscoelastic behaviour of PVA to the current understanding of the mechanical behaviour of PVA. This gives a more complete understanding of the viscoelastic behaviour of PVA under physiologically relevant loading conditions, allowing the decision process when defining PVA compositional parameters to be optimised. The results presented in this chapter have also demonstrated a causal relationship between the MR T_2 relaxation rate and viscoelastic properties of PVA. This is a novel result in itself, as it demonstrates that it is feasible to estimate the mechanical properties of PVA from MRI. This demonstrates the potential to image the composition-dependent viscoelastic properties of PVA remotely. Such an attribute could enable future *in situ* and non-invasive identification or monitoring of the mechanical properties of tissue scaffolds or implants manufactured from PVA.

STATEMENT OF CONTRIBUTIONS II

Chapter 4 includes research that has been previously published in a peer reviewed scientific journal (*MRS Advances*), of which I am the primary author. This publication is licensed under a Creative Commons Attribution 4.0 International License (https://creativecommons.org/licenses/by/4.0/), which permits the reproduction of the work in a thesis. Further information regarding the publication, including author contributions is given below.

J. P. Crolla, M. M. Britton, D. M. Espino, and L. E. J. Thomas- Seale. The orthotropic viscoelastic characterisation of sub-zero 3D- printed poly- (vinyl alcohol) cryogel. *MRS Advances*, 2021.

DOI: https://doi.org/10.1557/s43580-021-00086-1.

AUTHOR CONTRIBUTION

- **J.P. Crolla**: Conceptualization, investigation, data analysis, draft manuscript.
- M.M. Britton: Supervision, coordination, review & editing.
- D.M. Espino: Supervision, coordination, review & editing.
- L.E.J. Thomas-Seale: supervision, conceptualization, coordination, review & editing.

Chapter 4

SUB-ZERO AM AND VISCOELASTIC ANALYSIS OF PVA

4.1 Introduction

It is clear from the review presented in section 1.4.3 that the AM of PVA proves to be a compelling method to further control the mechanical behaviour of PVA constructs. However, sub-zero AM of PVA is in its infancy and little research has been presented to analyse the effect of AM process parameters on the mechanical behaviour of the material. The key contribution to literature of this chapter will be three-fold. Firstly, it will comprehensively assess the effect of key AM process parameters (nozzle size and print orientation), providing a more informed understanding regarding the differences between cast and AM PVA for future research. Secondly, it will continue the comprehensive study on the viscoelasticity of PVA presented in chapter 3, this time exploring the behaviour of AM PVA and cast control samples under tension in the same range of physiologically relevant frequencies. Finally, it will explore the novel potential to pro-

duce and control anisotropy in PVA constructs using AM, analogous to the anisotropic behaviour created by collagen fibre alignment in CT (section 1.2.1).

AM is a key enabler of design for materials, particularly to replicate the complexity of bioinspired features [7]. However, whilst AM can create enhanced geometrical complexity, currently there are a limited number of compatible biomaterials. The AM of materials to replicate CT (e.g. articular cartilage and arteries) is constrained by a trade-off between biocompatibility and representative mechanical properties [141].

PVA perpetuates research interest as a biomaterial capable of replicating the mechanical properties of tissue, for example it has long-standing applications in the mimicking of arterial tissue [39]. Recent studies have described the development of AM, to include sub-zero temperatures (C) or cryogenic printing platforms, which allow traditional biomaterials, such as PVA, to be manufactured additively [148]. Sub-zero AM has thus enabled the manufacture of composite PVA hydrogels through physical crosslinking upon deposition. Compressive characterisation has shown that AM of PVA composites can replicate the soft tissue mechanics of brain and cartilage [148, 9]. Furthermore, PVA itself has been shown to achieve properties akin to tendons [202]. However, the mechanical properties of PVA are highly dependent on freeze-thaw (FT) parameters [43], thus, any characterisation of sub-zero 3D printed PVA is only relevant to the reported manufacturing parameters.

CTs are not homogenous, isotropic materials, and the key mechanism that causes anisotropy in CT is the alignment of collagen fibres, which when under tension act as a fibre reinforcement [203]. If the collagen within a CT is not randomly oriented, they will provide more reinforcement in the same direction as the net alignment of fibres. The orientation of collagen is therefore dependant on the function of the CT, and on the region it is located within the CT. For example, collagen orientation varies between the three layers of arterial wall, meaning they exhibit different mechanical behaviours, and therefore have a different responsibility with regard to the function of the tissue

[203, 20].

Byrne *et al.* (2018) propose "biologicalisation in manufacturing" as a method by which bio-inspired principles can be used to develop new frontiers in digitalisation and advanced manufacturing [204]. This process of drawing inspiration from biological mechanisms has been previously applied to AM, where Saliba *et al.* explore the comparisons between developmental biology and AM [205]. In this case the use of manufacturing process parameters as variables of design was proposed, where time was used a dimension for design throughout manufacturing, analogous to the temporal response of foetal growth.

Extrusion based AM of traditional polymers (such as ABS) inherently creates a direction dependency of mechanical behaviour relative to the toolpath [206]. Although research into the mechanical behaviour of AM hydrogels is lacking [207], Ersumo *et al.* (2016) showed that AM changes the time-dependent mechanical properties of hydrogels [207]. The advent of AM of PVA offers a unique opportunity to explore the direction dependency of the mechanical properties of a viscoelastic soft biomaterial. To date however, sub-zero AM of PVA remains mechanically undefined with respect to manufacturing parameters. The inspiration of this research is to draw upon the intrinsic othrotropic properties of CT caused by the alignment of collagen fibres; exploring the potential for filament alignment of 3D printed PVA to introduce and control anisotropic behaviour of soft tissue replacements.

4.1.1 Aims & objectives

Drawing on the bioinspired concept of varying manufacturing parameters as a method by which to achieve enhanced material complexity [205]; this chapter aims to characterise the orthotropic viscoelastic properties of sub-zero AM PVA. This will be achieved through the following objectives:

- Develop and calibrate a sub-zero AM platform to 3D print PVA;
- Manufacture samples with three different nozzle sizes, maintaining a constant ratio between the filament width and diameter;
- Mechanically characterise samples manufactured with three nozzle sizes using DMA, with the loading condition oriented both parallel and perpendicular to the direction of printing;
- Viscoelastic properties will also be explored further in this chapter - analysing the effect of true stress and strain on viscoelastic moduli.

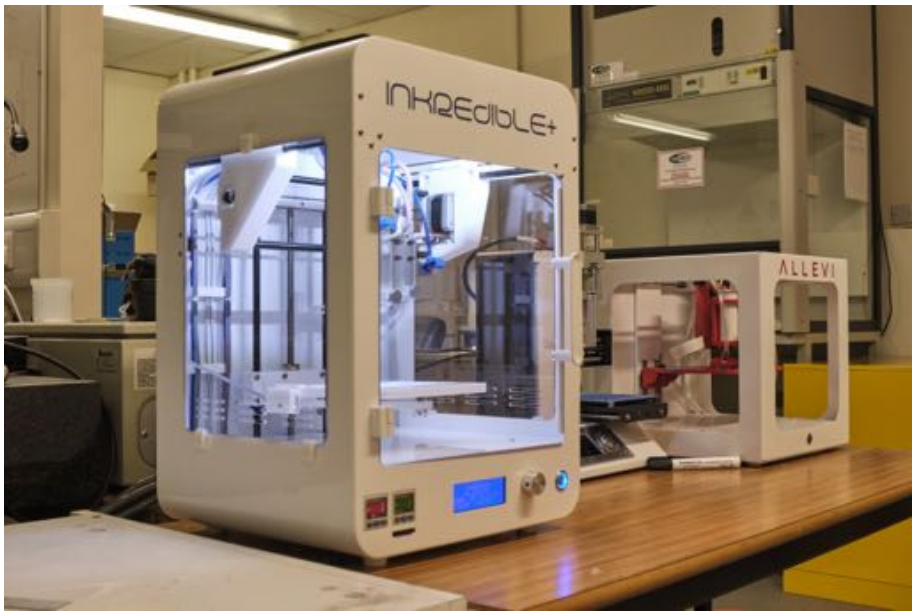

Figure 4.1: *The bioprinters used in this thesis. The Allevi 2 (right) used in Chapter 4, and Cellink Inkredible+ (left) used in Chapter 5.*

4.2 Methodology

4.2.1 Extrusion based bioprinting

This section will briefly explain how an extrusion based 3D printer works and how they are controlled. An understanding of this process is vital for understanding the

methodologies presented in chapters 4 and 5, as well as interpreting their discussion and conclusions.

Extrusion based bioprinting is heavily based on FDM, with the core process of manufacturing being the same, and only the method of extrusion, and manufacturing parameters differing. Extrusion 3D printers consist of a print head, which is normally attached to a gantry allowing movement in one (or sometimes more than one) direction (figure 4.1). This stage is held above a print bed where the part will be manufactured. Stepper motors are used to control the motion of all three axis, and often allow movements as small as 0.1 mm).

Unlike polymers typically used with FDM, which require being heated to $\approx 200°C$, the hydrogels and bioinks used with DIW tend to have viscous properties at room temperature, meaning the nozzle normally does not require heating. Instead of a polymer filament being mechanically extruded, the print head consists of a syringe in which the hydrogel is stored. Constant pressure is then applied to the syringe, either through pneumatic pressure, mechanical force, or through a turning screw (figure 4.2). Both the bioprinters used in this thesis use a pneumatic system to apply pressure.

Parts manufactured using most 3D printing techniques, are built up layer by layer. In this case, the print head will follow a toolpath, whilst extruding material. G-code is predominately used as the method of defining the toolpath, controlling the movements of the print head, as well as controlling its temperature and extrusion pressure. Simply, G-code is an instruction set listing commands to be carried out by the 3D printer. In the case of bioprinting, these will range from defining the speed at which the grouphead will travel, the pressure applied to the syringe, and a list of coordinates defining the movement of the print head.

Through commands, values for X, Y, and Z coordinates can be set, as well as a value for the feedrate, F which will define the speed of the print head. For a standard

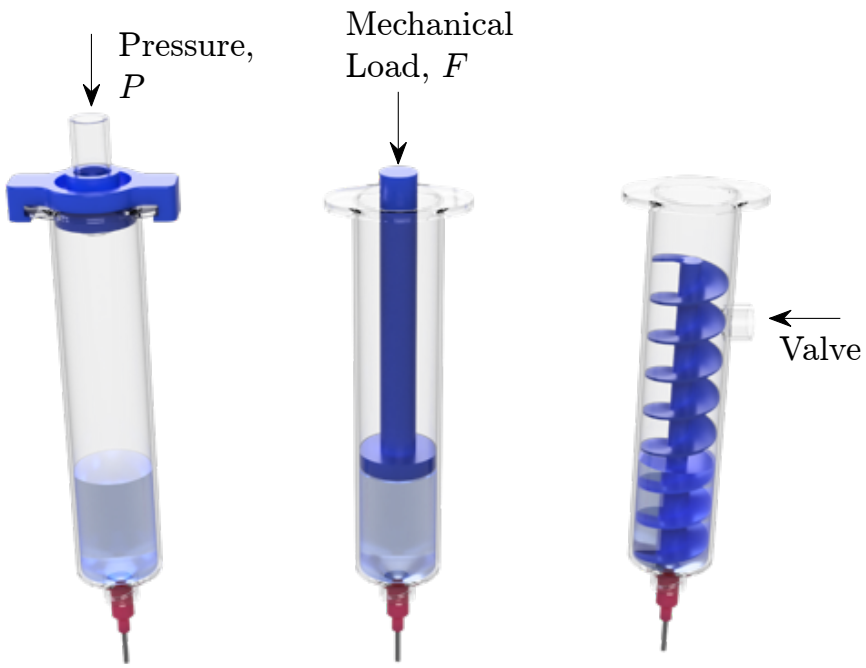

Figure 4.2: *An illustration of the three types of extrusion for direct ink writing: pressure (left), mechanical force (middle), and screw based (right).*

FDM printer (and some bioprinters applying pressure by mechanical force) a value of E is also given. This gives a command for the amount of filament to be extruded (or in the case of a bioprinter the speed of the motor used to depress the syringe). For the 3D printers relevant to this thesis, pneumatic pressure is used, and therefore this command is redundant. Instead, $M760$ and $M761$ commands are used to turn air pressure on and off. In this case, the pressure is set on the 3D printer, and is not defined by G-code.

For the majority of applications it is not necessary to directly write G-code, with software commonly used to generate the toolpath for a given 3D computer aided design (CAD) model, and a list of user defined printing parameters. Key parameters relevant to this thesis are listed in table 4.1. Although this means a thorough understanding of G-code is not required to use 3D printers, the brief overview given here helps understand the code used in chapter 5 and shown in appendix D, allowing the generation of custom toolpaths.

4.2.2 Sample preparation

PVA with a molecular weight of 146-186 kDa was dissolved in deionised water by mechanically stirring the solution at $90°C$ for one hour. Stirring was continued for 1 hour after removing from the hotplate, until the solution reached room temperature. A PVA concentration of 10% w/w was used for all samples.; After AM, all samples underwent 3 $\times$ 24 hour freeze thaw cycles (described in chapter 2). PVA was acquired from Sigma Aldrich (St Louis, Missouri, USA) and had a hydrolysis of 99+%.

Sub-zero AM was conducted on an Allevi 2 Bioprinter (Philadelphia, Pennsylvania, USA (figure 4.1. All samples were manufactured with dimensions of 10 $\times$ 6 mm. The final sample thickness was dependent on the nozzle size. Extrusion nozzles with standard needle gauges of $25G$, $22G$, and $18G$ were utilised (henceforth these will be referred to as small, medium, and large nozzles respectively); with 12 samples manufactured with each nozzle (table 4.2). All samples were manufactured with a print speed of 500 mm/min. For each nozzle size, 6 samples were mechanically tested in a parallel and 6 in a perpendicular orientation (relative to the print direction - shown in figure 4.3). A further 6 control samples were manufactured by casting (Table 4.2). Samples were extruded at a room temperature of $24°C$ (+/- $1°C$), onto a hardened steel printing platform (cooled to $-35°C$ ($\pm 1°C$) prior to the print). The time-dependent temperature profile of the printing platform is presented in appendix B in figure B.1. This methodology ensured the preservation of the PVA filament and overall geometry

Table 4.1: *Key print parameters relevant to this thesis.*

Print parameter	Definition
Extrusion pressure	Pressure applied to the syringe, Pa
Print speed	Speed of print head in the X and Y axes, mms^{-1}
Strand diameter	Desired diameter of the extruded hydrogel, mm
Layer height	Desired height of the extruded hydrogel, mm
Needle diameter	Diameter of the extrusion needle. This is not directly controlled by the printer, but influences other print parameters.

Table 4.2: *AM parameters for samples manufactured for DMA testing using an Allevi 2 Bioprinter.*

	25G (small)	22G (medium)	18G (large)	Cast
Inner Nozzle Diameter (mm)	0.26	0.34	0.84	N/A
Strand Diameter (mm)	0.45	0.7	1.2	N/A
Line Spacing (mm)	0.4	0.63	1	N/A
Pressure (kPa)	310	172	70	N/A
Sample Thickness (mm)	0.5	0.75	0.9	0.75

during extrusion. For all samples, the layer height was set as equal to the inner diameter of the nozzle. In bioprinting, the pressure is not linearly proportional to the extrusion rate. The chosen printing pressure and respective filament width, established through an empirical approach, are shown in Table 4.2. The line spacing used throughout the print was set as 90% of the filament width. This line spacing ensured a balance between manufacture with no defects and no over extrusion.

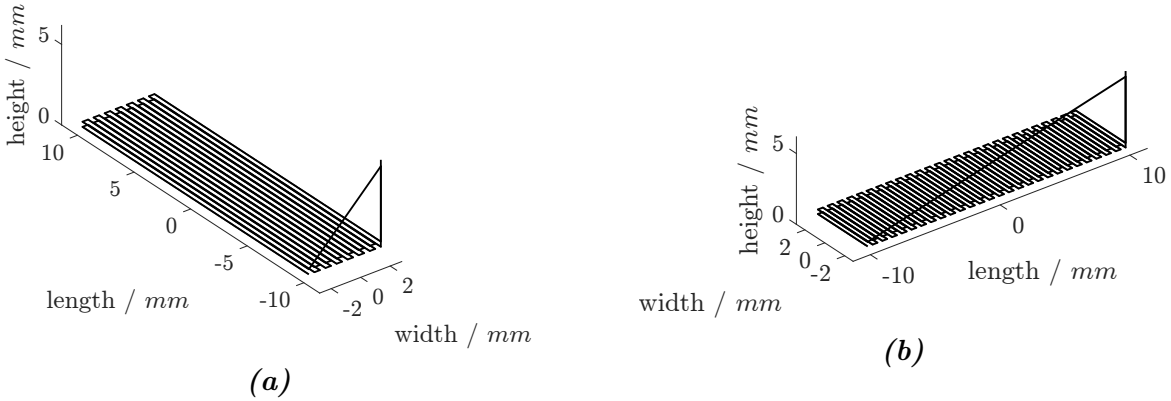

Figure 4.3: *Example toolpaths generated in Matlab, showing the parallel (a) and perpendicular (b) orientations. The testing condition was parallel to the sample length.*

To ensure that the extruded PVA was frozen immediately on contact with the printing platform, the sample thickness needed to remain less than 1mm. Therefore, all samples printed with the small and medium syringe sizes were manufactured with two layers, and samples printed with the large nozzle size had one layer. The variability of sample thickness was taken into account in the DMA analysis (section 4.2.3).

4.2.3 Dynamic mechanical analysis

The protocol used for DMA in this study is the same as described in chapter 3 (section 3.2.2.2), however samples in this chapter were tested under tension. Samples were tested under tension by 20% of their measured height using a frequency sweep of 0.5 – 10 Hz. Similarly to chapter 3, this frequency range was chosen to replicate the strain rates expected in different connective tissues; such as coronary arteries (0.5 – 10 Hz) [23], heart valve leaflets (0.5 – 10 Hz) [22], chordae tendineae (0.5 – 10 Hz), and articular cartilage under physiological loading (1 – 10 Hz) [31].

4.2.4 Effect of true stress and strain

The stiffest materials manufactured using the cast methods presented in chapter 3, and AM presented in this chapter, have been analysed further. In this case, samples of AM PVA manufactured with the smallest nozzle size analysed in the parallel orientation ($n = 6$), and cast PVA with a MW of 146-186 kDa and 3 FTC (PVAC) ($n = 6$) have been analysed.

When data is collected using the Electroforce 3200, values for storage and loss moduli are calculated using a shape factor in the Wintest software (TA Instruments, Delaware, USA). The shape factor takes into account only the *initial* cross-sectional area and height, therefore meaning the viscoelastic properties are calculated based on engineering stress and strain. The theory used by Wintest to calculate are given in full in chapter 3, and summarised below. Briefly, the load and displacement sine waves are Fourier transformed, resulting in the complex stiffness (and by extension, the storage and loss stiffness). Moduli are then calculated by dividing these stiffness values by the shape factor. To further analyse the effect of true stress and strain, a script was written using Matlab (MathWorks, Massachusetts, USA) to calculate the storage and

loss moduli using the raw time domain, load and displacement data. This code has been previously validated by Lawless (2019), and was adapted for this thesis to allow calculations of viscoelastic properties from true stress and strain [208]. In this case the true stress and strain were calculated from the raw data prior to the Fourier transform, with the output therefore being the 'true' complex modulus instead of the equivalent engineering complex stiffness calculated by Wintest.

In order to calculate true strain, the engineering strain is first calculated (equation 4.1). The true strain can then be calculated using equation 4.2 for samples under tension, and 4.3 for samples under compression [209].

$$\varepsilon_e = \frac{\Delta l}{L} \tag{4.1}$$

$$\varepsilon_t = ln(1 + \varepsilon) \tag{4.2}$$

$$\varepsilon_t = -ln(1 - \varepsilon) \tag{4.3}$$

Where Δl is the change in sample length, and L is the initial length.

Assuming the materials tested are incompressible and therefore the Poisson's ratio is approximately 0.5, the change in cross-sectional area (equations 4.4, 4.5, and 4.6), and therefore the true stress can be calculated (equation 4.7).

$$L = L_0 + \delta \tag{4.4}$$

$$\lambda = \frac{L}{L_0} \tag{4.5}$$

$$A_t = \frac{A_0}{\lambda} \tag{4.6}$$

$$\sigma_t = \frac{F}{A_t} \tag{4.7}$$

Where λ is the ratio of actual to initial sample length, A is the sample cross-sectional area, and F is the force applied to the sample.

The complex modulus can then be calculated as a ratio of the FFT of true stress and strain (equation 4.8), and storage and loss moduli can be calculated as described in Chapter 2.

$$E^* = \frac{fft(\sigma_t)}{fft(\varepsilon_t)} \tag{4.8}$$

4.2.5 Statistical analysis

All statistical analysis was performed using Matlab (MathWorks, Massachusetts, USA). 95% confidence intervals were calculated. Unpaired student t-tests were used to ascertain whether a statistically significant difference was present between the parallel and perpendicular orientations (complete data shown in Appendix B). A one-way ANOVA was used to assess the difference in storage moduli between all nozzle sizes and cast samples.

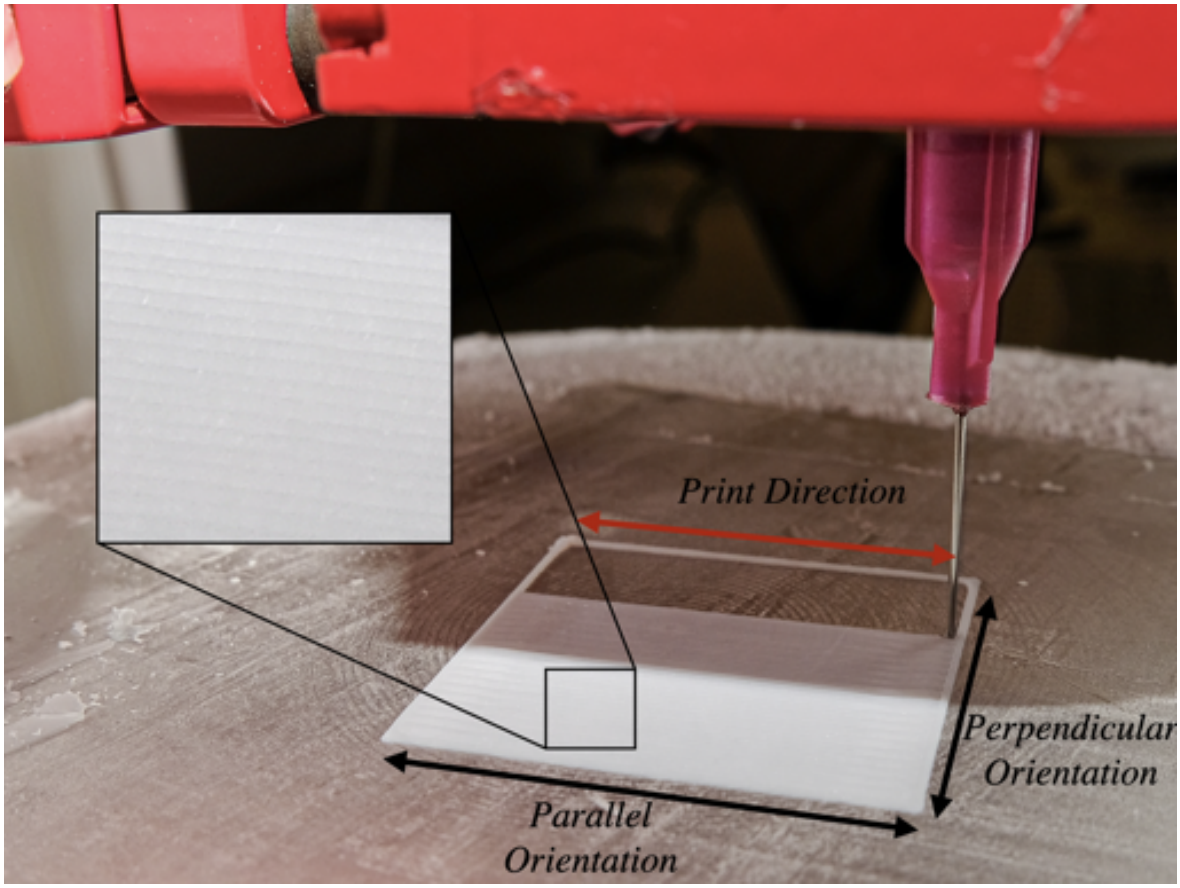

Figure 4.4: *Example print using a 25G syringe nozzle, indicating the parallel and perpendicular orientations, with respect to the print direction.*

4.3 Results

4.3.1 Dynamic mechanical analysis

Figure 4.4 shows an example of the surface of the samples. The toolpath dependent meso-structure of is clearly visible. The method of manufacturing, by nature, creates mechanical properties which are dependent on direction. This is demonstrated by comparing the moduli of the parallel (orange) and perpendicular (black) data sets in figures 4.5 and 4.6. Further to this, the orthotropic nature of additively manufactured PVA was shown to be significantly affected by the nozzle size relative to print direction (figures 4.5 and 4.6). Samples manufactured with the small nozzle showed an average

36.4 ± 0.26% increase in storage modulus across all frequencies when mechanically tested parallel to the print orientation (compared to perpendicular). In comparison, the medium nozzle samples demonstrated a 13.6 ± 0.18% increase in storage moduli between the parallel and perpendicular orientation. No statistically significant difference was seen for the large nozzle size ($p > 0.05$).

A significant difference in storage modulus was observed across the four groups across all frequencies ($p < 0.05$). A multiple comparison test then showed no statistically significant difference between the storage modulus of the medium, large nozzle size or cast samples ($p > 0.05$). This highlights that the storage modulus of the smaller nozzle size was significantly higher than all other groups across all frequencies.

A similar trend was seen with loss modulus (figure 4.6), with samples manufactured using the small nozzle showing the greatest increase in moduli between the parallel and perpendicular orientation. It was noted that this increase in loss moduli was also dependent on frequency, ranging from a 34.2% increase at 0.5 Hz to 25.6% increase at 10 Hz. A smaller increase was noted for samples manufactured using the medium nozzle, ranging from a 16.1% increase at 0.5 Hz to 11.0% increase at 10 Hz. No statistically significance was identified with frequency for samples manufactured with the largest nozzle.

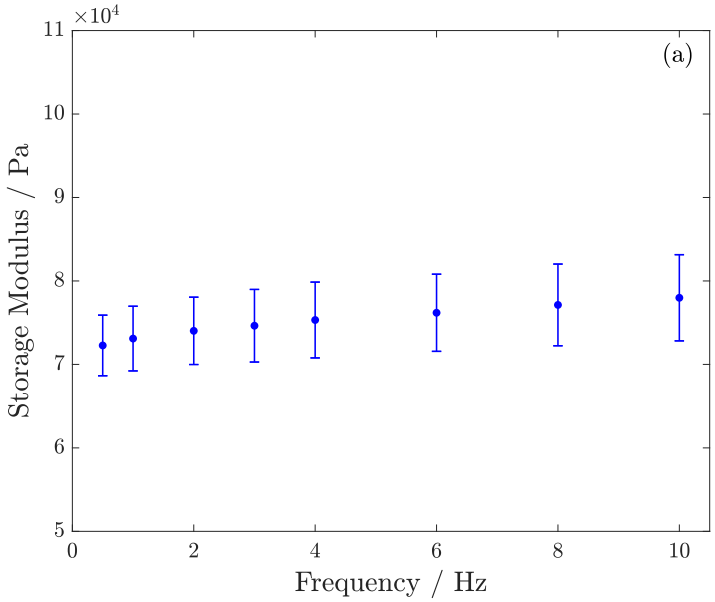

(a) *Cast control samples*

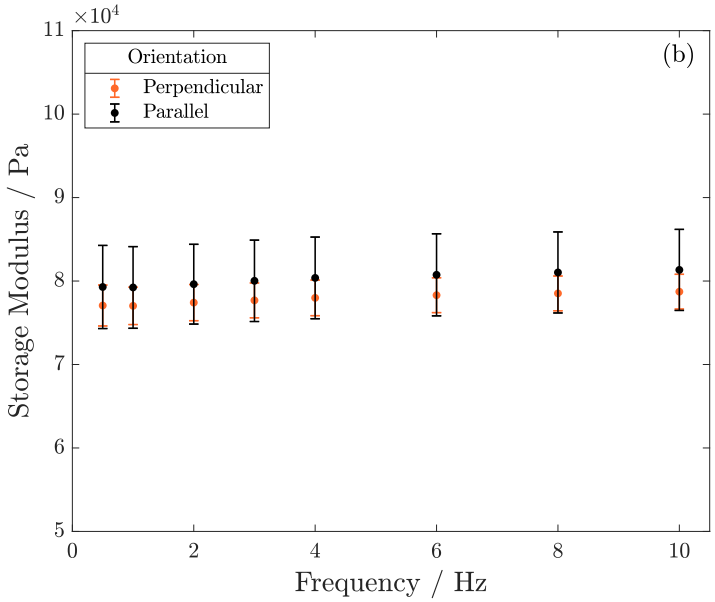

(b) *18G (large) Nozzle Diameter*

Figure 4.5: *Storage modulus for cast and additively manufactured PVA with varying nozzle diameter. Error bars show 95% Confidence intervals. (n = 6)*

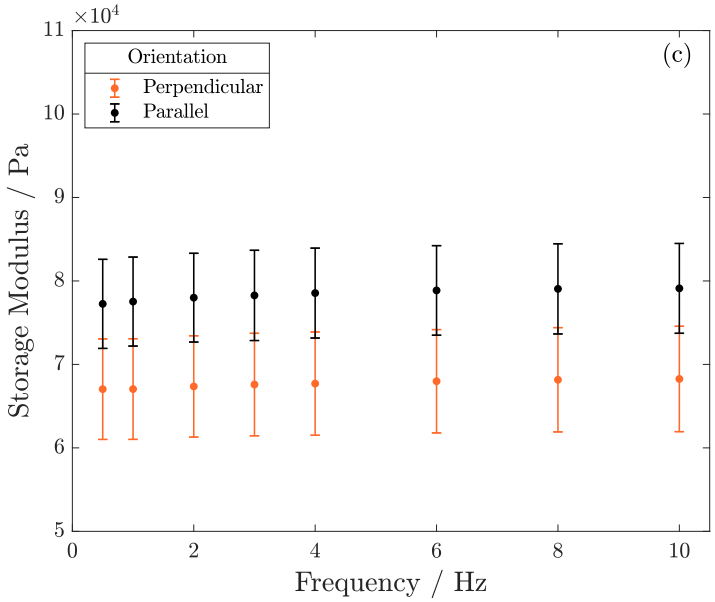

(c) *22G (medium) Nozzle diameter*

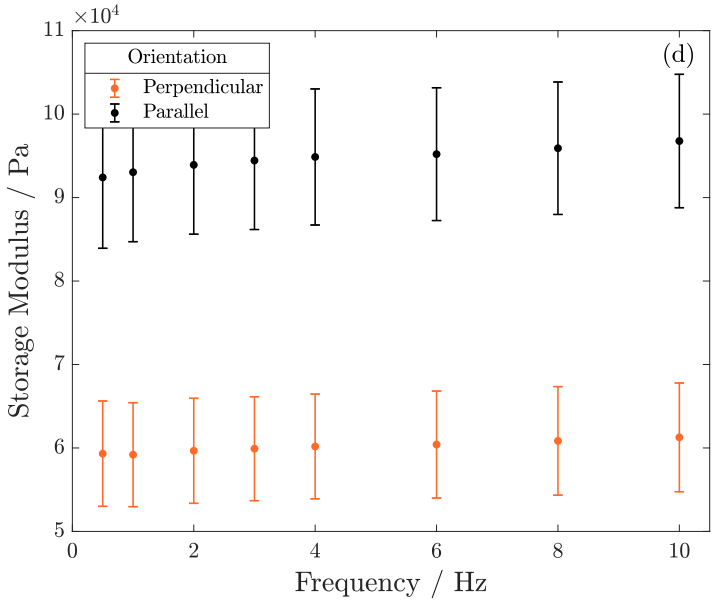

(d) *25G (small) Nozzle diameter*

Figure 4.5: *Storage modulus for cast and additively manufactured PVA with varying nozzle diameter. Error bars show 95% Confidence intervals. (n = 6)*

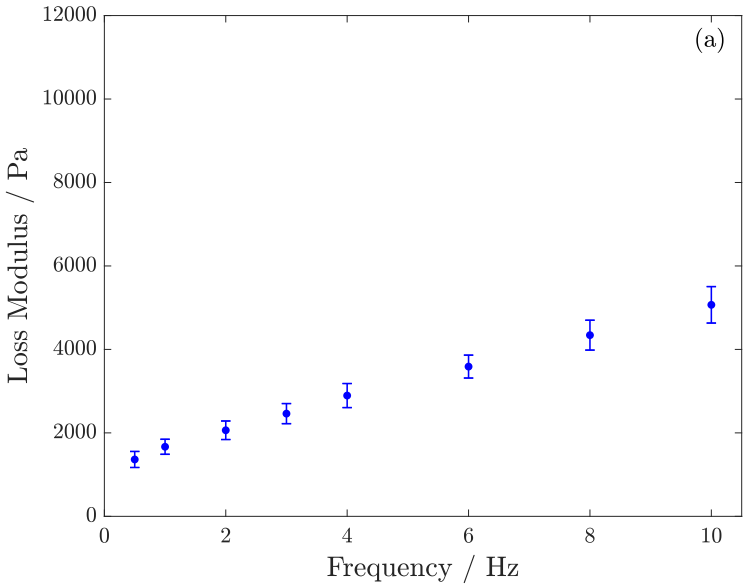

(a) *Cast control samples*

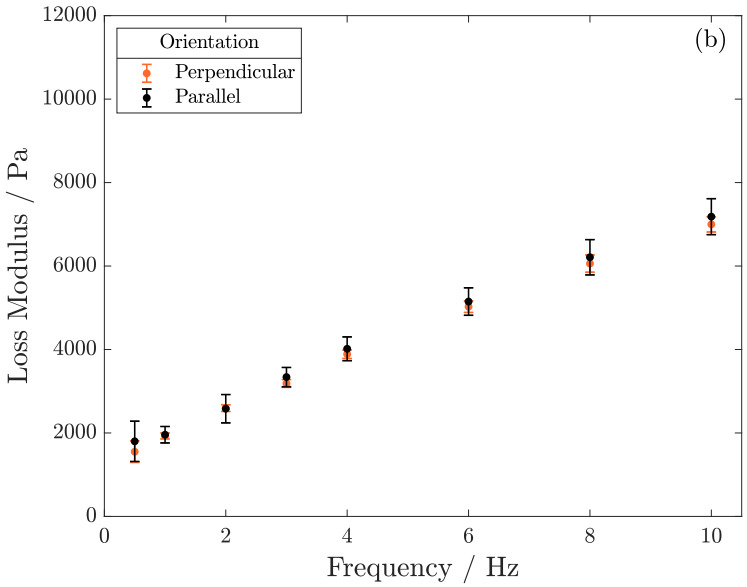

(b) *18G (large) Nozzle Diameter*

Figure 4.6: *Loss modulus for cast and additively manufactured PVA with varying nozzle diameter. Error bars show 95% Confidence intervals. (n = 6)*

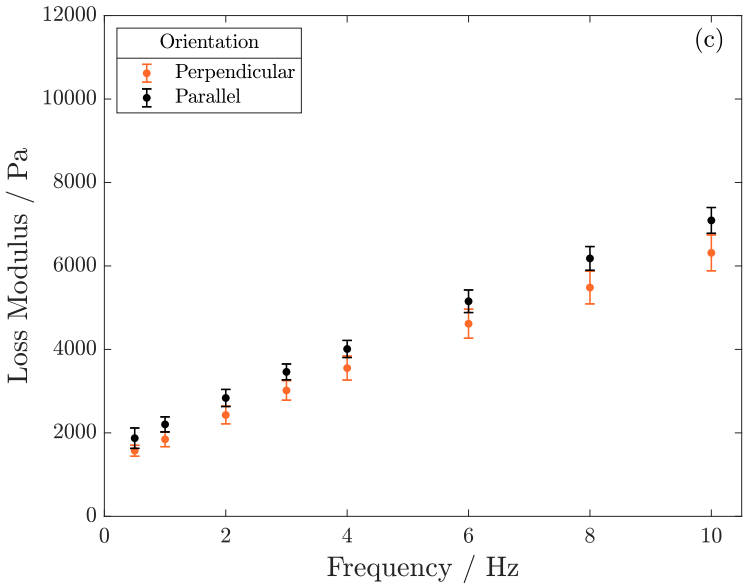

(c) *22G (medium) Nozzle diameter*

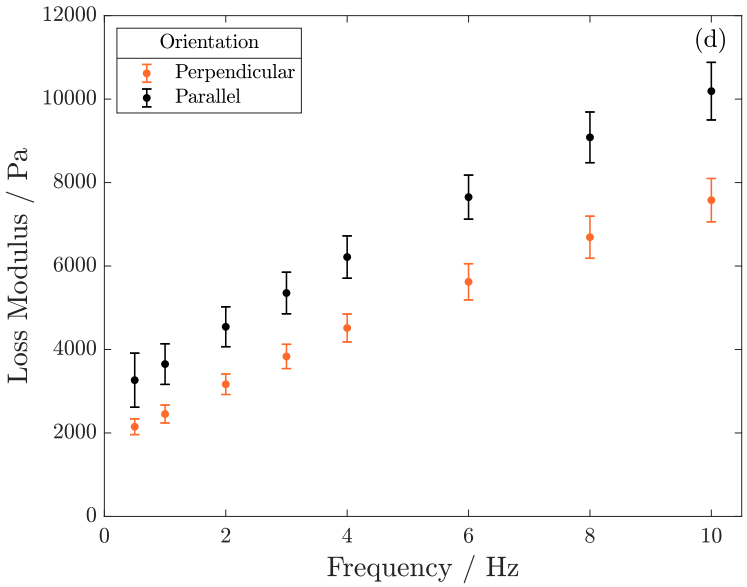

(d) *25G (small) Nozzle diameter*

Figure 4.6: *Storage modulus for cast and additively manufactured PVA with varying nozzle diameter. Error bars show 95% Confidence intervals. (n = 6)*

Figure 4.7, shows images of preliminary ramp tests of three samples. These tests were performed when defining the optimal print parameters, prior to the viscoelastic study presented above. Samples a, b and c were photographed before, during and after the test indicating the failures modes seen. Figure 4.7a shows a sample tested in the parallel orientation, 4.7b a sample in the perpendicular orientation, and 4.7c another sample in the perpendicular orientation where print defects were present. It was ensured all samples used for viscoelastic elastic analysis exhibited no print defects.

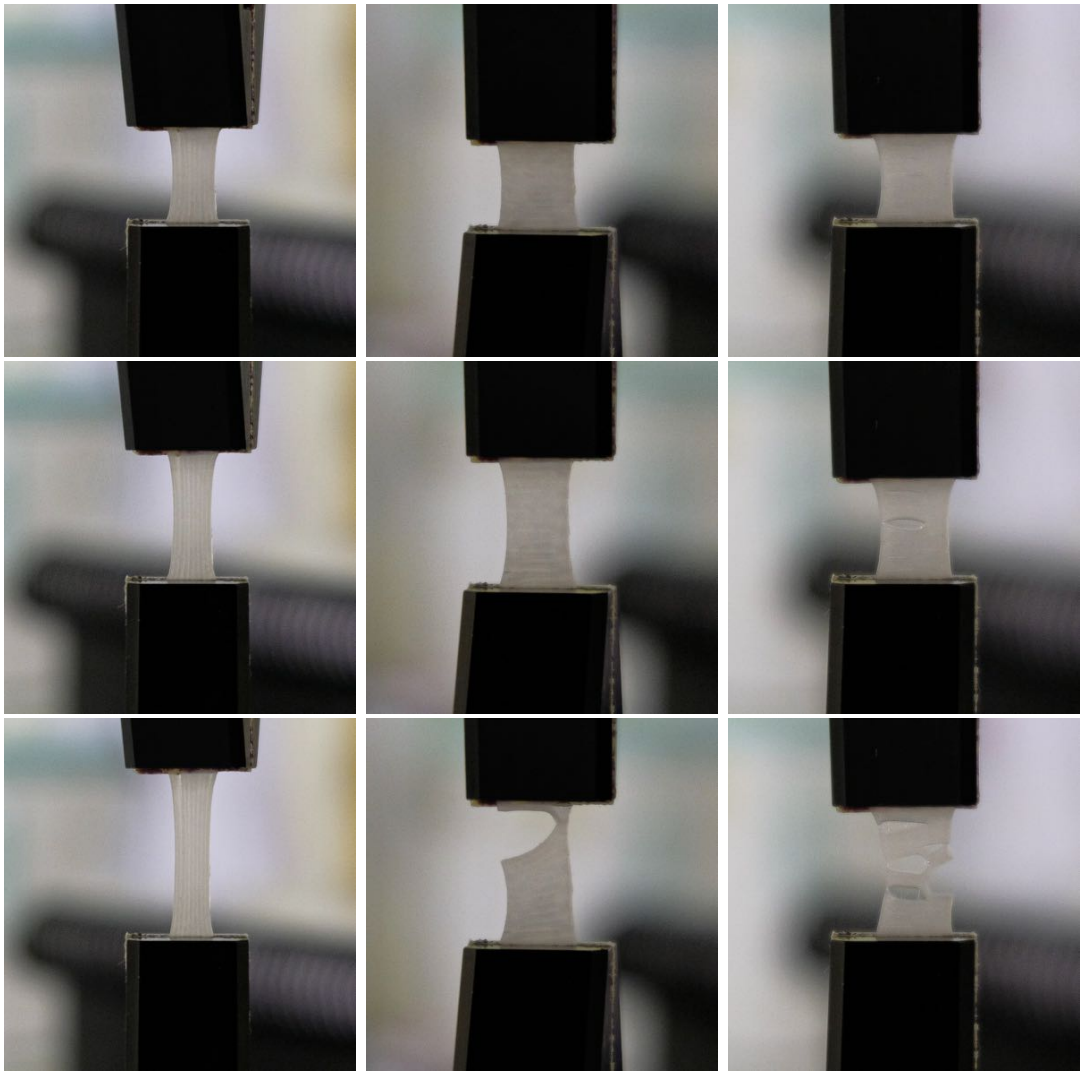

(a) *(b)* *(c)*

Figure 4.7: *Images of preliminary uniaxial tests of the medium nozzle size, showing the parallel (a), and perpendicular (b) orientations. (c) shows the failure mode of a a perpendicular sample, with print defects. Images were taken at the start of the test (top), during the test (middle), and at the end of the test (bottom)*

4.3.2 Analysis of the effect of true stress and strain on DMA

4.3.2.1 DMA under tension

Figure 4.8 shows an example of the raw data acquired from the Bose 3200 for one sample of AM PVA, after true stress and strain have been calculated. Peak true stress was higher than engineering stress for all samples, for example at 0.5 Hz a mean value of 17.7 ± 1 kPa was calculated, compared to 14.7 ± 0.8 kPa for engineering stress. The minimum stress was also observed to be higher with a mean value of 10.5 ± 1 kPa compared to 9.2 ± 0.9 kPa. A change in the minimum and maximum strain was also reported. The engineering strain was constant at 15 - 20% for all samples tested, and lower values of 14.0 - 18.2% were calculated for the true strain. Standard deviation has not been given for strain as any error was due to the precision of the Bose 3200, which is ± 0.005 mm. The hysteresis loops at 0.5 and 10 Hz have also been shown to further illustrate the effect of true stress and strain on the stress response during sinusoidal loading (figure 4.10).

Once viscoelastic properties were calculated based on true stress and strain, a difference in both storage and loss moduli was also seen (figure 4.9). For example at 0.5 Hz, the storage modulus calculated from engineering stress and strain was 92.4 ± 8.5 kPa, lower than 142 ± 12.1 kPa calculated from true values. Across all frequencies an average difference of 54 ± 0.3 % was observed. Likewise, a difference was also observed for the loss moduli. For example at 0.5 Hz, the loss modulus calculated from engineering values was 3.3 ± 0.6 kPa, higher than 4.5 ± 0.9 kPa for true values. The average difference across all frequencies was 40%.

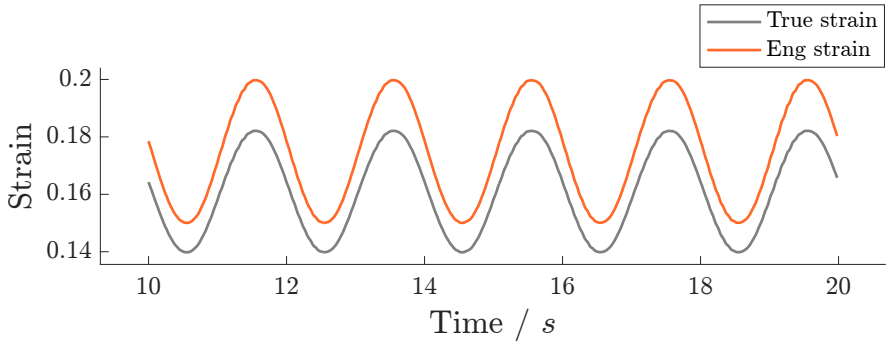

(a) *Strain*

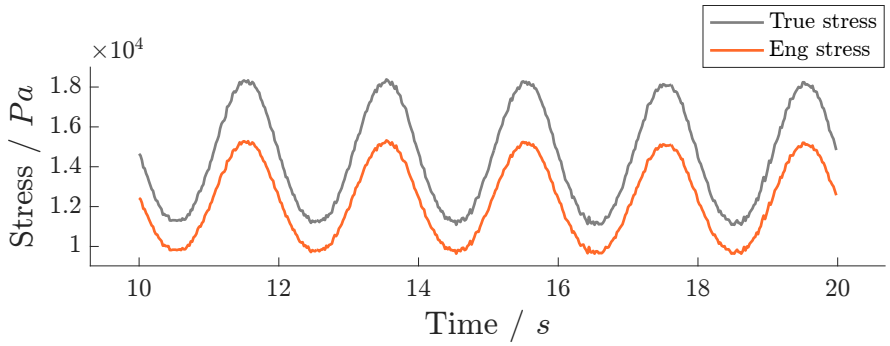

(b) *Stress*

Figure 4.8: *Engineering (Eng) and true stress (a) and strain (b) with respect to time, for 1 sample of AM PVA under sinusoidal tension at 0.5 Hz*

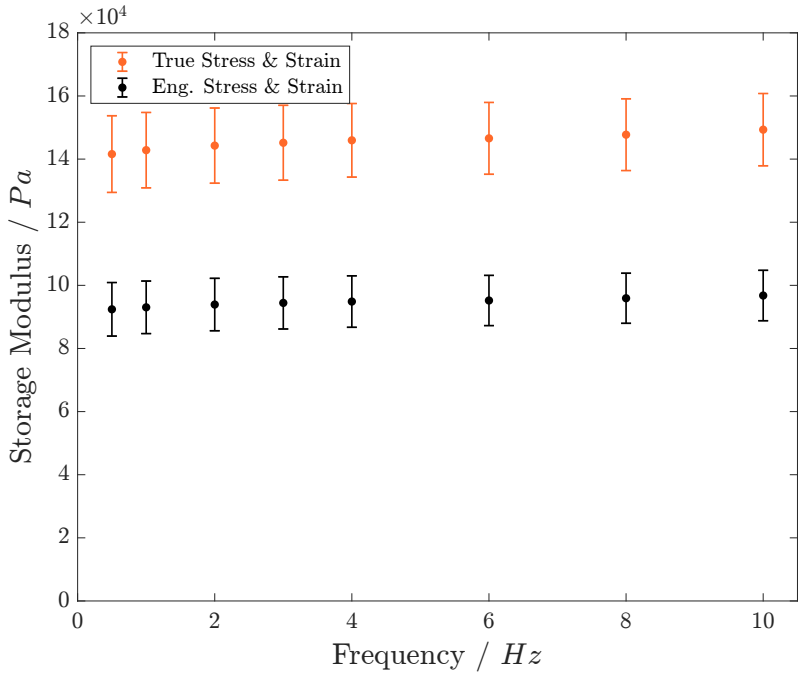

(a) *Storage modulus*

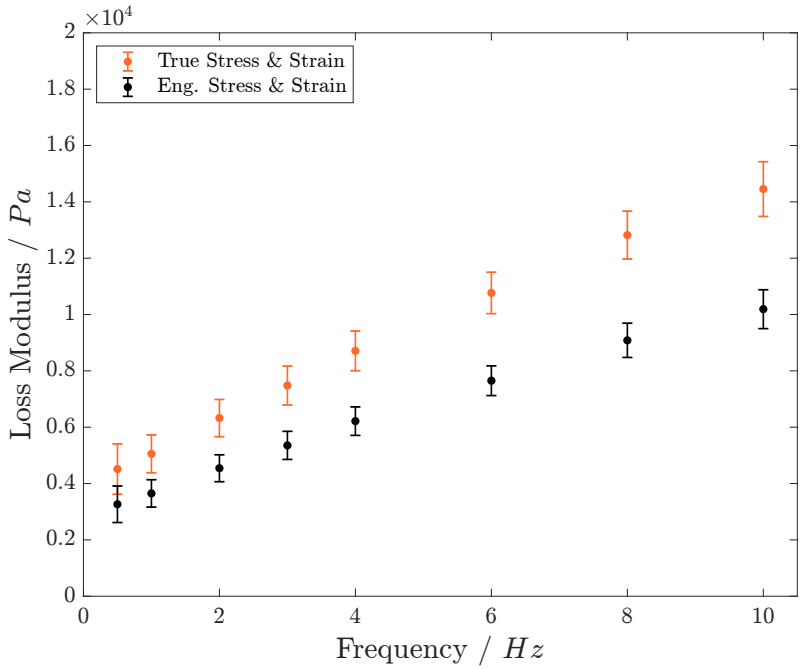

(b) *Loss modulus*

Figure 4.9: *Storage (a) and loss (b) modulus comparing true and engineering (Eng) stress & strain for AM samples. Error bars show 95% Confidence intervals ($n = 6$).*

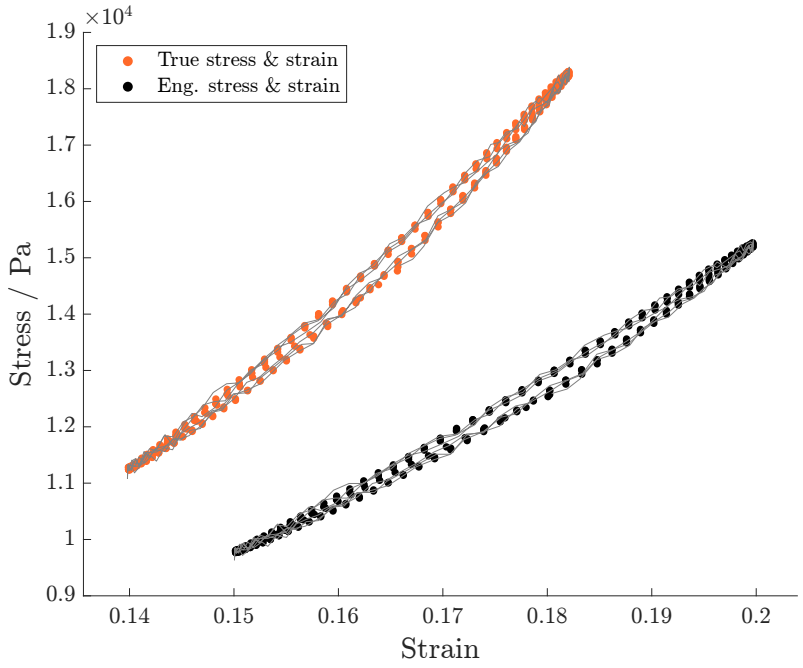

(a) *Hysteresis loop at 0.5 Hz*

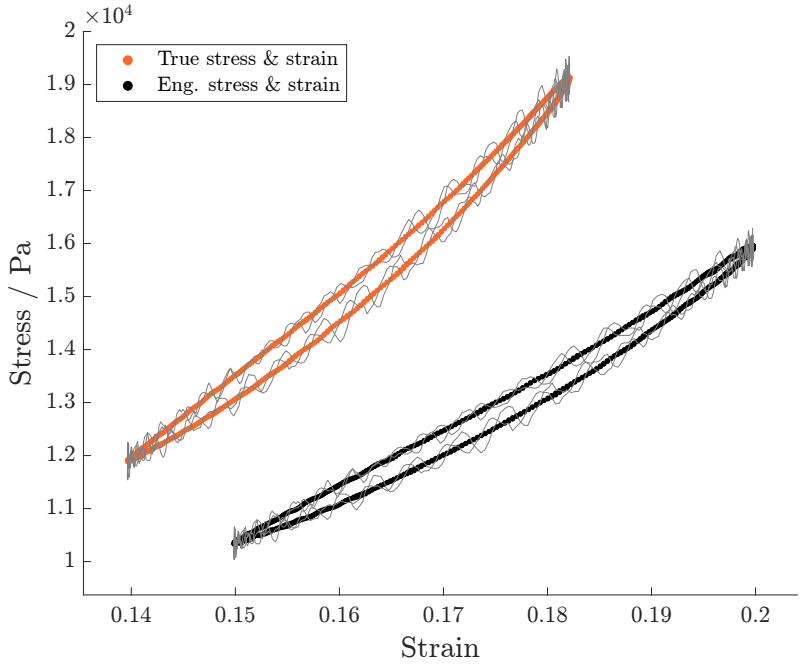

(b) *Hysteresis loop at 10 Hz*

Figure 4.10: *Hysteresis loops for one sample of AM PVA, at frequencies of 0.5 (a), and 10 Hz (b), calculated from true (orange), and engineering (Eng) (black) stress and strain. Data has been smoothed using a Savitzky-Golay filter in Matlab to improve clarity. For completeness, raw data has been in included in grey.*

4.3.2.2 DMA under compression

Figure 4.11 shows an example of the raw data acquired from the Bose 3200 for one sample of cast PVA tested under compression, after true stress and strain have been calculated. Peak true stress was lower than engineering stress for all samples, for example at 0.5 Hz, a mean value of 79.2 ± 3.9 kPa calculated, compared to 99.0 ± 4.9 kPa for engineering stress. The minimum stress was also observed to be lower with a mean value of 46.7 ± 2.4 kPa compared to 55.0 ± 2.8 kPa. A change in the minimum and maximum strain was also reported. The engineering strain was constant at 15 - 20% for all samples tested, and was higher with values of 16.2 - 22.3% for the measurement of true strain. As previously stated, standard deviation has not been given for strain data. These trends were seen for all frequencies tested. The hysteresis loops at 0.5 and 10 Hz have also been shown to further illustrate the effect of true stress and strain on the stress response during sinusoidal loading (figure 4.13).

Values of storage and loss moduli calculated based on true stress and strain were lower than those calculated with engineering stress and strain (figure 4.12. For example at 0.5 Hz, the storage modulus was 837 ± 56 kPa when calculated from engineering stress and strain, compared to 507 ± 34 kPa when calculated from true values. Across all frequencies an average difference of 39 ± 0.2 % was observed. Likewise, a difference was also observed for the values of loss moduli when calculated with true stress and strain. For example at 0.5 Hz, the loss modulus was 96.9 ± 6.9 kPa when calculated from engineering values, compared to 66.0 ± 4.7 kPa when calculated from true values. The average difference was 33 ± 0.7% across all frequencies.

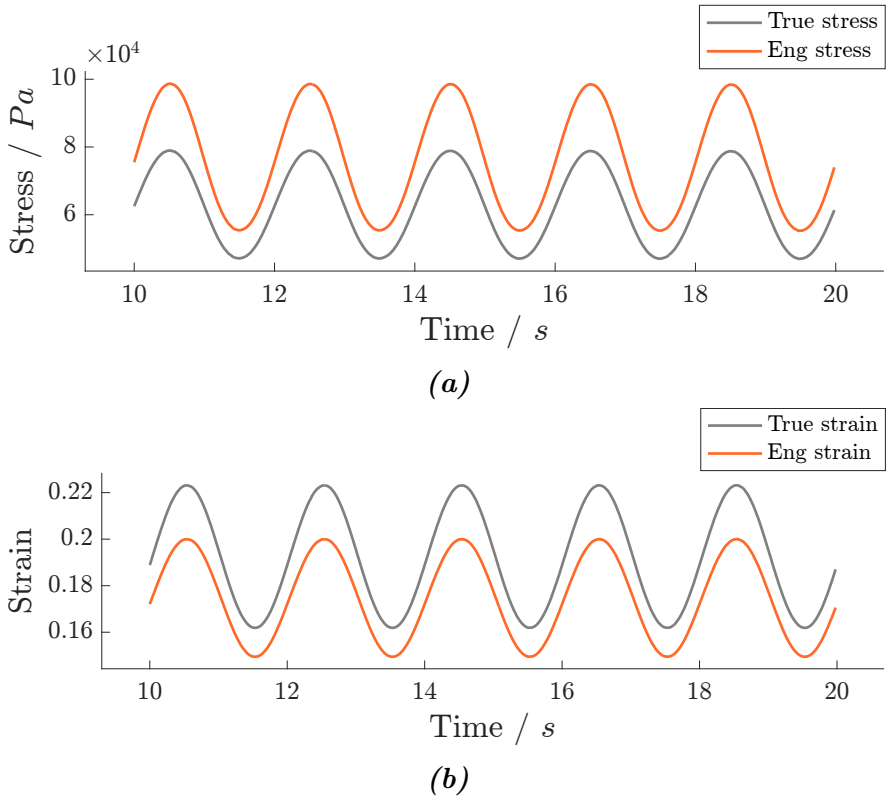

Figure 4.11: *Engineering (Eng) and True stress (a) and strain (b) with respect to time, for 1 sample of AM PVA under sinusoidal compression at 0.5 Hz.*

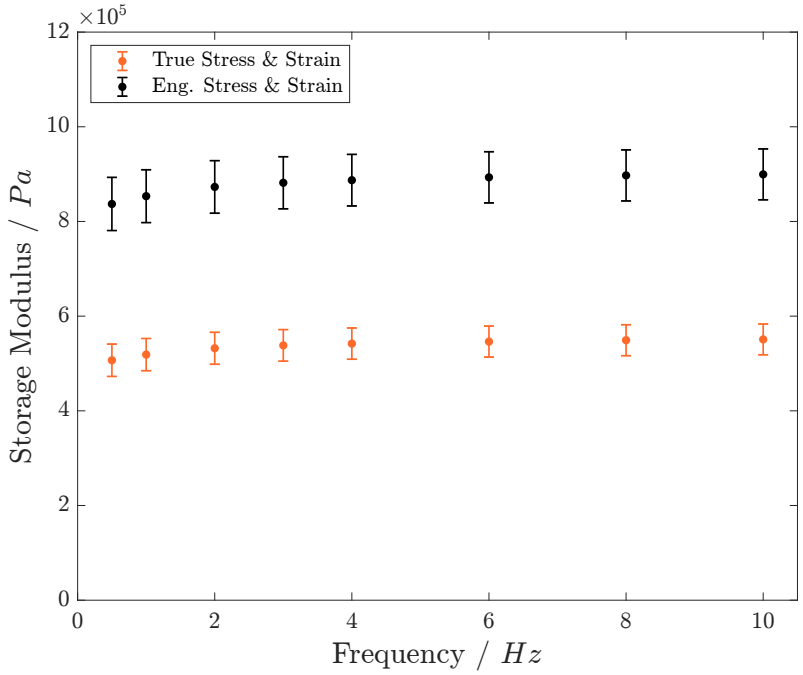

(a) *Storage modulus*

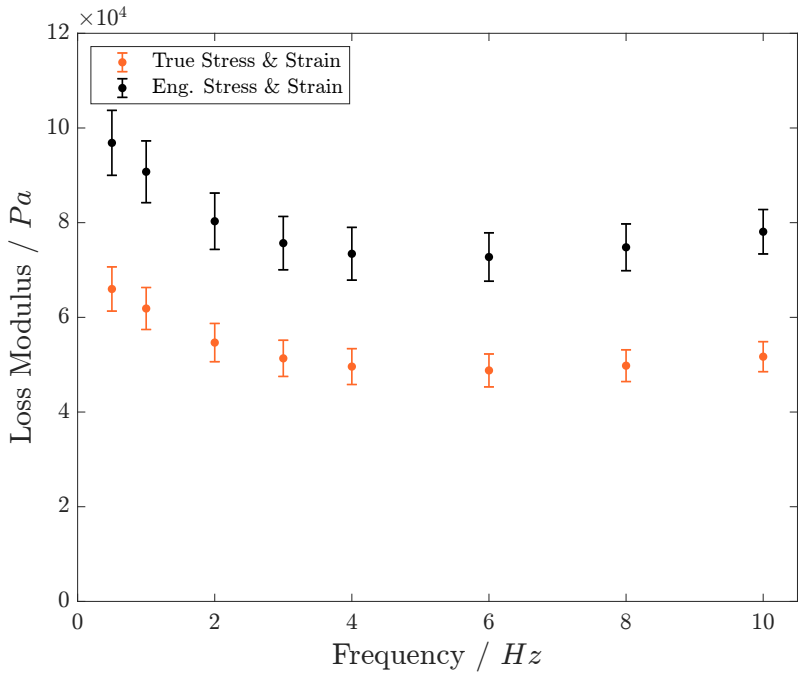

(b)

Figure 4.12: *Storage (a) and loss (b) modulus comparing true and engineering (Eng) stress & strain for cast cylindrical samples tested under compression ($n = 6$).*

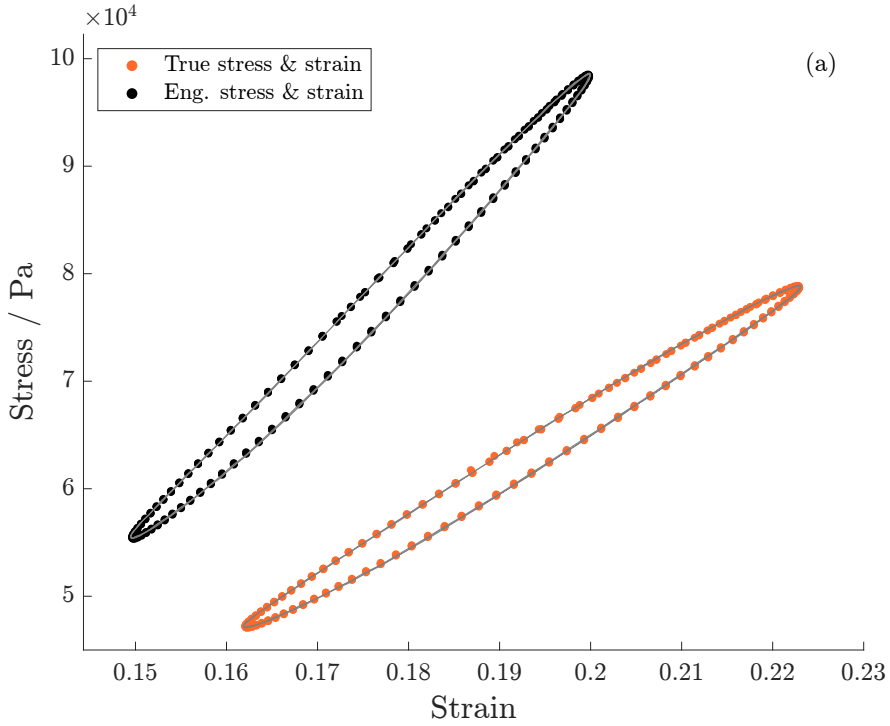

(a) *Hysteresis loop at 0.5 Hz*

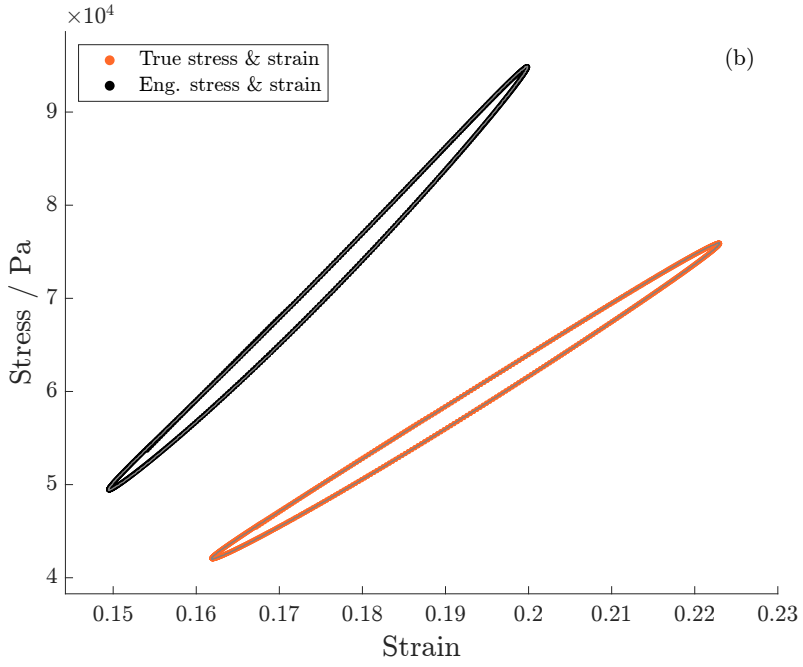

(b) *Hysteresis loop at 10 Hz*

Figure 4.13: *Hysteresis loops for one sample of cast PVA (PVAC), at frequencies of 0.5 (a), and 10 Hz (b), calculated from true, and engineering (Eng) stress and strain. Data has been smoothed using a Savitzky-Golay filter in Matlab to improve clarity. For completeness, raw data has been in included in grey.*

4.4 Discussion

4.4.1 Effect of orientation of filament on viscoelastic properties

This study has shown the capacity of AM to control and manufacture mechanical anisotropy into PVA cryogels whilst retaining constant material properties. A change in nozzle size created a change in the viscoelastic behaviour of the cryogel, relative to the printing direction. No statistically significant difference ($p > 0.05$) was seen between storage and loss moduli of the two orientations for the large nozzle (figures 4.5b and 4.6b). For the medium size, storage and loss moduli were 13.6 ± 0.2 and 12.9 ± 2.2% higher when tested parallel to print direction (figures 4.5a and 4.6a). A larger difference of 36.4 ± 0.25 and 28.9 ± 3.0% was reported for the small nozzle size. As the ratio of nozzle diameter and filament width was kept constant, the key parameter that varied between the the manufacturing processes was pressure, where a higher pressure of 310 kPa was required to extrude filament from the smallest nozzle size (compared to 172 and 70 kPa required for the medium and large sizes).

PVA has previously been shown to be a shear thinning fluid [210], and other shearing thinning fluids have been well researched for biomedical applications, with the majority of uses being for drug delivery and tissue engineering [211, 212]. The key mechanism that causes shear thinning in hydrogels is the disruption to reversible bonding upon application of a shear stress [213], and the shear properties of AM PVA composites has been studied with respect to printability [148]. However, this study did not ascertain the effect of pressure on the mechanical properties of PVA [148]. The author hypothesises that the process of extrusion through a nozzle, induces a shear force on the fluid, causing an alignment of the polymer chains within the PVA solution. This may explain the higher moduli observed for the small nozzle samples tested in the par-

allel orientation. For example, the storage modulus for these samples had an average magnitude of 94.6 ± 1.3 kPa, with the comparative values for the medium and large nozzles being 78.3 ± 0.65 kPa and 80.2 ± 0.74 kPa. This hypothesis is in agreement with Chen *et al.* (2019), who demonstrated that polymer chain alignment in PVA, results in anisotropy through a process of 'drawing' [214]. This theory also agrees with Millon *et al.* (2006 and 2007), who showed that the introduction of tensile stress during the FT manufacturing process increases and allows control over the anisotropy in PVA cryogels [34, 8]. However, this process is unlikely to retain sample geometry and is reliant on simple, cast methods of manufacture. This chapter has shown a further methodology to create anisotropy within PVA, which gives greater design control over the mechanical properties.

The samples which were tested in the perpendicular orientation, tended to fail along the boundaries between filament strands. Figure 4.7b, shows the failure mode of a preliminary sample, tested in the perpendicular orientation. Failure in this sample is seen along the boundary between filament strands, where fewer crosslinks are likely to have formed. This confirms the second mechanism by which anisotropy can be introduced into the cryogel; toolpath orientation. The length of time taken for PVA to freeze, has been shown to impact the number of physical crosslinks that form when undergoing FT cycles [215]. To retain the geometric properties of a PVA filament, there must be a short time period between deposition and freezing. However, this may also inhibit the formation of physical crosslinks between filament strands, as the PVA solution will not have as much contact time between strands of filament, before it is frozen into a cryogel.

When comparing samples manufactured in the perpendicular orientation, a clear relationship is present, with a decrease in nozzle diameter resulting in a greater number of filament strands, and thus an increase in the number of weaker region between strands, for a given unit length. This is observed when analysing the viscoelastic data

presented in figures 4.5b-d and 4.6b-d, where both storage and loss moduli decrease as the nozzle size decreases. For example, in the perpendicular orientation at 0.5 Hz, the storage modulus decreases from 77.0 $\pm$ 2.1 kPa for the large nozzle, to 67.0 $\pm$ 5.2 kPa and 59.3 $\pm$ 5.5 kPa for the medium and small nozzle. This results in weaker physical bonds between the filaments along the loading direction for the perpendicular samples. The significant decrease in storage modulus seen in the perpendicular orientation when the nozzle diameter is reduced to 0.26 mm, is due to the increased number of filament strands, and therefore number of weak boundaries. This smaller nozzle diameter also results in extrusion of a smaller mass flow rate, thus a reduction in thermal mass, and faster freezing time. Conversely, the lower number of weak filament boundaries, and higher mass flow rate explains the homogeneity of samples manufactured with the large nozzle size.

Figure 4.7c highlights the importance of correct line spacing, where minimal contact between filament strands, or at worse, no bonding present between strands, results in a sub-optimal mechanical strength, crack formation and ultimately premature failure of the material. Throughout the viscoelastic testing presented in this chapter, all samples were checked for print defects, and no samples showed signs of cracks or failure between filament strands due to the comparatively lower strains used during DMA.

The results of the research presented in this chapter, have shown that AM processing parameters have a measurable impact on the mechanical properties and visible meso-scale morphology of PVA. The evidence discussed above points towards there being two mechanisms at work, which both alter the orthotropy of AM PVA. These mechanisms are the hypothesised polymer chain alignment within the filament strand, and weak boundaries introduced between filamnents strands due to a short time period for crosslinking to occur. Although the authors suggest possible mechanisms to explain the orthotropic behaviour shown, these hypotheses could be investigated further through surface imaging techniques (e.g. scanning electron microscopy) to study

the morphology at a higher magnification. This chapter has shown the importance of understanding key process parameters involved in AM of PVA at sub-zero temperatures. By altering these parameters, it has been shown that it is possible to control the orthotropic behaviour, without changing the composition of PVA used, or introducing 'post-processing' techniques such as straining samples during the FT process.

4.4.2 Effect of true stress and strain on DMA

This chapter has also evaluated the effect that calculating viscoelastic properties using true stress and strain has on the resulting values of storage and loss moduli. To accurately measure the change in area for uniaxial tension, the dimensions of the sample must be measured throughout the test. This is generally achieved by using a multi-camera setup to image the sample from different axis, and requires precise calibration to acquire accurate data of the sample's dimensions [216, 217]. As this requires a complicated setup, it is rarely used, and if true stress is reported, it is most often estimated in a similar manner to the method used in this chapter. For example the convention for analysing the stress & strain response of the coronary artery is to plot true stress and stretch [20, 21, 218, 52]. This method is suitable only for incompressible materials with a Poisson's ratio of 0.5, meaning the total volume of the sample is preserved, and the increase in sample length is directly proportional to the decrease in area [219].

Although at small strains, the difference between true and engineering stress & strain is often negligible [220], the hysteresis loops in figures 4.10 and 4.13 illustrate the expected behaviour at higher strains, where an increase in sample length (under tension), results in a decrease in the cross sectional area of a sample, and therefore an increase in the stress measured. Whilst under compression the opposite is true, and an increase in area throughout the test is observed, resulting in a decrease in stress.

The comparison between calculations made with engineering and true stress and strain for uniaxial testing has been well documented[220, 221, 222], and as previously stated, mathematical approximations of true stress are commonly calculated for known materials. Viscoelastic data acquired from DMA has been extensively reported for a variety of connective tissues[23, 22, 24, 31, 201], and this data is all calculated from engineering stress and strain. In the case of data acquired from the Bose 3200 used in this study, this is due to the lack of any method to measure the change in shape during uniaxial testing, where only the initial sample shape is used to calculate viscoelastic moduli by Wintest. This study has successfully used Matlab to calculate and quantify the differences expected when true stress and strain are taken into account, showing for the strain rates tests in this thesis, that a maximum difference of 50% in the viscoelastic properties could be expected between the engineering stress used in prior studies and the actual stress the exerted on the material. This method could be applied to studies that have characterised materials using DMA, however it should be noted the the code used to calculate the viscoelastic properties has only been validated on the Bose 3200 used for mechanical testing in this thesis.

Ultimately, the literature values for the viscoelastic characterisation of connective tissues using DMA have been calculated using engineering stress and strain. Therefore, the data presented in this thesis has also been reported using engineering stress and strain, to allow the future comparison of results. However, it should at least be understood that the actual stress in a sample will be different, and this chapter quantifies the extent that viscoelastic moduli will change when taking into consideration the true stresses in the material.

4.5 Conclusion

This study demonstrates that sub-zero AM can be used to control the orthotropic viscoelastic behaviour of PVA through the process parameter variation, demonstrating the future potential to design connective tissue replacements which closer replicated the anisotropic behaviour of CT. This study has shown that for sub-zero AM of PVA:

- A decrease in nozzle size increases orthotropic mechanical properties, and two key mechanisms have been identified that could cause this.
- The first mechanism is polymer chain alignment, resulting in smaller nozzle sizes manufacturing stiffer materials in the parallel orientation.
- The second mechanism is the introduction of weak boundaries between filament strands, caused by the formation of fewer crosslinks. This results in smaller nozzle sizes producing materials which are less stiff in the perpendicular orientation.

For the first time, this chapter has considered the effect of key process parameters of sub-zero AM, contributing an assessment of the relationship between nozzle size and print orientation and mechanical behaviour of PVA to the relatively new field of PVA AM. This fundamental research is crucial to understanding and further developing the AM process to manufacture complex material properties. Through the assessment of AM process parameters shown in this chapter, a novel method of introducing and controlling anisotropic behaviour analogous to the role of collagen in CT has been presented. This fundamentally proves the ability of AM to repeatably introduce anisotropic behaviour without the need for complex pre- or post-processing of the material, leading to the potential to better replicate the fibre-reinforced, anisotropic nature of CT.

Chapter 5

SUB-ZERO AM AND HYPERELASTIC ANALYSIS OF PVA LATTICES

5.1 Introduction

The work presented in chapters 3 and 4 has been aimed towards comprehensively characterising all compositional and AM manufacturing parameters that are relevant to its use as a CT replacement material. This chapter aims to apply the knowledge learnt in the previous chapters (most pertinently the conclusions presented in chapter 4) to explore the design of novel AM toolpaths. This study will aim to introduce and control hyperelastic functionally graded properties often present in CT (section 1.2.1). The fundamental characterisation of the AM process parameters presented in chapter 4 is crucial to understanding the strengths and weaknesses of the sub-zero AM process used throughout this thesis. For example, it has shown that inherent weaknesses are present between filament lines for small nozzle sizes. This understanding has been used as a crucial design input when developing novel toolpaths to manufacture

functionally graded, hyperelastic PVA constructs in this chapter; as well as allowing for more informed interpretation of the results.

Functionally graded AM (FGAM) has been previously researched as a method of varying the mechanical and physical properties of a construct through tailoring AM parameters such as print directionality, density and the material used during the print [223, 224]. This gives engineers significant advantages and flexibility in the design process, allowing for local optimisation of material properties such as strength or weight, or mimicking internal structures, variations in density, and the mechanical strength of biological materials.

Three key methods of functional grading are commonly used: Multi-material functional grading, where a gradual change in material results in physical changes [225]; single material functional grading, where the grading is achieved through changes in porosity [226]; and functional grading achieved through changes in the material microstructure [227]. Functionally graded materials (FGMs) manufactured through these methods show distinct similarity to many structures in nature, such as biological connective tissues, which are often naturally graded structures. Examples can be found of functional grading between different biological materials, or through changes within the structure of a single CT [228, 120]. For example the changes in porosity, density and biological constituents of bone [229]; the interface between cartilage or tendon and bone [228]; the gradient between the three regions of the intervertebral disc [230]; arterial wall stiffening and thickening prior to the onset of atherosclerosis; as well as within these tissues themselves, where changes in the alignment of collagen or elastin may result in gradual changes in mechanical behaviour. To date, within the field of bioengineering, the majority of FGM have been designed and manufactured from traditional materials for orthopaedic or dental applications where grading has been used to change the porosity of implants. Mahmoud and Elbestawi give an overview of key studies where functional grading has been used for orthopaedic implants [119]. Simple

FGMs have also been used for mitral valve implants [231].

Although hydrogel AM has become more prominent, and sub-zero AM has been achieved in a few studies, the use of FGAM specifically for hydrogels has not been well studied. Functional grading of PVA was achieved by Wahab *et al.* (2019), who successfully demonstrated the concept of functional grading for PVA constructs through the freeze thaw cycling of different compositions of cast PVA [232]. This process cast two compositions of PVA between a divider, which once removed, allowed diffusion between the compositions. Undergoing further freeze thaw cycles then resulted in polymerisation between the two compositions, and therefore a gradient of material properties. However, the necessity of a divider means more complicated boundaries between the compositions will not be possible, as well as meaning the resulting gradient will be difficult to define. In this case, AM proves to be a promising solution, allowing for repeatable control over the infill geometry or composition of PVA used, in order to achieve a functionally graded construct. Meng *et al.*, produced AM PVA structures with varying infill density, however only uniaxial compression test were performed on the whole structure, giving little insight about the impact of infill density of the mechanical properties of PVA [148]. Little information was reported on the method used to define the gradient in infill. Overall, little research has been done in order to evaluate and quantify the use of AM processes to control the mechanical behaviour of PVA, therefore allowing the manufacture of functionally graded constructs.

Chapter 4 has shown that AM PVA exhibits significantly weaker mechanical properties when under uniaxial tension perpendicular to the filament orientation (section 4.3.1). This means that in order to reduce stress concentrations and the likelihood of failure, a constant line of filament must be present along the entire length of the sample in the direction of loading. This proves to be an interesting design problem, with the majority of computer aided manufacturing (CAM) for AM programmes not taking this into account, with even fewer allowing for functional grading of the material

by varying this throughout the manufacturing process. However, promising research has shown the potential to parametrically control manufacturing parameters, allowing for control of chosen parameters [233], as well as proving the concept of using mathematical equations to define the toolpath. This research shows the potential to control the mechanical behaviour of a 3D printed material through a mathematically driven toolpath, however no mechanical testing was performed to define the relationships between the generated toolpaths and the resulting mechanical behaviour [233]. The research presented in this chapter will continue the bio-inspired design approach started in chapter 4. In this case, the crimping patterns exhibited by collagen fibres will be used as inspiration to explore the use of sine-wave tool path design as a proof of concept to control the mechanical behaviour of PVA.

5.1.1 Aims & objectives

This chapter aims to design a novel method to manufacture FGAM PVA, whilst ensuring a constant extrusion of PVA in the direction of printing. This will allow for a variation in the pore size and shape of the geometry to be additively manufactured, without reducing the ultimate tensile strength of the material. The objectives for this chapter are as follows:

- A sine wave shaped toolpath has been chosen to parametrically control the toolpath, as it has specific parameters which can be evaluated directly.
- The impact of the wavelength and amplitude of the sine wave on hyperelastic mechanical properties will be assessed.
- Further to this, the corresponding density of PVA within the sample, and alignment of the PVA filament with respect to the direction of loading will be studied to ascertain the most important factors impacting the mechanical behaviour of AM PVA using this method of FGAM.

5.2 Methodology

5.2.1 Sample preparation

Sample preparation was identical to the method presented in section 4.2.2. PVA with a molecular weight of 146-186 kDa was dissolved in deionised water by mechanically stirring the solution at 90°C for one hour. Stirring was continued for 1 hour after removing from the hotplate, until the solution reached room temperature. A PVA concentration of 10% w/w was used for all samples, and all samples underwent 3×24 hour freeze thaw cycles. PVA was acquired from Sigma Aldrich (St Louis, Missouri, USA) and had a hydrolysis of 99+%.

5.2.2 Preliminary work

All samples for preliminary testing were additively manufactured using a Cellink Inkredible+ Bioprinter (Boston, Massachusetts, USA). It has been previously shown that AM introduces a number of complications with hydrogels, in terms of both the extrusion process, and the resulting geometry [234, 235, 236]. For example the geometry of AM hydrogels will not exactly match the toolpath used, where both the cross-sectional shape of the filament and size and shape of pores within the infill are altered due to the flow of material after extrusion, prior to sufficient cross-linking (or in the case of AM PVA, sufficient freezing) needed to maintain geometry [234]. As this chapter aims to additively manufacture lattice designs, which are much more susceptible to these complications compared with the methodology described in chapter 4 (section 4.2.2), preliminary work was undertaken to assess the relationship between extrusion pressure and the resulting diameter of the extruded PVA using a 0.51 mm nozzle (figure 5.1). It should be noted that this was also performed as a different bioprinter was used in this

chapter, and therefore the exact parameters from chapter 4 could not be used. Custom G-code was written to print 9 filament strands, with a layer height of 0.3 mm, at a print speed of 300 mm/min. A 0.51 mm nozzle was used for all samples manufactured. These parameters were chosen to be similar to those described for the small nozzle size in chapter 4 (section 4.2.2), with a layer height of 0.3 mm chosen to increase the thickness of the lattice samples without requiring significantly more layers. A print speed of 300 mm/min was used when manufacturing all lattice designs, as on this platform, this resulted in better geometry resolution. The diameter was measured at three points of each filament, and an average across all 9 was calculated (Figure 5.1j).

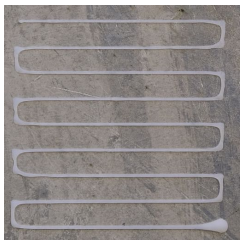

(a) *10 kPa*

(b) *15 kPa*

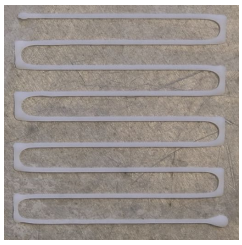

(c) *20 kPa*

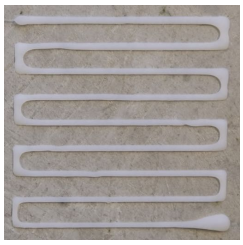

(d) *25 kPa*

(e) *30 kPa*

(f) *35 kPa*

(g) *40 kPa*

(h) *45 kPa*

(i) *50 kPa*

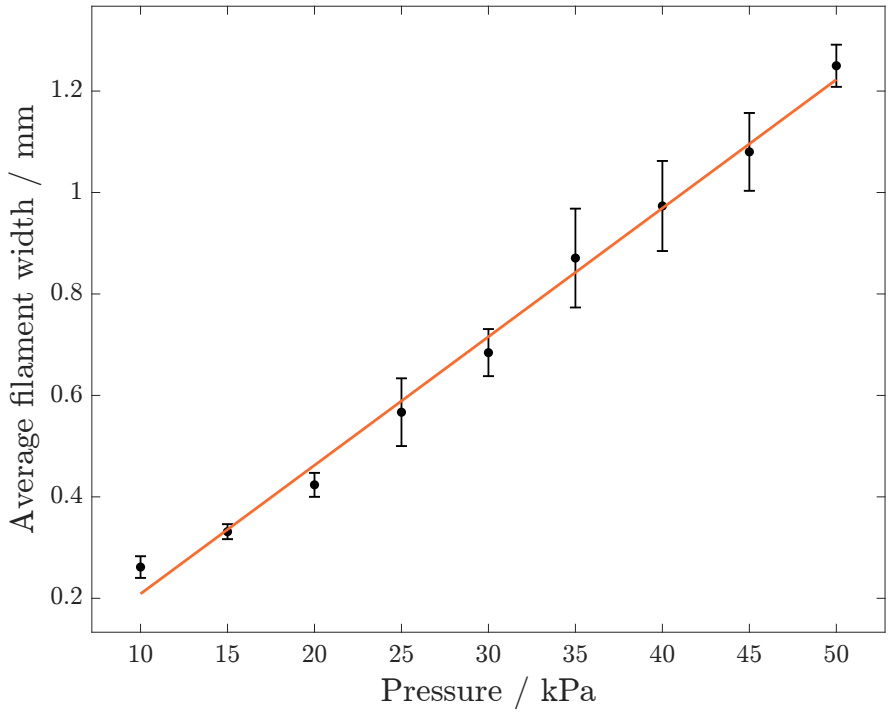

(j) *Av. filament width*

Figure 5.1: *Mean filament diameter compared to extrusion pressure for a 25G needle diameter. Error bars show standard deviation.*

Prior to the manufacture of lattice designs, solid samples (i.e. with a 100% infill) were manufactured using a sine wave toolpath with the a 0.5 mm filament diameter and 0.45 mm line spacing. This experiment was performed to establish whether the material response could be manipulated through changing only the toolpath of AM PVA. 4 samples were manufactured with a toolpath wavelength of 2 mm, and amplitude of 1 mm (Figure 5.2). The PVA composition used was consistent with the lattice samples described in 5.2.3. Similar to the samples with linear toolpaths described previously in Chapter 4 (section 4.2.2), samples were printed with 2 layers to avoid large increases in temperature that may affect the print quality.

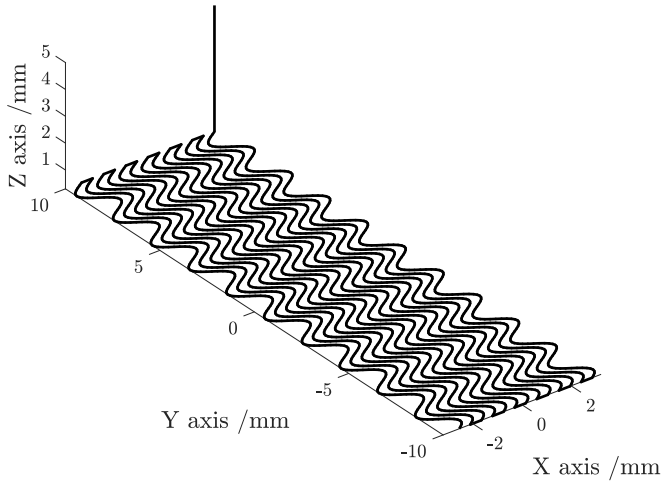

Figure 5.2: *The toolpath of a single layer of the samples manufactured with a wave toolpath, with 100% infill. Samples tested were manufactured with 2 layers.*

5.2.3 AM protocol for uniaxial test samples

All samples for uniaxial tests were additively manufactured using a Cellink Inkredible+ Bioprinter (Boston, Massachusetts, USA). This bioprinter was used to enable further customization of the toolpath, because it allows customised G-code to be uploaded to the platform, necessary to the design of the lattice structures. Matlab (MathWorks, Massachusetts, USA) was used to generate G-code for 2D lattice structures with a sine wave unit cell (Figures 2 & 3). Lattice samples with 5 different unit cell geometries were manufactured, with 3 samples manufactured for each lattice design (Table 2); allowing for samples to be manufactured comparing the wavelength and amplitude of the unit cell. All samples were 20 mm in height (8 mm testing region + 6 mm region to be clamped on both sides) and 0.8 mm in thickness. A constant number of filament "lines" were used for all samples, resulting in a different sample width depending on the amplitude of the lattice unit cell.

5.2.3.1 Toolpath design

Matlab was used to design custom toolpaths allowing for the manufacture of lattices with varying dimensions. Importantly, the design of the toolpath required a constant bonded filament from one end of the sample to the other, enabling mechanical strength along the axial length of the filament to be maintained. The full Matlab code is shown in appendix D.

The toolpath design was based on a sine wave, with both the frequency and amplitude being variables that may be controlled by the user. This resulted in a simple toolpath which allowed for both a constant filament along the length of the sample, and parametric control of the toolpath variables. To manufacture functionally graded constructs, the code then allowed for the frequency to be adjusted throughout the length

of a filament, as well as adjusting the amplitude and/or frequency along the height of the sample (However all of the samples manufactured in this chapter had constant parameters with respect to sample height). For the purpose of this study, only cuboid shapes were manufactured, however there is scope for this to be expanded to allow for more intricate geometries.

5.2.3.2 Programme functionality

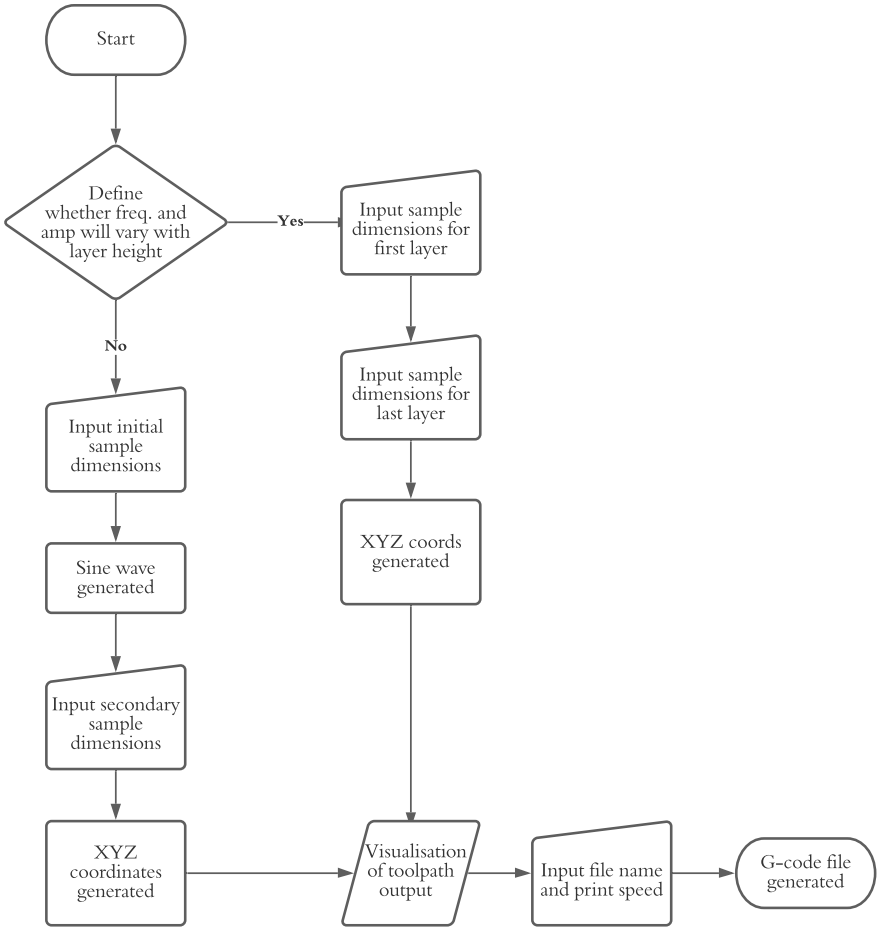

Figure 5.3: *Flow chart showing user process to generate lattice g-code*

Prior to inputting data, the user will be asked whether the sine wave parameters should be varied along the sample height (Z axis). If the user chooses this option, they will be required to input overall shape dimensions, as well as the sine wave parameters for the first and last layers, as well as a function to describe how these parameters will

change between the outer layers. A flow chart showing the overall workflow is shown in figure 5.3. The full code is given in appendix D. If a variation in parameters with respect to sample height is not required, the user is asked to input the sample length, the minimum and maximum frequency required along the length of the sample, the amplitude (mm) of the wave, and a function which will define how the wavelength will vary along the length of the sample.

An initial array is then created between 0 and the sample length; this will be used as the X coordinates to plot the sine wave. Data points are created every 0.1 mm. A second array of the same length is then created between the minimum and maximum frequency. If the same frequency is input for both, there will be no change in wavelength along the sample length. This array will be used as an input to the function defining how the frequency will be varied.

```
Fs = 10;       % Number of samples per mm
dt = 1/Fs;
X = 0:dt:width;      % create X coord array
len = length(w);         % Find length of X
f_in = linspace(min, max, len); % Create freq. array
```

Once this function has been applied to the array of frequencies, the sine wave is plotted using the following code. This is a simplification of equation 2.1 which will plot a sine wave with modulating frequency. This array is then multiplied by the amplitude to give the Y coordinate used to plot the sine wave.

```
    wave = (sin(2*pi*cumsum(f)/Fs)) / 2;
    Y = wave*amplitude
```

$$sin(2\pi \int f(t)dt) \tag{5.1}$$

Once a sine wave with the desired dimensions has been generated, it is plotted for the user. If required, the change in frequency across the length of the sample is also plotted (figure 5.4).

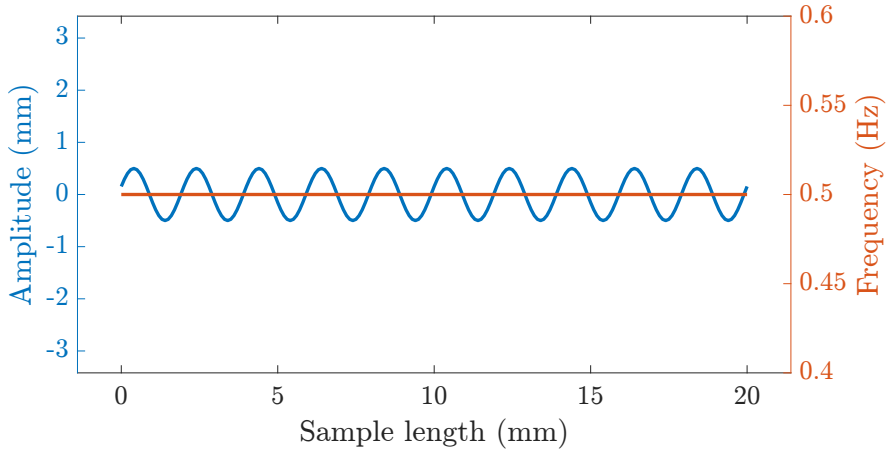

(a) *Toolpath with constant frequency*

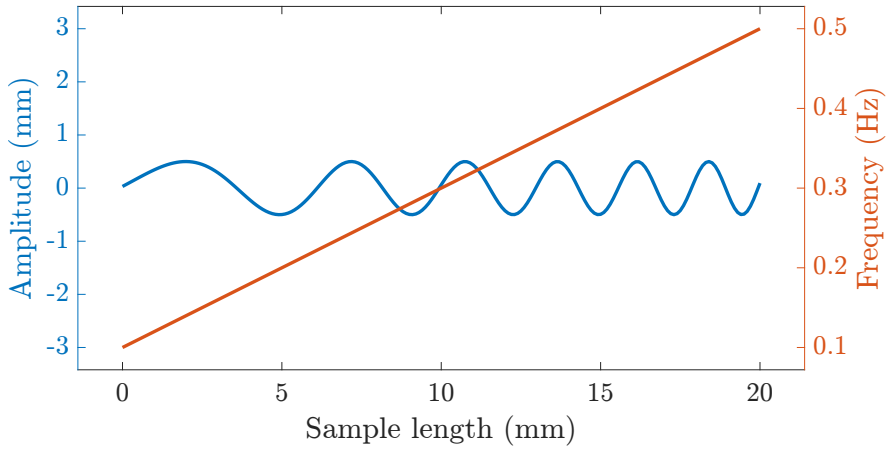

(b) *Toolpath with linearly increasing frequency*

Figure 5.4: *Matlab output visualizing sines waves with a constant frequency of 0.5 waves/mm (a), and a linearly varying wave between 0.1 and 0.5 waves/mm (b)*

Once a single wave has been generated, the user must give the remaining sample dimensions: sample width; strand diameter; sample thickness; and layer height. The strand diameter dictates the gap between filaments within the lattice, and must have been previously measured for the required layer height. A final prompt will ask for a

Table 5.1: *Unit cell geometry use to generate the G-code for 5 lattice designs.*

Lattice	A	B	C	D	E
Wavelength (mm)	10	4	2	2	2
Amplitude (mm)	1	1	1	1.5	2
Sample width (mm)	5	5	5	8	12

file name, and the required print speed. A G-code file is generated and can be sent to the 3D printer via USB, or SD card. A final plot is produced showing the toolpath generated for the sample. This is shown for all five lattice designs tested in this study in figure 5.5. To reiterate the differences between these lattices: Lattices A, B and C have constant amplitude (1 mm) and varying wavelength; and lattices C, D, and E have constant wavelength (2 mm) and varying amplitude (table 5.1).

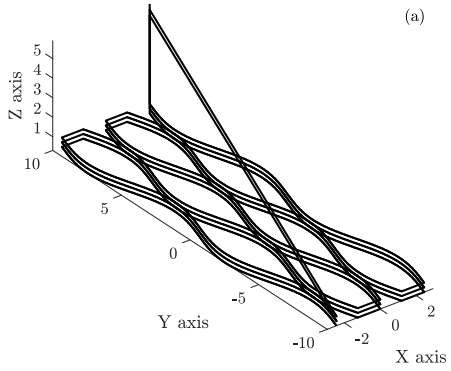

***(a)** Lattice A*

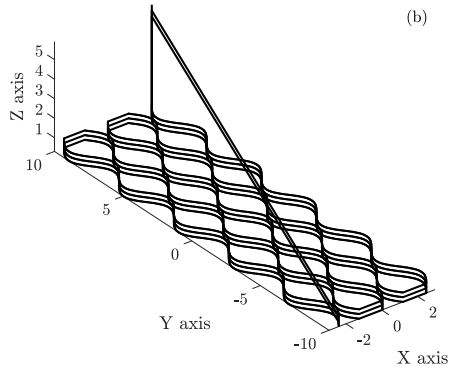

***(b)** Lattice B*

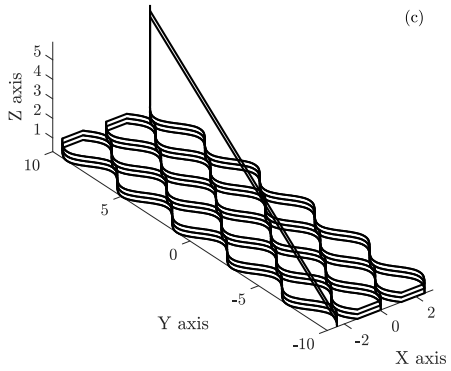

***(c)** Lattice C*

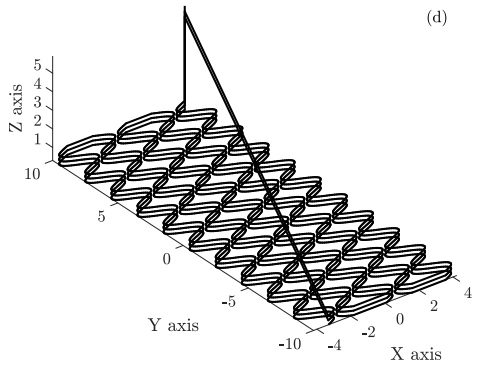

***(d)** Lattice D*

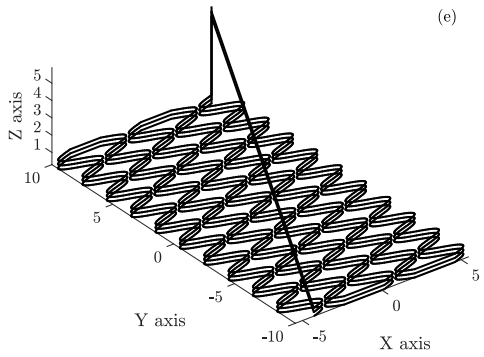

***(e)** Lattice E*

***Figure 5.5:** Matlab generated toolpaths for 5 lattices tested in this study*

5.2.4 Uniaxial tensile tests

Samples were held in place using grips lined with P120 emery paper. Uniaxial ramp tests were performed on a Bose Electroforce 3200 (mechanical testing machine, running Wintest software. Samples were tested axially under tension with a displacement of 10 mm at a strain rate of 0.25 mm/s. The applied strain was calculated using equation 5.2. The load was measured in grams and the corresponding force and stress was calculated using equations 5.3 and 5.4. The Young's modulus of each sample was then calculated using equation 5.5.

The area of PVA in each lattice was calculated using a colour threshold filter in Fiji [237] as a percentage of total enclosing sample area (Appendix C, Figure C.1). This allows for precise selection of an image based on the hue, saturation and brightness of each pixel. These parameters were manually adjusted to select only the pixels which were part of the PVA lattice. This was compared against the Young's modulus of each lattice to ascertain the impact of PVA volume percentage on mechanical stiffness.

$$\varepsilon = \frac{dl}{L} \tag{5.2}$$

$$F = mg \tag{5.3}$$

$$\sigma = \frac{F}{A} \tag{5.4}$$

$$\sigma = \frac{\sigma}{\varepsilon} \tag{5.5}$$

Table 5.2: *Strain energy density functions for the 6 models used in this chapter. N, μ_p and α_p are material constants for Ogden model. C_{ij} are material constants for the (reduced) polynomial models, $C_{0,0} = 0$, and I_1 and I_2 are the first two strain invariants of the left Cauchy–Green deformation tensor given in section 2.1.4*

Model type	Order (n)	Strain energy density function (W)
Ogden	1 2	$\sum_{p=1}^{N} \frac{\mu_p}{\alpha_p} \left(\lambda_1^{\alpha_p} + \lambda_2^{\alpha_p} + \lambda_3^{\alpha_p} - 3\right)$
Polynomial	1 (Mooney Rivilin) 2	$\sum_{i,j=0}^{n} C_{ij} \left(I_1 - 3\right)^i \left(I_2 - 3\right)^j$
Reduced polynomial	1 (Neo-Hookean) 3 (Yeoh)	$\sum_{i=0}^{n} C_{i0} \left(I_1 - 3\right)^i$

5.2.5 Hyperelastic characterisation

Each of the five lattice designs (mechanically characterised by 3 samples) were evaluated for hyperelastic Constitutive modelling in this study. Abaqus (Dassault Systèmes, Vélizy-Villacoublay, France) was used to calculate hyperelastic coefficients for all hyperelastic models used in this study. Raw data for stress and strain was sampled to reduce the total number of data points to 160 in order to reduce error from noise in the data. It was ensured that data points were taken at equal spaces throughout the total range. The Drucker stability criterion was used to assess the stability of each model.

Six different phenomenological models were examined, and the best fit was chosen. The criteria for choosing the model was based on both model stability within relevant strain ranges, and minimising fitting error. The simplest model which fitted these criteria was chosen. The models analysed were: polynomial n = 1 (Mooney-Rivelin), polynomial n = 2, Ogden n = 1, Ogden n = 2, reduced polynomial n = 1 (neo-Hookean), and reduced polynomial n = 3 (Yeoh). Information regarding the six models examined is shown in table 5.2, and further information regarding the models is given in section 2.1.4.

Briefly, as PVA has been shown to be an incompressible material [153], the volu-

metric term in a strain energy density function is not required, so the functions for all models can be simplified to the equations shown in table 5.2. The polynomial model can be further simplified by omitting the second strain invariant, resulting in the reduced polynomial model. In this case j is always zero. The Ogden model bases the strain density function on the principle stretches $(\lambda_1, \lambda_2, \lambda_3)$. As with the polynomial models, it is assumed the material is incompressible and that $\lambda_1\lambda_2\lambda_3 = 0$.

Based on this methodology, the Yeoh model was chosen as the best fit for all samples tested, and the average values of $C_{1,0}, C_{2,0}$ and $C_{3,0}$ were analysed when both lattice amplitude and frequency were varied, as well as comparing cast samples and preliminary AM samples with a 100% infill.

5.2.6 Statistical analysis and data smoothing

All statistical analysis was performed using Matlab (MathWorks, Massachusetts, USA). Where required, unpaired student t-tests were used to ascertain whether a statistically significant difference was present between values of Young's moduli or hyperelastic coefficients.

5.3 Results

5.3.1 Preliminary testing

Sine wave toolpath samples manufactured with a 100% infill (figure 5.6) showed significantly different ($p < 0.001$) mechanical properties to cast samples at low strains (0-20%) with a Young's modulus of 52.6 ± 3.2 kPa, compared with 90.0 ± 6.3 kPa (Figure 5.7). However, no significant difference ($p = 0.19$) in Young's modulus at high strains (80-100%) was seen, with a mean of 127 ± 8.8 kPa compared to the 142 ±

9.0 kPa seen in the cast samples. It should be noted the peak stress in cast samples (measured at 100%) was significantly higher in cast samples ($p = 0.007$) with a mean of 133 $\pm$ 8.4 kPa compared with 97.0 $\pm$ 3.6 kPa for the AM samples.

Figure 5.6: *Example sample printed with a sine wave toolpath and 100% infill. Note the print defects present in some places between filament strands. Sample is 20 mm in length.*

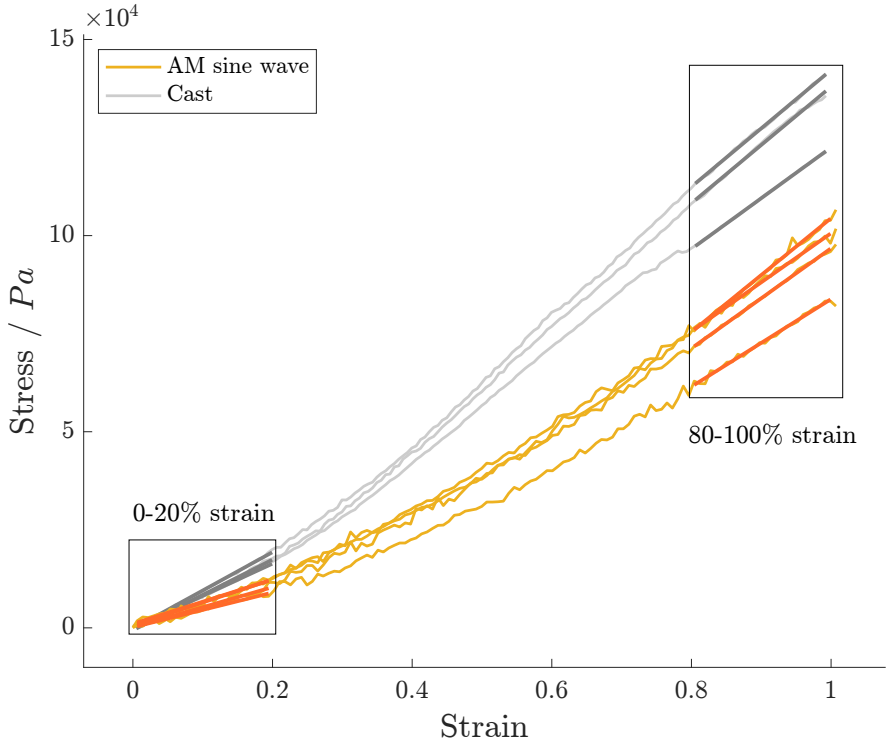

Figure 5.7: *Uniaxial ramp tests for cast control samples (grey), and samples manufactured with a wave toolpath with a 100% infill (orange).*

5.3.1.1 Hyperelastic fitting of wave toolpaths with 100% infill

A significant difference was seen for all three coefficients when comparing cast and AM samples with a 100% infill, with $C_{1,0}$ being 14.3 ± 1.5 and 10.1 ± 2.1 kPa for cast and AM samples respectively ($p = 0.018$). $C_{2,0}$ was shown to be 13.0 ± 1.4 and 6.53 ± 1.3 kPa ($p = 0.001$), whilst median values for $C_{3,0}$ were -2.69 ± 0.36 and -0.763 ± 0.2 kPa ($p < 0.001$) respectively (Figure 5.8). Analysis of selection criteria of all models is described in section 5.3.3.

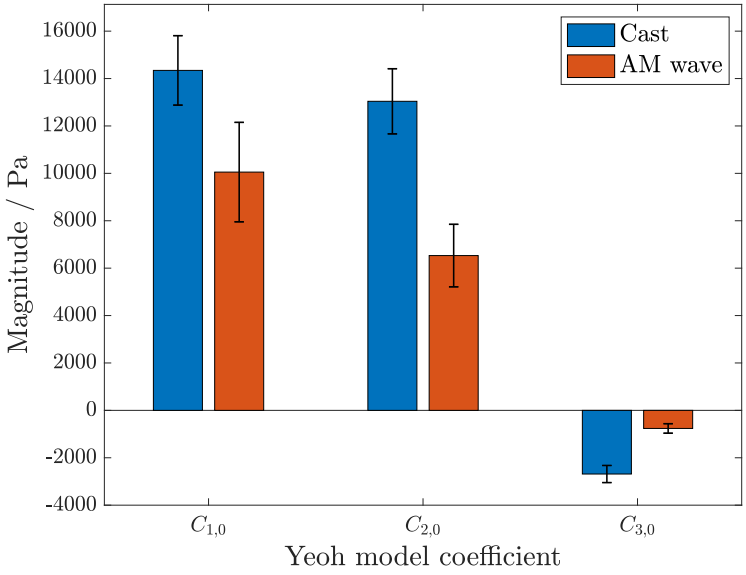

Figure 5.8: *Median and SD for $C_{2,0}$ & $C_{3,0}$ coefficient for a Yeoh hyperelastic model (n=3), showing a comparison between cast and AM samples.*

5.3.2 Uniaxial testing of lattice designs

Images of all samples manufactured are shown in figure 5.9. It was shown that an increase of wave amplitude resulted in a decrease in stiffness of additively manufactured PVA (Figure 5.10a), with the average Young's modulus between 0-20% strain, decreasing from 30.3 ± 1.38 kPa at an amplitude of 1 mm to 15.1 ± 1.7 kPa at an amplitude of 1.5 mm ($p < 0.001$)(table 5.3). The Young's modulus at 2 mm was 12.1 ± 0.64 kPa, however there was no statistical difference between 1.5 mm to 2 mm ($p = 0.081$). Similarly the Young's modulus between 80-100% strain decreased from 75.0 ± 4.7 kPa at 1 mm to 30.9 ± 1.44 kPa at 2 mm (Figure 5.11a). This decrease was significant both from 1 → 1.5 ($p = 0.002$), and 1.5 → 2 mm ($p = 0.006$).

Similarly, a significant difference in stiffness was measured with respect to a variation in wavelength (Figure 5.10b). A decrease in Young's modulus was observed between 0-20% strain from 30.3 ± 1.4 kPa at a wavelength of 2 mm, to 23.7 ± 1.5 kPa at a wavelength of 4 mm ($p = 0.009$). A further decrease to 17.6 ± 1.7 kPa at a wavelength of 10 mm was also seen ($p = 0.019$). Again, this decrease was also seen at 80-100% strain, decreasing from 75.0 ± 4.8 kPa at 2 mm → 58.9 ± 2.5 kPa at 4 mm ($p = 0.013$) → 37.6 ± 2.3 kPa at 10 mm ($p < 0.001$) (Figure 5.11b). All samples tested measured lower values for Young's modulus compared to the cast control samples, which had values of 81.1 ± 6.3 kPa between 0-20% strain and 142 ± 9.0 kPa at strains of 80-100%.

Table 5.3: *Mean Young's modulus for all lattice desings between 0-20% and 80-100% strains (n=3).*

	Amplitude (mm)	Wavelength (mm)	Low strain		High strain	
			Mean (kPa)	SD	Mean (kPa)	SD
A	1	10	17.6	1.66	37.6	2.34
B	1	4	23.7	1.45	58.9	2.49
C	1	2	30.3	1.38	75	4.74
D	1.5	2	15.1	1.74	44.9	3.34
E	2	2	12.1	0.64	30.9	1.44
Cast samples			81.1	6.26	142	9.04

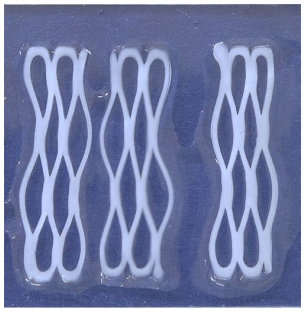

(a) *Lattice A: W = 10 mm, A = 1 mm*

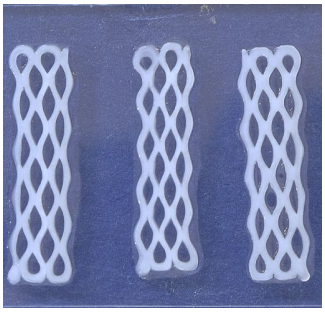

(b) *Lattice B: W = 4 mm, A = 1 mm*

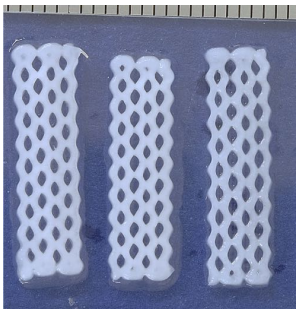

(c) *Lattice C: W = 2 mm, A = 1 mm*

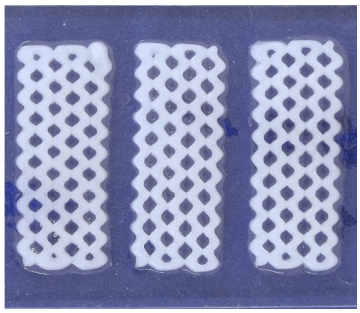

(d) *Lattice D: W = 2 mm, A = 1.5 mm*

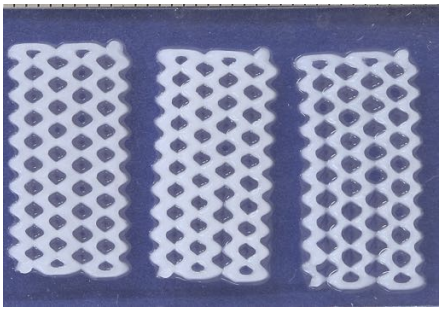

(e) *Lattice E: W = 2 mm, A = 2 mm*

Figure 5.9: *All manufactured lattice samples (A-E) prior to uniaxial testing. The height of each image is 2.5 cm.*

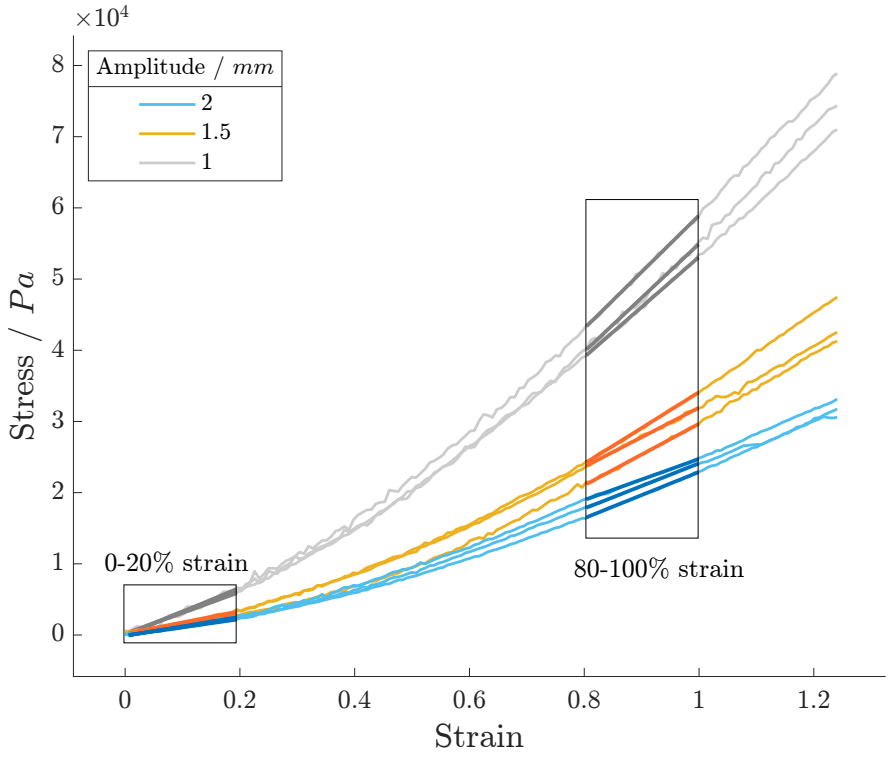

(a) *Variation in Amplitude*

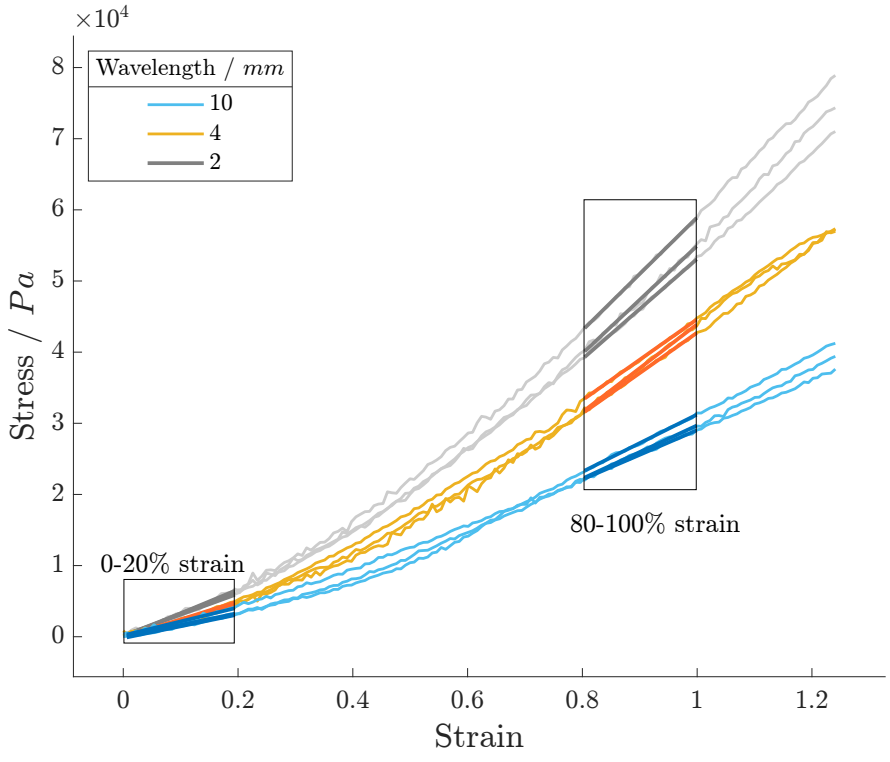

(b) *Variation in Wavelength*

Figure 5.10: *Uniaxial ramp tests of Lattices A-E, showing the effect of a variation in Amplitude (a), and Wavelength (b).*

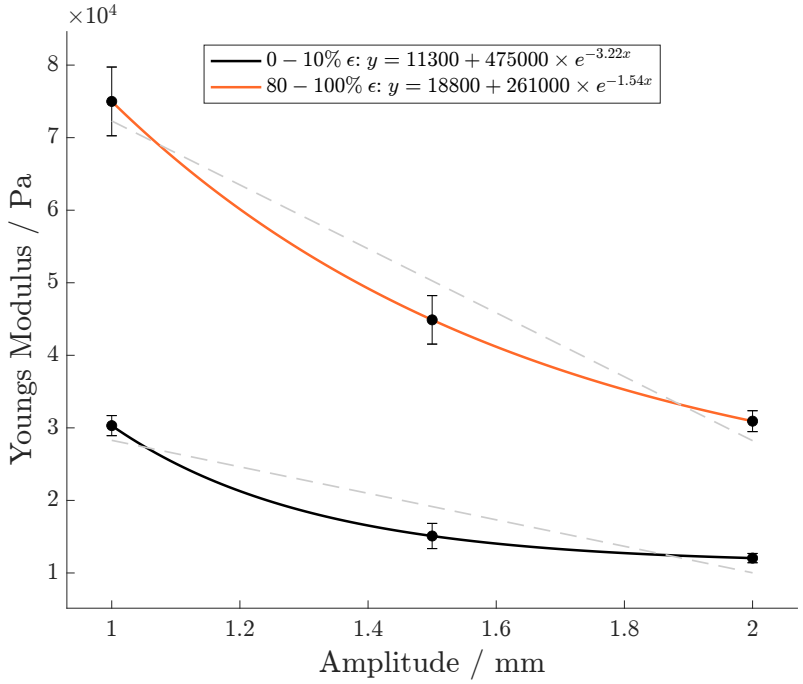

(a) *Variation in Amplitude*

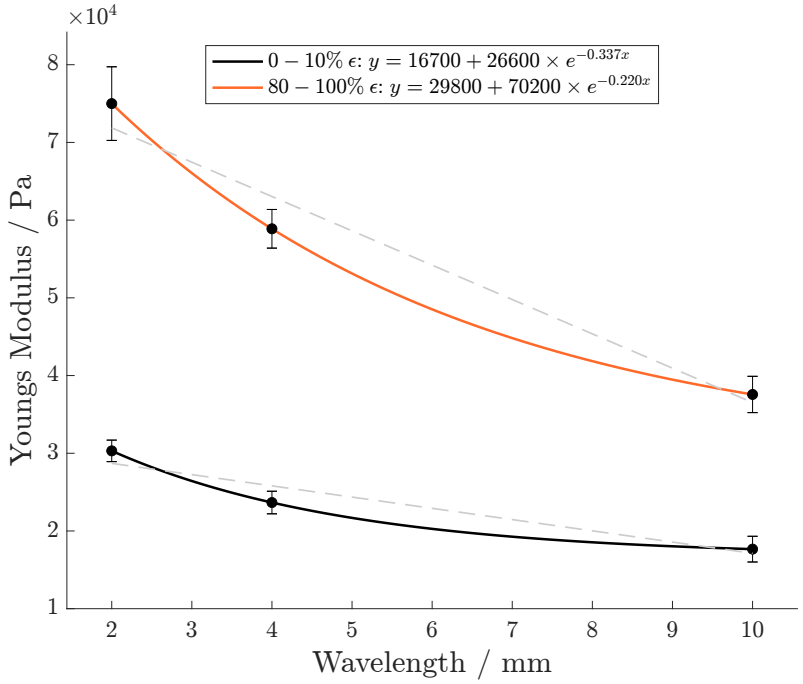

(b) *Variation in Wavelength*

Figure 5.11: *Average Youngs modulus at 0-20% and 80-100% strain for Lattices A-E, showing the effect of a variation in Amplitude (a), and Wavelength (b). Error bars show SD. (n = 3).*

A linear relationship was observed between PVA percentage and infill wavelength (Figure 5.12). An exponential regression was empirically derived for the relationship between Young's modulus and infill amplitude. Despite significantly higher density, lattices D and E showed comparatively lower Young's moduli compared to lattices A and B. A 10% reduction in PVA density resulted in a 60% drop in Young's modulus when amplitude was varied (C → E). Whereas a 40% reduction in PVA density resulting in a 45% drop in Young's modulus when wavelength was varied (C →A). Figure 5.12 is broken down to more easily observe the relationship between Young's modulus and PVA volume in figure 5.13.

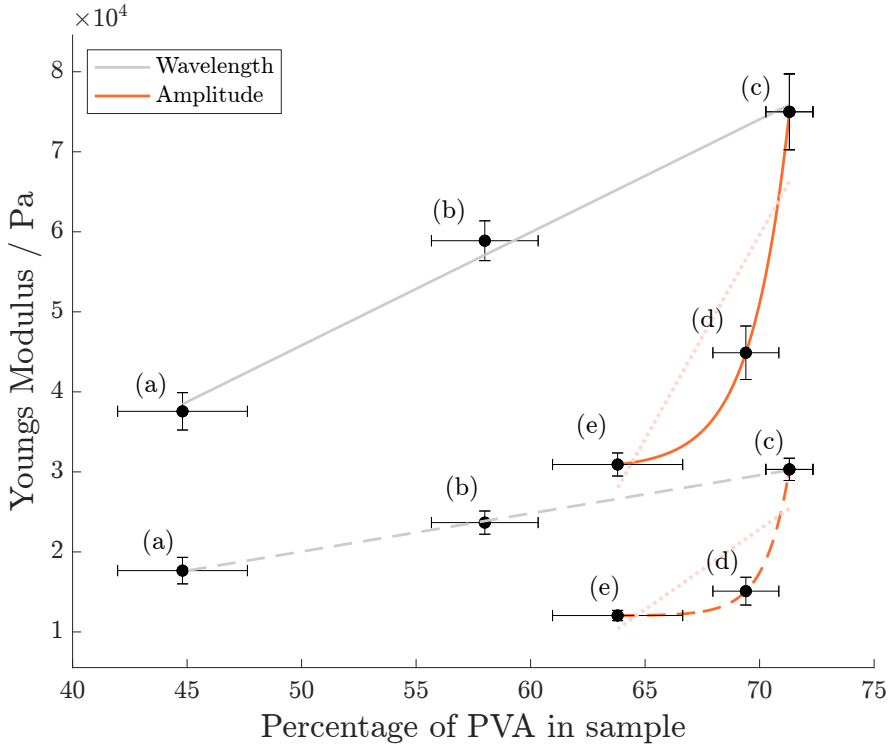

Figure 5.12: *Average Young's modulus at 0-20% (dashed) and 80-100% (solid) strain for Lattices A-E, compared against the percentage by area of PVA in the sample for variations in wavelength (grey) and amplitude (orange). Linear regression is also shown for amplitude (dotted) to mitigate over-fitting data. Lattice type is given in brackets.*

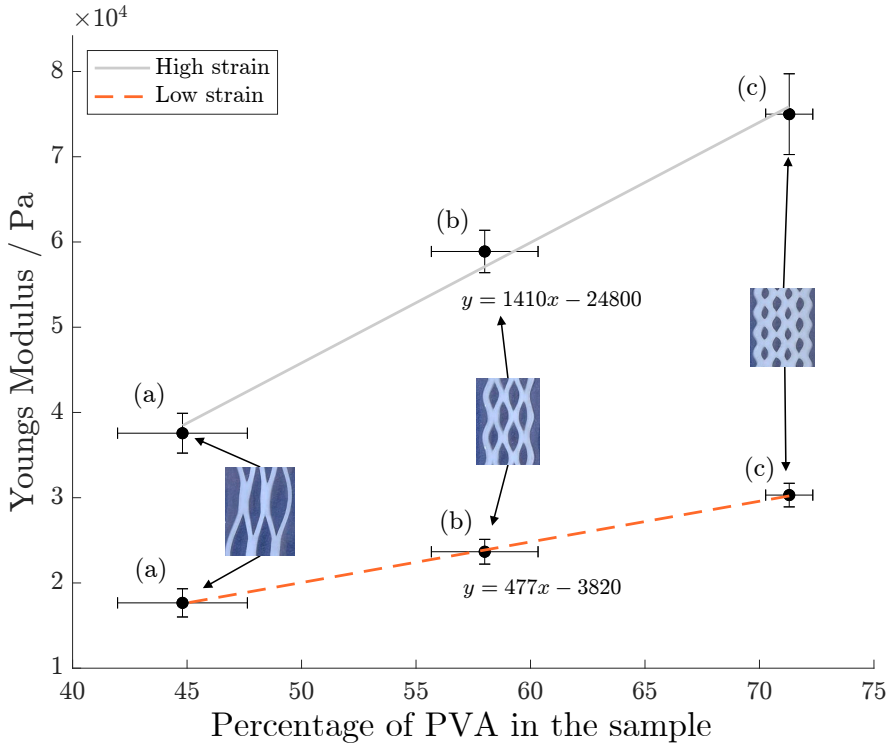

(a) *Variation in Wavelength*

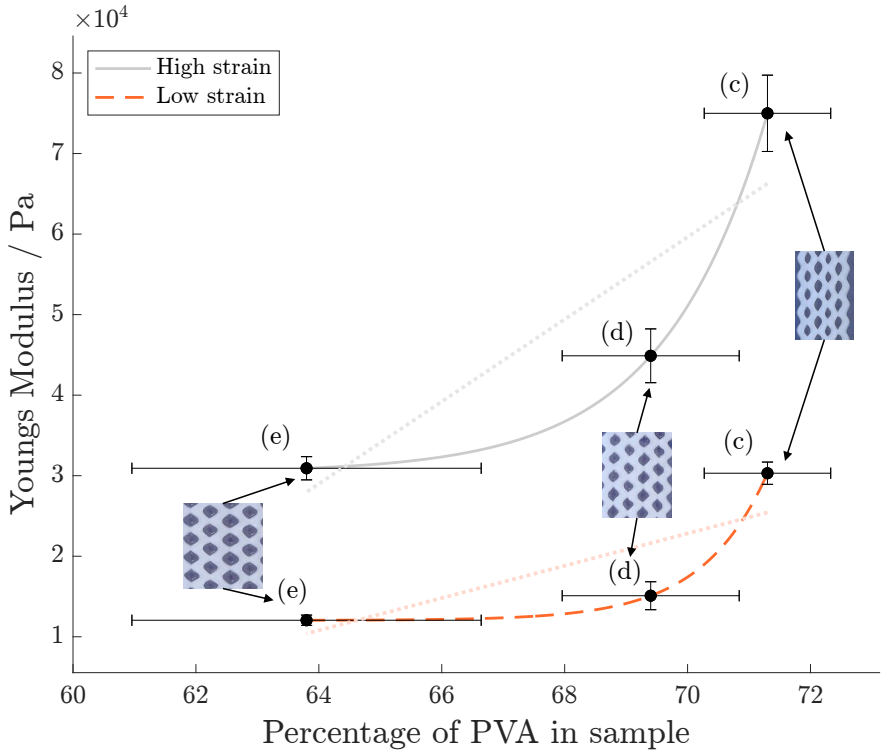

(b) *Variation in Amplitude*

Figure 5.13: *Average Young's modulus at 0-20% (dashed) and 80-100% (solid) strain for Lattices A-E, compared against the percentage by area of PVA in the sample for variations in wavelength (a) and amplitude (b).*

Similarly, a comparison was made between the infill angle with respect to the loading direction, and the Young's modulus of each lattice. It is well known that AM does not perfectly reproduce toolpaths [236]. Therefore, angles were approximated based on the sample images, and not based off of the simulated toolpaths presented in figure 5.5. Figure C.2 in appendix C illustrates the angle in each lattice. A linear relationship was seen for both a variation in wavelength and amplitude (figure 5.14). Again this figure is broken down to more easily observed the relationship between the lattice angle and Young's modulus in figure 5.15.

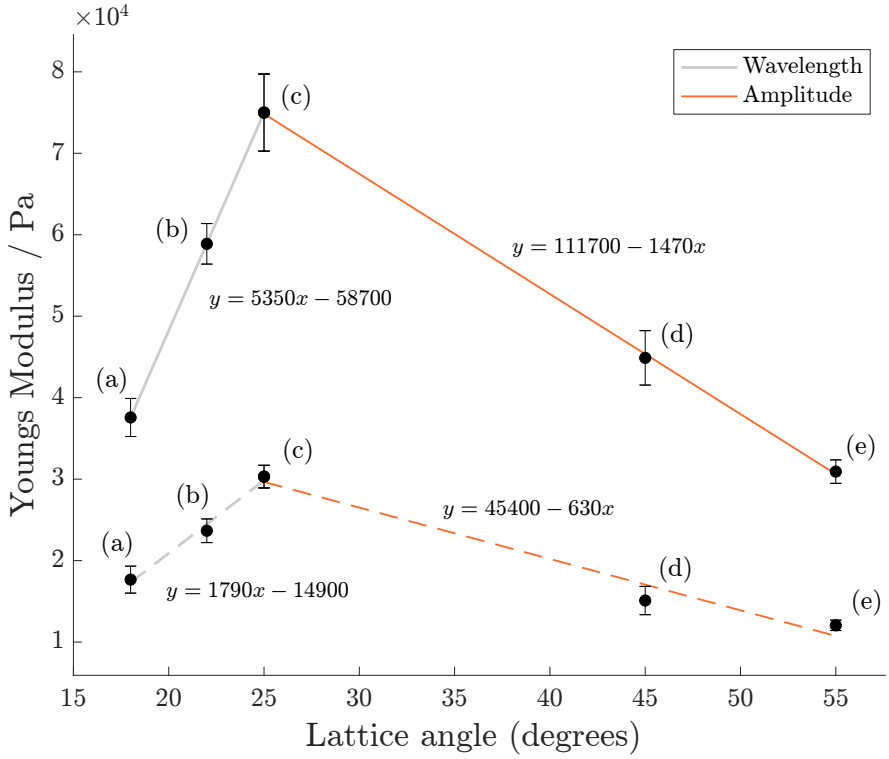

Figure 5.14: *Average Young's modulus at 0-20% (dashed) and 80-100% (solid) strain for Lattices A-E, compared against the lattice infill angle with respect to the loading direction for variations in wavelength (grey) and amplitude (orange).Lattice type is given in brackets.*

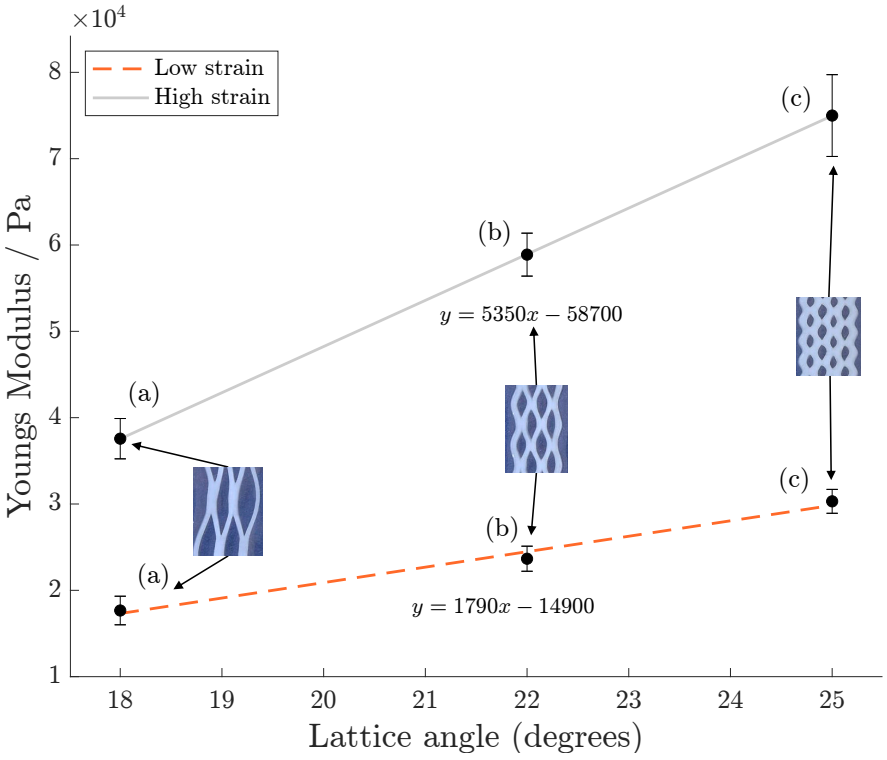

(a) *Variation in Wavelength*

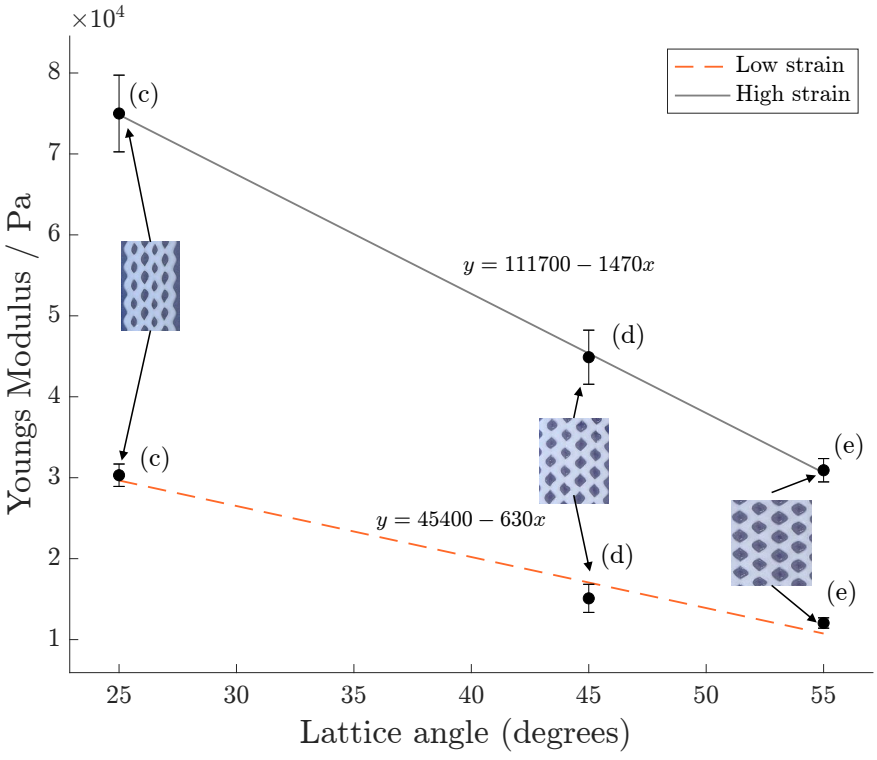

(b) *Variation in Amplitude*

Figure 5.15: *Average Young's modulus at 0-20% (dashed) and 80-100% (solid) strain for Lattices A-E, compared against the lattice infill angle with respect to the loading direction for variations in wavelength (a) and amplitude (b).*

Table 5.4: *Fitting error and stability for all samples (n = 18), for the Ogden, polynomial, and reduced polynomial models tested.*

		Fitting Error (%)		
	Order (n)	Mean	SD	Stability
Ogden	1	1.41	0.37	Stable
	2	10.2	0.25	Unstable
Polynomial	1 (Mooney-Rivilin)	1.38	0.35	Unstable
	2	1.02	0.24	Unstable
Reduced polynomial	1 (Neo-Hookean)	7.7	1.8	Stable
	3 (Yeoh)	1.12	0.31	Stable

5.3.3 Analysis of hyperelastic models

Of the six models selected in this study, three were deemed unsuitable due to instability throughout the relevant strain ranges (table 5.4). These were Ogden, n = 2, Mooney Rivelin (Poly n = 1), and Polynomial n = 2. Of the remaining three models, Yeoh was shown to have the lowest fitting error (1.12 ± 0.31 %), and was therefore chosen as the model to analyse for the rest of this study. All six hyperelastic models have been shown for a single sample of lattice C (figure 5.16) to demonstrate the fit of each model. For completeness, figures showing the analysis for all samples are shown in the appendix C (Figures C.3 - C.9). Figure 5.17 shows the Yeoh fit against the raw data of one sample per lattice, showing the variation of both lattice frequency and amplitude.

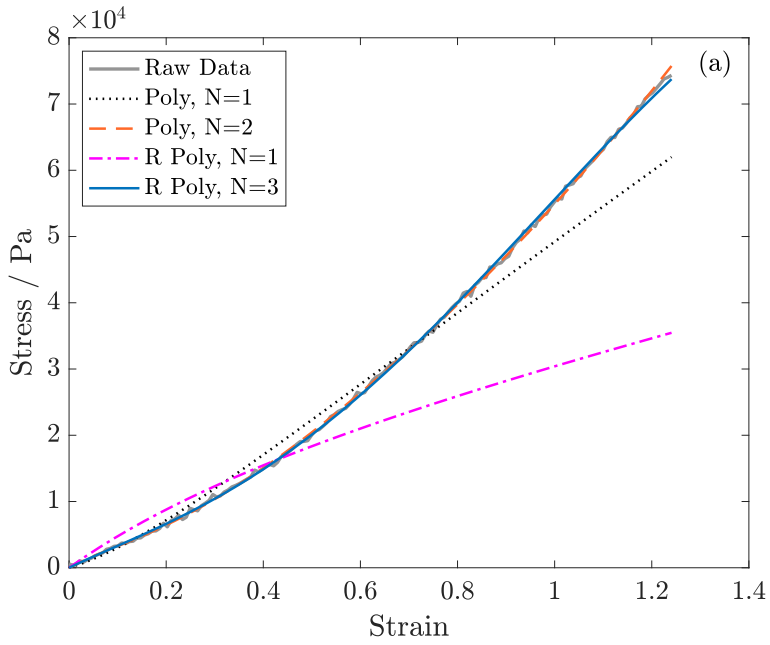

(a) *Lattice C3, Polynomial*

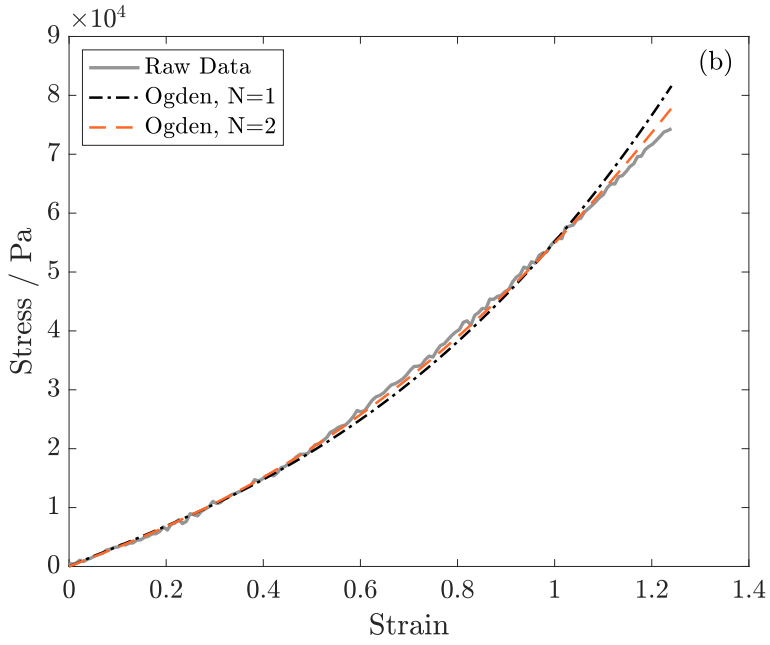

(b) *Lattice C3, Ogden*

Figure 5.16: *Polynomial and Ogden hyperelastic models for Lattice C. Where: poly, $N = 1$ is Mooney Rivilin; R poly, N=1 is neo-Hookean; and R poly, N=3 is Yeoh.*

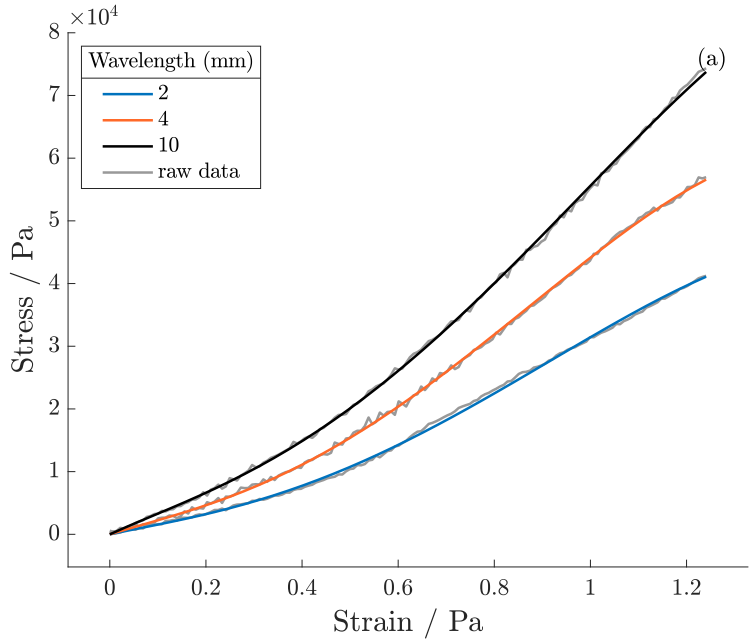

(a) *Comparison of wavelength*

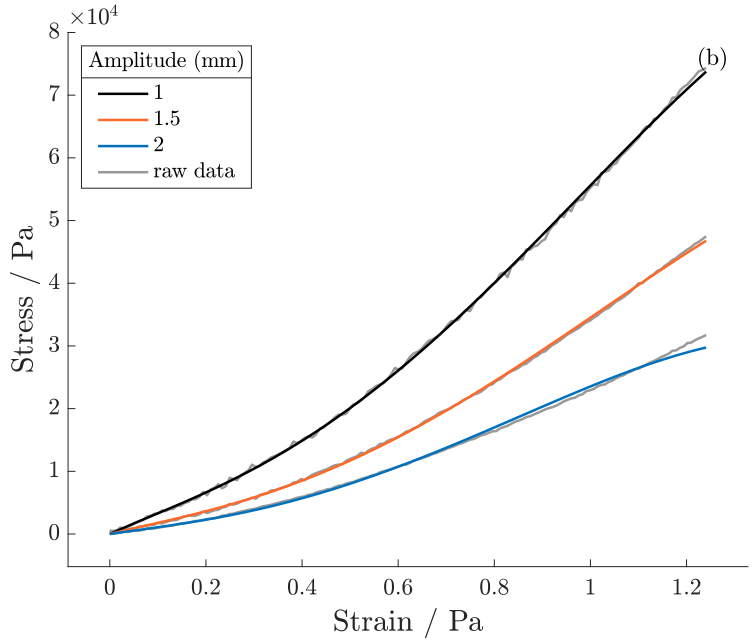

(b) *Comparison of amplitude*

Figure 5.17: *Yeoh models and raw data for 1 of each of the five lattices, showing a comparison of wavelength (a), and amplitude (b).*

Table 5.5: *Hyperelastic coefficients (median & SD) for all sample types tested (n=3).*

	$C_{(1,0)}$ Pa		$C_{(2,0)}$ Pa		$C_{(3,0)}$ Pa	
	Mean	SD	Mean	SD	Mean	SD
Lattice A	2.71	0.83	2.24	0.51	-0.223	0.10
Lattice B	4.13	0.18	3.2	0.25	-0.370	0.07
Lattice C	5.61	0.31	3.61	0.75	-0.386	0.15
Lattice D	2.56	0.40	2.24	0.39	-0.185	0.11
Lattice E	1.89	0.10	2.15	0.22	-0.287	0.052
Cast	14.3	1.5	13.0	1.4	-2.69	0.36
AM wave	10.1	2.1	6.53	1.3	-0.763	0.20

5.3.4 Analysis of Yeoh model coefficients

A significant decrease was seen in $C_{1,0}$ as amplitude was increased from 1 to 2 mm, decreasing from 5.61 $\pm$ 0.31 to 1.89 $\pm$ 0.10 kPa ($p < 0.05$)(Figure 5.18). Similarly, a decrease in $C_{1,0}$ was seen as the lattice wavelength was increased from 2 to 10 mm, decreasing from 5.61 $\pm$ 0.31 to 2.71 $\pm$ 0.83 kPa (Figure 5.18). It should be noted, that although a decrease in $C_{1,0}$ was observed between wavelengths of 4 and 10 mm (4.13 $\pm$ 0.18 $\rightarrow$ 2.71 $\pm$ 0.83 kPa), this difference was not statistically significant ($p = 0.085$). The trend for both relationships between $C_{1,0}$ was empirically shown to an exponential decay. However, as only three data points are given, a linear regression is also shown on the relevant figures, to avoid over-fitting the data.

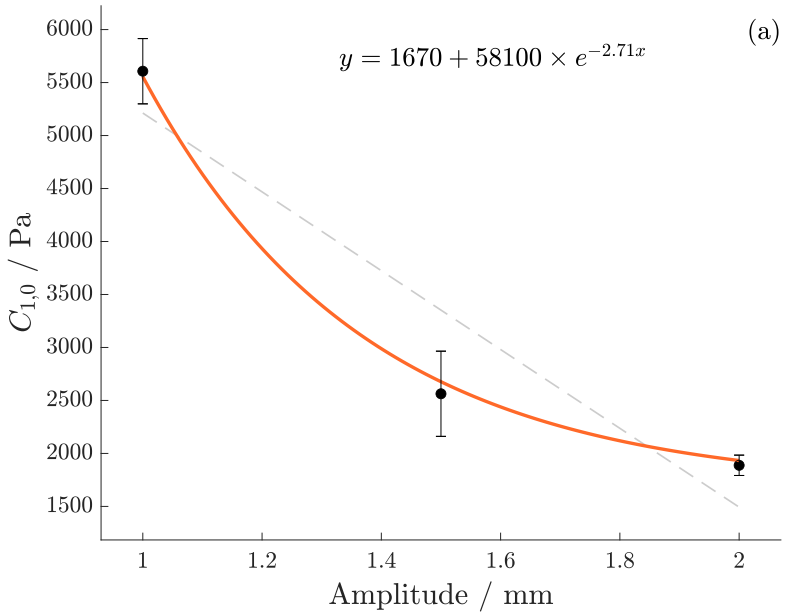

(a) *Variation in $C_{1,0}$ with amplitude*

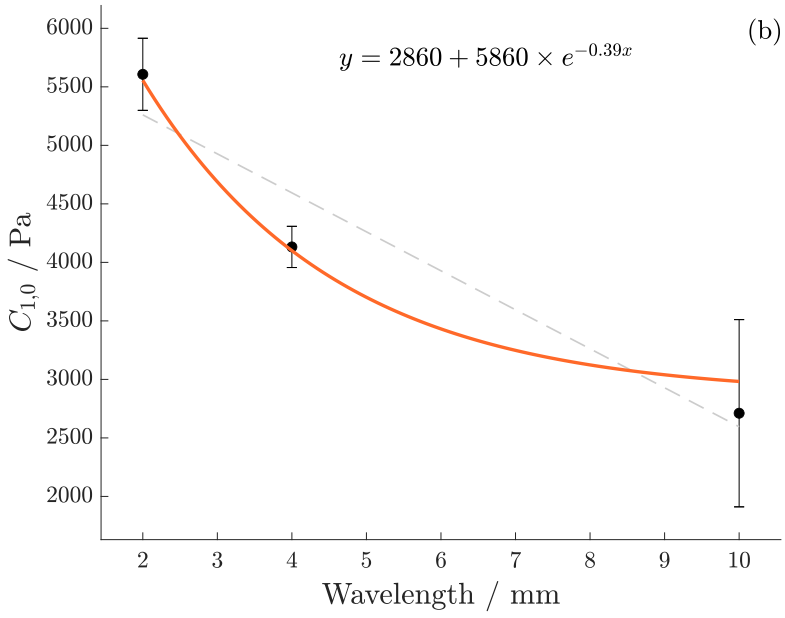

(b) *Variation in $C_{1,0}$ with frequency*

Figure 5.18: *Median and SD for $C_{1,0}$ coefficient for a Yeoh hyperelastic model (R poly, $n = 3$), showing a variation in amplitude (a) and frequency (b).*

A decrease in $C_{2,0}$ was seen as the lattice amplitude was increased from 1 to 1.5 mm, reducing from 3.61 ± 0.75 to 2.24 ± 0.39 kPa ($p = 0.03$) (Figure 5.19). However no significant difference was seen as the amplitude was increased again to 2 mm, with $C_{2,0} = 2.15 \pm 0.22$ kPa ($p = 0.35$). A decrease in $C_{2,0}$ was observed as the lattice frequency was increased from 2 to 10 mm, decreasing from 3.61 ± 0.75 to 2.24 ± 0.51 kPa (Figure 5.19), although it was not significant from $2 \rightarrow 4$ mm ($p = 0.25$).

The values for $C_{3,0}$ were negative for all samples, and an order of magnitude smaller than both $C_{1,0}$ and $C_{2,0}$. No significant trend was seen between $C_{3,0}$ as either lattice wavelength or amplitude were varied ($p > 0.05$), therefore no line of best fit was empirically derived for either relationship (table 5.5).

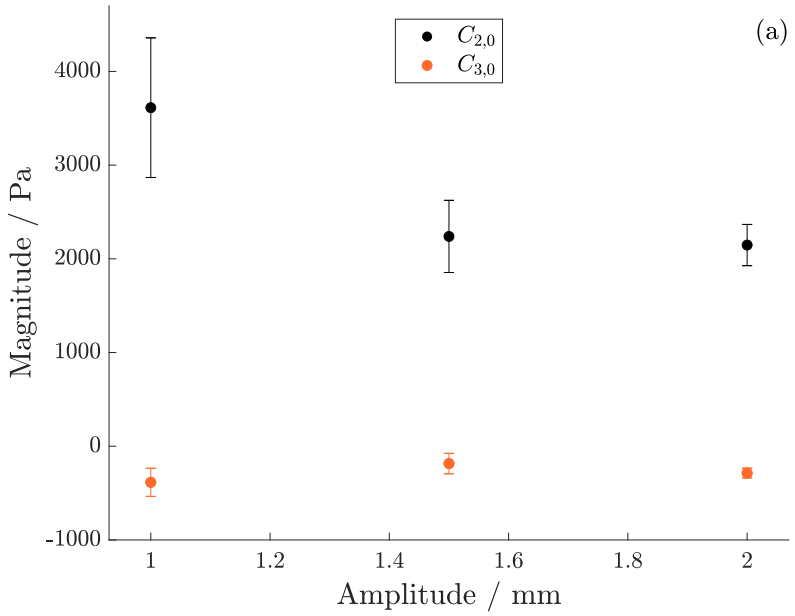

(a) *Variation in $C_{2,0}$ & $C_{3,0}$ with amplitude*

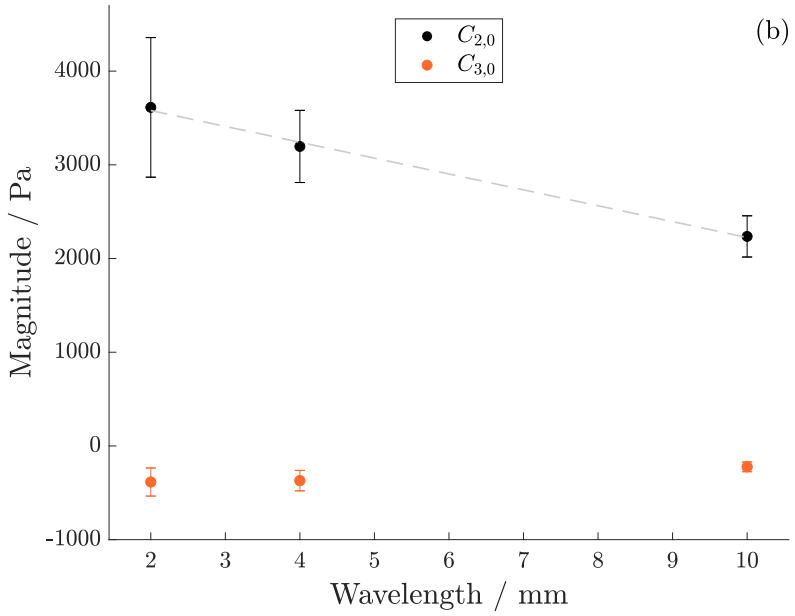

(b) *Variation in $C_{2,0}$ & $C_{3,0}$ with wavelength*

Figure 5.19: *Median and SD for $C_{2,0}$ & $C_{3,0}$ coefficients for a Yeoh hyperelastic model (R poly, $n = 3$), showing a variation in amplitude and wavelength.*

5.3.5 Functionally graded lattices

To demonstrate "proof-of-concept" FGAM, samples with a varying wavelength were successfully manufactured using a Cellink Inkredible+ bioprinter (Figure 5.20). Based on the results shown in section 5.3.2, these samples should theoretically exhibit functionally graded mechanical properties. Using the data collected in this study, it is possible to plot the theoretical change in Young's modulus along the length of these samples (Figure 5.21). This demonstrates that a linear change in wavelength between 2 and 10 *mm* (Figure 5.20a), should result in a quadratic relationship between the sample length and Young's modulus (Figure 5.21a. Similarly, a parabolic change in wavelength with minimum and maximum wavelengths of 2 and 10 *mm* respectively 5.20b), should result in a 4^{th} order polynomial relationship between the sample length and Young's modulus 5.21b.

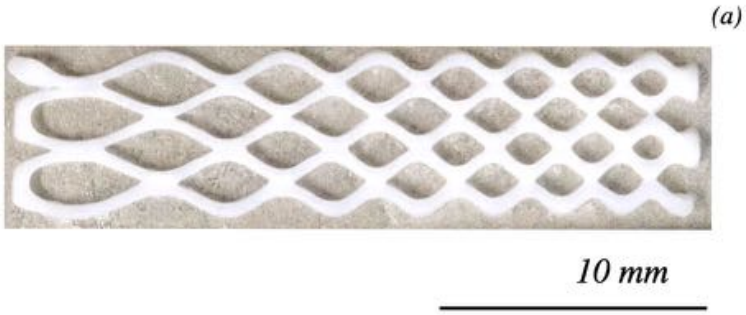

(a) *Sample with frequency defined by linear function*

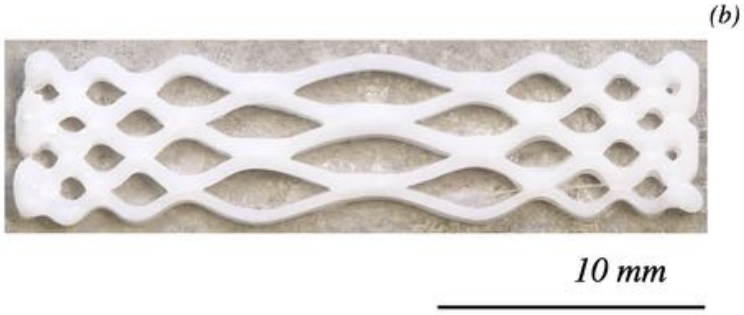

(b) *Sample with frequency defined by polynomial equation*

Figure 5.20: *Images showing two samples manufactured with a custom toolpath, varying the toolpath frequency linearly (a), or parabolically (b).*

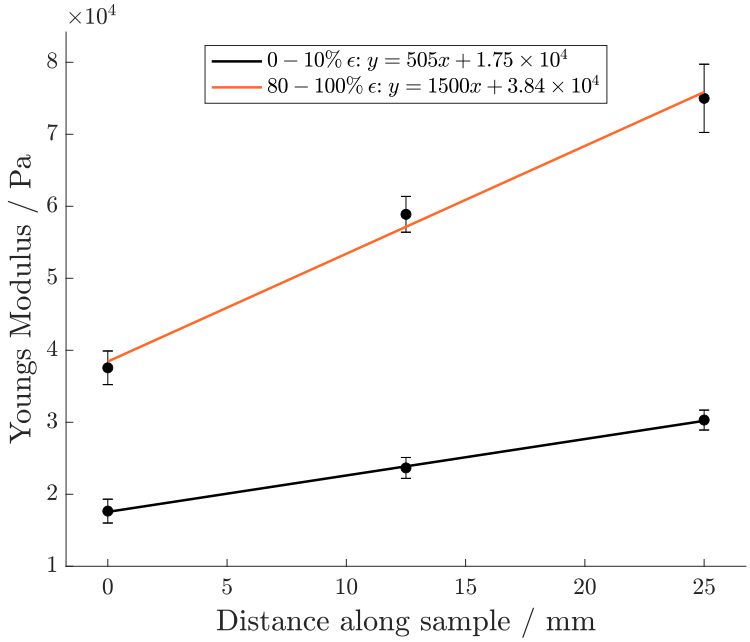

(a) *Sample with frequency defined by linear function*

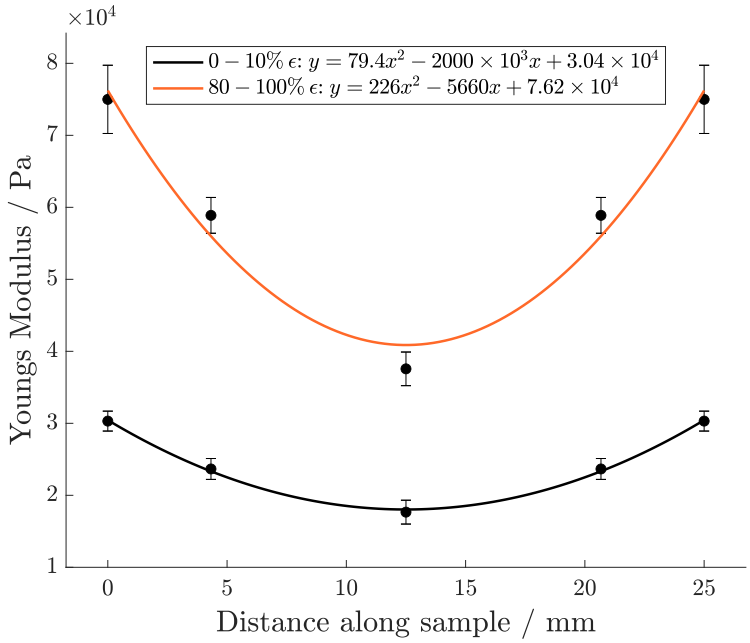

(b) *Sample with frequency defined by polynomial equation*

Figure 5.21: *Hypothetical variation in average Young's modulus for previous samples (a) and (b) between 0-20% strain, based on experimental data presented in this chapter.*

5.4 Discussion

This chapter has explored the ability to further vary the mechanical properties of additively manufactured PVA by utilising and varying parameters of a sine wave toolpath. It has also shown this methods potential to manufacture functionally graded PVA constructs using a single composition of PVA. A sine wave shaped toolpath was used to alter infill density, whilst meeting the requirement of having a constant filament of PVA in the direction of loading. This mitigates the inherent weakness between PVA filaments that may result in premature failure, and has shown that an increase in both the wavelength and amplitude of the sine wave results in a less stiff material.

5.4.1 Discussion of preliminary results

Initially, AM constructs with a sine wave shaped toolpath and a 100% infill were tested. This preliminary test was performed to understand whether the AM toolpath, could be used to change the mechanical behaviour of the resulting construct. Both the macro alignment of PVA filament and inherent weaknesses between PVA filaments have been shown in chapter 4, to have an impact on the mechanical behaviour of AM PVA. This could allow the tailoring of the relationship between stress and strain of AM PVA to closer represent the connective tissue in question. For example, it could be used to replicate and control the 'J' shaped curve seen for connective tissues under uniaxial tension [17, 18]. Promising results were presented, with a comparison of the Young's modulus showing that the AM samples were less stiff at low strains ($52.6 \pm 3.2\ kPa$ vs $90.0 \pm 6.3\ kPa$), yet showed no statistically significant difference at high strains ($p = 0.19$). This implies that the AM samples exhibited a more 'J' shaped response compared to cast samples. This difference in non-linearity is further reinforced when comparing the hyperelastic coefficients for both materials, where a

significant difference between $C_{1,0}$, $C_{2,0}$, and $C_{3,0}$ were seen, implying differences in the hyperelastic properties of PVA. The stress observed in AM samples was lower when compared to cast samples. This can be attributed to the lower stiffness seen at low strains, and based on the results of chapter 4 the author hypothesises is due to the weak boundaries between filaments being initially more orthogonal to the loading condition. As the sample is tensed, the sine wave will straighten, meaning these weak boundaries will become more parallel to the load. Therefore, the weak boundaries between filaments will become less of a component in dictating material stiffness.

Ultimately, this line of testing was not continued due to issues with the repeatability of manufacturing AM PVA constructs with a sine wave toolpath. Due to the small inconsistencies in the filament diameter within one sample, and the high viscosity of PVA, replicating geometry using a constantly changing infill resulted in frequent printing defects, most commonly holes between filament strands. These issues with have been previously reported with the additive manufacture of other hydrogels, including PVA, and solving them is ongoing research [236]. Therefore, the promising results reported here may be followed up in in future research as AM of PVA improves, with testing of a wide variety of wave parameters required in order to understand the impact of the toolpath on the hyperelastic properties of AM PVA with 100% infill.

5.4.2 The development of a method to functionally grade AM PVA

A reduction in infill density was shown to correlate with a decrease in mechanical stiffness, with all samples tested reporting lower Young's moduli values than the cast control samples. This is in agreement with literature, where infill density is commonly used to reduce material stiffness, or optimise the strength to weight ratio of the material [124, 238]. However, in this chapter it was found that for the AM of PVA, the

method by which the infill density of the lattice is varied has a clear impact on the relationship observed. A linear relationship was observed between infill density and Young's modulus at both low and high strain rates when the wavelength was varied, implying that the reduction in stiffness seen is greatly influenced by a reduction in volume of PVA in the sample 5.13a.

Conversely, although an increase in amplitude also resulted in a decrease in density, and therefore a decrease in the stiffness of the PVA lattice, this was seen to be a significantly more non-linear relationship 5.13b. A 1.9% decrease in infill density resulting in a 50% decrease in Young's modulus at both low and high strains when the amplitude was increased from 1 to 1.5 mm (lattice C $\rightarrow$ D). A further 10% decrease in Young's modulus was seen at an amplitude of 2 mm, with a respective decrease in infill density of 5.6% (lattice D $\rightarrow$ E). However, it should be noted that the difference in Young's modulus between 1.5 and 2 mm was only significant at high strains. It is hypothesised that for these samples at low strains, the driving factor in material stiffness is the alignment of the filament to the loading direction. Therefore at low strains both lattices exhibit similarly low mechanical stiffness. At higher strains, the filament in lattice D (amplitude of 1.5 mm) will align to the direction of loading quicker, reinforcing the material and explaining the resulting higher stiffness.

The impact of different infill parameters can be further evaluated by comparing lattices B and E, with these two lattices exhibiting very similar infill densities of $58 \pm 2.3\%$ and $63 \pm 2.8\%$ respectively. However, different sine wave parameters were used for both, with lattice B manufactured with a wavelength of 4 mm and amplitude of 1 mm, and lattice E with a wavelength of 2 mm and amplitude of 2 mm. This provides the opportunity to isolate the impact of the only the infill parameters, showing a significant difference between the stiffness of both, with Young's moduli of $23.8 \pm 1.4\ kPa$ and $12 \pm 0.64\ kPa$ at low strains and $58.9 \pm 2.5\ kPa$ and $30.9 \pm 1.4\ kPa$ at high strains for B and E respectively. Similarly, a comparison can be made between lattice A and

lattices D and E. Again these lattices have very different infill properties, with lattice A manufactured with a wavelength of 10 and amplitude of 1, lattice D with a wavelength of 2 and amplitude of 1.5, and E with a wavelength of 2 mm and amplitude of 2 mm. In this case, these lattices exhibit a large difference in infill density, with densities of $44.9 \pm 2.8\%$, $69.4 \pm 1.9\%$, and $63 \pm 2.8\%$ respectively; however, despite having a lower infill density, lattice A was shown to have similar stiffness than both lattices D and E, with a Young's modulus of $17.6 \pm 1.6kPa$ at low strains and $37.6 \pm 2.3\ kPa$ at high strains compared to $15.0 \pm 1.4\ kPa$ and $44.9 \pm 3.3\ kPa$ measured for lattice D and $12 \pm 0.64\ kPa$ and $30.9 \pm 1.4\ kPa$ for lattice E.

This reinforces the hypothesis that differences noted in the mechanical behaviour of AM PVA lattices is not solely influenced by the volume of PVA within the sample, but by other mechanisms impacting the mechanical behaviour of AM PVA. The author hypothesises that the resulting mechanical behaviour of AM PVA is a function of both the density of the lattice, and the directionality of the filament with respect to the loading condition, which was shown to be directly proportional to the mechanical stiffness of the material when both amplitude and wavelength were varied (Figure 5.14). This aids in explaining the significant decrease in Young's modulus of $\approx 60\%$ when the sine wave amplitude is increased from 1 to 2 mm, despite a significantly smaller decrease in PVA density of 7.5%, as well as the striking difference between lattice A and lattices D and E, which show the extremes of the parameters explored in this study. In this case a key difference between the lattices is the filament alignment, with lattice A showing significantly greater alignment compared to D and E (Figure C.2 in appendix C). This reinforces the hypothesis that filament alignment impacts the mechanical strength of AM PVA, with alignment with the the loading direction resulting in an increase in mechanical stiffness, and is in agreement with the findings of chapter 4.

Functionally graded PVA has previously been manufactured [232, 148]. Wahab *et*

al. was achieved this by casting two different compositions of PVA in a mould with a divider [232]. The sample then underwent a short pre-processing freeze-thaw cycle, before the divider was removed to allow the two compositions to diffuse. Although this process successfully created a functionally graded construct, several limitations of this method are clear, with this methodology unlikely to be transferable to more intricate geometries and grading, for example models where it is required for material properties to vary in multiple axes. The process of diffusion between different compositions is likely complicated, with variables such as concentration, MW, and the length and temperature of pre-processing FTCs all being factors which may affect it, resulting in difficulty controlling the rate at which properties will vary across the material. It should also be noted that Wahab *et al.* did not perform tensile tests to assess the strength of the boundary between PVA compositions. Meng *et al.* manufactured graded structures using AM, varying the infill density of PVA [148]. In this case only uniaxial compression of the structure was performed, therefore not fully quantifying the effect of changing porosity. This chapter has provided an alternative to achieve the functional grading of PVA, by using AM to allow for a method to quantify not only the change in material properties, but also control over the gradient which this occurs.

Previous studies have shown PVA cryogels to be hyperelastic under both compression and tension [239, 36]. Therefore, in order to obtain a complete picture of the impact of infill parameters on the uniaxial testing of AM PVA, several phenomenological hyperelastic models were constitutively fit to the data, with the Yeoh model resulting in the best fit of all the samples tested. As with data for Young's moduli, section 5.3.4 describes the relationship seen between infill parameters and $C_{1,0}$, $C_{2,0}$, and $C_{3,0}$. It should be noted that, although the three coefficients of the Yeoh model relate to the shear behaviour of a material, more practically speaking $C_{2,0}$ and $C_{3,0}$ alter the localised gradient at a given strain rate [183]. Therefore, these coefficients describe the stress & strain relationship over the strain ranges tested, and how this relationship alters as infill parameters are varied. This study has demonstrated the

potential to calculate the infill parameters required to best estimate the hyperelastic properties of a connective tissue, if hyperelastic coefficients have been measured for the tissue. It should be noted that there is uncertainty in the trends presented, due to: only one mode of deformation has been studied; the assumed incompressibility of the material; the small sample size ($n = 3$); and the fact that hyperelastic models only provide an approximation of material behaviour. This study has shown the potential for a correlation to be made between the wavelength and amplitude of a sine wave tool path, and the resulting hyperelastic material response, however more data points are likely needed to fully assess and confirm the relationships suggested.

The anisotropy present in additively manufactured PVA will impact the way in which AM can be used as a manufacturing method for biomedical devices and implants. In some cases this can be used as an advantage in order to tailor the orthotropic properties of PVA to further match that of connective tissues, for example the layers of the arterial wall [20, 240]. However, it must therefore also be taken into account when AM is used to manufacture homogeneous materials, or materials that may be under high strains, where bonds between filament strands may cause stress concentrations, and premature sample failure. Importantly, the bulk properties of PVA do not necessarily match the properties of AM PVA, with AM PVA being shown exhibit orthotropic behaviour [199]. This means that design for additive manufacture must be carefully planned in order to avoid any potential failure of an implant or device. As well as illustrating the impact of the infill dimensions of the AM PVA, this study has produced a novel, equation driven approach for the manufacture of functionally graded PVA using AM, which allows for a constant filament along the length of sample to reduce the likelihood of failure in the required direction.

This gives the potential to manufacture implants, medical devices, and phantoms with functionally graded material properties, both along the length and between the layers of the construct. This allows the ability to better mimic the changes of mechan-

ical behaviour of connective tissues, for example when modelling an atherosclerotic plaque, by varying the mechanical properties along the length of a sample in order to manufacture a region of increased stiffness. Alternatively, when changing the material properties between the layers of the construct in order to mimic the differences in mechanical stiffness of the intima, media, and adventitia in the arterial wall.

5.4.3 Conclusion

This chapter has described and validated the development of a novel parametric AM design process, tailored specifically for PVA. This has allowed for the additive manufacture of hyperelastic functionally graded PVA constructs, taking into account the specific design constraints present with sub-zero AM. The contribution of this methodology to the field of PVA AM, allows for the future potential to incorporate tuned, functionally graded properties, allowing closer replication of specific CTs. However, the results of this study could impact broader applications, as it has also proven the ability to control hyperelasticity of a material by adjusting the AM toolpath, a concept which could be applied to other materials in the future. To summarise, this study has:

- Presented successful method to generate G-code with parametrically defined changes in infill density and filament alignment through amplitude and wavelength, allowing the manufacture of functionally graded PVA constructs from a single composition.
- Shown an increase in the amplitude and wavelength of the sine wave reduces the stiffness of AM PVA.
- Shown sample density is not always linearly related to mechanical behaviour.
- Shown filament alignment was a key factor in determining mechanical behaviour.

Chapter 6

GENERAL DISCUSSION

6.1 Thesis summary

The aim of this thesis was to explore the characterisation, advanced design and manufacturing of PVA cryogel as a physical model for connective tissue. It has achieved this by analysing the impact of composition changes of PVA on its mechanical behaviour and MR properties; as well as exploring the potential to use novel AM techniques to introduce and control complex orthotropic viscoelastic and hyperelastic mechanical behaviour. This thesis has therefore furthered the understanding of the viscoelastic and hyperelastic mechanical behaviour of PVA, allowing for more informed material and design choices when it is used as a physical model of connective tissue, as well as outlining a framework for the additive manufacture of functionally graded PVA constructs.

The objectives of this thesis were met as follows:

- The dynamic viscoelastic properties of PVA were quantitatively characterised, showing the impact of concentration, MW and FTC. The impact of these pa-

rameters on T_2 relaxation time was also characterised, and correlation between viscoelastic properties and T_2 relaxation time was shown.

- A sub-zero AM platform was developed to allow the additive manufacture of PVA, with the PVA solution freezing on contact with the print bed to facilitate the retention of geometry. The orthotropic properties of AM PVA was shown for the first time.

- A novel approach to alter the stiffness of AM PVA by allowing the infill of the material to be defined by a parametric function, and the impact of the input parameters of material stiffness an hyperelasticity was assessed.

Chapter 3 explored the dynamic viscoelastic properties of PVA cryogel, contributing a comprehensive assessment of the viscoelastic behaviour of PVA to the current understanding of the mechanical behaviour of PVA. Key results show, in general, that an increase in concentration, MW, and the number of FTCs resulted in a significant increase in both storage and loss modulus, where only 15 $\rightarrow$ 20% concentration PVA-C showing no significant increase in loss moduli (See section 3.2.1 for a description of the PVA compositions). This gives a more complete understanding of the viscoelastic behaviour of PVA under physiologically relevant loading conditions, allowing the decision process when defining PVA compositional parameters to be optimised. The same compositions were also characterised using MRI, and linear relationships between concentration and T_2 relaxation time were seen for all three compositions assessed 3.3.2. This allowed for novel analysis of the causal relationship between viscoelastic mechanical properties and T_2 relaxation time, showing the potential for non-invasive imaging techniques to assess the mechanical properties of implants or tissue scaffolds.

Additive manufacture poses a significant advantage for the manufacture of biomedical devices, allowing for cost effective production of patient specific implants, or the rapid prototyping of phantoms or scaffolds. Chapter 4 successfully developed a sub-

zero AM platform for hydrogels, and has quantitatively assessed the difference in the dynamic viscoelastic properties between cast and AM PVA. The contribution of this comprehensive analysis of AM process parameters is crucial to understanding and further developing the AM process to manufacture complex material properties. It was shown that AM PVA is orthotropic, with its anisotropy dependant on the nozzle diameter (section 4.3.1). This anisotropy is inherent to the manufacturing process, and must be taken into account when designing for AM. It was hypothesised that the anisotropy present, was most likely caused by shear thinning of the polymer during extrusion, and weak molecular interactions between the PVA filament strands. This fundamentally proves the ability of AM to repeatably introduce anisotropic behaviour without the need for complex pre- or post-processing of the material, leading to the potential to better replicate the fibre-reinforced, anisotropic nature of CT.

Finally, a novel parametric approach to additively manufacture functionally graded PVA was achieved in chapter 5. The method chosen to do this was by defining a sine wave shaped toolpath with user controllable amplitude and wavelength. The contribution of this methodology to the field of PVA AM, allows for the future potential to incorporate tuned, functionally graded properties, allowing closer replication of specific CTs. This process was validated by manufacturing and testing five lattices with different input parameters, showing that an increase in both the wavelength and amplitude of the sine wave resulted in a decrease in stiffness (section 5.3.2). The density and filament alignment was also analysed, and it was observed that both showed a strong relationship with stiffness, with a decrease in the volume of PVA in the sample relating to a decrease in stiffness. Most importantly, the relationship between alignment with the loading condition and mechanical stiffness was shown to be linear.

The novel parametric CAM methodology developed for this thesis, also allows the control of both the amplitude and wavelength of the sine wave to be varied during the manufacture of the construct through a user-defined parametric function. This leads

to the exciting potential to accurately control the mechanical properties of complex additively manufactured geometries. The direction of this area of research is further discussed in section 6.2.

6.2 Limitations and future perspectives

Throughout this thesis the compositional and process-dependant material properties of PVA have been explored, working towards the goal to better replicate the mechanical behaviour of CT. It should be noted that the focus of this thesis was not to determine the 'ideal' compositional parameters of PVA required to replicate a particular CT. Rather the focus has been to systematically analyse key parameters, composition or process related, that contribute to the material properties of the resulting structure, and in turn the body of understanding of PVA.

Chapter 3 has evaluated the viscoelastic properties of PVA for the first time, and has shown the impact of key compositional properties on mechanical behaviour and T_2 relaxation of the material. It is clear that it has not studied an exhaustive list of compositional parameters, but due to its systematic approach, it has highlighted key areas of interest for future work. For example it was discussed in section 3.4 that the materials manufactured in this thesis were in the order of less stiff CTs [141]. It has also shown that the relationship between dissipation of energy (quantified by the loss modulus) and concentration is not the same for all compositions (figure 3.6), and therefore that you cannot extrapolate the viscoelastic response of a stiffer composition of PVA based on the results presented here. Despite this, the results presented in chapter 3 are still valid for comparing to less stiff CTs, and the finding that water content does not always correspond to the dissipation of energy is a key finding in itself. This gives rise to an important potential area of future research: the viscoelastic properties of stiffer compositions of PVA. An increase in concentration, MW or FTC

results in the restriction of water trapped within the lattice structure [37]. It was hypothesised that this restriction inhibits the dissipation of energy in PVA, and it may therefore be the case that stiffer compositions of PVA, in the order of magnitude of stiffer CT, may not see a proportional increase in its ability to dissipate energy, which may be undesirable. Taking into account the AM of PVA, where higher viscosities resulting from higher concentration or MW, may become difficult to extrude, the best method to increase stiffness may be to increase the number of FTCs. In this case the use of imaging techniques such as MRI may prove useful to assess the heterogeneity of PVA, as an increase in FTCs has been shown to increase the disparity between polymer-rich and polymer-poor regions.

This thesis has outlined a framework and methodology that uses sub-zero AM to introduce orthotropic and functionally graded behaviour into PVA. In order to move this work forward to the eventual goal of systemically defining the required compositional and manufacturing parameters to replicate a specific CT, future projects further exploring and refining the AM methods presented in chapters 4 and 5 could be undertaken.

Chapter 4 demonstrates the feasibility of controlling the anisotropy of PVA through AM process parameters. The results presented in section 4.3.1 have empirically shown a difference in viscoelastic behaviour between nozzle sizes in the parallel orientation. Polymer alignment caused by the shear thinning of extruded PVA has been hypothesised to explain this finding, however this cannot be confirmed within the scope of this study. The novel finding that small nozzle sizes result in stiffer material properties is still valid, as it was empirically shown through mechanical testing. This finding is useful in itself, as it helps understand to the effect of the AM process on the mechanical behaviour of PVA. However, understanding the physical process behind this finding finding will provide additional information on the to further the current understanding of PVA AM. This limitation could be addressed through analysis of the

rheological properties of the PVA composition used was beyond the scope of this work. The rheological behaviour of aqueous PVA solutions has been shown to vary depending on the concentration of PVA used [241], meaning the relationship between the shear rate and subsequent viscosity of the solution is dependant on compositional parameters [241]. This means the impact of pressure (and therefore shear rate) on the shear thinning properties of PVA cannot be inferred from literature. Future empirical work could focus on further exploring this relationship by testing significantly more nozzle sizes, allowing for a relationship between nozzle size and mechanical behaviour to be calculated. As the entanglement of polymer chains will quickly return after PVA solution has been extruded [213], the use of imaging techniques such as SEM may also give quantifiable insight into the polymeric structure of PVA hydrogels manufactured from AM. Alternatively mathematical research could be used to define this relationship analytically [234, 235]. Despite this limitation, chapter 4 has demonstrated the bio-inspired principle of introducing orthotropy into AM PVA through control of filament alignment, where future empirical testing and work analysing the micro-structure of AM PVA may allow further analogies to be drawn between the fibre reinforcement of collagen, and the role of the structure of AM PVA on its mechanical behaviour.

Chapter 5 has presented a CAM program aimed at manufacturing functionally graded constructs, defined by a parametric function. As this work has characterised the effect of the current input parameters to the program (the amplitude and wave length of the toolpath), it is possible to evaluate the relationship between the these parameters and the mechanical behaviour of the resulting construct, as presented in section 5.3.2. In future this could allow for the required stiffness, or hyperelastic coefficients of a known material or connective tissue to be the inputs of the parametric function, allowing for the manufacture of an biomedical device with tailored mechanical properties. Curve fitting would then allow the required toolpath parameters to be estimated and the corresponding G-code created. This would then become an optimisation problem, as this study has shown there are different combinations of input

parameters that will achieve similar resulting mechanical properties. Other conditions pertinent to the desired output could be factored in, for example desired anisotropy or density of the material, and other design constraints that may impact the outcome.

A qualitative assessment of the orthotropic behaviour of the AM lattices was made with lattice A showing negligible strength normal to the filament direction. Qualitatively, in some instances, the surface tension of water was seen to pull the filament strands together, closing the pores within the sample. Lattice B was also qualitatively assessed orthogonally to be less stiff than lattices C - E. Due to the evidence described in chapter 4 showing the anisotropy of AM PVA (Figures 4.5 and 4.6), and the evidence shown in this chapter implicating that directionality of the filament impacts mechanical behaviour (Figure 5.14, the author hypothesises that non-linear relationships may also be present in the mechanical properties of these lattices when tested perpendicular to the loading conditions described. For example despite being significantly stiffer in this study, lattice A is likely significantly weaker than lattices D and E when tested perpendicular to this, due both to the filament alignment relative to the loading direction, and the considerably interactions between the filament strands within a given area of the samples. It should be noted that, regardless of this hypothesis, all the lattices tested in this study are likely to exhibit orthotropic behaviour due to the inherent weakness between filament strands described and explained in chapter 4.

Another key limitation of the study presented in chapter 5, is the uncertainty in some trends presented with respect to the hyperelastic response of the lattices. This is due to: only one mode of deformation has been studied; the assumed incompressibility of the material; the small sample size (n = 3); and the fact that hyperelastic models only provide an ap- proximation of material behaviour. However, despite these uncertainties the key finding from this study is still valid: the results presented in chapter 5 have proven the feasibility of using a parametrically controlled toolpath to control the mechanical properties of AM PVA.

In order for this work to progress, it is therefore important to improve the statistical significance of the results. This could be achieved by increasing the number of infill parameters and sample numbers, as well as characterise their orthotropic properties; allowing the relationships between them, and the resulting mechanical behaviour to be fully evaluated. This could be exploited, in tandem with the previous chapter to allow a huge range of control in the anisotropy and mechanical behaviour of AM PVA, where the PVA composition (and FTCs), nozzle size, print orientation and lattice dimensions can all be tuned to impact the final constructs mechanical behaviour. This could ultimately result in an exciting, powerful tool to tailor the mechanical behaviour of a PVA cryogel implant or phantom, which mimics a naturally graded connective tissue.

Although the aims of this thesis have a clear biomedical application, the work presented is fundamental engineering and material science. For the successful application of the knowledge and insights generated from this thesis, it is crucial to place it within the context of the overarching application; discussing the translation from the fundamental science presented here, to its eventual clinical use. Technology readiness levels (TRLs) are used ubiquitously throughout engineering as a method to track and monitor the progression of a specific technology for a given application [242]. Briefly, TRLs were originally developed by NASA for the aerospace industry and describe technology in nine levels, from 'basic principles observed and reported' (TRL 1), to 'Actual system "flight proven" through successful mission operations' (TRL 9) [242]. This has been widely adopted by many other industries, and ultimately can be used to describe a technology proving the concept and performing fundamental research (TRL 1-3) to developing working prototypes and ultimately technology maturity and wide adoption (TRL 9).

TRLs have been applied to the medical engineering field and offer a clear perspective of how a given technology will developed and incorporated into the design of a medical device [243]. To explain the translation of the science presented in this thesis to a

clinical application, the example of a multi-layered hyperelastic replacement for the arterial wall will be discussed. Ultimately the work presented in chapters 3, 4, and 5 fit into TRLs 1-3, as they prove the fundamental concept of the technology (figure 6.1). The next stage in the development process would be to define the PVA composition to replicate each layer of the artery using the data presented in this thesis as a starting point to inform choices. The AM methodology presented in chapters 4 and 5 could then be used to further refine the material properties of each layer. For example, a smaller nozzle size may be used for the media to increase stiffness and anisotropy, whereas the toolpath of the adventitia may be adapted to alter its hyperelastic response. A first prototype of the arterial wall replacement would then be manufactured, giving an indication of the feasibility of the technology. These stages would be considered TRL 3 or 4.

Stages 4 and 5 would then encompass rigorous testing of the device which may include *in vitro* testing, or the use of animal modules. At this stage the longevity and fatigue of the implant would also be tested, which could incorporate MRI as a method to non-invasively monitor the implant whilst *in vitro* or in an animal model. TRLs 6 to 8 encompass *in vivo* testing of the implant, initially in small numbers under very controlled conditions, before running larger human trials to fundamentally prove the safety and efficacy of the implant compared to other solutions. Finally, TRL 9 indicates the implant is safe, effective, and can be readily used in a clinical environment. As before, MRI could be used a non-invasive method to routinely monitor the implant *in vivo* during its lifetime.

Although far from an exhaustive explanation of the design process of a medical device, this example serves to provide context of how the science presented in this thesis translates into a clinical application. Fundamentally, this thesis aims to expand the knowledge base of the mechanical behaviour of PVA, opening avenues to develop more mechanically similar replacements for CT.

Figure 6.1: *The original TRL system developed by NASA (grey), and the biomedical engineering equivalent (black). The example of an arterial wall replacement is shown on the right.*

6.3 Final conclusions

As the mechanical behaviour of connective tissue is non-trivial, and they exhibit viscoelastic behaviour which is frequency dependant, it is important to assess biomaterials within the range of physiological conditions expected for a given connective tissue. For the first time, this thesis has successfully explored the dynamic viscoelastic properties of both cast (chapter 3) and additively manufactured PVA (chapter 4), showing effects of compositional changes (chapter 3), orthotropic properties (chapter 4), and the frequency of loading on the storage and loss moduli. This thesis has also shown that both the viscoelastic properties and MR T_2 relaxation time are proportional to the concentration of PVA in the sample, therefore giving the potential to non-invasively assess the mechanical properties of implants in-vivo.

The AM of PVA is a novel method of manufacturing, and offers the potential to manufacture bespoke geometry in an economically viable manner. This thesis has continued novel sub-zero methods of 3D printing hydrogels, and has added to the literature by analysing the orthotropic properties of AM PVA, intrinsic to the method of manufacture. It has shown that this anisotropy is dependent on nozzle size, allowing larger nozzle sizes to be used to reduce the anisotropy if required, at the cost of lower print resolution (chapter 4).

Finally, and of most interest for future work, this thesis has developed a method to parametrically define the toolpath during the AM of hydrogels (chapter 5). The toolpath chosen to illustrate this concept was a sine wave, and the amplitude and wavelength of the sine wave has been analysed with respect to the Young's moduli and hyperelastic properties of the resulting lattice. This therefore allows for the capability to control the material properties throughout the geometry of the resulting PVA, allowing for replication of the functionally grading and variation in material properties of natural biomaterials.

REFERENCES

[1] J. G. Betts, K. A. Young, J. A. Wise, E. Johnson, B. Poe, D. H. Kruse, O. Korol, J. E. Johnson, M. Womble, and P. DeSaix, *Anatomy and Physiology*. https://openstax.org/books/anatomy-and-physiology/pages/1-introduction: OpenStax, 2013.

[2] T. C. Gasser, R. W. Ogden, and G. A. Holzapfel, "Hyperelastic modelling of arterial layers with distributed collagen fibre orientations," *Journal of The Royal Society Interface*, vol. 3, no. 6, pp. 15–35, 2006.

[3] J. C. Mansfield, V. Mandalia, A. Toms, C. P. Winlove, and S. Brasselet, "Collagen reorganization in cartilage under strain probed by polarization sensitive second harmonic generation microscopy," *Journal of The Royal Society Interface*, vol. 16, no. 150, p. 20180611, 2019.

[4] M. J. Peltola, P. K. Vallittu, V. Vuorinen, A. A. J. Aho, A. Puntala, and K. M. J. Aitasalo, "Novel composite implant in craniofacial bone reconstruction," *European Archives of Oto-Rhino-Laryngology*, vol. 269, no. 2, pp. 623–628, 2012.

[5] M. M. Shalabi, J. G. C. Wolke, V. M. J. I. Cuijpers, and J. A. Jansen, "Evaluation of bone response to titanium-coated polymethyl methacrylate resin (PMMA) implants by X-ray tomography," *Journal of Materials Science: Materials in Medicine*, vol. 18, no. 10, pp. 2033–2039, 2007.

[6] K. S. Lim, F. Abinzano, P. N. Bernal, A. Albillos Sanchez, P. Atienza-Roca, I. A. Otto, Q. C. Peiffer, M. Matsusaki, T. B. F. Woodfield, J. Malda, and R. Levato, "One-step photoactivation of a dual-functionalized bioink as cell carrier and cartilage-binding glue for chondral regeneration," *Advanced Healthcare Materials*, vol. 9, p. 1901792, 2022/03/14 2020.

[7] T. J. Hinton, Q. Jallerat, R. N. Palchesko, J. H. Park, M. S. Grodzicki, H. J. Shue, M. H. Ramadan, A. R. Hudson, and A. W. Feinberg, "Three-dimensional printing of complex biological structures by freeform reversible embedding of suspended hydrogels," *Sci Adv*, vol. 1, no. 9, p. e1500758, 2015.

[8] L. E. Millon, M.-P. Nieh, J. L. Hutter, and W. Wan, "SANS characterization of an anisotropic poly(vinyl alcohol) hydrogel with vascular applications," *Macromolecules*, vol. 40, no. 10, pp. 3655–3662, 2007.

[9] Z. Tan, C. Parisi, L. Di Silvio, D. Dini, and A. E. Forte, "Cryogenic 3D printing of super soft hydrogels," *Sci Rep*, vol. 7, no. 1, p. 16293, 2017.

[10] S. J. Hollister, "Porous scaffold design for tissue engineering," *Nature Materials*, vol. 4, no. 7, pp. 518–524, 2005.

[11] V. Sardinha, L. Lima, W. Belangero, C. Zavaglia, V. Bavaresco, and J. Gomes, "Tribological characterization of polyvinyl alcohol hydrogel as substitute of articular cartilage," *Wear*, vol. 301, no. 1, pp. 218–225, 2013. Wear of Materials 2013.

[12] R. Luengo-Fernandez, J. Leal, A. Gray, S. Petersen, and M. Rayner, "Cost of cardiovascular diseases in the united kingdom," *Heart*, vol. 92, no. 10, pp. 1384–9, 2006.

[13] "Cardiovascular disease: A costly burden for America," report, 2017.

[14] "British heart foundation statistics factsheet - UK," report, 2021 (March).

[15] J. A. Singh, S. Yu, L. Chen, and J. D. Cleveland, "Rates of total joint replacement in the United States: Future projections to 2020-2040 using the national inpatient sample," *J Rheumatol*, vol. 46, no. 9, pp. 1134–1140, 2019.

[16] C. P. Brown, T. C. Nguyen, H. R. Moody, R. W. Crawford, and A. Oloyede, "Assessment of common hyperelastic constitutive equations for describing normal and osteoarthritic articular cartilage," *Proceedings of the Institution of Mechanical Engineers, Part H: Journal of Engineering in Medicine*, vol. 223, pp. 643–652, 2022/03/03 2009.

[17] J. A. López-Campos, J. P. S. Ferreira, A. Segade, J. R. Fernández, and R. M. Natal, "Characterization of hyperelastic and damage behavior of tendons," *Computer Methods in Biomechanics and Biomedical Engineering*, vol. 23, pp. 213–223, 04 2020.

[18] H. M. Ngwangwa and F. Nemavhola, "Evaluating computational performances of hyperelastic models on supraspinatus tendon uniaxial tensile test data," *Journal of Computational Applied Mechanics*, vol. 52, no. 1, pp. 27–43, 2021.

[19] G. A. Holzapfel and T. Gasser, "A new constitutive framework for arterial wall mechanics and a comparative study of material models," *Journal of Elasticity*, vol. 61, 2000.

[20] G. A. Holzapfel, G. Sommer, C. T. Gasser, and P. Regitnig, "Determination of layer-specific mechanical properties of human coronary arteries with nonatherosclerotic intimal thickening and related constitutive modeling," *Am J Physiol Heart Circ Physiol*, vol. 289, no. 5, pp. H2048–58, 2005.

[21] G. A. Holzapfel and R. W. Ogden, "Constitutive modelling of arteries," *Proceedings of the Royal Society A: Mathematical, Physical and Engineering Sciences*, vol. 466, pp. 1551–1597, 2022/03/05 2010.

[22] J. Baxter, K. G. Buchan, and D. M. Espino, "Viscoelastic properties of mitral valve leaflets: An analysis of regional variation and frequency-dependency," *Proc Inst Mech Eng H*, vol. 231, no. 10, pp. 938–944, 2017.

[23] H. E. Burton, J. M. Freij, and D. M. Espino, "Dynamic viscoelasticity and surface properties of porcine left anterior descending coronary arteries," *Cardiovasc Eng Technol*, vol. 8, no. 1, pp. 41–56, 2017.

[24] M. Constable, H. E. Burton, B. M. Lawless, V. Gramigna, K. G. Buchan, and D. M. Espino, "Effect of glutaraldehyde based cross-linking on the viscoelasticity of mitral valve basal chordae tendineae,," *Biomed Eng Online*, vol. 17, no. 1, p. 93, 2018.

[25] S. Fraser, C. G. Barberio, T. Chaudhry, D. M. Power, S. Tan, B. M. Lawless, and D. M. Espino, "The effect of injurious compression on the elastic, hyper-elastic and visco-elastic properties of porcine peripheral nerves," *Journal of the Mechanical Behavior of Biomedical Materials*, vol. 121, p. 104624, 2021.

[26] B. M. Lawless, S. C. Barnes, D. M. Espino, and D. E. T. Shepherd, "Viscoelastic properties of a spinal posterior dynamic stabilisation device," *J Mech Behav Biomed Mater*, vol. 59, pp. 519–526, 2016.

[27] B. M. Lawless, H. Sadeghi, D. K. Temple, H. Dhaliwal, D. M. Espino, and D. W. L. Hukins, "Viscoelasticity of articular cartilage: Analysing the effect of induced stress and the restraint of bone in a dynamic environment," *J Mech Behav Biomed Mater*, vol. 75, no. May, pp. 293–301, 2017.

[28] H. Sadeghi, D. M. Espino, and D. E. T. Shepherd, "Variation in viscoelastic properties of bovine articular cartilage below, up to and above healthy gait-relevant loading frequencies," *Proceedings of the Institution of Mechanical Engineers. Part H, Journal of engineering in medicine*, vol. 229, pp. 115–123, 02 2015.

[29] J. M. Fick and D. M. Espino, "Articular cartilage surface failure: An investigation of the rupture rate and morphology in relation to tissue health and hydration," *Proceedings of the Institution of Mechanical Engineers, Part H: Journal of Engineering in Medicine*, vol. 226, no. 5, pp. 389–396, 2012.

[30] D. M. Espino, D. W. L. Hukins, D. E. T. Shepherd, M. A. Watson, and K. Buchan, "Determination of the pressure required to cause mitral valve failure," *Medical Engineering & Physics*, vol. 28, no. 1, pp. 36–41, 2006.

[31] H. Sadeghi, D. E. T. Shepherd, and D. M. Espino, "Effect of the variation of loading frequency on surface failure of bovine articular cartilage," *Osteoarthritis Cartilage*, vol. 23, no. 12, pp. 2252–2258, 2015.

[32] B. Pearson and D. M. Espino, "Effect of hydration on the frequency-dependent viscoelastic properties of articular cartilage," *Proceedings of the Institution of Mechanical Engineers, Part H: Journal of Engineering in Medicine*, vol. 227, pp. 1246–1252, 2022/03/07 2013.

[33] M. H. Alves, B. E. Jensen, A. A. Smith, and A. N. Zelikin, "Poly(vinyl alcohol) physical hydrogels: new vista on a long serving biomaterial," *Macromol Biosci*, vol. 11, no. 10, pp. 1293–313, 2011.

[34] L. E. Millon, H. Mohammadi, and W. K. Wan, "Anisotropic polyvinyl alcohol hydrogel for cardiovascular applications," *J Biomed Mater Res B Appl Biomater*, vol. 79, no. 2, pp. 305–11, 2006.

[35] J. A. Stammen, S. Williams, D. N. Ku, and R. E. Guldberg, "Mechanical properties of a novel PVA hydrogel in shear and unconfined compression," *Biomaterials*, vol. 22, no. 8, pp. 799–806, 2001.

[36] W. Świeszkowski, D. N. Ku, H. E. N. Bersee, and K. J. Kurzydlowski, "An elastic material for cartilage replacement in an arthritic shoulder joint," *Biomaterials*, vol. 27, no. 8, pp. 1534–1541, 2006.

[37] W. Wan, A. Dawn Bannerman, L. Yang, and H. Mak, "Poly(vinyl alcohol) cryogels for biomedical applications," *Advances in Polymer Science*, 2014.

[38] C. M. Hassan and N. A. Peppas, "Structure and applications of poly(vinyl alcohol) hydrogels produced by conventional crosslinking or by freezing/thawing methods," *Advances in Polymer Science*, vol. 153, pp. 37–65, 2000.

[39] K. C. Chu and B. K. Rutt, "Polyvinyl alcohol cryogel an ideal phantom material for MR studies of arterial flow and elasticity," *Magn Reson Med*, vol. 37, no. 2, pp. 314–9, 1997.

[40] S. Cournane, L. Cannon, J. E. Browne, and A. J. Fagan, "Assessment of the accuracy of an ultrasound elastography liver scanning system using a PVA-cryogel phantom with optimal acoustic and mechanical properties," *Phys Med Biol*, vol. 55, no. 19, pp. 5965–83, 2010.

[41] S. Chatelin, M. Bernal, T. Deffieux, C. Papadacci, P. Flaud, A. Nahas, C. Boccara, J. L. Gennisson, M. Tanter, and M. Pernot, "Anisotropic polyvinyl alcohol hydrogel phantom for shear wave elastography in fibrous biological soft tissue: a multimodality characterization," *Phys Med Biol*, vol. 59, no. 22, pp. 6923–40, 2014.

[42] H. Jiang, G. Campbell, D. Boughner, W. K. Wan, and M. Quantz, "Design and manufacture of a polyvinyl alcohol (PVA) cryogel tri-leaflet heart valve prosthesis," *Med Eng Phys*, vol. 26, no. 4, pp. 269–77, 2004.

[43] W. K. Wan, G. Campbell, Z. F. Zhang, A. J. Hui, and D. R. Boughner, "Optimizing the tensile properties of polyvinyl alcohol hydrogel for the construction of a bioprosthetic heart valve stent," *J Biomed Mater Res*, vol. 63, no. 6, pp. 854–61, 2002.

[44] M. Oka, Y. S. Chang, T. Nakamura, K. Ushio, J. Toguchida, and H. O. Gu, "Synthetic osteochondral replacement of the femoral articular surface," *J Bone Joint Surg Br*, vol. 79, no. 6, pp. 1003–7, 1997.

[45] E. Y. L. Wong and D. W. Wan, "Poly (vinyl alcohol) nanocomposite hydrogels for intervertebral disc prostheses," *Electronic Thesis and Dissertation Repository*, vol. 731, 2012.

[46] M. Mobaraki, M. Ghaffari, A. Yazdanpanah, Y. Luo, and D. K. Mills, "Bioinks and bioprinting: A focused review," *Bioprinting*, vol. 18, 2020.

[47] M. Salmi, "Additive manufacturing processes in medical applications," *Materials (Basel, Switzerland)*, vol. 14, p. 191, 01 2021.

[48] N. A. Sears, D. R. Seshadri, P. S. Dhavalikar, and E. Cosgriff-Hernandez, "A review of three-dimensional printing in tissue engineering," *Tissue Eng Part B Rev*, vol. 22, no. 4, pp. 298–310, 2016.

[49] E. Peña, A. Chanda, and C. Callaway, "Tissue anisotropy modeling using soft composite materials," *Applied Bionics and Biomechanics*, vol. 2018, p. 4838157, 2018.

[50] D. W. L. Hukins, *Connective Tissue Matrix Part 2*. Red Globe Press London, 1990.

[51] L. J. Gathercole and A. Keller, "Crimp morphology in the fibre-forming collagens," *Matrix*, vol. 11, no. 3, pp. 214–234, 1991.

[52] J. M. Freij, H. E. Burton, and D. M. Espino, "Objective uniaxial identification of transition points in non-linear materials: Sample application to porcine coronary arteries and the dependency of their pre- and post-transitional moduli with position," *Cardiovascular Engineering and Technology*, vol. 10, no. 1, pp. 61–68, 2019.

[53] E. Han, S. S. Chen, S. M. Klisch, and R. L. Sah, "Contribution of proteoglycan osmotic swelling pressure to the compressive properties of articular cartilage," *Biophysical journal*, vol. 101, pp. 916–924, 08 2011.

[54] F. Guilak, G. R. Erickson, and H. P. Ting-Beall, "The effects of osmotic stress on the viscoelastic and physical properties of articular chondrocytes," *Biophysical Journal*, vol. 82, no. 2, pp. 720–727, 2002.

[55] P. D. Richardson, "Biomechanics of plaque rupture: progress, problems, and new frontiers," *Annals of biomedical engineering*, vol. 30, no. 4, pp. 524–536, 2002.

[56] H. J. Carpenter, A. Gholipour, M. H. Ghayesh, A. C. Zander, and P. J. Psaltis, "A review on the biomechanics of coronary arteries," *International Journal of Engineering Science*, vol. 147, p. 103201, 2020.

[57] K. L. Fegan, N. C. Green, M. M. Britton, A. J. Iqbal, and L. E. J. Thomas-Seale, "Design and simulation of the biomechanics of multi-layered composite poly(vinyl alcohol) coronary artery grafts," *Frontiers in Cardiovascular Medicine*, vol. 9, 2022.

[58] J. B. Weiss and M. I. V. Jayson, "Collagen in health and disease," *The Lancet*, vol. 311, pp. 1077–1079, 1978.

[59] P. B. Canham, H. M. Finlay, J. G. Dixon, D. R. Boughner, and A. Chen, "Measurements from light and polarised light microscopy of human coronary arteries fixed at distending pressure," *Cardiovascular research*, vol. 23, no. 11, pp. 973–982, 1989.

[60] A. J. Sophia Fox, A. Bedi, and S. A. Rodeo, "The basic science of articular cartilage: structure, composition, and function.," *Sports Health*, vol. 1, pp. 461–468, Nov 2009.

[61] J. P. Crolla, B. M. Lawless, A. A. Cederlund, R. M. Aspden, and D. M. Espino, "Analysis of hydration and subchondral bone density on the viscoelastic properties of bovine articular cartilage," *BMC Musculoskeletal Disorders*, vol. 23, no. 1, pp. 1–11, 2022.

[62] A. Tathe, M. Ghodke, and A. P. Nikalje, "A brief review: Biomaterials and their application," *International Journal of Pharmacy and Pharmaceutical Sciences*, vol. 2, no. 4, pp. 19–23, 2010.

[63] J. A. López-López, R. L. Humphriss, A. D. Beswick, H. H. Z. Thom, L. P. Hunt, A. Burston, C. G. Fawsitt, W. Hollingworth, J. P. T. Higgins, N. J. Welton, A. W. Blom, and E. M. R. Marques, "Choice of implant combinations in total hip replacement: systematic review and network meta-analysis," *BMJ*, vol. 359, 2017.

[64] L. Tian, N. Tang, T. Ngai, C. Wu, Y. Ruan, L. Huang, and L. Qin, "Hybrid fracture fixation systems developed for orthopaedic applications: A general review," *Journal of Orthopaedic Translation*, vol. 16, pp. 1–13, 2019.

[65] B. O'Brien and W. Carroll, "The evolution of cardiovascular stent materials and surfaces in response to clinical drivers: A review," *Acta Biomaterialia*, vol. 5, no. 4, pp. 945–958, 2009.

[66] B. R. Freedman and D. J. Mooney, "Biomaterials to mimic and heal connective tissues," *Advanced Materials*, vol. 31, no. 19, p. 1806695, 2019.

[67] R. B. Osman and M. V. Swain, "A critical review of dental implant materials with an emphasis on titanium versus zirconia," *Materials*, vol. 8, no. 3, pp. 932–958, 2015.

[68] M. F. Refojo, "Current status of biomaterials in ophthalmology," *Survey of Ophthalmology*, vol. 26, no. 5, pp. 257–265, 1982.

[69] B. Basa, G. Jakab, N. Kállai-Szabó, B. Borbás, V. Fülöp, E. Balogh, and I. Antal, "Evaluation of biodegradable PVA-based 3D printed carriers during dissolution," *Materials*, vol. 14, no. 6, 2021.

[70] N. Sykaras, A. M. Iacopino, V. A. Marker, R. G. Triplett, and R. D. Woody, "Implant materials, designs, and surface topographies: their effect on osseointegration. a literature review," *Int J Oral Maxillofac Implants*, vol. 15, no. 5, pp. 675–90, 2000.

[71] E. Gibon, L. A. Córdova, L. Lu, T.-H. Lin, Z. Yao, M. Hamadouche, and S. B. Goodman, "The biological response to orthopedic implants for joint replacement. II: Polyethylene, ceramics, pmma, and the foreign body reaction," *Journal of Biomedical Materials Research Part B: Applied Biomaterials*, vol. 105, no. 6, pp. 1685–1691, 2017.

[72] L. Carlsson, T. Röstlund, B. Albrektsson, T. Albrektsson, and P.-I. Brånemark, "Osseointegration of titanium implants," *Acta Orthopaedica Scandinavica*, vol. 57, no. 4, pp. 285–289, 1986. PMID: 3788488.

[73] X. Zhao, "1 - introduction to bioactive materials in medicine," in *Bioactive Materials in Medicine* (X. Zhao, J. Courtney, and H. Qian, eds.), Woodhead Publishing Series in Biomaterials, pp. 1–13, Woodhead Publishing, 2011.

[74] S. Pina and J. F. Ferreira, "Bioresorbable plates and screws for clinical applications: A review," *Journal of Healthcare Engineering*, vol. 3, p. 846435, 2012.

[75] R. Kumar, M. Kumar, and J. S. Chohan, "The role of additive manufacturing for biomedical applications: A critical review," *Journal of Manufacturing Processes*, vol. 64, pp. 828–850, 2021.

[76] J. Wang, C. McMullen, P. Yao, N.-D. Jiao, M. Kim, J.-W. Kim, L. Liu, and S. Tung, "3D-printed peristaltic microfluidic systems fabricated from thermoplastic elastomer," *Microfluidics and Nanofluidics*, vol. 21, 06 2017.

[77] M. Doshi, A. Mahale, S. Kumar Singh, and S. Deshmukh, "Printing parameters and materials affecting mechanical properties of FDM-3D printed parts: Perspective and prospects," *Materials Today: Proceedings*, vol. 50, pp. 2269–2275, 2022. 2nd International Conference on Functional Material, Manufacturing and Performances (ICFMMP-2021).

[78] C. N. Maganaris and J. P. Paul, "*In vivo* human tendon mechanical properties.," *J Physiol*, vol. 521 Pt 1, pp. 307–313, Nov 1999.

[79] J. P. Heggers, N. Kossovsky, R. W. Parsons, M. C. Robson, R. P. Pelley, and T. J. Raine, "Biocompatibility of silicone implants.," *Ann Plast Surg*, vol. 11, pp. 38–45, Jul 1983.

[80] A. M. Goldfain, P. Lemaillet, D. W. Allen, K. A. Briggman, and J. Hwang, "Polydimethylsiloxane tissue-mimicking phantoms with tunable optical properties.," *J Biomed Opt*, vol. 27, Nov 2021.

[81] J. H. Kim, P. Chhai, and K. Rhee, "Development and characterization of viscoelastic polydimethylsiloxane phantoms for simulating arterial wall motion.," *Med Eng Phys*, vol. 91, pp. 12–18, May 2021.

[82] S. G. Yazdi, L. Huetter, P. D. Docherty, P. N. Williamson, D. Clucas, M. Jermy, and P. H. Geoghegan, "A novel fabrication method for compliant silicone phantoms of arterial geometry for use in particle image velocimetry of haemodynamics," *Applied Sciences*, vol. 9, no. 18, 2019.

[83] T. J. Hinton, A. Hudson, K. Pusch, A. Lee, and A. W. Feinberg, "3D printing PDMS elastomer in a hydrophilic support bath via freeform reversible embedding," *ACS Biomaterials Science & Engineering*, vol. 2, pp. 1781–1786, 10 2016.

[84] O. Wichterle and D. Lim, "Hydrophilic gels for biological use," *Nature*, vol. 185, no. 4706, pp. 117–118, 1960.

[85] J. Maitra and V. Shukla, "Cross-linking in hydrogels - a review," *Am J Polym Sci*, vol. 4, pp. 25–31, 01 2014.

[86] B. E. Mirzaei, A. Ramazani, M. Shafiee, and M. Danaei, "Studies on glutaraldehyde crosslinked chitosan hydrogel properties for drug delivery systems," *International Journal of Polymeric Materials and Polymeric Biomaterials*, vol. 62, no. 11, pp. 605–611, 2013.

[87] H. S. Mansur, C. M. Sadahira, A. N. Souza, and A. A. Mansur, "FTIR spectroscopy characterization of poly (vinyl alcohol) hydrogel with different hydrolysis degree and chemically crosslinked with glutaraldehyde," *Materials Science and Engineering: C*, vol. 28, no. 4, pp. 539–548, 2008. Proceedings of the Symposium on Nanostructured Biological Materials, V Meeting of the Brazilian Materials Research Society (SBPMat).

[88] D. A. Gyles, L. D. Castro, J. O. C. Silva, and R. M. Ribeiro-Costa, "A review of the designs and prominent biomedical advances of natural and synthetic hydrogel formulations," *European Polymer Journal*, vol. 88, pp. 373–392, 2017.

[89] U. S. K. Madduma-Bandarage and S. V. Madihally, "Synthetic hydrogels: Synthesis, novel trends, and applications," *Journal of Applied Polymer Science*, vol. 138, no. 19, p. 50376, 2021.

[90] K. Y. Lee and D. J. Mooney, "Alginate: Properties and biomedical applications.," *Prog Polym Sci*, vol. 37, pp. 106–126, Jan 2012.

[91] D. E. Clark and H. C. Green, "Alginic acid and process of making same. 2036922," *US Patent*, 1936.

[92] M. A. Samp, N. C. Iovanac, and A. J. Nolte, "Sodium alginate toughening of gelatin hydrogels," *ACS Biomaterials Science & Engineering*, vol. 3, no. 12, pp. 3176–3182, 2017.

[93] P. Jaipan, A. Nguyen, and R. J. Narayan, "Gelatin-based hydrogels for biomedical applications," *MRS Communications*, vol. 7, no. 3, pp. 416–426, 2017.

[94] A. I. Van Den Bulcke, B. Bogdanov, N. De Rooze, E. H. Schacht, M. Cornelissen, and H. Berghmans, "Structural and rheological properties of methacrylamide

modified gelatin hydrogels," *Biomacromolecules*, vol. 1, no. 1, pp. 31–38, 2000. PMID: 11709840.

[95] T. Bhattacharjee, S. M. Zehnder, K. G. Rowe, S. Jain, R. M. Nixon, W. G. Sawyer, and T. E. Angelini, "Writing in the granular gel medium," *Science advances*, vol. 1, no. 8, p. e1500655, 2015.

[96] C. B. Highley, C. B. Rodell, and J. A. Burdick, "Direct 3D printing of shear-thinning hydrogels into self-healing hydrogels," *Advanced Materials*, vol. 27, no. 34, pp. 5075–5079, 2015.

[97] M. Zare, A. Bigham, M. Zare, H. Luo, E. Rezvani Ghomi, and S. Ramakrishna, "pHEMA: An overview for biomedical applications.," *Int J Mol Sci*, vol. 22, Jun 2021.

[98] P. Zarrintaj, J. D. Ramsey, A. Samadi, Z. Atoufi, M. K. Yazdi, M. R. Ganjali, L. M. Amirabad, E. Zangene, M. Farokhi, K. Formela, M. R. Saeb, M. Mozafari, and S. Thomas, "Poloxamer: A versatile tri-block copolymer for biomedical applications," *Acta Biomaterialia*, vol. 110, pp. 37–67, 2020.

[99] S. Muppalaneni and H. Omidian, "Polyvinyl alcohol in medicine and pharmacy: A perspective," *Journal of Developing Drugs*, vol. 02, no. 03, pp. 1–5, 2013.

[100] L. E. Millon, C. J. Oates, and W. Wan, "Compression properties of polyvinyl alcohol–bacterial cellulose nanocomposite," *J Biomed Mater Res B Appl Biomater*, vol. 90, no. 2, pp. 922–9, 2009.

[101] A. Thangprasert, C. Tansakul, N. Thuaksubun, and J. Meesane, "Mimicked hybrid hydrogel based on gelatin/PVA for tissue engineering in subchondral bone interface for osteoarthritis surgery," *Materials & Design*, vol. 183, p. 108113, 2019.

[102] M. Oka, K. Ushio, P. Kumar, K. Ikeuchi, S. H. Hyon, T. Nakamura, and H. Fujita, "Development of artificial articular cartilage," *Proc Inst Mech Eng H*, vol. 214, no. 1, pp. 59–68, 2000.

[103] T. Noguchi, T. Yamamuro, M. Oka, P. Kumar, Y. Kotoura, S. Hyon, and Y. Ikada, "Poly(vinyl alcohol) hydrogel as an artificial articular cartilage: evaluation of biocompatibility," *J Appl Biomater*, vol. 2, no. 2, pp. 101–7, 1991.

[104] Y.-S. Pan, D.-S. Xiong, and R.-Y. Ma, "A study on the friction properties of poly(vinyl alcohol) hydrogel as articular cartilage against titanium alloy," *Wear*, vol. 262, no. 7-8, pp. 1021–1025, 2007.

[105] M. I. Baker, S. P. Walsh, Z. Schwartz, and B. D. Boyan, "A review of polyvinyl alcohol and its uses in cartilage and orthopedic applications," *J Biomed Mater Res B Appl Biomater*, vol. 100, no. 5, pp. 1451–7, 2012.

[106] M. Kobayashi, Y.-S. Chang, and M. Oka, "A two year *in vivo* study of polyvinyl alcohol-hydrogel (PVA-H) artificial meniscus.," *Biomaterials*, vol. 26, pp. 3243–3248, Jun 2005.

[107] A. J. Malone, S. Cournane, I. G. Naydenova, A. J. Fagan, and J. E. Browne, "Polyvinyl alcohol cryogel based vessel mimicking material for modelling the progression of atherosclerosis," *Phys Med*, vol. 69, no. December 2019, pp. 1–8, 2020.

[108] J. Fromageau, E. Brusseau, D. Vray, G. Gimenez, and P. Delachartre, "Characterization of PVA cryogel for intravascular ultrasound elasticity imaging," *IEEE Trans Ultrason Ferroelectr Freq Control*, vol. 50, no. 10, pp. 1318–24, 2003.

[109] T. Seale Lej, K. P, and H. L, "Magnetic resonance elastography through atherosclerosis: A feasibility study," *Journal of Clinical and Experimental Cardiology*, vol. 7, no. 12, 2016.

[110] R. K. Tubbs, "Sequence distribution of partially hydrolyzed poly(vinyl acetate)," *Journal of Polymer Science Part A-1: Polymer Chemistry*, vol. 4, no. 3, pp. 623–629, 1966.

[111] F. Yokoyama, I. Masada, K. Shimamura, T. Ikawa, and K. Monobe, "Morphology and structure of highly elastic poly(vinyl alcohol) hydrogel prepared by repeated freezing-and-melting," *Colloid and Polymer Science*, vol. 264, no. 7, pp. 595–601, 1986.

[112] J. L. Holloway, A. M. Lowman, and G. R. Palmese, "The role of crystallization and phase separation in the formation of physically cross-linked PVA hydrogels," *Soft Matter*, vol. 9, pp. 826–833, 2013.

[113] H. Adelnia, R. Ensandoost, S. Shebbrin Moonshi, J. N. Gavgani, E. I. Vasafi, and H. T. Ta, "Freeze/thawed polyvinyl alcohol hydrogels: Present, past and future," *European Polymer Journal*, vol. 164, p. 110974, 2022.

[114] S. Gupta, S. Goswami, and A. Sinha, "A combined effect of freeze–thaw cycles and polymer concentration on the structure and mechanical properties of transparent PVA gels," *Biomed Mater*, vol. 7, no. 1, p. 015006, 2012.

[115] Y. Liu, L. M. Geever, J. E. Kennedy, C. L. Higginbotham, P. A. Cahill, and G. B. McGuinness, "Thermal behavior and mechanical properties of physically crosslinked PVA/gelatin hydrogels," *J Mech Behav Biomed Mater*, vol. 3, no. 2, pp. 203–9, 2010.

[116] H. Kosukegawa, K. Mamada, K. Kuroki, L. Liu, K. Inoue, T. Hayase, and M. Ohta, "Measurements of dynamic viscoelasticity of poly (vinyl alcohol) hydrogel for the development of blood vessel biomodeling," *Journal of Fluid Science and Technology*, vol. 3, no. 4, pp. 533–543, 2008.

[117] J.-S. Park, J.-W. Park, and E. Ruckenstein, "On the viscoelastic properties of poly(vinyl alcohol) and chemically crosslinked poly(vinyl alcohol)," *Journal of Applied Polymer Science*, vol. 82, no. 7, pp. 1816–1823, 2001.

[118] A. Hadj Henni, C. Schmitt, M. E. Tremblay, M. Hamdine, M. C. Heuzey, P. Carreau, and G. Cloutier, "Hyper-frequency viscoelastic spectroscopy of biomaterials," *J Mech Behav Biomed Mater*, vol. 4, no. 7, pp. 1115–22, 2011.

[119] D. Mahmoud and M. A. Elbestawi, "Lattice structures and functionally graded materials applications in additive manufacturing of orthopedic implants: A review," *Journal of Manufacturing and Materials Processing*, vol. 1, no. 2, 2017.

[120] A. Sola, D. Bellucci, and V. Cannillo, "Functionally graded materials for orthopedic applications –an update on design and manufacturing," *Biotechnology Advances*, vol. 34, no. 5, pp. 504–531, 2016.

[121] S. Ford and M. Despeisse, "Additive manufacturing and sustainability: an exploratory study of the advantages and challenges," *Journal of Cleaner Production*, vol. 137, pp. 1573–1587, 2016.

[122] M. Gebler, A. J. M. Schoot Uiterkamp, and C. Visser, "A global sustainability perspective on 3D printing technologies," *Energy Policy*, vol. 74, pp. 158–167, 2014.

[123] T. Pereira, J. V. Kennedy, and J. Potgieter, "A comparison of traditional manufacturing vs additive manufacturing, the best method for the job," *Procedia Manufacturing*, vol. 30, pp. 11–18, 2019.

[124] A. Panesar, M. Abdi, D. Hickman, and I. Ashcroft, "Strategies for functionally graded lattice structures derived using topology optimisation for additive manufacturing," *Additive Manufacturing*, vol. 19, pp. 81–94, 2018.

[125] D. Bourell, J. P. Kruth, M. Leu, G. Levy, D. Rosen, A. M. Beese, and A. Clare, "Materials for additive manufacturing," *CIRP Annals*, vol. 66, no. 2, pp. 659–681, 2017.

[126] V. Dhinakaran, K. P. Manoj Kumar, P. M. Bupathi Ram, M. Ravichandran, and M. Vinayagamoorthy, "A review on recent advancements in fused deposition modeling," *Materials Today: Proceedings*, vol. 27, pp. 752–756, 2020.

[127] W. L. Ng, J. M. Lee, M. Zhou, Y.-W. Chen, K.-X. A. Lee, W. Y. Yeong, and Y.-F. Shen, "Vat polymerization-based bioprinting—process, materials, applications and regulatory challenges," *Biofabrication*, vol. 12, no. 2, p. 022001, 2020.

[128] O. Gülcan, K. Günaydın, and A. Tamer, "The state of the art of material jetting-a critical review," *Polymers*, vol. 13, p. 2829, 08 2021.

[129] S. Sun, M. Brandt, M. Easton, and M. Brandt, *2 - Powder bed fusion processes: An overview*, pp. 55–77. Woodhead Publishing, 2017.

[130] A. Dass and A. Moridi, "State of the art in directed energy deposition: From additive manufacturing to materials design," *Coatings*, vol. 9, p. 418, 06 2019.

[131] S.-h. Hsu, H.-J. Yen, C.-S. Tseng, C.-S. Cheng, and C.-L. Tsai, "Evaluation of the growth of chondrocytes and osteoblasts seeded into precision scaffolds fabricated by fused deposition manufacturing," *Journal of Biomedical Materials Research Part B: Applied Biomaterials*, vol. 80B, no. 2, pp. 519–527, 2007.

[132] X. Chen, G. Chen, G. Wang, P. Zhu, and C. Gao, "Recent progress on 3D-printed polylactic acid and its applications in bone repair," *Advanced Engineering Materials*, vol. 22, no. 4, p. 1901065, 2020.

[133] T. Cao, K.-H. Ho, and S.-H. Teoh, "Scaffold design and *in vitro* study of osteochondral coculture in a three-dimensional porous polycaprolactone scaffold fabricated by fused deposition modeling," *Tissue Engineering*, vol. 9, no. supplement 1, pp. 103–112, 2003. PMID: 14511474.

[134] S. H. Park, B. G. Yun, J. Y. Won, W. S. Yun, J. H. Shim, M. H. Lim, D. H. Kim, S. A. Baek, Y. D. Alahmari, J. H. Jeun, S. H. Hwang, and S. W. Kim, "New application of three-dimensional printing biomaterial in nasal reconstruction," *The Laryngoscope*, vol. 127, no. 5, pp. 1036–1043, 2017.

[135] E. K. Park, J. Y. Lim, I. S. Yun, J. S. Kim, S. H. Woo, D. S. Kim, and K. W. Shim, "Cranioplasty enhanced by three-dimensional printing: Custom-made three-dimensional-printed titanium implants for skull defects," *J Craniofac Surg*, vol. 27, no. 4, pp. 943–9, 2016.

[136] J. Imanishi and P. F. Choong, "Three-dimensional printed calcaneal prosthesis following total calcanectomy," *Int J Surg Case Rep*, vol. 10, pp. 83–7, 2015.

[137] R. J. Mobbs, M. Coughlan, R. Thompson, C. E. Sutterlin, and K. Phan, "The utility of 3D printing for surgical planning and patient-specific implant design for complex spinal pathologies: case report," *J Neurosurg Spine*, vol. 26, no. 4, pp. 513–518, 2017.

[138] S. Vanaei, M. Parizi, S. Vanaei, F. Salemizadehparizi, and H. Vanaei, "An overview on materials and techniques in 3D bioprinting toward biomedical application," *Engineered Regeneration*, vol. 2, pp. 1–18, 2021.

[139] N. Faramarzi, I. K. Yazdi, M. Nabavinia, A. Gemma, A. Fanelli, A. Caizzone, L. M. Ptaszek, I. Sinha, A. Khademhosseini, J. N. Ruskin, and A. Tamayol, "Patient-specific bioinks for 3D bioprinting of tissue engineering scaffolds," *Adv Healthc Mater*, vol. 7, no. 11, p. e1701347, 2018.

[140] S. J. Buwalda, K. W. Boere, P. J. Dijkstra, J. Feijen, T. Vermonden, and W. E. Hennink, "Hydrogels in a historical perspective: from simple networks to smart materials," *J Control Release*, vol. 190, pp. 254–73, 2014.

[141] S. Miramini, K. L. Fegan, N. C. Green, D. M. Espino, L. Zhang, and L. E. J. Thomas-Seale, "The status and challenges of replicating the mechanical properties of connective tissues using additive manufacturing," *J Mech Behav Biomed Mater*, vol. 103, p. 103544, 2020.

[142] A. Skardal, J. Zhang, L. McCoard, X. Xu, S. Oottamasathien, and G. D. Prestwich, "Photocrosslinkable hyaluronan-gelatin hydrogels for two-step bioprinting," *Tissue Engineering Part A*, vol. 16, no. 8, pp. 2675–2685, 2010.

[143] I. Cotabarren and L. Gallo, "3D printing of PVA capsular devices for modified drug delivery: design and *in vitro* dissolution studies," *Drug Development and Industrial Pharmacy*, vol. 46, no. 9, pp. 1416–1426, 2020.

[144] A. Goyanes, M. Kobayashi, R. Martínez-Pacheco, S. Gaisford, and A. W. Basit, "Fused-filament 3D printing of drug products: Microstructure analysis and drug release characteristics of PVA-based caplets," *International Journal of Pharmaceutics*, vol. 514, no. 1, pp. 290–295, 2016. In Honour of Professor Alexander T. Florence.

[145] S. Deville, E. Saiz, R. K. Nalla, and A. P. Tomsia, "Freezing as a path to build complex composites," *Science*, vol. 311, no. 5760, pp. 515–518, 2006.

[146] M. Adamkiewicz and B. Rubinsky, "Cryogenic 3D printing for tissue engineering," *Cryobiology*, vol. 71, no. 3, pp. 518–21, 2015.

[147] C. Wang, Y. Zhou, and M. Wang, "In situ delivery of rhBMP-2 in surface porous shape memory scaffolds developed through cryogenic 3D plotting," *Materials Letters*, vol. 189, pp. 140–143, 2017.

[148] Y. Meng, J. Cao, Y. Chen, Y. Yu, and L. Ye, "3D printing of a poly(vinyl alcohol)-based nano-composite hydrogel as an artificial cartilage replacement and the improvement mechanism of printing accuracy," *J Mater Chem B*, vol. 8, no. 4, pp. 677–690, 2020.

[149] H. Kim, G. H. Yang, C. H. Choi, Y. S. Cho, and G. Kim, "Gelatin/PVA scaffolds fabricated using a 3D-printing process employed with a low-temperature plate for hard tissue regeneration: Fabrication and characterizations," *Int J Biol Macromol*, vol. 120, no. Pt A, pp. 119–127, 2018.

[150] H. H. Trieu and S. Qutubuddin, "Polyvinyl alcohol hydrogels i. microscopic structure by freeze-etching and critical point drying techniques," *Colloid and Polymer Science*, vol. 272, no. 3, pp. 301–309, 1994.

[151] S. Jiang, S. Liu, and W. Feng, "PVA hydrogel properties for biomedical application," *Journal of the Mechanical Behavior of Biomedical Materials*, vol. 4, no. 7, pp. 1228–1233, 2011.

[152] R. Ricciardi, F. Auriemma, C. De Rosa, and F. Lauprêtre, "X-ray diffraction analysis of poly(vinyl alcohol) hydrogels, obtained by freezing and thawing techniques," *Macromolecules*, vol. 37, no. 5, pp. 1921–1927, 2004.

[153] J. Fromageau, J.-L. Gennisson, C. Schmitt, R. Maurice, R. Mongrain, and G. Cloutier, "Estimation of polyvinyl alcohol cryogel mechanical properties with four ultrasound elastography methods and comparison with gold standard testings," *IEEE transactions on ultrasonics, ferroelectrics, and frequency control*, vol. 54, pp. 498–509, 04 2007.

[154] T. N. Orr, J. Winter, G. Campbell, R. T. Thompson, and N. Gelman, "A phantom material for MRI of the neonatal brain," *CMBES Proceedings*, vol. 30, no. 1, 2007.

[155] Y. S. Zhang and J. Yao, "Imaging biomaterial-tissue interactions," *Trends in biotechnology*, vol. 36, pp. 403–414, 04 2018.

[156] N. England, "Diagnostic imaging dataset statistical release," 2020.

[157] J. A. C. Lima and M. Y. Desai, "Cardiovascular magnetic resonance imaging: Current and emerging applications," *Journal of the American College of Cardiology*, vol. 44, no. 6, pp. 1164–1171, 2004.

[158] C. M. Kramer and J. D. Anderson, "MRI of atherosclerosis: diagnosis and monitoring therapy," *Expert review of cardiovascular therapy*, vol. 5, pp. 69–80, 01 2007.

[159] C. Yuan and W. S. Kerwin, "MRI of atherosclerosis," *Journal of Magnetic Resonance Imaging*, vol. 19, no. 6, pp. 710–719, 2004.

[160] R. C. I. Wüst, C. Calcagno, M. R. R. Daal, A. J. Nederveen, B. F. Coolen, and G. J. Strijkers, "Emerging magnetic resonance imaging techniques for atherosclerosis imaging," *Arteriosclerosis, Thrombosis, and Vascular Biology*, vol. 39, pp. 841–849, 2022/02/26 2019.

[161] F. H. Epstein, "MRI of left ventricular function," *Journal of Nuclear Cardiology*, vol. 14, no. 5, pp. 729–744, 2007.

[162] N. Lahoti, R. J. Jabbour, B. Ariff, and B. X. Wang, "Cardiac MRI in cardiomyopathies," *Future Cardiology*, vol. 18, pp. 51–65, 2022/02/26 2021.

[163] C. Pierre-Jerome, V. Moncayo, and M. R. Terk, "MRI of the achilles tendon: A comprehensive review of the anatomy, biomechanics, and imaging of overuse tendinopathies," *Acta Radiologica*, vol. 51, no. 4, pp. 438–454, 2010.

[164] F. Eckstein, D. Burstein, and T. M. Link, "Quantitative MRI of cartilage and bone: degenerative changes in osteoarthritis," *NMR in Biomedicine*, vol. 19, no. 7, pp. 822–854, 2006.

[165] A. T. Collins, M. L. Kulvaranon, H. C. Cutcliffe, G. M. Utturkar, W. A. R. Smith, C. E. Spritzer, F. Guilak, and L. E. DeFrate, "Obesity alters the *in vivo* mechanical response and biochemical properties of cartilage as measured by MRI," *Arthritis Research & Therapy*, vol. 20, no. 1, p. 232, 2018.

[166] L. M. Benneker, P. F. Heini, S. E. Anderson, M. Alini, and K. Ito, "Correlation of radiographic and MRI parameters to morphological and biochemical assessment of intervertebral disc degeneration," *European Spine Journal*, vol. 14, no. 1, pp. 27–35, 2005.

[167] D. Smith, M. Sacks, P. Pattany, and R. Schroeder, "High-resolution magnetic resonance imaging to characterize the geometry of fatigued porcine bioprosthetic heart valves," *The Journal of heart valve disease*, vol. 6, no. 4, pp. 424–432, 1997.

[168] C. P. Neu, H. F. Arastu, S. Curtiss, and A. H. Reddi, "Characterization of engineered tissue construct mechanical function by magnetic resonance imaging," *Journal of Tissue Engineering and Regenerative Medicine*, vol. 3, no. 6, pp. 477–485, 2009.

[169] K. Potter, D. E. Sweet, P. Anderson, G. R. Davis, N. Isogai, S. Asamura, H. Kusuhara, and W. J. Landis, "Non-destructive studies of tissue-engineered phalanges by magnetic resonance microscopy and X-ray microtomography," *Bone*, vol. 38, no. 3, pp. 350–358, 2006.

[170] S. Tchoketch Kebir, S. Mekaoui, and M. Bouhedda, "A fully automatic methodology for MRI brain tumour detection and segmentation," *The Imaging Science Journal*, vol. 67, pp. 42–62, 01 2019.

[171] A. Shukla-Dave and H. Hricak, "Role of MRI in prostate cancer detection," *NMR in Biomedicine*, vol. 27, no. 1, pp. 16–24, 2014.

[172] A. M. Hassan and M. El-Shenawee, "Review of electromagnetic techniques for breast cancer detection," *IEEE Reviews in Biomedical Engineering*, vol. 4, pp. 103–118, 2011.

[173] E. D. Gareth, K. Nisha, L. Yit, G. Soujanye, H. Emma, N. J. Massat, A. J. Maxwell, I. Sarah, E. Rosalind, M. O. Leach, H. Anthony, D. Stephen, and M. Group, "MRI breast screening in high-risk women: cancer detection and survival analysis," *Breast Cancer Research and Treatment*, vol. 145, no. 3, pp. 663–672, 2014.

[174] P. Hoskins, K. Martin, and A. Thrush, *Diagnostic Ultrasound, Third Edition: Physics and Equipment*. CRC Press, 2019.

[175] P. R. Hoskins, "A review of the measurement of blood velocity and related quantities using doppler ultrasound," *Proceedings of the Institution of Mechanical Engineers, Part H: Journal of Engineering in Medicine*, vol. 213, no. 5, pp. 391–400, 1999.

[176] K. E. Stull, M. L. Tise, Z. Ali, and D. R. Fowler, "Accuracy and reliability of measurements obtained from computed tomography 3D volume rendered images," *Forensic Science International*, vol. 238, pp. 133–140, 2014.

[177] M. Rednam and V. Tiwari, *Fluoroscopy Orthopedic Assessment, Protocols, and Interpretation.* Katuri Medical College and Hospital, Guntur, India; All India Institute of Medical Sciences, Nagpur: StatPearls Publishing, Treasure Island (FL), Jan 2021.

[178] R. C. Hibbeler, *Mechanics of materials*. Pearson, 10 ed., 2017.

[179] G. Holzapfel and R. Ogden, *Multiscale Soft Tissue Mechanics and Mechanobiology: State-of-the-art Modeling*. Springer, 2018.

[180] D. Gutierrez-Lemini, *Engineering viscoelasticity*. Springer, 2014.

[181] K. P. Menard and N. R. Menard, *Dynamic mechanical analysis*. CRC press, 2020.

[182] V. Goyal, C. Garcia, and E. Irizarry, "Micro damage initiation of isotropic and composites structures using strain invariant failure theory," *Structural Dynamics and Materials Conference*, 01 2016.

[183] O. H. Yeoh, "Some forms of the strain energy function for rubber," *Rubber Chemistry and Technology*, vol. 66, pp. 754–771, 3/1/2022 1993.

[184] O. H. Yeoh, G. Allen, and J. C. Bevington, *Phenomenological Theory of Rubber Elasticity*. Amsterdam: Pergamon, 1989.

[185] M. M. Britton, "Magnetic resonance imaging of chemistry," *Chem Soc Rev*, vol. 39, no. 11, pp. 4036–43, 2010.

[186] B. M. Dale, *MRI : basic principles and applications*. West Sussex, England : Wiley Blackwell, 2015., fifth edition. ed., 2015.

[187] K. Liu and T. C. Ovaert, "Poro-viscoelastic constitutive modeling of unconfined creep of hydrogels using finite element analysis with integrated optimization method," *J Mech Behav Biomed Mater*, vol. 4, no. 3, pp. 440–50, 2011.

[188] J.-K. Suh, Z. Li, and S. L.-Y. Woo, "Dynamic behavior of a biphasic cartilage model under cyclic compressive loading," *Journal of Biomechanics*, vol. 28, no. 4, pp. 357–364, 1995.

[189] J. Hennig, A. Nauerth, and H. Friedburg, "Rare imaging: a fast imaging method for clinical mr," *Magn Reson Med*, vol. 3, no. 6, pp. 823–33, 1986.

[190] M. M. Britton, "MRI of chemical reactions and processes," *Prog Nucl Magn Reson Spectrosc*, vol. 101, pp. 51–70, 2017.

[191] G. M. Cimmarusti, A. Shastry, M. N. Boone, V. Cnudde, K. Braeckman, A. D. M. Brooker, E. S. J. Robles, and M. M. Britton, "Characterization of open-cell sponges via magnetic resonance and X-ray tomography," *Materials (Basel)*, vol. 14, no. 9, p. 2187, 2021.

[192] C. M. Hassan and N. A. Peppas, "Structure and morphology of freeze/thawed PVA hydrogels," *Macromolecules*, vol. 33, no. 7, pp. 2472–2479, 2000.

[193] T. Kanaya, M. Ohkura, K. Kaji, M. Furusaka, and M. Misawa, "Structure of poly(vinyl alcohol) gels studied by wide- and small-angle neutron scattering," *Macromolecules*, vol. 27, no. 20, pp. 5609–5615, 2002.

[194] F. Fergg, F. J. Keil, and H. Quader, "Investigations of the microscopic structure of poly(vinyl alcohol) hydrogels by confocal laser scanning microscopy," *Colloid and Polymer Science*, vol. 279, no. 1, pp. 61–67, 2001.

[195] J. R. Meakin, D. W. L. Hukins, C. T. IMRIe, and R. M. Aspden, "Thermal analysis of poly(2-hydroxyethyl methacrylate) (pHEMA) hydrogels," *Journal of Materials Science: Materials in Medicine*, vol. 14, no. 1, pp. 9–15, 2003.

[196] L. E. Thomas-Seale, D. Klatt, P. Pankaj, N. Roberts, I. Sack, and P. R. Hoskins, "A simulation of the magnetic resonance elastography steady state wave response through idealised atherosclerotic plaques," *IAENG International Journal of Computer Science*, vol. 38, no. 4, pp. 394–400, 2011.

[197] D. B. Kolesky, R. L. Truby, A. S. Gladman, T. A. Busbee, K. A. Homan, and J. A. Lewis, "3D bioprinting of vascularized, heterogeneous cell-laden tissue constructs," *Advanced Materials*, vol. 26, no. 19, pp. 3124–3130, 2014.

[198] S. Khalil, J. Nam, and W. Sun, "Multi-nozzle deposition for construction of 3D biopolymer tissue scaffolds," *Rapid Prototyping Journal*, 2005.

[199] J. P. Crolla, M. M. Britton, D. M. Espino, and L. E. J. Thomas-Seale, "The orthotropic viscoelastic characterisation of sub-zero 3D-printed poly(vinyl alcohol) cryogel," *MRS Advances*, 2021.

[200] J. Leijten, J. Seo, K. Yue, G. Trujillo-de Santiago, A. Tamayol, G. U. Ruiz-Esparza, S. R. Shin, R. Sharifi, I. Noshadi, M. M. Álvarez, Y. S. Zhang, and A. Khademhosseini, "Spatially and temporally controlled hydrogels for tissue engineering," *Materials Science and Engineering: R: Reports*, vol. 119, pp. 1–35, 2017.

[201] W. Li, D. E. Shepherd, and D. M. Espino, "Dynamic mechanical characterization and viscoelastic modeling of bovine brain tissue," *Journal of the Mechanical Behavior of Biomedical Materials*, vol. 114, p. 104204, 2021.

[202] M. Hua, S. Wu, Y. Ma, Y. Zhao, Z. Chen, I. Frenkel, J. Strzalka, H. Zhou, X. Zhu, and X. He, "Strong tough hydrogels via the synergy of freeze-casting and salting out," *Nature*, vol. 590, no. 7847, pp. 594–599, 2021.

[203] G. Holzapfel, "Biomechanics of soft tissue," *The Handbook of Materials Behavior Models*, vol. 3, pp. 1049–1063, 12 2001.

[204] G. Byrne, D. Dimitrov, L. Monostori, R. Teti, F. van Houten, and R. Wertheim, "Biologicalisation: Biological transformation in manufacturing," *CIRP Journal of Manufacturing Science and Technology*, vol. 21, pp. 1–32, 2018.

[205] S. Saliba, J. C. Kirkman-Brown, and L. E. J. Thomas-Seale, "Temporal design for additive manufacturing," *The International Journal of Advanced Manufacturing Technology*, vol. 106, no. 9-10, pp. 3849–3857, 2020.

[206] A. R. Torrado and D. A. Roberson, "Failure analysis and anisotropy evaluation of 3D-printed tensile test specimens of different geometries and print raster patterns," *Journal of Failure Analysis and Prevention*, vol. 16, no. 1, pp. 154–164, 2016.

[207] N. Ersumo, C. E. Witherel, and K. L. Spiller, "Differences in time-dependent mechanical properties between extruded and molded hydrogels," *Biofabrication*, vol. 8, no. 3, p. 035012, 2016.

[208] B. Lawless, *Biostability of an orthopaedic device and its long-term implantable biomaterials. University of Birmingham.* PhD thesis, University of Birmingham, 2019.

[209] J. Chakrabarty, *Applied plasticity*, vol. 758. Springer, 2010.

[210] H. Gao, J. He, R. Yang, and L. Yang, "Characteristic rheological features of high concentration PVA solutions in water with different degrees of polymerization," *Journal of Applied Polymer Science*, vol. 116, no. 5, pp. 2734–2741, 2010.

[211] M. Guvendiren, H. D. Lu, and J. A. Burdick, "Shear-thinning hydrogels for biomedical applications," *Soft Matter*, vol. 8, no. 2, pp. 260–272, 2012.

[212] S. Uman, A. Dhand, and J. A. Burdick, "Recent advances in shear-thinning and self-healing hydrogels for biomedical applications," *Journal of Applied Polymer Science*, vol. 137, no. 25, p. 48668, 2020.

[213] E. A. Appel, J. del Barrio, X. J. Loh, and O. A. Scherman, "Supramolecular polymeric hydrogels," *Chemical Society Reviews*, vol. 41, no. 18, pp. 6195–6214, 2012.

[214] Y. Chen, C. Jiao, X. Peng, T. Liu, Y. Shi, M. Liang, and H. Wang, "Biomimetic anisotropic poly(vinyl alcohol) hydrogels with significantly enhanced mechanical properties by freezing–thawing under drawing," *Journal of Materials Chemistry B*, vol. 7, no. 20, pp. 3243–3249, 2019.

[215] T. Hatakeyama, A. Yamauchi, and H. Hatakeyama, "Effect of thermal hysteresis on structural change of water restrained in poly(vinyl alcohol) pseudo-gel," *European Polymer Journal*, vol. 23, no. 5, pp. 361–365, 1987.

[216] J. Li, G. Yang, T. Siebert, M. F. Shi, and L. Yang, "A method of the direct measurement of the true stress–strain curve over a large strain range using multi-camera digital image correlation," *Optics and Lasers in Engineering*, vol. 107, pp. 194–201, 2018.

[217] H. Hoffmann and C. Vogl, "Determination of true stress-strain-curves and normal anisotropy in tensile tests with optical strain measurement," *CIRP Annals*, vol. 52, no. 1, pp. 217–220, 2003.

[218] M. H. Kural, M. Cai, D. Tang, T. Gwyther, J. Zheng, and K. L. Billiar, "Planar biaxial characterization of diseased human coronary and carotid arteries for computational modeling," *Journal of Biomechanics*, vol. 45, no. 5, pp. 790–798, 2012.

[219] E. Claes, J. Atienza, G. Guinea, F. Rojo, J. Bernal, J. Revuelta, and M. Elices, "Mechanical properties of human coronary arteries," *Conference proceedings : Annual International Conference of the IEEE Engineering in Medicine and Biology Society. IEEE Engineering in Medicine and Biology Society. Conference*, vol. 2010, pp. 3792–5, 08 2010.

[220] I. Faridmehr, M. Osman, A. Adnan, A. Nejad, R. Hodjati, and M. Amin, "Correlation between engineering stress-strain and true stress-strain curve," *American Journal of Civil Engineering and Architecture*, vol. 2, pp. 53–59, 03 2014.

[221] J. M. Choung and S. R. Cho, "Study on true stress correction from tensile tests," *Journal of Mechanical Science and Technology*, vol. 22, no. 6, pp. 1039–1051, 2008.

[222] C. Vergari, P. Pourcelot, L. Holden, B. Ravary-Plumioën, G. Gerard, P. Laugier, D. Mitton, and N. Crevier-Denoix, "True stress and Poisson's ratio of tendons during loading," *Journal of Biomechanics*, vol. 44, no. 4, pp. 719–724, 2011.

[223] G. H. Loh, E. Pei, D. Harrison, and M. D. Monzón, "An overview of functionally graded additive manufacturing," *Additive Manufacturing*, vol. 23, pp. 34–44, 2018.

[224] N. Oxman, "Variable property rapid prototyping," *Virtual and Physical Prototyping*, vol. 6, pp. 3–31, 03 2011.

[225] P. Popoola, G. Farotade, O. Fatoba, and O. Popoola, *Laser Engineering Net Shaping Method in the Area of Development of Functionally Graded Materials (FGMs) for Aero Engine Applications - A Review*, ch. 17. IntechOpen, 03 2016.

[226] R. Gabbrielli, I. Turner, and C. Bowen, "Development of modelling methods for materials to be used as bone substitutes," *Key Engineering Materials - KEY ENG MAT*, vol. 361-363, pp. 903–906, 01 2008.

[227] V. A. Popovich, E. V. Borisov, A. A. Popovich, V. S. Sufiiarov, D. V. Masaylo, and L. Alzina, "Functionally graded inconel 718 processed by additive manufacturing: Crystallographic texture, anisotropy of microstructure and mechanical properties," *Materials & Design*, vol. 114, pp. 441–449, 2017.

[228] A. Seidi, M. Ramalingam, I. Elloumi-Hannachi, S. Ostrovidov, and A. Khademhosseini, "Gradient biomaterials for soft-to-hard interface tissue engineering," *Acta Biomaterialia*, vol. 7, no. 4, pp. 1441–1451, 2011.

[229] G. Haïat, S. Naili, Q. Grimal, M. Talmant, C. Desceliers, and C. Soize, "Influence of a gradient of material properties on ultrasonic wave propagation in cortical bone: Application to axial transmission," *The Journal of the Acoustical Society of America*, vol. 125, no. 6, pp. 4043–4052, 2009.

[230] I. M. Shapiro and M. V. Risbud, *Introduction to the Structure, Function, and Comparative Anatomy of the Vertebrae and the Intervertebral Disc*, pp. 3–15. Vienna: Springer Vienna, 2014.

[231] M. K. Rausch, W. Bothe, J.-P. E. Kvitting, J. C. Swanson, D. C. Miller, and E. Kuhl, "Mitral valve annuloplasty," *Annals of Biomedical Engineering*, vol. 40, no. 3, pp. 750–761, 2012.

[232] A. H. A. Wahab, A. P. M. Saad, M. N. Harun, A. Syahrom, M. H. Ramlee, M. A. Sulong, and M. R. A. Kadir, "Developing functionally graded PVA hydrogel using simple freeze-thaw method for artificial glenoid labrum," *Journal of the Mechanical Behavior of Biomedical Materials*, vol. 91, pp. 406–415, 2019.

[233] A. Gleadall, "Fullcontrol gcode designer: Open-source software for unconstrained design in additive manufacturing," *Additive Manufacturing*, vol. 46, p. 102109, 2021.

[234] Z. Fu, S. Naghieh, C. Xu, C. Wang, W. Sun, and X. Chen, "Printability in extrusion bioprinting," *Biofabrication*, vol. 13, no. 3, p. 033001, 2021.

[235] A. Schwab, R. Levato, M. D'Este, S. Piluso, D. Eglin, and J. Malda, "Printability and shape fidelity of bioinks in 3D bioprinting," *Chemical Reviews*, vol. 120, pp. 11028–11055, 10 2020.

[236] Y. He, F. Yang, H. Zhao, Q. Gao, B. Xia, and J. Fu, "Research on the printability of hydrogels in 3D bioprinting," *Scientific Reports*, vol. 6, no. 1, p. 29977, 2016.

[237] J. Schindelin, I. Arganda-Carreras, E. Frise, V. Kaynig, M. Longair, T. Pietzsch, S. Preibisch, C. Rueden, S. Saalfeld, B. Schmid, J.-Y. Tinevez, D. J. White, V. Hartenstein, K. Eliceiri, P. Tomancak, and A. Cardona, "Fiji: an open-source platform for biological-image analysis," *Nature Methods*, vol. 9, no. 7, pp. 676–682, 2012.

[238] E. Tosoratti, I. Incaviglia, O. Liashenko, C. Leinenbach, and M. Zenobi-Wong, "Additively manufactured semiflexible titanium lattices as hydrogel reinforcement for biomedical implants," *Advanced NanoBiomed Research*, vol. 1, no. 1, p. 2000031, 2021.

[239] V. Pazos, R. Mongrain, and J. C. Tardif, "Polyvinyl alcohol cryogel: Optimizing the parameters of cryogenic treatment using hyperelastic models," *Journal of the Mechanical Behavior of Biomedical Materials*, vol. 2, no. 5, pp. 542–549, 2009.

[240] G. Sommer, P. Regitnig, L. Költringer, and G. A. Holzapfel, "Biaxial mechanical properties of intact and layer-dissected human carotid arteries at physiological and supraphysiological loadings," *American Journal of Physiology-Heart and Circulatory Physiology*, vol. 298, no. 3, pp. H898–H912, 2009.

[241] H. Gao, R. Yang, J. He, and L. Yang, "Rheological behaviors of PVA/H_2O solutions of high-polymer concentration," *Journal of applied polymer science*, vol. 116, no. 3, pp. 1459–1466, 2010.

[242] J. C. Mankins, "Technology readiness assessments: A retrospective," *Acta Astronautica*, vol. 65, no. 9, pp. 1216–1223, 2009.

[243] A. Savoini and A. Tronchin, "Definition of technology readiness levels (TRL) and application to biomedical field," 2014.

Appendix A

DMA & MRI SUPPLEMENTARY DATA

Appendix A includes supplementary data for chapter 3, this includes: complete data for DMA of all compositions of PVA discussed; constants for curve fitting coefficients for DMA data, at all frequencies; curve fitting coefficients for T_2 relaxation time with respect to concentration; and curve fitting coefficients for DMA data with respect to T_2 relaxation time.

Table A.1: *Storage Modulus (Mean ± SD) for all PVA-A samples tested at frequencies between 0.5-10 Hz.*

Freq. (Hz)	Storage Modulus (Pa)							
	10% W/W		15% W/W		17.5% W/W		20% W/W	
	Mean	SD	Mean	SD	Mean	SD	Mean	SD
0.5	158000	9500	298000	5500	362000	16000	484000	24000
1	159000	8400	301000	3900	373000	15000	501000	22000
2	163000	8500	308000	4700	388000	14000	518000	24000
3	165000	8600	312000	5200	397000	13000	529000	25000
4	167000	8600	315000	5400	404000	13000	535000	26000
6	169000	8700	319000	5800	414000	13000	546000	26000
8	171000	8800	323000	5900	421000	14000	552000	27000
10	172000	8800	324000	5900	425000	14000	557000	27000

Table A.2: *Storage Modulus (Mean ± SD) for all PVA-B samples tested at frequencies between 0.5-10 Hz.*

Freq. (Hz)	Storage Modulus (Pa)							
	10% W/W		15% W/W		17.5% W/W		20% W/W	
	Mean	SD	Mean	SD	Mean	SD	Mean	SD
0.5	55000	2400	172000	4400	245000	36000	361000	25000
1	55700	2200	175000	4800	247000	36000	367000	27000
2	56600	2200	177000	4900	251000	37000	373000	27000
3	57100	2200	179000	5000	253000	37000	376000	28000
4	57500	2300	180000	5000	254000	37000	378000	28000
6	58100	2300	183000	5100	256000	38000	382000	28000
8	58500	2300	184000	5200	258000	38000	385000	28000
10	58900	2300	185000	5200	259000	39000	387000	29000

Table A.3: *Storage Modulus (Mean ± SD) for all PVA-C samples tested at frequencies between 0.5-10 Hz.*

Freq. (Hz)	Storage Modulus (Pa)							
	10% W/W		15% W/W		17.5% W/W		20% W/W	
	Mean	SD	Mean	SD	Mean	SD	Mean	SD
0.5	333000	59000	588000	34000	655000	31000	840000	36000
1	336000	59000	605000	35000	674000	30000	862000	39000
2	343000	60000	627000	37000	692000	28000	883000	40000
3	348000	60000	639000	37000	702000	27000	892000	41000
4	350000	60000	646000	38000	708000	26000	898000	41000
6	355000	60000	656000	38000	715000	25000	906000	42000
8	357000	60000	661000	38000	720000	24000	909000	42000
10	359000	59000	664000	38000	722000	23000	912000	43000

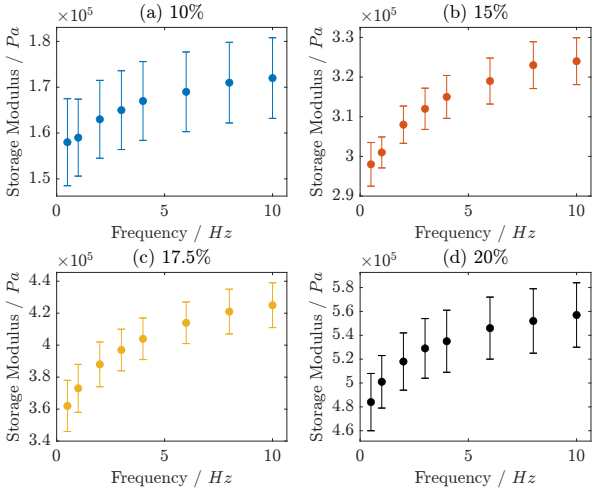

(a) PVA-A

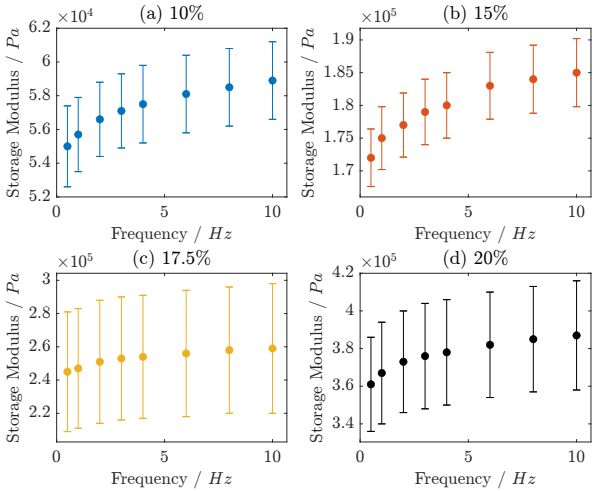

(b) PVA-B

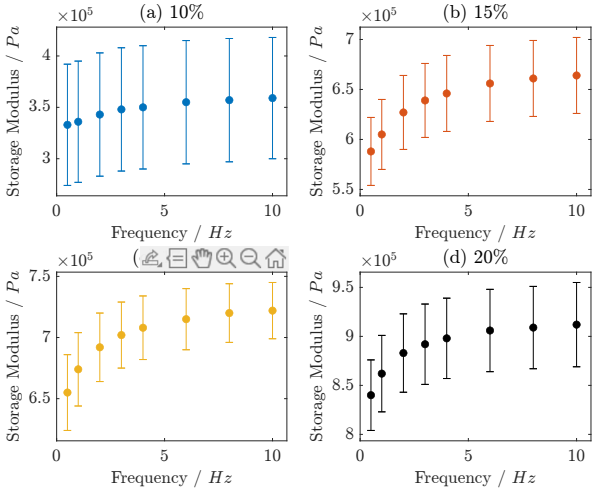

(c) PVA-C

Figure A.1: *Figure 1: Storage modulus indicating frequency dependency at 10, 15, 17.5, and 20% for PVA-A (top left), PVA-B (top right), and PVA-C (bottom).*

Table A.4: *Loss Modulus (Mean ± SD) for all PVA-A samples tested at frequencies between 0.5-10 Hz.*

Freq. (Hz)	Loss Modulus (Pa)							
	10% W/W		15% W/W		17.5% W/W		20% W/W	
	Mean	SD	Mean	SD	Mean	SD	Mean	SD
0.5	25400	2300	45700	2700	65500	5700	86500	2300
1	26400	2100	46600	2700	67600	6400	88200	3800
2	27200	2400	47400	2900	69200	7900	89300	5100
3	28000	2400	47900	3400	70300	8900	90200	5500
4	28700	2400	48700	3800	70800	9400	91200	5600
6	29900	2700	50100	4200	71800	9800	93500	5900
8	31200	2800	51800	4600	72900	9800	96200	6200
10	32300	2900	53600	4600	75300	9800	99400	6500

Table A.5: *Loss Modulus (Mean ± SD) for all PVA-B samples tested at frequencies between 0.5-10 Hz.*

Freq. (Hz)	Loss Modulus (Pa)							
	10% W/W		15% W/W		17.5% W/W		20% W/W	
	Mean	SD	Mean	SD	Mean	SD	Mean	SD
0.5	2820	240	8890	1800	12300	1700	20900	7800
1	2980	200	8920	890	12800	1900	19700	5100
2	3260	160	9670	550	13800	2200	20400	3500
3	3550	150	10700	420	15200	2500	22100	2900
4	3820	150	11700	370	16600	2800	24000	2800
6	4410	170	13700	300	19400	3300	27900	2700
8	4990	180	15600	310	22200	3900	31700	2900
10	5550	210	17600	340	24800	4300	35700	3100

Table A.6: *Loss Modulus (Mean ± SD) for all PVA-C samples tested at frequencies between 0.5-10 Hz.*

Freq. (Hz)	Loss Modulus (Pa)							
	10% W/W		15% W/W		17.5% W/W		20% W/W	
	Mean	SD	Mean	SD	Mean	SD	Mean	SD
0.5	38100	5400	87800	11000	90200	5800	103000	14000
1	38700	4900	87100	13000	85300	6000	95000	10000
2	37900	3900	81900	15000	78400	7000	84700	10000
3	37400	3400	77800	15000	74800	7100	79700	9500
4	37300	3100	75000	15000	72600	7000	77200	9000
6	37700	2700	72300	14000	71300	6500	76100	8000
8	38600	2800	71900	13000	72000	5900	77800	7400
10	39900	3000	73100	13000	74000	5500	81000	7000

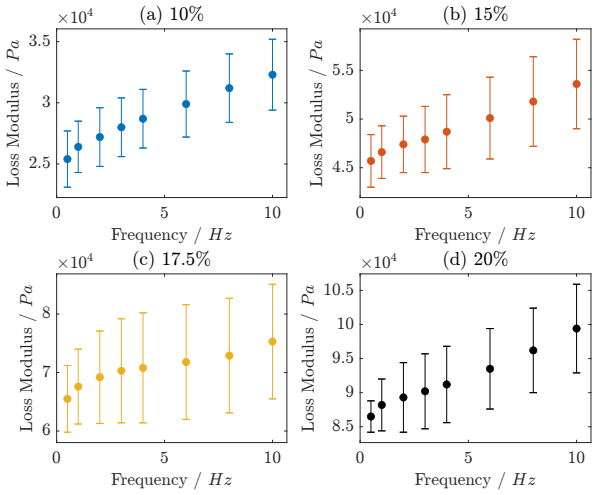

(a) PVA-A

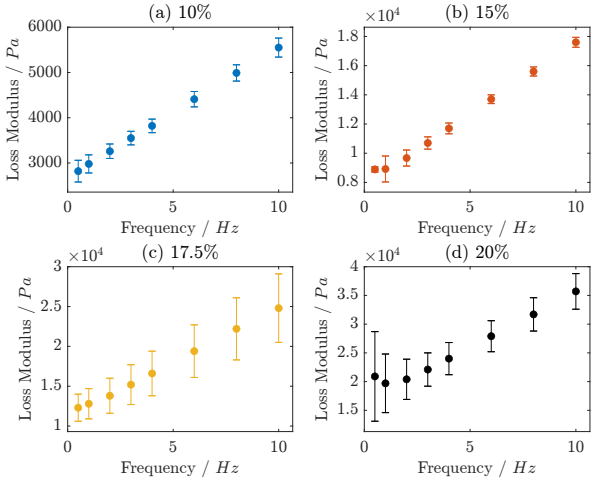

(b) PVA-B

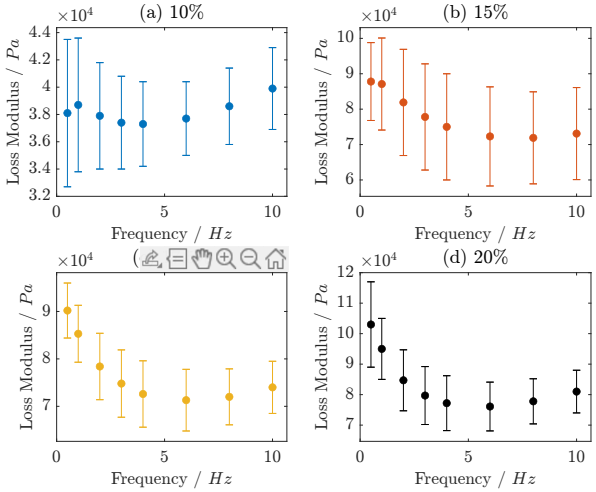

(c) PVA-C

Figure A.2: *Figure 1: Loss modulus indicating frequency dependency at 10, 15, 17.5, and 20% for PVA-A (top left), PVA-B (top right), and PVA-C (bottom).*

Table A.7: *Storage and Loss constants with respect to concentration of PVA-A and PVA-B for frequencies between 0.5 and 10 Hz. (Equations 7 & 8)*

	Freq.	Storage Modulus (Pa)				Loss Modulus (Pa)			
	(Hz)	as	bs	ds	R2	al	bl	dl	R2
PVA-A	0.5	-86400	108000	0.083	0.98	-1640	8080	0.12	0.97
	1	-70600	94800	0.09	0.98	-2170	8690	0.117	0.97
	2	-75700	97400	0.09	0.98	-2780	9390	0.115	0.95
	3	-76400	98000	0.091	0.99	-1630	9140	0.116	0.94
	4	-86700	104000	0.089	0.99	157	8550	0.119	0.94
	6	-99200	113000	0.087	0.99	3480	7460	0.125	0.93
	8	-108000	118000	0.086	0.99	6680	6470	0.132	0.93
	10	-103000	115000	0.087	0.99	7360	6510	0.133	0.94
PVA-B	0.5	-92000	48700	0.114	0.96	-339	536	0.183	0.94
	1	-89000	46800	0.114	0.96	-2320	1330	0.14	0.83
	2	-88700	46800	0.114	0.96	-4360	2390	0.117	0.9
	3	-91600	48000	0.114	0.96	-5950	3260	0.107	0.92
	4	-91600	48000	0.114	0.96	-7560	4160	0.101	0.93
	6	-90700	47900	0.114	0.96	-9720	5360	0.0973	0.94
	8	-91600	48500	0.114	0.96	-12000	6640	0.0941	0.94
	10	-90300	47600	0.112	0.96	-13600	7500	0.0939	0.93

Table A.8: *Storage constants with respect to concentration of PVA-C for frequencies between 0.5 and 10 Hz. (Equation 9)*

	Freq. (Hz)	f	g	R2
PVA-C	0.5	-167000	53200	0.93
	1	-171000	50600	0.94
	2	-174000	51900	0.94
	3	-174000	52400	0.94
	4	-173000	52700	0.94
	6	-170000	53000	0.94
	8	-168000	53100	0.94
	10	-158000	48700	0.93

Table A.9: *Mean MR T2 relaxation rate constants for PVA-A. B. and C. (Equation 10)*

	f	g	R2
PVA-A	0.0040	0.00043	0.99
PVA-B	-0.00020	0.00080	0.99
PVA-C	0.0034	0.00050	0.97

Table A.10: *Multiplication factors comparing variation of viscoelastic properties when MW is increased from 89-98 kDa to 146-186 kDa (10-20% PVA-A and C) between frequencies of 0.5 and 10 Hz.*

Freq. (Hz)	Storage Modulus (Pa)				Loss Modulus (Pa)			
	10% W/W	15% W/W	17.5% W/W	20% W/W	10% W/W	15% W/W	17.5% W/W	20% W/W
0.5	2.1 ×	2.0 ×	1.8 ×	1.7 ×	1.5 ×	2.0 ×	1.4 ×	1.2 ×
1	2.1 ×	2.0 ×	1.8 ×	1.7 ×	1.5 ×	1.9 ×	1.3 ×	1.1 ×
2	2.1 ×	2.0 ×	1.8 ×	1.7 ×	1.4 ×	1.7 ×	1.1 ×	0.93 ×
3	2.1 ×	2.1 ×	1.8 ×	1.7 ×	1.3 ×	1.6 ×	1.1 ×	0.87 ×
4	2.1 ×	2.1 ×	1.7 ×	1.7 ×	1.3 ×	1.5 ×	1.0 ×	0.83 ×
6	2.1 ×	2.1 ×	1.7 ×	1.7 ×	1.3 ×	1.4 ×	1.0 ×	0.80 ×
8	2.1 ×	2.1 ×	1.7 ×	1.7 ×	1.2 ×	1.4 ×	1.0 ×	0.80 ×
10	2.1 ×	2.1 ×	1.7 ×	1.6 ×	1.2 ×	1.4 ×	1.0 ×	0.80 ×
Average	**2.1 ×**	**2.0 ×**	**1.8 ×**	**1.7 ×**	**1.2 ×**	**1.6 ×**	**1.1 ×**	**0.91 ×**
SD	**0.0083**	**0.027**	**0.039**	**0.033**	**0.094**	**0.21**	**0.14**	**0.14**

Table A.11: *Multiplication factors comparing variation of viscoelastic properties when the number of freeze thaw cycles is increased from 1 to 3 (10-20% PVA-B and C) between frequencies of 0.5 and 10 Hz.*

Freq. (Hz)	Storage Modulus (Pa)				Loss Modulus (Pa)			
	10% W/W	15% W/W	17.5% W/W	20% W/W	10% W/W	15% W/W	17.5% W/W	20% W/W
0.5	6.1 ×	3.4 ×	2.7 ×	2.3 ×	14 ×	9.9 ×	7.3 ×	4.9 ×
1	6.0 ×	3.5 ×	2.7 ×	2.3 ×	13 ×	9.8 ×	6.7 ×	4.8 ×
2	6.1 ×	3.5 ×	2.8 ×	2.4 ×	12 ×	8.5 ×	5.7 ×	4.2 ×
3	6.1 ×	3.6 ×	2.8 ×	2.4 ×	11 ×	7.3 ×	4.9 ×	3.6 ×
4	6.1 ×	3.6 ×	2.8 ×	2.4 ×	9.8 ×	6.4 ×	4.4 ×	3.2 ×
6	6.1 ×	3.6 ×	2.8 ×	2.4 ×	8.5 ×	5.3 ×	3.7 ×	2.7 ×
8	6.1 ×	3.6 ×	2.8 ×	2.4 ×	7.7 ×	4.6 ×	3.2 ×	2.5 ×
10	6.1 ×	3.6 ×	2.8 ×	2.4 ×	7.2 ×	4.2 ×	3.0 ×	2.3 ×
Average	**6.1 ×**	**3.5 ×**	**2.8 ×**	**2.4 ×**	**10 ×**	**7.0 ×**	**4.9 ×**	**3.5 ×**
SD	**0.026**	**0.063**	**0.039**	**0.015**	**2.2**	**2.1**	**1.5**	**0.97**

Table A.12: *Storage and loss constants with respect to MR T2 relaxation rate of PVA-A for frequencies between 0.5 and 10 Hz. (Equations 11 & 13)*

Freq. (Hz)	Storage Modulus (Pa)				Loss Modulus (Pa)			
	as	bs	ds	*R2*	al	bl	dl	*R2*
0.5	86800	2680	388	0.98	17000	119	496	0.98
1	91100	2200	406	0.98	17500	130	491	0.97
2	91900	2210	409	0.98	17900	143	485	0.95
3	93400	2180	412	0.98	18800	137	488	0.94
4	91900	2340	408	0.99	19800	124	496	0.94
6	90600	2530	404	0.99	21600	102	511	0.93
8	89600	2670	401	0.99	23400	83.2	528	0.93
10	92000	2560	405	0.99	24400	82.8	531	0.94

Table A.13: *Storage and loss constants with respect to MR T2 relaxation rate of PVA-B for frequencies between 0.5 and 10 Hz. (Equations 12 and 14)*

Freq. (Hz)	Storage Modulus (Pa)			Loss Modulus (Pa)		
	as	bs	R2	al	bl	R2
0.5	-243000	35200000	0.95	-14900	2030000	0.70
1	-247000	35700000	0.95	-13500	1910000	0.82
2	-250000	36200000	0.95	-13500	1970000	0.89
3	-252000	36500000	0.95	-14500	2130000	0.92
4	-254000	36700000	0.95	-15700	2320000	0.92
6	-256000	37000000	0.95	-18400	2700000	0.93
8	-257000	37300000	0.95	-20900	3080000	0.94
10	-259000	37500000	0.95	-23500	3460000	0.94

Appendix B

SUB ZERO AM DMA DATA

Appendix B includes supplementary data relevant to chapter 4. This includes: The temperature profile of the sub-zero AM print bed; complete DMA data for all frequencies tested; average increases for all frequencies between nozzle sizes; p-values for t-tests performed comparing nozzle sizes; and the Matlab code used to calculate DMA data from engineering or true stress & strain.

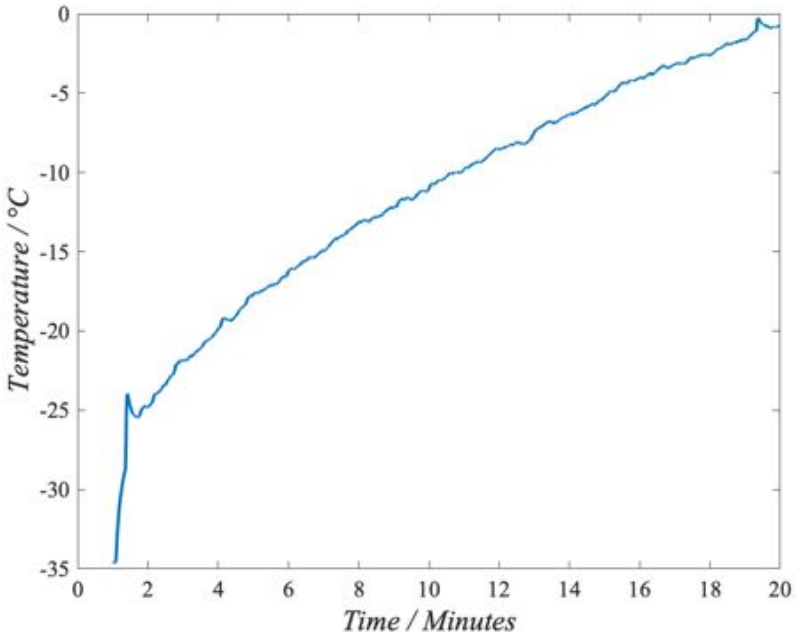

Figure B.1: *Temperature profile of the steel print bed during the first 20 minutes upon removal from the freezer. Samples were manufactured within the first 5 minutes of removal from the freezer.*

Table B.1: *Mean Values and Standard Deviation for storage and loss moduli of additively manufactured samples of PVA using a 25G nozzle. (N = 6)*

	Perpendicular		Parallel	
Freq (Hz)	E' (Pa)	SD	E' (Pa)	SD
0.5	59300	5490	92400	7380
1	59200	5420	93000	7240
2	59700	5470	93900	7230
3	59900	5420	94400	7190
4	60200	5460	94900	7090
6	60400	5580	95200	6920
8	60800	5660	95900	6900
10	61300	5670	96800	6950
	E" (Pa)	SD	E" (Pa)	SD
0.5	2150	164	3260	564
1	2450	187	3650	423
2	3170	214	4540	416
3	3830	253	5350	434
4	4520	291	6220	441
6	5620	377	7650	459
8	6690	439	9080	528
10	7580	451	10200	600

Table B.2: *Mean Values and Standard Deviation for storage and loss moduli of additively manufactured samples of PVA using a 22G nozzle. (N = 6)*

	Perpendicular		Parallel	
Freq (Hz)	E' (Pa)	SD	E' (Pa)	SD
0.5	67000	5240	77300	4640
1	67000	5240	77500	4640
2	67400	5280	78000	4620
3	67600	5340	78300	4700
4	67700	5380	78500	4680
6	68000	5380	78900	4670
8	68200	5430	79100	4700
10	68300	5490	79100	4680
	E" (Pa)	SD	E" (Pa)	SD
0.5	1570	114	1870	213
1	1850	154	2200	157
2	2430	185	2840	179
3	3020	203	3460	165
4	3550	250	4010	178
6	4620	302	5150	235
8	5480	341	6180	247
10	6310	374	7090	269

Table B.3: *Mean Values and Standard Deviation for storage and loss moduli of additively manufactured samples of PVA using a 18G nozzle. (N = 6)*

	Perpendicular		Parallel	
Freq (Hz)	E' (Pa)	SD	E' (Pa)	SD
0.5	77100	2130	79300	4330
1	77000	1950	79200	4250
2	77400	1880	79600	4160
3	77700	1820	80000	4240
4	78000	1860	80400	4260
6	78300	1820	80700	4280
8	78500	1810	81000	4220
10	78700	1810	81300	4220
	E" (Pa)	SD	E" (Pa)	SD
0.5	1550	225	1800	420
1	1930	61.4	1960	171
2	2590	70.3	2580	295
3	3190	81.3	3340	201
4	3890	88.8	4020	248
6	5030	119	5150	286
8	6060	180	6210	368
10	7000	158	7180	375

Table B.4: *Mean Values and Standard Deviation for storage and loss moduli of cast control samples of PVA. (N = 6)*

Freq	E' (Pa)	SD	E" (Pa)	SD
0.5	72300	2930	1360	155
1	73100	3120	1670	145
2	74000	3250	2060	179
3	74600	3500	2460	194
4	75300	3660	2890	232
6	76200	3720	3590	221
8	77100	3940	4340	288
10	78000	4160	5070	352

Table B.5: *Average increase in storage and loss moduli when comparing additively manufactured samples of PVA tested in perpendicular and parallel orrientiatons for three nozzle sizes. (N = 6)*

	0.51 mm		0.71 mm		1.28 mm	
Freq	E'	E"	E'	E"	E'	E"
0.1	35.8	34.2	13.2	16.1	2.8	13.8
1	36.4	32.8	13.5	16.2	2.78	1.51
2	36.5	30.3	13.6	14.4	2.77	-0.538
3	36.6	28.4	13.6	12.8	2.93	4.59
4	36.6	27.3	13.8	11.4	2.98	3.23
6	36.5	26.5	13.8	10.4	3.02	2.4
8	36.6	26.3	13.8	11.3	3.1	2.42
10	36.7	25.6	13.7	11	3.21	2.57
Average	36.4	28.9	13.6	12.9	2.95	3.75
SD	0.255	2.96	0.181	2.17	0.148	4.04

Table B.6: *P-values for unpaired t-tests comparing storage and loss moduli tested in perpendicular and parallel orientations for 3 nozzle sizes.*

Freq (Hz)	25G (small)		22G (medium)		18G (large)	
	E' (Pa)	E" (Pa)	E' (Pa)	E" (Pa)	E' (Pa)	E" (Pa)
0.5	1.10E-05	0.0017	0.0085	0.019	0.33	0.27
1	7.90E-06	0.00018	0.0074	0.0046	0.32	0.72
2	7.30E-06	6.20E-05	0.0069	0.0053	0.3	0.92
3	6.40E-06	4.90E-05	0.0073	0.0035	0.28	0.15
4	5.80E-06	2.90E-05	0.0068	0.0076	0.28	0.3
6	5.30E-06	1.80E-05	0.0066	0.011	0.27	0.39
8	5.10E-06	1.50E-05	0.0069	0.0041	0.25	0.43
10	4.80E-06	1.50E-05	0.0072	0.0037	0.23	0.33
Average	6.70E-06	2.60E-04	7.20E-03	7.30E-03	2.80E-01	4.40E-01
SD	1.90E-06	5.20E-04	5.30E-04	4.70E-03	2.90E-02	2.30E-01

```
%% DMA_eng
%This script will calculate storage and loss moduli based on engineering stress and strain
%Calculations of moduli will be made AFTER the FFT.
%Inputs
% all .dat files for the sample should be placed in the same folder as this
% script
%h = height of sample
%w = width of sample
%t = thickness of sample
%sample_name = user defined name for output file of viscoelastic properties

%Outputs
%A graph of storage and loss modulus plotted against frequency
% A .xlsx output file called sample_name, containing:
%Test frequency
%Complex modulus
%Storage modulus
%Loss modulus
%Phase angle

h = ; %Sample height
w  = ; %Sample width
t = ; %Sample thickness

sample_name = 'sample';

DatFiles = dir ('*.dat');

for file = DatFiles'

    fprintf(1, 'Calculating viscoelastic properties for: %s.\n', file.name)
    currentfile = file.name;

    outputfile = create_output(sample_name); %create output file
    [time, dispdata, loaddata]= import_file(currentfile);    % import data
    [maxload, maxdisp, frequency, degrees, radians] = fourier_eng(loaddata, dispdata, time);    %Fourier transform
    [complex, storage, loss] = visc_properties(maxload, maxdisp, radians, w, h, t);     %Calc. viscoelastic properties
    export_data (outputfile, frequency, complex, storage, loss, degrees)    %Export data
    disp('Continuing...')

end
```

```
42
43      plot_data (outputfile, sample_name)
44
45      disp('End of Results')
```

```
1  %% DMA_true
2  %This script will calculate storage and loss moduli based on true
       stress and strain
3
4  %Inputs
5  % all .dat files for the sample should be placed in the same folder
       as this
6  % script
7  %h = height of sample
8  %w = width of sample
9  %t = thickness of sample
10
11 %sample_name = user defined name for output file of viscoelastic
       properties
12
13 %Outputs
14 %A graph of storage and loss modulus plotted against frequency
15 % A .xlsx output file called sample_name, containing:
16 %Test frequency
17 %Complex modulus
18 %Storage modulus
19 %Loss modulus
20 %Phase angle
21
22
23 h = 8.5;
24 w  = 19;
25 t = 0.4;
26
27 sample_name = 'eng_S3';
28
29 DatFiles = dir ('*.dat');
30
31 for file = DatFiles'
32
33      fprintf(1, 'Calculating viscoelastic properties for: %s.\n',
           file.name)
34      currentfile = file.name;
35
36      outputfile = create_output(sample_name); %create output file
37
38      [time, dispdata, loaddata]= import_file(currentfile); %import
           data
39
40      [truestress, truestrain] = eng_stress_strain(w,h,t, dispdata,
```

```
        loaddata, currentfile);

        [maxstress, maxstrain, frequency, degrees, radians] =
            fourier_true(truestress, truestrain, time); %Fourier
            transform

        [complex, storage, loss] = visc_properties_true(maxstress,
            maxstrain, radians); %Calc. viscoelastic properties

        export_data (outputfile, frequency, complex, storage, loss,
            degrees); %Export data

    disp('Continuing...')

end
    plot_data (outputfile, sample_name)

    disp('End of Results')
```

```
%% Import_file
%This function will import raw data from data file

%Inputs:
%f = .dat file containing raw data from Bose 3200

%Outputs:
%Time = raw time data
%Disp = raw displacement data
%Load = raw load data

function [Time, Disp, Load] = import_file(f)
CurrentFile = f;
FileArray = readmatrix(CurrentFile);
Line = FileArray(:,1) < 0;
FileArray(Line,:) = [];

Time = FileArray(:,1);
Disp = FileArray(:,2);
Mass = FileArray(:,3);
Load = Mass;% * (9.807*10^-3);

Disp = abs(Disp);
Load = abs(Load);

writematrix(Time, 'time')

end


\begin{lstlisting}[basicstyle=\small]
```

```
%% eng_stress_strain

%This function will calculate the engineering stress and strain PRIOR to
%the FFT

%Inputs
%w = sample width
%h = sample height
%t = sample thickness
%d = raw displacement data
%l = raw load data

%Outputs
%stress = stress data
%strain = strain data

function [stress, strain] = eng_stress_strain(w,h,t, d, l)

CSA = w*t; % Rectangle CSA (mm^2) For a cylindrical sample: CSA = pi*(w^2);

strain = d/h; %Strain Calculation

stress = l./CSA; %Engineering Stress Calculation

end
```

```
%% true_stress_strain

%This function will calculate the true stress and strain PRIOR to
%the FFT

%Inputs
%w = sample width
%h = sample height
%t = sample thickness
%d = raw displacement data
%l = raw load data

%Outputs
%stress = stress data
%strain = strain data

function [truestress, truestrain] = true_stress_strain(w,h,t, d, l)

%CSA = w*t; % Rectangle CSA (mm^2)
CSA = pi*(w^2);

correctedH = h-d;  %Calculating actual height (+ for extension, -
```

```
    for compression)
Lambda = correctedH/h; %Ratio between actual and inital length
correctedCSA = CSA./Lambda; %Corrected Rectangle CSA

Strain = d/h; %Strain Calculation

%truestrain = log(1+Strain); %True Strain Calculation - extension
truestrain = -log(1-Strain); %True Strain Calculation -
    compresssion
truestress = l./correctedCSA; %True Stress Calculation

end
```

```
%% fourier_eng
%This function will calculate the fourier transform of the raw
    displacement
%and load data.
%Inputs
%l = raw load data
%d = raw displacement data
%t = raw time data

%Outputs
%max_load = peak of load FFT
%max_disp = peak of displacement FFT
%freq = actual test frequency
%deg = phase angle in degrees
%rad = phase angle in radians

function [max_load, max_disp, freq, deg, rad] = fourier_eng(l, d, t
    )

L = length(l);
T = abs(t(find(diff(t),1)+1)-t(1));     % Measuring the Time Step
Fs = 1/T;                                % Sampling
    Frequency
f = Fs*(0:(L/2))/L;

fftL = fft(l);
fftD = fft(d);

DispP2 = abs(fftD/L);                   %Compute two sided spectrum
    for displacement
DispP1 = DispP2(1:floor(L/2+1));
DispP1(2:end-1) = 2*DispP1(2:end-1);     %Compute single sided
    spectrum for Displacement

LoadP2 = abs(fftL/L);                   %Compute two sided spectrum
    for Load
LoadP1 = LoadP2(1:floor(L/2+1));
```

```
LoadP1(2:end-1) = 2*LoadP1(2:end-1);    %Compute single sided spectrum for Load

% plot(f, LoadP1, 'k', 'LineWidth', 1.5)
% set(gca,'TickLabelInterpreter','latex','FontSize',18)
% ylabel('Load Magnitude', 'Interpreter', 'latex', 'fontsize', 22)
% xlabel('Frequency / Hz', 'Interpreter', 'latex', 'fontsize', 22)
% set(gca, 'XScale', 'log', 'YScale', 'log')
% axis padded
% set(gca,'YTick',[],'XTick',[])
% exportgraphics(gcf,'Load_fft.pdf')
%%
% plot(f, DispP1, 'k', 'LineWidth', 1.5)
% set(gca,'TickLabelInterpreter','latex','FontSize',18)
% ylabel('Displacement Magnitude', 'Interpreter', 'latex', 'fontsize', 22)
% xlabel('Frequency / Hz', 'Interpreter', 'latex', 'fontsize', 22)
% set(gca, 'XScale', 'log', 'YScale', 'log')
% axis padded
% set(gca,'YTick',[],'XTick',[])
% exportgraphics(gcf,'Disp_fft.pdf')


[max_load, x1]=max(LoadP1(2:end)); % Finding the position of the peak of the fft of load
[max_disp, x2]=max(DispP1(2:end)); % Finding the position of the peak of the fft of disp


r = abs(angle(fftL(x1+1))-angle(fftD(x2+1))); %Measure of phase angle in radians
deg = r*180/pi;
if deg > 90                                  % If the phase angle is greater that 90 degree
 disp('WARNING: THE PHASE ANGLE IS GREATER THAT 90 DEGREES!')
 degr=180-deg;
else                                         % if the phase angle is less than 90 degree
 degr= deg;
end

freq = f(x2+1);
deg = (0.1323*freq)+degr;
rad = (deg*pi)/180; % Converting phase angle from deg to radians
end
```

```
%% fourier_true
%This function will calculate the fourier transform of the stress and strain data displacement
%and load data.
```

```
4  %Inputs
5  %stress = stress data (calculated by eng_stress_strain or
6  %true_stress_strain
7  %strain = raw displacement data
8  %t = raw time data
9
10 %Outputs
11 %max_stress = peak of stress FFT
12 %max_strain = peak of strain FFT
13 %freq = actual test frequency
14 %deg = phase angle in degrees
15 %rad = phase angle in radians
16
17
18 function [max_stress, max_strain, freq, deg, rad] = fourier_true(
       stress, strain, t)
19
20 S = length(stress);
21 T = abs(t(find(diff(t),1)+1)-t(1));     % Measuring the Time Step
22 Fs = 1/T;                                % Sampling
       Frequency
23 f = Fs*(0:(S/2))/S;
24
25 fftStress = fft(stress);
26 fftStrain = fft(strain);
27
28 DispP2 = abs(fftStrain/S);                %Compute two sided
       spectrum for displacement
29 DispP1 = DispP2(1:S/2+1);
30 DispP1(2:end-1) = 2*DispP1(2:end-1);     %Compute single sided
       spectrum for Displacement
31
32 StressP2 = abs(fftStress/S);              %Compute two sided
       spectrum for Load
33 StressP1 = StressP2(1:S/2+1);
34 StressP1(2:end-1) = 2*StressP1(2:end-1);     %Compute single sided
       spectrum for Load
35
36 [max_stress, x1]=max(StressP1(2:end)); % Finding the position of
       the peak of the fft of load
37 [max_strain, x2]=max(DispP1(2:end)); % Finding the position of the
       peak of the fft of disp
38
39
40 r = abs(angle(fftStress(x1+1))-angle(fftStrain(x2+1))); %Measure of
        phase angle in radians
41 deg = r*180/pi;
42 if deg > 90                              % If the phase angle is
       greater that 90 degree
```

```
43  disp('WARNING: THE PHASE ANGLE IS GREATER THAT 90 DEGREES!')
44  degr=180-deg;
45 else                                    % if the phase angle is
     less than 90 degree
46  degr= deg;
47 end
48
49 freq = f(x2+1);
50 deg = (0.1323*freq)+degr;
51 rad = (deg*pi)/180; % Converting phase angle from deg to radians
52 end
```

```
1  %% visc_properties
2
3  %This function will calculate the complex, storage, and loss moduli
       AFTER
4  %the FFT, based on a shape factor, SF.
5
6  %Inputs:
7  %L = peak value of load FFT
8  %D = peak value of displacement FFT
9  %a = phase angle
10 %w = sample width
11 %h = sample height
12 %t = sample thickness
13
14 %Outputs:
15 %C = complex modulus / Pa
16 %S = storage modulus / Pa
17 %L = loss modulus / Pa
18
19 function [C, S, L] = visc_properties(L, D, a, w, h, t)
20
21 SF = (w*t)/h; %Rectangular
22 %SF = (pi/h)*((w/2)^2); %Cyclindrical
23 ComplexS = L/D; % Calculation ofComplex Stiffness (N/mm)
24 StorageS = ComplexS*cos(a); %Calculation of Storage Stiffness (N/mm
     )
25 LossS = ComplexS*sin(a); %Calculation of Loss Stiffness (N/mm)
26
27 C = (ComplexS/SF)*10^6;     %Calculation of Complex Modulus (Pa)
28 S = (StorageS/SF)*10^6;     %Calculation of Storage Modulus (Pa)
29 L = (LossS/SF)*10^6;         %Calculation of Loss Modulus (Pa)
30
31 end
```

```
1  %% visc_properties_true
2
3  %This function will calculate the complex, storage, and loss moduli
       based on the
```

```
%output of the stress and strain FFTs

%Inputs:
%stress = peak value of stress FFT
%strain = peak value of strain FFT
%a = phase angle

%Outputs:
%C = complex modulus / Pa
%S = storage modulus / Pa
%L = loss modulus / Pa

function [C, S, L] = visc_properties_true(stress, strain, a)

C_Nmm2 = (stress/strain); % Calculation of complex modulus
S_Nmm2 = (C_Nmm2*cos(a)); %Calculation of storage modulus
L_Nmm2 = (C_Nmm2*sin(a)); %Calculation of loss modulus

C = C_Nmm2*10^6;
S = S_Nmm2*10^6;
L = L_Nmm2*10^6;
end
```

```
%% Export data
%This function will export viscoelastic data for frequencies
    calculated

%Inputs
%file = output file
%f = array of frequencies
%c = array of complex moduli
%s = array of storage moduli
%l = array of loss moduli
%a = array of phase angles

%Output
%.xlsx saved with all data calculated

function [] = export_data(file, f, c, s, l, a)
OutputMatrix = readmatrix(file);
NumRows = size(OutputMatrix, 1);
NextRow = NumRows+1;
NextCell = ['A',num2str(NextRow)];

DataOutput = [(NumRows), (f), (c), (s), (l), (a)]; % Write data to
    output file
writematrix(DataOutput, file, 'range', NextCell);
end
```

```
%% plot_data
```

```
2
3  %This function will plot data saved to the output file
4
5  %Inputs:
6  %OutputFile = output file containging previously calculated
       viscoelastic
7  %data
8  %InputFile = input file with original raw data, used to label
       figure.
9
10 %Output:
11 %Figure of storage and loss moduli and phase angle in degrees
12
13 function [] = plot_data(OutputFile, InputFile)
14 OutputMatrix = readmatrix(OutputFile);
15 Freq = OutputMatrix(:,2);
16 Storage = OutputMatrix(:,4);
17 Loss = OutputMatrix(:,5);
18 Angle = OutputMatrix(:,6);
19
20 set(gca,'TickLabelInterpreter','latex','FontSize',14)
21 yyaxis left
22 scatter(Freq,Storage, 'filled')
23 hold on
24 scatter(Freq, Loss)
25 ylabel('Storage, Loss Moduli / $Pa$', 'Interpreter', 'latex', '
       fontsize', 18)
26 title(['Viscoelastic properties of: ', InputFile], 'Interpreter', '
       latex', 'fontsize', 18)
27
28 yyaxis right
29 scatter(Freq, Angle, 'filled')
30 ylabel ('Phase angle / $degrees$', 'Interpreter', 'latex', '
       fontsize', 18)
31
32 xlabel('Frequency / $Hz$', 'Interpreter', 'latex', 'fontsize', 18)
33 axis padded
34 end
```

Appendix C

LATTICES AND HYPERELASTIC MODELLING DATA

Appendix C includes supplementary data pertinent to chapter 5. This includes: Colour threshold images of lattice samples, used to calculate PVA volume; approximate lattice angle calculations; and complete data for all hyperelastic models for all samples. Note for figures of hyperelastic models: Poly, $N = 1$ = Mooney-Rivilin; R Poly, $N = 1$ = neo-Hookean; and R Poly, $N = 3$ = Yeoh.

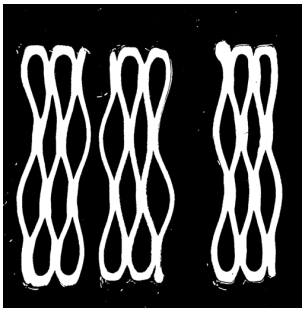

(a) *Lattice A: W = 10 mm, A = 1 mm*

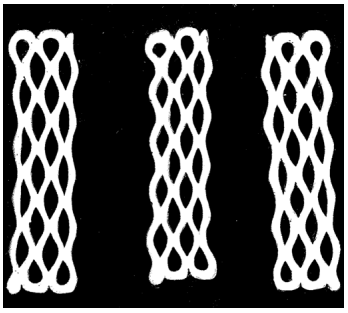

(b) *Lattice B: W = 4 mm, A = 1 mm*

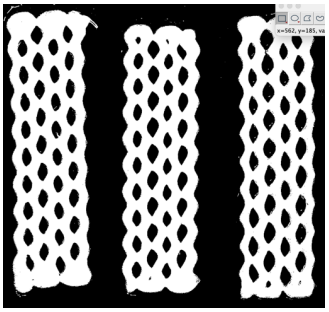

(c) *Lattice C: W = 2 mm, A = 1 mm*

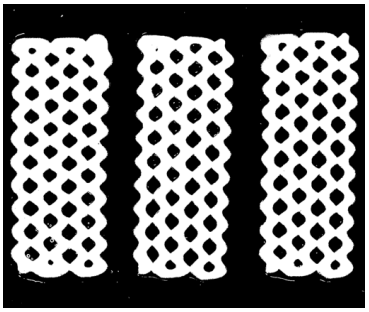

(d) *Lattice D: W = 2 mm, A = 1.5 mm*

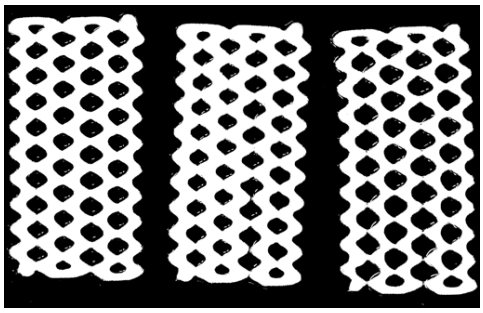

(e) *Lattice E: W = 2 mm, A = 2 mm*

Figure C.1: *Threshold images produced in Fiji in order to calculate the percentage by area of PVA in each lattice.*

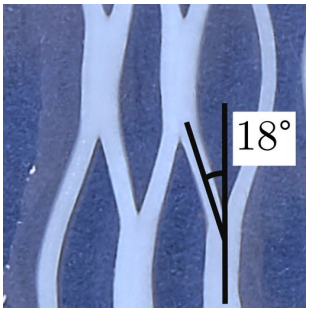

(a) Lattice A

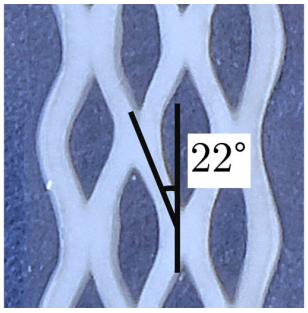

(b) Lattice B

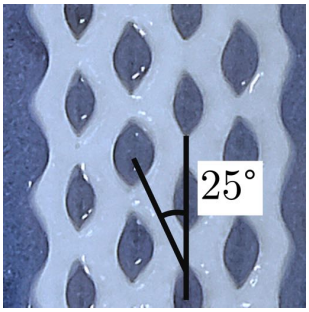

(c) Lattice C

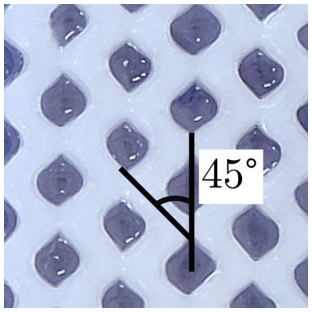

(d) Lattice D

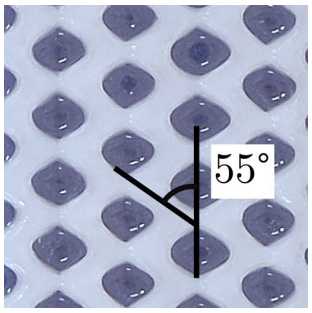

(e) Lattice E

Figure C.2: *Approximate infill angles of 3D printed lattices, illustrating the differences in filament allignment for lattices A, D and E.*

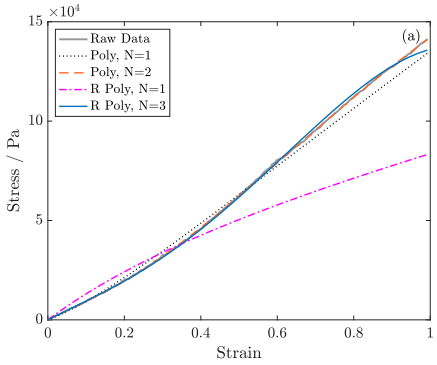

(a) *Cast S1, Polynomial*

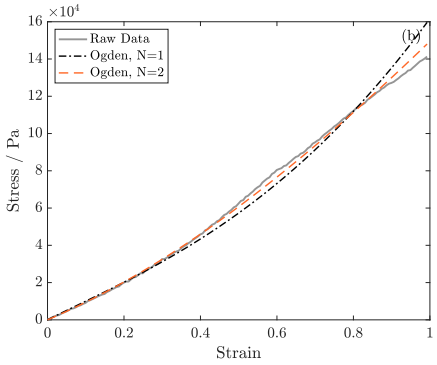

(b) *Cast S1, Ogden*

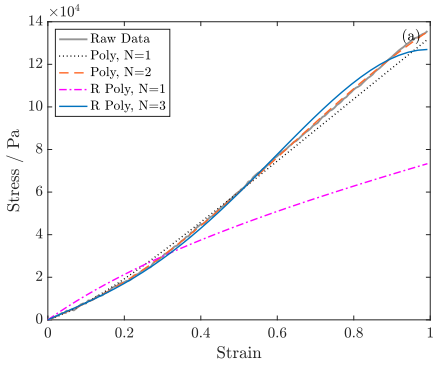

(c) *Cast S2, Polynomial*

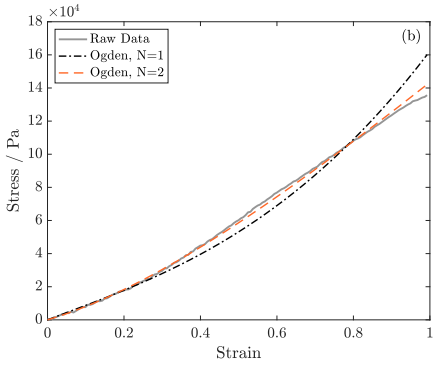

(d) *Cast S2, Ogden*

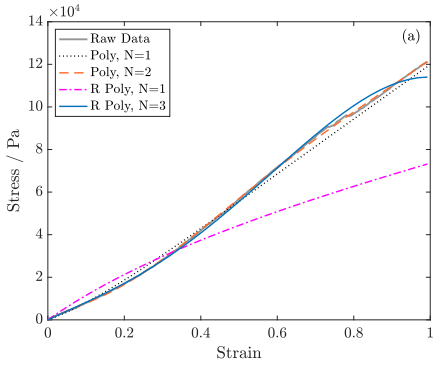

(e) *Cast S3, Polynomial*

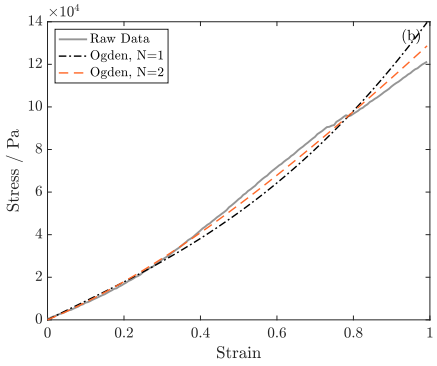

(f) *Cast S3, Ogden*

Figure C.3: *Polynomial and Ogden hyperelastic models for Lattice E*

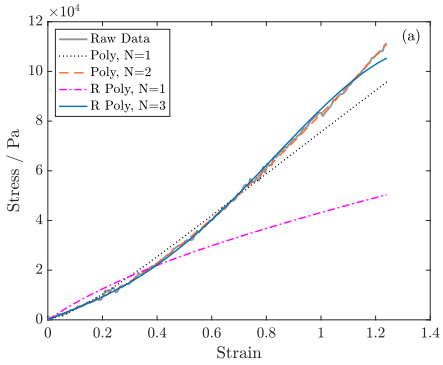

(a) AM Wave S1, Polynomial

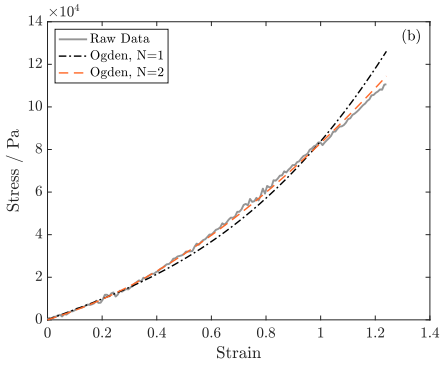

(b) AM Wave S1, Ogden

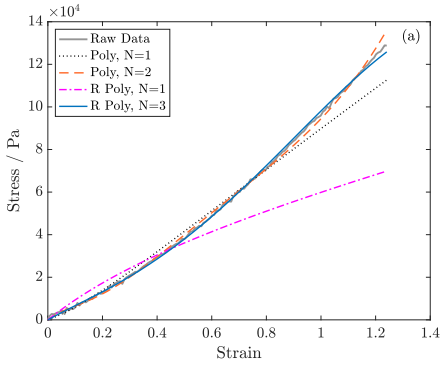

(c) AM Wave S2, Polynomial

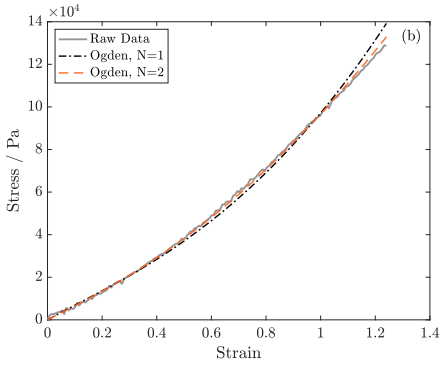

(d) AM Wave S2, Ogden

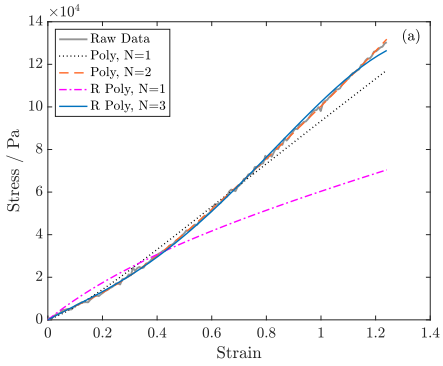

(e) AM Wave S3, Polynomial

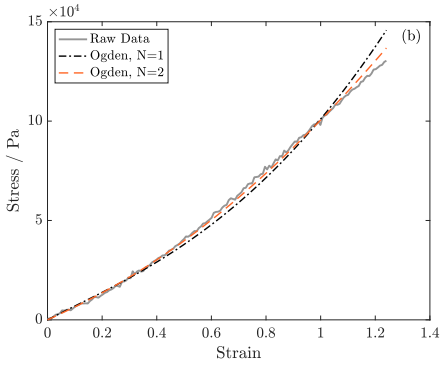

(f) AM Wave S3, Ogden

Figure C.4: *Polynomial and Ogden hyperelastic models for Lattice E*

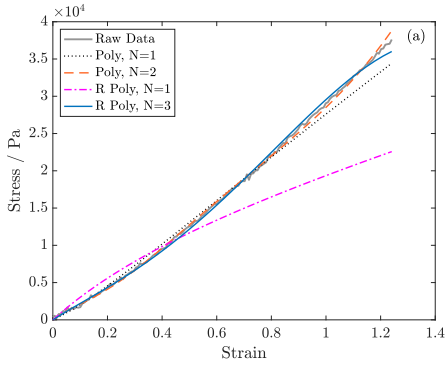

(a) Lattice A1, Polynomial

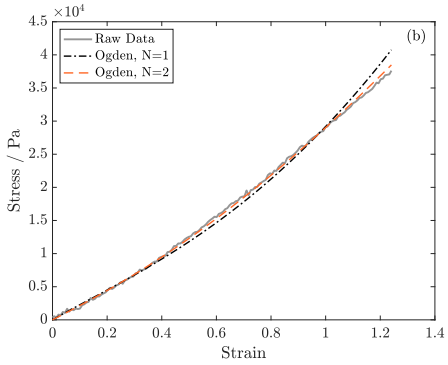

(b) Lattice A1, Ogden

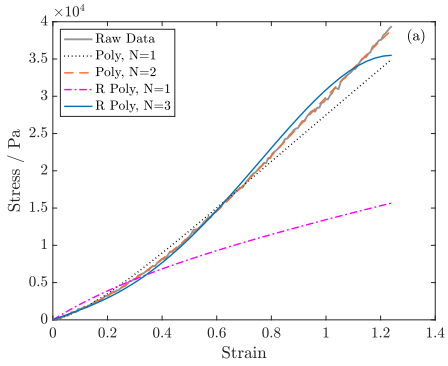

(c) Lattice A2, Polynomial

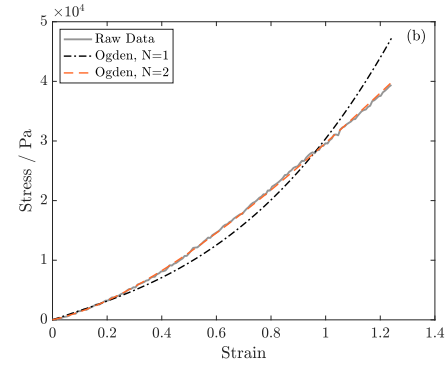

(d) Lattice A2, Ogden

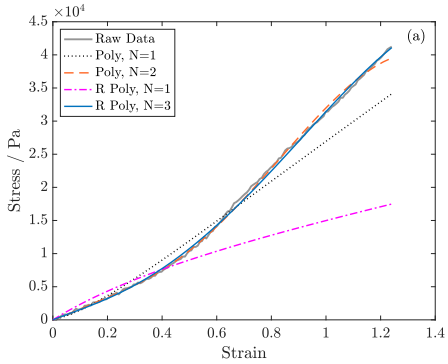

(e) Lattice A2, Polynomial

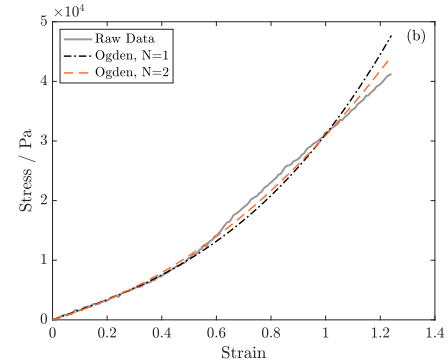

(f) Lattice A2, Ogden

Figure C.5: *Polynomial and Ogden hyperelastic models for Lattice A*

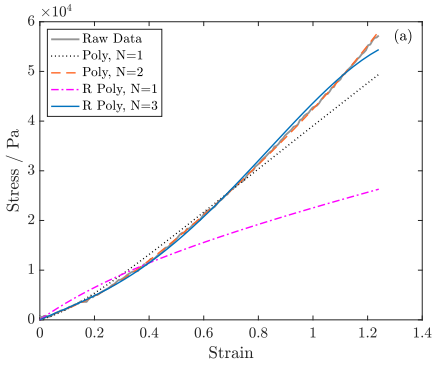

(a) Lattice B1, Polynomial

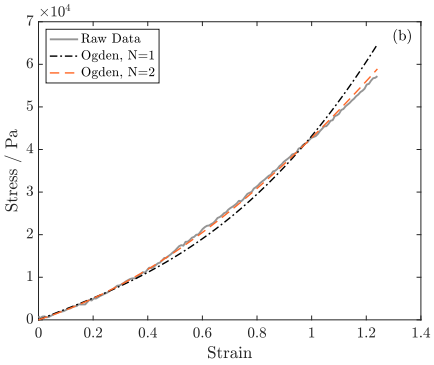

(b) Lattice B1, Ogden

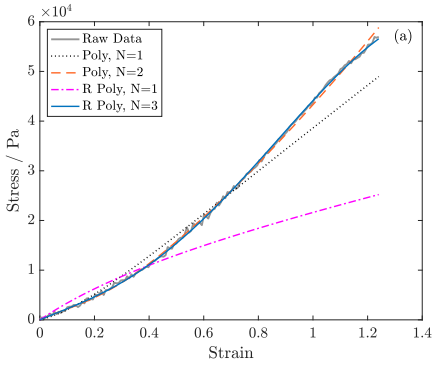

(c) Lattice B2, Polynomial

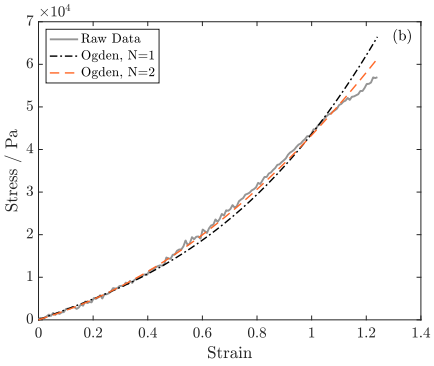

(d) Lattice B2, Ogden

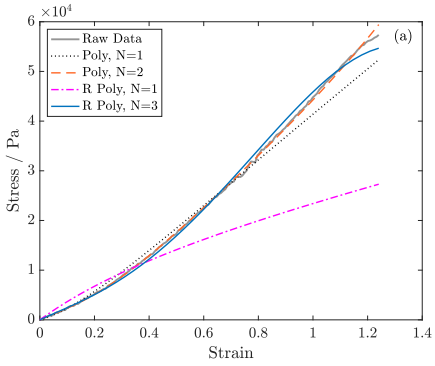

(e) Lattice B3, Polynomial

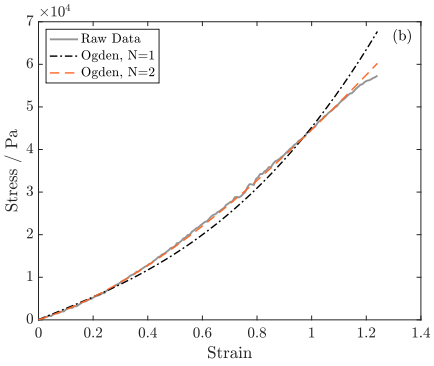

(f) Lattice B3, Ogden

Figure C.6: *Polynomial and Ogden hyperelastic models for Lattice B*

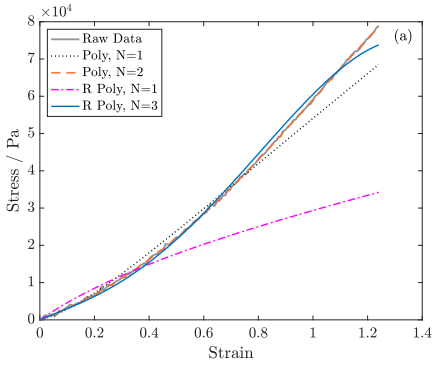

(a) Lattice C1, Polynomial

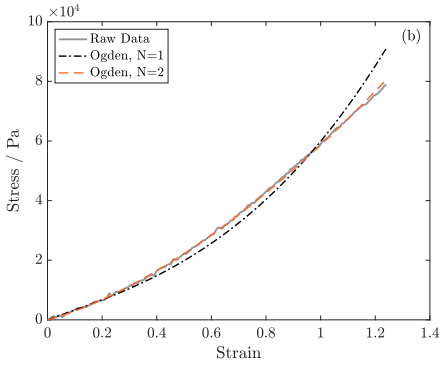

(b) Lattice C1, Ogden

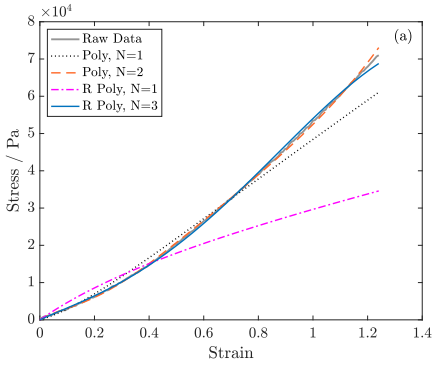

(c) Lattice C2, Polynomial

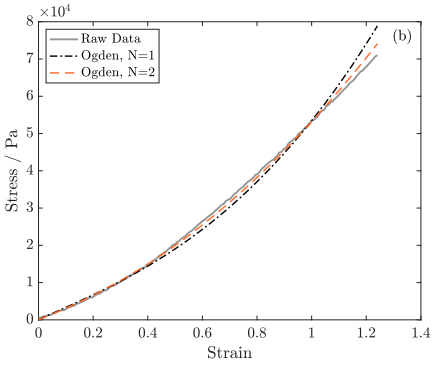

(d) Lattice C2, Ogden

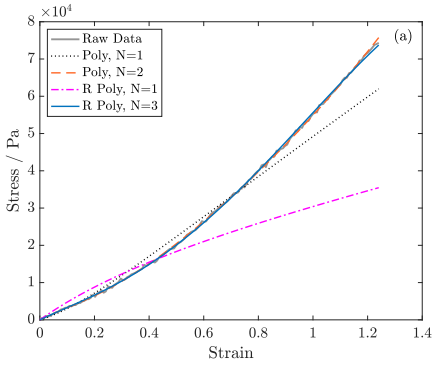

(e) Lattice C3, Polynomial

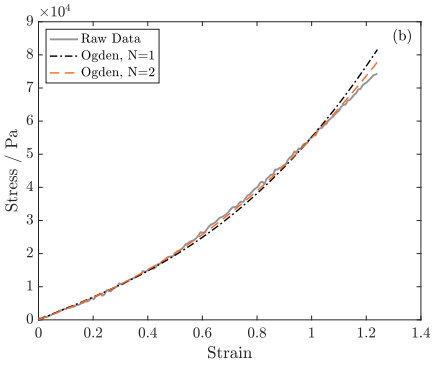

(f) Lattice C3, Ogden

Figure C.7: *Polynomial and Ogden hyperelastic models for Lattice C*

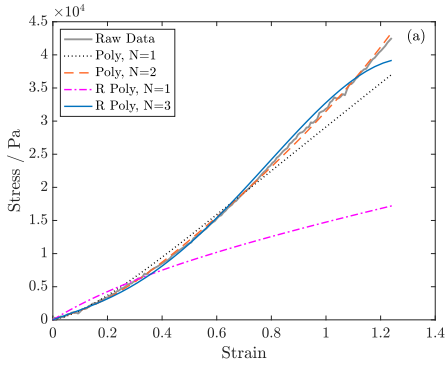

(a) Lattice D1, Polynomial

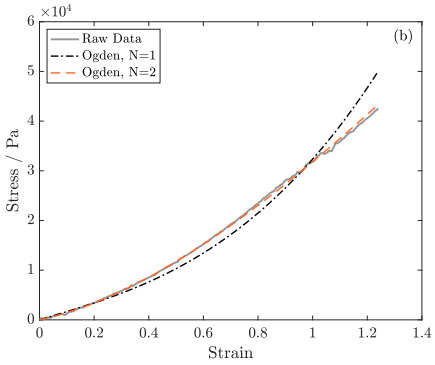

(b) Lattice D1, Ogden

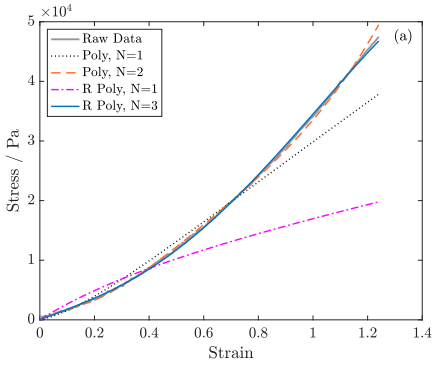

(c) Lattice D2, Polynomial

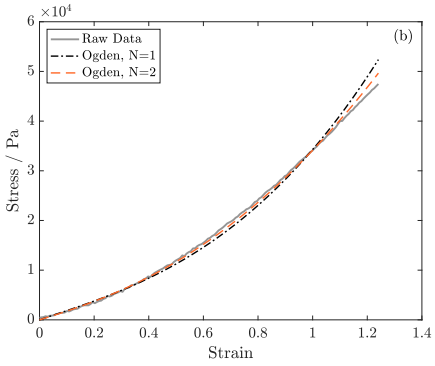

(d) Lattice D2, Ogden

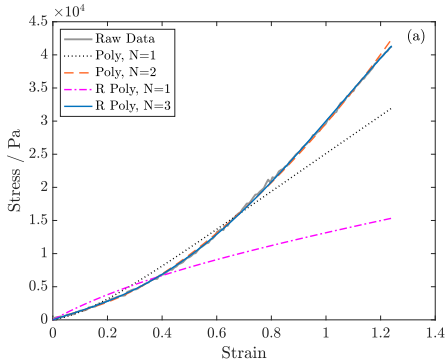

(e) Lattice D3, Polynomial

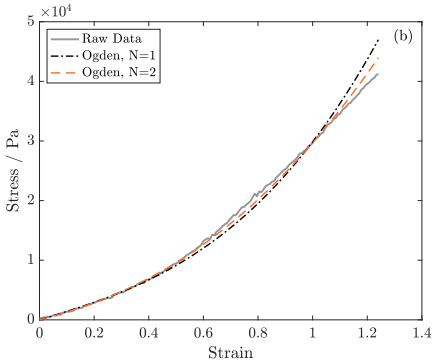

(f) Lattice D3, Ogden

Figure C.8: *Polynomial and Ogden hyperelastic models for Lattice D*

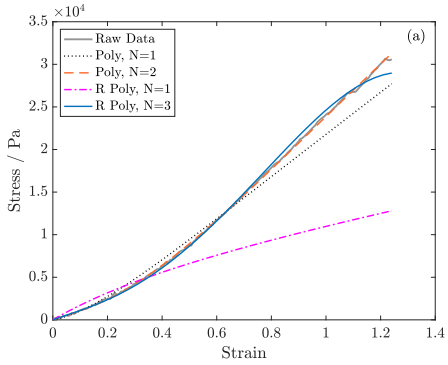

(a) Lattice E1, Polynomial

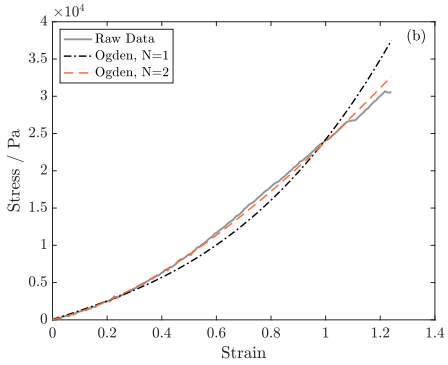

(b) Lattice E1, Ogden

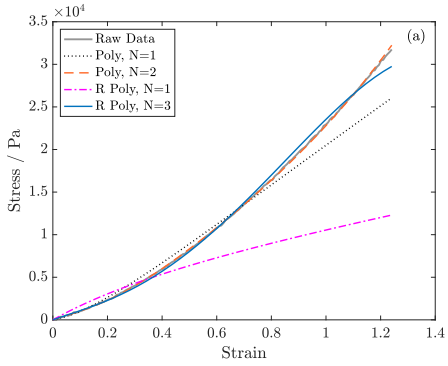

(c) Lattice E2, Polynomial

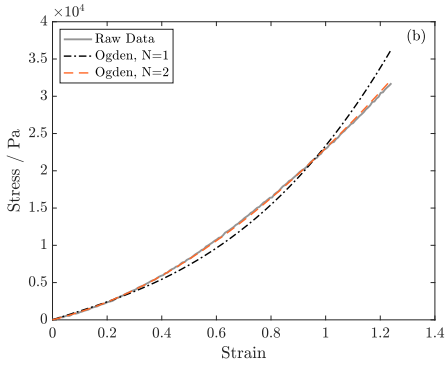

(d) Lattice E2, Ogden

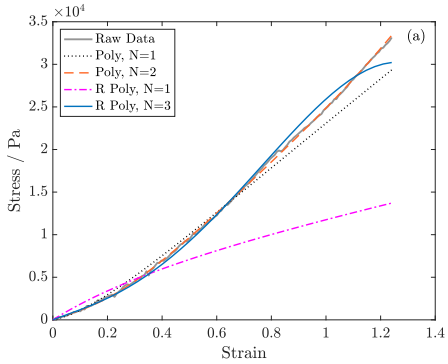

(e) Lattice E3, Polynomial

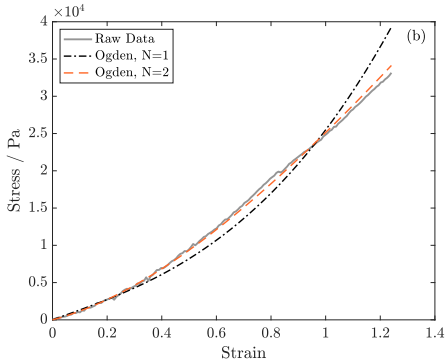

(f) Lattice E3, Ogden

Figure C.9: *Polynomial and Ogden hyperelastic models for Lattice E*

Appendix D

G-CODE FOR FUNCTIONALLY GRADED PVA LATTICES

Appendix D includes the complete Matlab code used to generate the sine wave toolpaths presented in chapter 5.

```
% This will allow the user to create the G-code for a rectangular shaped
% sample with dimensions X, Y, Z, with a sinusiodal lattice toolpath. the sinusoid
% will have a user define wavelength (mm) and amplitude (mm).

% The wavelength can either be constant along the samples width and height, or
%  defined by a function of the width (and/or height).

%To do:
    % check resolution
    % change angle of layer
    % Add explanation to all functions
    % patch(X_tot, Y_tot, Z_tot, Z_tot,'EdgeColor','interp', 'FaceColor', 'none', 'LineWidth', 2)

function [] = main()

    close all

    dlgTitle    = 'Z axis';
    dlgQuestion = 'Would you like to vary wavelength with respect to the Z axis?';
    Z_type = questdlg(dlgQuestion,dlgTitle,'Yes','No', 'No');

        switch Z_type

```

```
24              case 'Yes'
25
26                  % Input Sample Properties
27
28                  sample_dimensions = inputdlg({' Sample Length, mm (
                        X axis)', 'Sample Width, mm (Y axis)'...
29                  'Sample height, mm (Z axis)', 'Strand Diameter, mm'
                        , 'Layer Height, mm (Z axis)'});
30
31                  L = str2double(sample_dimensions{1}); % Sample
                        Length
32                  W= str2double(sample_dimensions{2}); % Sample Width
33                  T = str2double(sample_dimensions{3}); % Sample
                        Thickness
34                  Strand_diameter = str2double(sample_dimensions{4});
                            % Diameter of Extruded PVA
35                  L_height = str2double(sample_dimensions{5});
                              % layer Height
36
37                  % Input 1st layer func
38                  waitfor(msgbox ('Please enter the wave dimensions
                        and wave function with respect to X axis for the
                         FIRST layer. The same function will be used for
                         all layers.', 'First Layer'));
39                  layer_1 = inputdlg({'Min Wavelength, mm','Max
                        Wavelength, mm', ...
40                  'Define function of wavelength (l) in terms of
                        length, l:  f(l) =  ',...
41                  'Wave amplitude, mm'});
42                  L1_min = str2double(layer_1{1}); % Minimum
                        wavelength of first layer
43                  L1_max = str2double(layer_1{2}); % maximum
                        wavelength of first layer
44                  func = layer_1{3}; % function defining change in
                        wave across length
45                  L1_amp = str2double(layer_1{4}); % Amplitude of
                        first layer
46
47                  % Input last layer func
48                  waitfor(msgbox ('Please enter the wave dimensions
                        for the LAST layer. Wave wavelength and
                        amplitude will vary linearly with height.', '
                        Last Layer'));
49                  layer_n = inputdlg({'Min Wavelength, mm','Max
                        Wavelength, mm', 'Wave amplitude, mm'});
50                  Ln_min = str2double(layer_n{1}); % Minimum
                        wavelength of last layer
51                  Ln_max = str2double(layer_n{2}); % maximum
                        wavelength of last layer
```

```
52                  Ln_amp = str2double(layer_n{3}); % Amplitude of
                        last layer
53
54                  % Create G-code
55                  [XYZ] = vary_Z (L1_min, L1_max, L1_amp, Ln_min,
                        Ln_max, Ln_amp, L, W, Strand_diameter, T,
                        L_height, func);
56
57              case 'No'
58
59                  %Input sample Properties
60
61                  wave_dim = inputdlg({'Sample Length, mm (X axis)',
                        'Min Wavelength, mm',...
62                  'Max Wavelength, mm', 'Define function of
                        wavelength in terms of length, l      f(l) ='
                        ,...
63                  'Wave amplitude, mm'});
64
65                  length = str2double(wave_dim{1}); % Sample Length
66                  F_min = str2double(wave_dim{2}); % Minimum
                        Wavelength
67                  F_max = str2double(wave_dim{3}); % Maximum
                        Wavelength
68                  func = wave_dim{4}; % function defining change in
                        wave across length
69                  amplitude = str2double(wave_dim{5}); % Amplitude of
                         wave
70
71                  [X, Y] = function_wave (length, F_min, F_max, func,
                         amplitude);  % Create wave
72
73                  % Create G-code
74                  [XYZ] = constant_Z (X, Y, amplitude);
75          end
76
77      % Define output file name, and print speed
78
79      define_file = inputdlg({'Enter file name (without file
            extension): ', 'Print Speed (mm/min)'});
80      filename = define_file{1}; % Ouput file name
81      speed = str2double(define_file{2}); % Print speed
82      write_Gcode (XYZ, filename, speed); %write G-code to file.
83
84      msgbox (cat(2,' G-code saved as: ', filename, '.gcode'), '
            Success');
85
86  end
```

```
1  % This function is called if the user does not want to vary freq/
```

```
    amp with
% sample height.

% Inputs:
% X = X coords from either function_wave or graphical_wave
% Y = Y coords from either function_wave or graphical_wave
% amplitude = amplitude of wave to be used throughout print

% Outputs:
%       XYZ = G-code for all layers


function [XYZ] = constant_Z (X,Y, amplitude)

    % Input Sample Properties

    Input_2 = inputdlg({'Sample Width (in mm)', 'Strand Diameter (
        in mm)',...
            'Sample Thickness (in mm)', 'Layer Height (in mm)'});

    width = str2double(Input_2{1});% Sample Width
    d_strand = str2double(Input_2{2});  % Strand Diameter
    thickness = str2double(Input_2{3}); % Sample Thickness
    layer_height = str2double(Input_2{4}); % Layer Height


    [X_layer, Y_layer] = create_XY (X, Y, width, amplitude,
        d_strand); % Coordinates and toolpath length for single
        layer.
    [XYZ] = create_Z (X_layer, Y_layer, thickness, layer_height); %
        Coordinates and toolpath length for all layers.

    end
```

```
% This function will output the G-code for a sample with a variable
    wavelength
% and/or amplitude in the Z axis
% Inputs:
% L1_min = minimum wavelength of first layer wave
% L1_max = maximum wavelength of first layer wave
% L1_amp = amplitude of first layer wave
% Ln_min = minimum wavelength of last layer wave
% Ln_max = maximum wavelength of last layer wave
% Ln_amp = amplitude of last layer wave
% L = length of sample (Y axis)
% W = width of sample (X axis)
% strand_diameter = Diameter of extrueded PVA (This should
    calculated separately)
% T = Sample thickness
% L_layer = layer thickness
```

```
15 % func = function of wavelength with respect to the sample width
16 % Example = a function of f(l) = l, will mean wavelength will vary
       linearly between min and max along the sample width
17
18 function [XYZ_Gcode] = vary_Z (L1_min, L1_max, L1_amp, Ln_min,
       Ln_max, Ln_amp, L, W, strand_diameter, T, Layer_height, func)
19
20     N_layers = T/Layer_height; % Calcualte number of layers
21
22     min_array = linspace(L1_min, Ln_min, N_layers); % Calculate
          array of length N_layers for minimum wavelength
23     max_array = linspace(L1_max, Ln_max, N_layers); % Calculate
          array of length N_layers for maximum wavelength
24     amp_array = linspace(L1_amp, Ln_amp, N_layers); % Calculate
          array of length N_layers for amplitude
25
26     XYZraw = []; % Create empty array for raw coordinates (This will
           be used to plot toolpath)
27     XYZ_Gcode = []; % Empty array for G-code of all layers
28
29
30     for i = 1:N_layers
31
32         [X, Y] = function_wave(L, min_array(i), max_array(i), func,
              amp_array(i)); % wave function for current layer
33         [X_layer, Y_layer] = create_XY (X, Y, W, amp_array(i),
              strand_diameter); % X, Y coords for current layer
34
35         midpoint = find_midpoint(X_layer, Y_layer); % Midpoint for
              current layer
36
37         XY = cat(2, X_layer, Y_layer); % Concatenate X and Y
              coordinates
38         XYcentred = XY - midpoint; % Centre Coords about midpoint
39
40         Xcoord = "X" + XYcentred(:,1); % G-code for X coordinate (
              string array)
41         Ycoord = "Y" + XYcentred(:,2); %G-code for Y coordinate (
              string array)
42         space = " "; % a space!
43         space_array = repmat((space), length(Xcoord), 1); % Array of
               spaces same length as X,Y coordinate
44         G1 = repmat(("G1"), length(Xcoord), 1); % array of 'G1' same
               length as X,Y coordinates
45         XY_Gcode = strcat(G1, space_array, Xcoord, space_array,
              Ycoord); % Concatenate X and Y Gcode into single string
              array
46
47         XY_layer = XYcentred; % Copy Raw G-code data to be
```

```
        manipulated
48      Initial_XY = strcat('G0 ', (Xcoord(1,:)), space, (Ycoord
        (1,:))); % G-code for inital X and Y coords - This will
        be used to move extruder into place before printing
49
50
51
52      if i == 1
53
54          Z_layer = repmat((Layer_height), length(XY_layer), 1); %
            Array of Z coordinates for one layer.
55          Z_Gcode = 'G0 Z' + Layer_height + ' ;New Layer'; % G-code
             instruction for Z axis
56
57      else
58
59          offset = ((i-1)*0.2*Layer_height); % Calculate offset
            (20% of layer height * number of previous layers)
60          Adjusted_l_height = i*Layer_height - offset; % Adjust
            layer height
61          Z_layer = repmat((Adjusted_l_height), length(XY_layer),
            1); % Array of Z coordinates for one layer.
62          Z_Gcode = 'G0 Z' + Adjusted_l_height + ' ;New Layer'; % G
            -code instruction for Z axis
63
64      end
65
66      XYZ_layer = cat(2, XYcentred, (Z_layer)); % Concatenate XY
        and Z coords for current (single) layer (Raw data)
67
68      clearance_val = 5 + (i*Layer_height); % calculate Z
        clearance
69      clearance_raw = XYZ_layer((length(XYZ_layer)),:); % Find
        last line in XYZ_layer
70      clearance_raw(3) = (clearance_val); % Change last Z coord in
         XYZ_layer to clearance value
71
72      XYZraw = cat(1, XYZraw, XYZ_layer); % Concatenate data for
        current layer onto XYZ_raw
73      XYZraw = cat(1, XYZraw, clearance_raw); % Concatenate
        clearance XYZ_raw
74
75      Pressure_on = 'M760 ;Turn on PH1'; % G-code to turn pressure
         on
76      Pressure_off = 'M761 ;Turn off PH1'; % G-code to turn
        pressure off
77      clearance_Gcode = 'G0 Z' + clearance_val; % G-code for
        clearance
78
```

```
79          XYZ_Gcode = cat(1, XYZ_Gcode, Initial_XY, Z_Gcode, space,
                Pressure_on, XY_Gcode, Pressure_off, space,
                clearance_Gcode); % Concatenate all data for current
                layer onto YXZ_Gcode
80      end
81
82      XYZ_length = length(XYZ_Gcode); % Find length of XYZ_Gcode
83      XYZ_Gcode(XYZ_length, :) = []; % Delte last line (clearance is
            not need at the end of print)
84
85
86      figure()
87      plot3(XYZraw(:,1), XYZraw(:,2), XYZraw(:,3), 'k', 'linewidth',
            2) % 3D plot visualizing toolpath.
88      axis equal
89      axis padded
90      set(gca,'TickLabelInterpreter','latex','FontSize',14)
91      xlabel('Sample width (mm)', 'Interpreter', 'Latex','FontSize'
            ,18)
92      ylabel('Sample length (mm)', 'Interpreter', 'Latex','FontSize'
            ,18)
93      zlabel('Sample height (mm)', 'Interpreter', 'Latex','FontSize'
            ,18)
94  end

1   % This function will create the X and Y coordinates of a single
        wave.
2   % The use will define how the wavelength will vary along the length
         of the
3   % sample by inputing a function
4
5   % Inputs:
6   % width = sample width, mm  (X axis)
7   % min = minimum wavelength of wave (mm)
8   % max = max wavelength of wave (mm)
9   % func = function defining how frequenct will vary (from min to max
        )
10  % along the width of the sample
11  % amplitude = wave amplitude in Y axis
12
13  % Outputs:
14  % X = X coordinates for a single wave
15  % Y = Y coordinates for a single wave
16  % 2D plot showing toolpath for a single wave
17
18
19  function [X, Y] = function_wave(width, w_min, w_max, func,
        amplitude)
20
21    f_min = 1/w_min; % Calculate minimum frequency from wavelength
```

```
22    f_max = 1/w_max; % Calculate maximum frequency from wavelength
23
24    Fs = 10; %Number of samples per mm
25    dt = 1/Fs;
26    w = 0:dt:width; % create array from 0 to width with steps of dt
27    len = length(w); % Find length of w
28    f_in = linspace(f_min, f_max, len); % create a linear array of
          frequencies from min to max with the same length as w
29
30    Eq = strcat('@(l)',func); % prepare function
31    func_out = str2func(char(Eq)); % convert from string to function
32    f = func_out(f_in); % Apply function to linear wavelength array
33
34    wave = (sin(2*pi*cumsum(f)/Fs)) / 2;
35    X = w; % x coordinate in mm
36    Y = wave*amplitude;  % y coordinate in mm
37
38    %plot wave, and change in wavelength along the sample length:
39
40    set(gca,'TickLabelInterpreter','latex','FontSize',16)
41
42    pbaspect([2 1 1])
43    yyaxis left;
44    plot(X,Y, 'linewidth', 2)
45    axis padded
46
47    ylabel('Amplitude (mm)', 'Interpreter', 'Latex','FontSize',18),
          xlabel('Sample length (mm)', 'Interpreter', 'Latex','FontSize'
          ,18)
48    ylim ([-3 3])
49
50    yyaxis right
51    plot(X,f, 'linewidth', 2)
52    ylabel ('Frequency (Hz)', 'Interpreter', 'Latex','FontSize',18)
53
54 end
```

```
1  % This function will create the X and Y coordinates for a single
       layer.
2  % Inputs:
3  % X = list of X coordinates output from  function_wave
4  % Y = list of Y coordinates output from either function_wave
5  % width = sample length (Y axis)
6  % amp = amplitude of wave
7  % d_strand = diamter of the strand of extruded PVA.
8  %
9  % Outputs:
10 % X_layer = list of X coordinates for a single layer
11 % Y_layer = list of X coordinates for a single layer
12
```

```
13 function [X_layer, Y_layer] = create_XY (X, Y, width, amp, d_strand
       )
14
15     X_layer = transpose(X); % transpose X coords (vertical array of
           coords)
16     Y_layer = transpose(Y); %% transpose Y coords (vertical array
       of coords)
17     x1 = transpose(X); % Copy X coordinates to be manipulated
18     y1 = transpose(Y); % Copy Y coordinates to be manipulated
19
20     line_space = amp + (d_strand/2); % Calculate line spacing
21     num_strands = width / line_space; % calcualte number of strands
22
23 for i = 1:num_strands
24     x1 = flip(x1); % Reverse direction of X coords from previous
       strand
25     y1 = flip(y1)+line_space; % Reverse direction of Y coords for
       previous strand and add offset
26     offset = i*line_space; % Calulate Y offset from 0
27     y0 = y1 - offset; % offset Y about 0
28     y0 = -y0; % reverse Y about 0
29     y1 = y0 +offset; % Re-add offset
30     X_layer = cat(1,X_layer, x1); % Concatenate X coords onto
       X_layer
31     Y_layer = cat(1,Y_layer, y1); % Concatenate Y coords onto
       Y_layer
32 end
33
34     X_layer = round(X_layer, 2, 'decimals');% Round X coords to 3
       significant figures
35     Y_layer = round(Y_layer, 2, 'decimals');% Round Y coords to 3
       significant figures
36 end
```

```
1 % This function will find the midpoint of a list of X, Y
      coordinates
2
3 % Inputs:
4 % X = list of X coordinates
5 % Y = list of corresponding Y coordinates
6
7 % Output:
8 % midpoint = the X and Y coordiantes of the midpoint of the
      inputted
9 % coordinate system.
10 % This will be repeated in an array of length X.
11
12
13 function [midpoint] = find_midpoint(X,Y)
14 maxX = max(X); % Find maximum of X
```

```
minX = min(X); % Find minimum of X
midX = maxX - (maxX-minX)/2; % Calc Midpoint

maxY = max(Y); % Find maximum of Y
minY = min(Y); % Find minimum of Y
midY = maxY - (maxY-minY)/2; % Calc Midpoint

midpoint = repmat([midX; midY], 1, length(X)); % Repeat Midpoint in an array of length XY
midpoint = transpose(midpoint); % Transpose array
end
```

```
% This function will create the X and Y coordinates for a all layers.
% Inputs:
% X_layer = list of X coordinates for a single layer (output from create_XY)
% Y = list of Y coordinates for a single layer (output from create_XY)
% T = sample thickness
% L_layer = layer thickness
%
%Outputs:
% XYZ_Gcode = G-code for all layers.
% 3D plot visualizing toolpath for the print

function [XYZ_Gcode] = create_Z (X_layer, Y_layer, T, Layer_height)

N_layers = T/Layer_height; % Calcualte number of layers

midpoint = find_midpoint(Y_layer, X_layer); % Find midpont of layer

XY = cat(2, Y_layer, X_layer); % Concatenate X and Y coordinates
XYcentred = XY - midpoint; % Centre Coords about midpoint
XYZ_raw = []; % Create empty array for raw coordinates (This will be used to plot toolpath)

Xcoord = "X" + XYcentred(:,1); % G-code for X coordinate (string array)
Ycoord = "Y" + XYcentred(:,2); %G-code for Y coordinate (string array)
space = " "; % a space!
space_array = repmat((space), length(Xcoord), 1); % Array of spaces same length as X,Y coordinates
G1 = repmat(("G1"), length(Xcoord), 1); % array of 'G1' same length as X,Y coordinates
XY_Gcode = strcat(G1, space_array, Xcoord, space_array, Ycoord); % Concatenate X and Y Gcode into single string array

Initial_XY = strcat("G0 ", (Xcoord(1,:)), space, (Ycoord(1,:))); %
```

```
    G-code for inital X and Y coords - This will be used to move
    extruder into place before printing
XYZ_Gcode = []; % Empty array for G-code of all layers

for i = 1:N_layers

XY_layer = XYcentred; % Copy Raw G-code data to be manipulated


if i == 1

        Z_layer = repmat((Layer_height), length(XY_layer), 1); %
            Array of Z coordinates for one layer.
        Z_Gcode = "G0 Z" + Layer_height + " ;New Layer";  % G-code
            instruction for Z axis

else

        offset = ((i-1)*0.2*Layer_height); % Calculate offset (20%
            of layer height * number of previousz  layers)
        Adjusted_l_height = i*Layer_height - offset; % Adjust layer
            height
        Z_layer = repmat((Adjusted_l_height), length(XY_layer), 1);
            % Array of Z coordinates for one layer.
        Z_Gcode = "G0 Z" + Adjusted_l_height + " ;New Layer"; % G-
            code instruction for Z axis

end

XYZ_layer = cat(2, XY_layer, (Z_layer)); % Concatenate XY and Z
    coords for current (single) layer (Raw data)

clearance_val = 5 + (i*Layer_height); % calculate Z clearance
clearance_raw = XYZ_layer((length(XYZ_layer)),:); % Find last line
    in XYZ_layer
clearance_raw(3) = (clearance_val); % Change last Z coord in
    XYZ_layer to clearance value

XYZ_raw = cat(1, XYZ_raw, XYZ_layer); % Concatenate data for
    current layer onto XYZ_raw
XYZ_raw = cat(1, XYZ_raw, clearance_raw); % Concatenate clearance
    XYZ_raw

Pressure_on = "M760 ;Turn on PH1"; % G-code to turn pressure on
Pressure_off = "M761 ;Turn off PH1"; % G-code to turn pressure off
clearance_Gcode = "G0 Z5"; % G-code for clearance


XYZ_Gcode = cat(1, XYZ_Gcode, Initial_XY, Z_Gcode, space,
```

```
    Pressure_on,  XY_Gcode, Pressure_off, space, clearance_Gcode);
          % Concatenate all data for current layer onto YXZ_Gcode
end

XYZ_length = length(XYZ_Gcode); % Find length of XYZ_Gcode
XYZ_Gcode(XYZ_length, :) = []; % Delete last line (clearance is not
    need at the end of print)

figure();
plot3(XYZ_raw(:,1), XYZ_raw(:,2), XYZ_raw(:,3), 'k', 'linewidth',
   2) % 3D plot visualizing toolpath.

axis equal
axis padded
set(gca,'TickLabelInterpreter','latex','FontSize',14)
xlabel('Sample width (mm)', 'Interpreter', 'Latex','FontSize',18)
ylabel('Sample length (mm)', 'Interpreter', 'Latex','FontSize',18)
zlabel('Sample height (mm)', 'Interpreter', 'Latex','FontSize',18)

end
```

```
% This funciton will write Gcode to a .gcode file in the current
   Matlab folder
% Inputs:
% XYZ = string array of G-code output from either constant_Z.m or
% vary_Z.m
% Filename = name of output file. e.g. test_Gcode
% This should not include file extension
% Speed = Desired print speed in mm/minute

function [] = write_Gcode(XYZ, filename, speed)


  feedrate = sprintf(" F%d ;Feedrate = %d /min", speed, speed); %
     Create G-code to assign feedrate
  XYZ(5,:) = strcat((XYZ(5,:)), feedrate); % concatenate feedrate
     onto first line of g-code for extrusion

  Start = [ % G-code start
          "G90  ;Use absolute coordinates";
          "G0 Z5";
          ];

  End = [ % G-code end
  "G0 Z5";
  "G0 X0 Y0";
  "M84 ;Disable Steppers";
  " ";
  ";End of Gcode"];
```

```
27    txt_ext = strcat(filename, '.txt'); % Filename with .txt
          extension
28    gcode_ext = strcat(filename, '.gcode');% Filename with .gcode
          extension
29
30    writematrix(Start, txt_ext); % Write start to .txt file
31    writematrix(XYZ, txt_ext,'WriteMode','append'); % Write G-code to
          .txt file
32    writematrix(End, txt_ext,'WriteMode','append'); % Write end to .
          txt file
33
34    file = dir(txt_ext);
35    movefile(file.name, gcode_ext); % Convert .txt file to .gcode
          file
36
37 end
```